MTL TR 88-46

AD

A COMBINED ISOTROPIC-KINEMATIC HARDENING MODEL FOR LARGE DEFORMATION METAL PLASTICITY

CHARLES S. WHITE
MATERIALS DYNAMIC BRANCH

December 1988

US ARMY
LABORATORY COMMAND
MATERIALS TECHNOLOGY LABORATORY

U.S. ARMY MATERIALS TECHNOLOGY LABORATORY
Watertown, Massachusetts 02172-0001

The findings in this report are not to be construed as an official Department of the Army position, unless so designated by other authorized documents.

Mention of any trade names or manufacturers in this report shall not be construed as advertising nor as an official indorsement or approval of such products or companies by the United States Government.

DISPOSITION INSTRUCTIONS

Destroy this report when it is no longer needed.
Do not return it to the originator.

REPORT DOCUMENTATION PAGE

READ INSTRUCTIONS BEFORE COMPLETING FORM

1. REPORT NUMBER: MTL TR 88-46
2. GOVT ACCESSION NO.
3. RECIPIENT'S CATALOG NUMBER

4. TITLE (and Subtitle): A COMBINED ISOTROPIC-KINEMATIC HARDENING MODEL FOR LARGE DEFORMATION METAL PLASTICITY
5. TYPE OF REPORT & PERIOD COVERED: Final Report
6. PERFORMING ORG. REPORT NUMBER

7. AUTHOR(s): Charles S. White
8. CONTRACT OR GRANT NUMBER(s)

9. PERFORMING ORGANIZATION NAME AND ADDRESS:
U.S. Army Materials Technology Laboratory
Watertown, Massachusetts 02172-0001
ATTN: SLCMT-MRD
10. PROGRAM ELEMENT, PROJECT, TASK AREA & WORK UNIT NUMBERS: D/A Project: 1L263102D077

11. CONTROLLING OFFICE NAME AND ADDRESS:
U.S. Army Laboratory Command
2800 Powder Mill Road
Adelphi, Maryland 20783-1145
12. REPORT DATE: December 1988
13. NUMBER OF PAGES: 248

14. MONITORING AGENCY NAME & ADDRESS(if different from Controlling Office)
15. SECURITY CLASS. (of this report): Unclassified
15a. DECLASSIFICATION/DOWNGRADING SCHEDULE

16. DISTRIBUTION STATEMENT (of this Report)

Approved for public release; distribution unlimited.

17. DISTRIBUTION STATEMENT (of the abstract entered in Block 20, if different from Report)

18. SUPPLEMENTARY NOTES

Submitted to the Department of Mechanical Engineering, MIT, in partial fulfillment of the requirements for the Degree of Doctor of Philosophy in Mechanical Engineering.

19. KEY WORDS (Continue on reverse side if necessary and identify by block number)

Plastic properties	Stainless steel	Mathematical models
Plastic deformation	Aluminum	Stress strain relations
Metals	Carbon steels	Strain hardening

20. ABSTRACT (Continue on reverse side if necessary and identify by block number)

(SEE REVERSE SIDE)

Block No. 20

ABSTRACT

The need for increased accuracy in material modeling has been driven in recent years by advances in computing capability and the complexity of problems which now may be analyzed. Current material models are unable to represent many of the important multi-dimensional effects of the plastic deformation of metals to large strain. These effects can become very important at the level of deformation reached in metal processing operations, shear band formation, penetration mechanisms, and crack tip processes.

An experimental program was conducted to produce a number of different types of tests on several materials. The types of tests included: tension, large strain compression, symmetric cyclic, unsymmetric cyclic, single reverse and large strain torsion. Materials tested were type 316 stainless steel and 1100-O aluminum. Also data for 3 carbon steels was analyzed.

A new constitutive model for metal deformation is introduced to analyze and predict these experiments. The model contains both isotropic and kinematic hardening components but overcomes some of the shortcomings of previous such models by introducing new material functions. The two important new features are: 1) The back stress moduli depend upon the position of the back stress within a surface defined by its previous maximum norm, and 2) During a reversing event the isotropic component initially softens. The effects of these features are discussed and implemented using simple functions in the constitutive model.

The model captures key features of small strain uniaxial cyclic behavior very well including the additional hardening due to nonproportional cycling in tension-torsion. The predictions of the finite torsion results are not as close. The inclusion of plastic spin does not affect these results.

Preface

The research presented in this report was carried out at the U.S. Army Materials Technology Laboratory and at the Massachusetts Institute of Technology in Cambridge, Massachusetts.

This report is excerpted from the Ph.D. thesis of the author and was completed in August, 1988 in the Department of Mechanical Engineering at the Massachusetts Institute of Technology. The thesis was supervised by Professor Lallit Anand of the Department of Mechanical Engineering at MIT. Also serving on the thesis advisory committee were Professors David M. Parks and Klaus-Jurgen Bathe of MIT and Dr. Dennis M. Tracey of MTL.

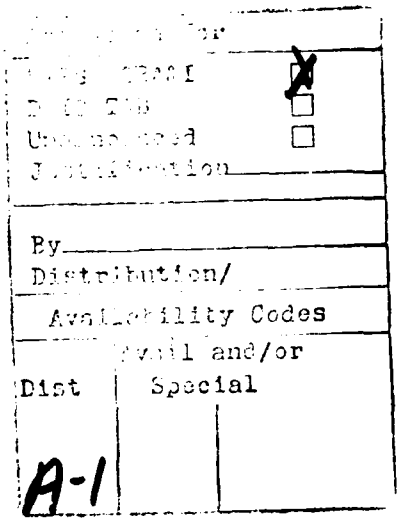

Table of Contents

Chapter 1

Introduction

In recent years there has been an increased interest in the formulation of finite deformation, elastoplastic, constitutive equations. Current material models are unable to represent many of the important multi-dimensional effects of the plastic deformation of metals to large strain. These effects can become very important at the level of deformation reached in metal processing operations, shear band formation, penetration mechanisms, and crack tip processes.

The great advances in computing capability and numerical procedures in the last decade have led to a tremendous increase in the types and complexity of problems which may be now analyzed. The computer revolution has far outstripped the precision of available material models. Previously, a first order prediction from simple constitutive equations was thought to be sufficient since that coincided with the accuracy of the available anaylsis techniques. Now the material models greatly lag our ability to apply them in analysis.

One reason that constitutive development has suffered is the limited experimental data available to describe large strain behavior. Even more important than the volume of data available is the type. Pure uniaxial information is not sufficient

when many of the discrepancies of the classical theories derive from their tensorial generalizations. Chief among these phenomena are the differences between material behavior in tension/compression and in torsion. When comparing the Mises equivalent stress versus equivalent strain curves for torsion and compression, the results are seen to differ. The torsion results generally fall below the compression results.

Attempts to model this, and other findings, have led some to consider variations of the classical kinematic hardening plasticity law. These efforts have illustrated problems that arise when simple, small strain, constitutive laws are hastily generalized to the finite deformation regime. The most notable of these is the prediction of an oscillating shear stress response for monotonic loading in simple shear.

Many authors have considered this problem from an analytical point-of-view over the past five years. Consequently, many theories or constitutive assumptions have been postulated. None of these have been properly investigated experimentally. A consistent and complete experimental data base has not been available for evaluating the models.

The purpose of this work is to conduct a complete set of experiments, on several materials, that would allow proper comparisons to be made. This set of experiments includes, of course, large strain compression and torsion tests. Additionally, it was realized that a proper model would need to correctly model the back stress or kinematic hardening as well as the isotropic portion. To aid these determinations, reverse loading and cyclic experiments were also conducted. These were necessary to quantify the Bauschinger effect.

The most extensive experimentation and modeling of back stress phenomena is in the small strain cyclic regime. A proper model of the back stress and its evolution

would need to be consistent with the results seen there. Currently none of the large strain theories correctly model this regime. Different theories have been used by researchers working in these different regimes. No constitutive model unifying these different areas has been available.

It is well known that the back stress builds up quickly in the first few percent strain. This is where most of the *action* occurs. Its effects can be important at both small and large strain. A theory which desires to model the effect of the back stress at large strain needs to also correctly model its behavior at small strain.

This work has two major parts. The first is the experimental results. These provide a coherent set of tests, useful for plasticity model construction and verification. The second is the modeling ideas which allow unification of the different strain regimes. These are brought out in a new constitutive model which is applied to the experimental results.

This document has two main parts, each giving a slightly different perspective. It is organized in the following way. The first part examines the Bauschinger Effect from a material scientist's viewpoint. Chapter 2 contains a review of the experimental literature concerning measurement and description of the Bauschinger Effect. The quantitative models are not discussed but the causes of the effect are emphasized. In Chapter 3, micromodeling of the Bauschinger Effect in a particle hardened alloy is presented. A finite element model was used to model the effects of the particle-matrix interaction. The results demonstrate many of the experimental observations of nonmonotonic loading.

The second main part of this document takes a continuum mechanics viewpoint. The modeling of metal plasticity is reviewed in Chapter 4. A new constitutive

model is presented in Chapter 5. It contains new features motivated by the reviews of the literature. Chapter 6 contains the experimental program and results. The comparison of the theory with these experiments is given in Chapter 7. Finally, the conclusions drawn from this study are presented and discussed in Chapter 8.

Chapter 2

Review of Bauschinger Effect

2.1 Scope of Chapter

In this chapter the relevant, published work on the anisotropic hardening behavior of metals as exhibited by the Bauschinger Effect is reviewed. This is important behavior to consider, as will be shown, since the influence of the causes of this behavior have far reaching effects in small strain, cyclic, and large strain metal plasticity. There exists an extensive literature containing observations of the Bauschinger Effect. Only a brief review is given here. Major results are listed as well as a review of some individual investigator's findings. It is valuable to understand the underlying focus of the studies presented in the literature. This is important when reinterpreting the results of these previous investigators in light of more recent findings. The summary of this chapter contains some of these new results and how they impact previous work.

2.2 Review of the Literature

This section is intended to review the experimental measurement of the Bauschinger effect in metals. It does not include experimental techniques but rather presents ma-

jor experimental results in a historical manner leading to the current understanding of the phenomenon. The Bauschinger effect should not be considered an anomolous material behavior because it will be shown to be present in a large variety of metals ranging from pure single crystals to multiphase, polycrystals. The viewpoint of concern is the phenomenological approach describing macroscopic behavior.

In 1881, Johann Bauschinger [1886] reported that a metal specimen (Bessemer steel), after receiving an axial extension into the plastic range showed a decrease in the magnitude of the yield stress upon subsequent compression. This reduction in yield stress upon reversal of straining is known as the "Bauschinger effect". This phenomenon has been noted in both rate independent and rate dependent regimes of material behavior. This review will concentrate on the rate independent observations since different classes of experiments are required to determine back stress existence and magnitude in the viscoplastic response regime.

We will also use the term **back stress** to denote a modeling concept first put forth by Prager [1956] to describe a multiaxial generalization of this phenomenon noted in one dimension by Bauschinger. Many of the modern constitutive theories for elevated temperature structural applications contain back stress variables. For a review of these applications and a discussion of the modeling of back stress at elevated temperature see Swearengen and Holbrook [1985].

Just as manifestations of the Bauschinger effect have been seen in the very slow strain rate (creep) regime, so has it been observed in the high strain rate regime. Ogawa [1985] demonstrated that the Bauschinger effect at high strain rate ($5 \times 10^2 \text{sec}^{-1}$) has similar features to the quasistatic case. We will not consider the high strain rate environment separately here.

The microscopic approach of requiring the critical shear stress on a slip plane within a crystal to depend upon the direction of slipping has also been recently pursued (Weng [1980]). These shear components can then be averaged over the available slip systems to yield the macroscopic behavior of the polycrystalline sample. Models such as these may lead to increased understanding of the mechanisms underlying the observed Bauschinger effect but are outside of the domain of the phenomenological approach and will not be considered in detail here.

The alloy systems which generally show the largest Bauschinger effect, or differences in yield stresses, is the two phase system where hard particles are contained in a relatively soft matrix. Reasons for this will be discussed later but since this type of system dramatically shows the effect, proportionately much of the experimental work has looked at these systems.

In order to clarify some of the terms that have been used rather loosely until now consider Figure 2.1. Let curve A represent the stress strain behavior of a specimen loaded monotonically in tension. If the specimen is loaded from zero up to some stress and then unloaded and compressed along curve B it will yield in compression at a stress level whose magnitude σ_r may be much less than σ_f from which it was unloaded. To make this even more clear invert the compressive portion of curve B so that it appears as a reloading curve (curve C).

Another general feature often observed is the high degree of roundedness to the reverse flow curve after re-yielding. This is reminiscent of the stress strain curve for an annealed specimen. If a specimen that is loaded in tension to σ_f is unloaded to zero stress then reloaded in tension it will nearly retrace its unloading curve to σ_f then continue flowing along curve A as if the unloading had never occurred.

The re-yield point may be sharp and it is sufficient to use σ_f as the yield point. For the specimen which is compressed after unloading, the definition of yield is very important since there is a gradual transition from elastic to fully plastic flow. Bauschinger used the elastic limit as his definition of yield. This is very nearly the proportional limit in the absence of anelastic effects.

For the purposes of structural design where small dimensional changes are important, this proportional limit is the proper yield point of concern since that gives the design stress limit to avoid plastic flow. On the other hand, when large plastic flow is anticipated or desired, such as in metal forming or limit load analysis, the more steady state flow stress may be desired. To model this effect we consider the observed permanent softening, $\Delta\sigma_o$, given by the stress difference between curves A and C after they become nearly parallel. A discussion of how this difference can be determined if the curves are not parallel is given by Sowerby, Uko and Tomita [1979]. The permanent softening is a way to measure the effect of the reverse loading on the flow stress rather than just on the yield point. For large uniaxial strain problems many authors have felt that this is the important effect to quantify.

The region of gradual re-yielding extends over a reverse strain range of from 1-3% (Orowan [1959]) up to a maximum of 5-10% (Wilson and Bate [1986]). Orowan felt that the back stress concept could be used to model the permanent softening much better than this region of nonlinearity (Orowan [1959]).

This same duality of the proportional limit and the large offset strain measurement of yield has also been extensively observed in biaxial experimentation (Phillips, Tang and Ricciuti [1974]). In his review article Hecker [1976] discusses the results of many yield surface probing experiments. Here thin walled tubular

specimens are loaded in various combinations of axial tension, internal pressure and torsion to achieve stress states throughout the plane stress subspace. By defining yield as the accumulation of a certain amount of plastic strain, yield surfaces can be constructed. This has been done for a few materials, most often a relatively pure system like 1100 aluminum. Yield surfaces both before and after prestraining have been determined. The results are very dependent on the definition of yield. For a very small accumulated strain definition the yield surface often shows a translation in stress space in the direction of the prestrain. This is generally accompanied by a distortion where the yield surface develops a rounded nose in the prestrain direction. This is in contrast to using a large offset definition of yield which shows expansion and a small amount of translation of the yield surface but little change of shape.

These observations are the multiaxial extensions of the behavior we note in the uniaxial Bauschinger effect experiments; the different amounts of yield surface translation account for the difference between the proportional limit and the permanent softening.

In passing we note that although these observations have been made for materials prestrained relatively small amounts ($\leq$10% strain), the same effects are seen in large strain testing. In a recent study, Stout et al. [1985] strained a tubular specimen of 1100 aluminum in torsion to an engineering shear strain of 50% and measured the original and subsequent yield surfaces using both large and small offset yield definitions. They found that translation and formation of a rounded nose occurred using a $5x10^{-6}$ strain offset yield definition but that predominately expansion with a small translation was observed when they used the back extrapolated definition

of yield. These results are qualitatively similar to the small strain studies cited by Hecker [1976].

In order to see how the back stress contribution quantitatively affects the total strain hardening we turn our attention to the detailed unidirectional experiments reported in the literature.

The early experiments of Bauschinger have already been cited. They primarily described the phenomenon of the lowering of the elastic limit upon strain reversal but were not thoroughly discussed by Bauschinger since his greatest interest at that time was in time dependent, strain aging effects (Bell [1984]).

In 1923 Masing [1923] presented a theory for the Bauschinger effect which predicts the reverse loading behavior to be identical to the initial forward loading but with a doubled stress scale and reversed sign. In 1926, Masing and Mauksch [1926] presented results of tension-compression reverse loading tests on brass with prestrains between 0.7% and 17.5%. They did not obtain good agreement with the theory. Later, Rahlfs and Masing [1950] conducted reverse loading tests in torsion using wire specimens of various polycrystalline metals to test Masing's theory. Again good agreement with the theory was not obtained.

Sachs and Shoji [1927] studied the Bauschinger effect using brass single crystals in tension and compression. This appears to be the first study establishing that the effect is seen in single crystals and can not be entirely due to mismatch between deforming grains.

An extensive investigation into the Bauschinger effect in torsion was reported by Woolley [1953]. He studied Cu, Al, Pb, Ni, and Fe with prestrains ranging from 1% to 120% in shear. Among these results was the observation that the effect is

independent of the grain size. He also cited the need for more experimental results on single crystals.

In the late 1950's E. Orowan first investigated the mechanism of the Bauschinger effect. The thinking current at that time was that a residual stress is built up in the polycrystal during deformation due to the anisotropic properties of the individual grains. Those grains more favorably oriented yield first. The result is an internal residual stress due to the developed mismatch of the grains. Orowan's students Wu [1958] and Canal [1960] showed that this was not entirely correct. They reasoned that if the permanent softening was a result of these residual stresses that a strong anneal given after the prestrain should remove this stress and the subsequent reverse loading not exhibit the lowered yield. They did not find this to be the case, in fact, permanent softening persisted even up to levels of annealing which reduced the forward flow stress of the copper.

Orowan [1959] interpreted their results differently, inferring that the permanent softening seemed to disappear after a relatively mild annealing, although he stated that full softening and recrystallization occurred before the post anneal reverse loading curve came halfway back to the original forward loading curve. This discussion demonstrates confusion that was present at the time of these results regarding the way permanent softening would be induced by a back stress.

Referring to Figure 2.2, the permanent softening, $\Delta\sigma_o$, can be modeled by a back stress, $\sigma_b{}^{p_\theta}$, defined by $\sigma_b{}^{p_\theta} = \frac{1}{2}\Delta\sigma_o$. If annealing after the prestrain removes the back stress but the isotropic hardening is still present then the reverse loading curve would shift from C to D. Removal of the back stress would also cause the continued forward loading curve to shift from E to D. Hence if the back stress were removed

both forward and reverse loading occur along the same stress level and that level would be halfway between the original forward and reverse loading curves. The confusion of Orowan, Wu and Canal was in trying to compare the reverse loading curve *after* annealing with the forward loading curve *without* annealing. If the back stress were completely removed there would still be a stress difference of $\sigma_b{}^{p_a}$. The reverse curve would shift from C to D due to annealing out the back stress but the continued forward loading would remain at E. This is just about the difference noted by Orowan [1959] before full softening and recrystallization occurred.

Deak [1962] conducted reverse loading tests in which he prestrained specimens in the forward direction and, after annealing, strained some in the forward direction and some in the reverse direction. Therefore he was able to determine when the permanent softening had been annealed out (when the forward and reverse curves come together) and whether the annealing had softened the isotropic component (by comparing the stress level with the prestress level).

For decarburized steel specimens annealing the prestrained specimens for 1 hour at less than $400°C$ had almost no effect. Above $400°C$ the forward flow curve reduced but the reverse flow curve was largely unaffected by the anneal. Finally after a one hour anneal at $700°C$ both the forward and reverse flow curves coincide but at a stress level less than what would be predicted by just removing a back stress. The results were slightly below that of the unannealed reverse flow curve. Figure 2.3 shows Deak's results for a decarburized steel that had been annealed at 700° C for 1 hour. The same result was observed for polycrystalline copper although the corresponding annealing temperatures were lower, as would be expected from the lower melting temperature of copper. *This result demonstrates that the understand-*

ing of the permanent softening as a measure of the back stress does not agree with the assumption that the back stress is annealed out.

By noticing that the annealing affects the reloading in the forward direction but not in the reverse direction we can understand a little about the dislocation structure in the deformed specimen. Consider that the specimen after uniaxial loading has a system of dislocations which contain both those which become locked in to the substructure due to pinning or tangling and those for which motion is relatively free. These more mobile dislocations are the ones which easily glide during reverse deformation. If the reverse glide of these dislocations causes annhilation then the total dislocation density would decrease. Reverse flow occurs at a lower stress level then the continued forward loading. Of course, this is what is observed macroscopically. This is consistent with the affect that annealing would have on this microsystem. The more mobile dislocations would glide due to thermal activation and annhilate leaving a lower dislocation density. Then the subsequent reverse flow would be largely unaffected by the annealing because this is the structure that develops after a small reverse strain without annealing. The proportional limit during reverse straining should increase as a result of the annealing because the dislocations that glide easily have been removed by the annealing. This is seen in the experimental results of Deak [1962].

The effect of the annealing upon subsequent forward loading should be dramatic if the dislocations have been removed. The flow stress in the forward direction would be reduced due to the lower dislocation density. In fact, if all of the deformation induced dislocations are removed then the forward flow curve should match the reverse flow curve. This is just what was observed by Deak [1962].

We can now see that the effect of reverse loading is similar to that of annealing. The more mobile dislocations move away from the obstacles that were blocking their forward motion and can annhilate reducing the flow stress level for large flow. A reduction of dislocation density is expected. We will see later that this agrees with the experimental results of Wilson and Bate [1986] and Hasegawa, Yako and Karashima [1975].

Orowan [1959] proposed that the Bauschinger effect was due to dislocation pile-up against a barrier, such as a particle. The elastic stresses that are set up make reverse glide easier than forward glide. In addition to particle characteristics, the permanent softening would then be a function of obstacle forming characteristics such as stacking fault energy.

In the early 1960's D.V. Wilson conducted reverse torsion testing on a number of polycrystalline metals including low and high carbon steel, brass Al-3 Mg, and Al-4 Cu. Wilson and Konnan [1964] noted that the work hardening rate was much higher in steel containing spheroidal cementite particles then in low carbon steel but that this additonal work hardening approached a limiting value after 6-8% strain. Wilson [1965] was led to the idea that permanent softening was due to long range internal stresses. He employed X-ray diffraction to measure the residual internal stresses. He found it to be about one half of the softening measured at the reverse strain that just brings the internal stress to zero. Many people have misunderstood this result and interpreted it to say that the experimentally measured internal lattice stress is equal to one half of the permanent softening. This is not what was noted by Wilson but has been used by many authors as a justification for the approach of modeling the permanent softening using a back stress. The back stress magnitude

is commonly assumed to be one half of the measured permanent softening. This will be discussed in more detail at the end of this section.

In 1966, Abel and Ham [1966] published the results of a Bauschinger effect study on Al-4 wt% Cu single crystals. They found that when the precipitates were coherent with the matrix that the result could be explained by the work hardening of the matrix. When the precipitates were not coherent, the Bauschinger effect was very large and could be explained by internal stresses continuing to build up at the particles during forward flow. They used a proportional limit definition for the effect.

The tension-compression testing of low carbon steel in the Luders strain region was carried out by Abel and Muir [1972a]. In this region the definition of permanent softening collapses. The forward strain occurs at a constant stress level but the reverse flow exhibits a gradual yield with constantly increasing flow stress magnitude. The reverse strain does not show the Luders band instability. To describe the non-linear reverse yield the authors define the Bauschinger strain as the reverse strain required to reach the same flow stress magnitude as was reached in the forward loading. This strain based description of the Bauschinger effect has been used by a number of authors (e.g. Stoltz and Pelloux [1974]; Pederson, Brown and Stobbs [1981]) and is valuable when the concern is for the actual micro-yield point. Abel and Muir also considered stress and energy based descriptions of the Bauschinger effect.

The purpose that Abel and Muir had for these tests was to differentiate between the effects due to two dislocation based theories. The first theory had the Bauschinger effect arising from the long range stress built up during deformation.

Current thinking on Luders band propagation along with the horizontal flow curve suggested that no large build up of elastic back stress occur in the Luders strain region. Any Bauschinger effect could then be due predominately to the second mechanism which suggested that anisotropic resistance to dislocation motion is developed by prestraining. Upon stress reversal the dislocations glide easier in the reverse direction until they meet new obstacles. The experimental results suggest that the Bauschinger strain is, in fact, due to this second reason.

Abel and Muir [1972b] went on to test copper and copper-aluminum alloys to study the effect of stacking fault energy on the Bauschinger effect. The equilibrium separation of dislocation partials is determined by the stacking fault energy. For a large separation, such as seen in a low stacking fault energy material, cross slip is difficult and requires a larger stress to become active. Cross slip is one of the mechanisms that limits dislocation pile-ups and back stress development. Hence, lowering the stacking fault energy lessens the cross slip and increases the Bauschinger effect. Without being able to make exact quantitative determinations, the above trend was observed. The Bauschinger effect increased with increasing aluminum content of the alloy.

This result is reinforced in a study by Marukawa and Sanpei [1971] who tested single crystals of 99.999% pure copper. This purity has a very high stacking fault energy and few obstacles to dislocation motion. The authors observed very little difference in forward or reverse flow. After the reversal, the deformation proceeded with approximately the same flow stress and hardening rate as before the load reversal. Etch pit results showed that the dislocation arrangement was not compatible with directional arrangements such as would be expected if long range internal

stresses were present.

The conclusions that can be reached from these experimental studies covering the period up through the early 1970's are largely qualitative but give a good idea what mechanisms are important in the Bauschinger effect. The early idea that it develops primarily from residual stress caused by plastic incompatibility between deforming grains is not sustained. The evidence for this conclusion is that, the Bauschinger effect survives strong annealing, it is largely independent of grain size, and single crystals still exhibit the effect. The role of inclusions and second phase particles appears to be particularly strong. The Bauschinger effect increases with increasing numbers of particles. The qualitative modeling of the effect by dislocation pile-up against inclusions can reasonably describe the Bauschinger strain (easier initial dislocation glide in the reverse direction).

The studies in this area during the 1970's turned to attempt better analytical modeling of the phenomenon. This required studying how the effect develops as a function of strain.

Kishi and Tanabe [1973] conducted experiments on a large variety of metals including: copper, brass, aluminum, iron, and various steels. They determined a back stress from the permanent softening as a function of prestrain by conducting reverse loading at a variety of forward strain levels. They found that the back stress could be expressed in a power law relationship:

$$\sigma_b^{p^a} = k\epsilon^m.$$

Here the constants k and m are material properties different from the corresponding constants in the power law relationship which describes just the forward flow:

$$\sigma = k'\epsilon^{m'}.$$

The fact that $m \neq m'$ implies that the relative magnitude of the back stress to the total amount of hardening is not constant but varies with the amount of deformation.

The work hardening rate of some pearlitic steels was measured by Tanaka et al. [1973]. They determined the permanent softening back stress up to 5% forward strain. Again the permanent softening was greater for a higher carbon content. They proposed a simple model for calculating the internal stress due to the cementite. This matched the back stress results quite well at strains below 0.5% but drastically overestimates the back stress at larger strains. The authors attributed this to relaxation of the internal stress due to either cracking or plastic deformation of the cementite. The back stress tended toward saturation at 5% plastic strain.

Atkinson, Brown and Stobbs [1974] conducted tests on dispersion strengthened single crystals. They modeled their Bauschinger effect results with the use of a mean internal stress. This was one element of a detailed model having a number of components in the total hardening response. These included: friction stress, Orowan stress, mean stress in the matrix, source-shortening stress, and the contribution due to forest dislocations.

Mori and Narita [1975] also tested copper-silica single crystals in reverse torsion. They separated the strain hardening into two components: that due to a back stress and that due to forest hardening. By measuring the permanent softening as a function of plastic strain they were able to give separate plots of the total hardening, forest hardening and permanent softening back stress up to a shear strain of 25%. In the first 2-3% strain all of the hardening was due to the back stress. At 10% shear strain the back stress reached a saturation value but the forest hardening continued

to increase almost linearly with strain. This saturation state indicates a limit in the dislocations that can pile-up against a given array of obstacles. High stacking fault materials rarely have significant pile-ups. Additional hardening is then achieved by tangling of gliding dislocations and formation of subgrain walls.

The authors stated that low temperature annealing removed the back stress without affecting the forest hardening. They conducted hysteresis loop tests both before and after annealing and saw that the effect of the anneal was to shift the hysteresis loop in the reverse loading direction.

Gould, Hirsch and Humphreys [1974] tested single crystals of copper containing dispersions of Al_2O_3. They found a large Bauschinger effect which could be removed by suitable annealing. They estimated that the number of Orowan loops reachs a limit of about 3 to 5 after a few percent strain. Cross slip then takes over and the back stress saturates. This is in agreement with observed trends.

Ibrahim and Embury [1975] introduced the idea of a "Bauschinger effect parameter" (B.E.P.). They defined it as twice the ratio of the permanent softening back stress to the total hardening. Referring to Figure 2.1 they defined it as

$$B.E.P. = \frac{\Delta\sigma_o}{\sigma_f - \sigma_y}.$$

Since much of the testing had been conducted on two phase systems these authors choose to characterize two single phase materials: Armco iron and zone refined niobium. They measured the B.E.P. as a function of plastic strain. They made the suprising discovery that, in the range they measured (0.5% to 7% strain), the B.E.P. was a constant (0.10) independent of strain. This was unexpected in the light of the earlier tests on two phase systems that exhibited a large stress development in the first few percent of strain followed by saturation. Ibrahim and Embury interpreted

their results as showing that the back stress and forest hardening contributions are proportional to each other throughout deformation.

Hasegawa et al. [1974,1975] conducted Bauschinger effect tests on polycrystalline aluminum strained to about 10% prestrain. They noted a slight decrease in the work hardening rate at an early stage of reversed straining compared with the hardening rate before stress reversal. This effect became more pronounced at elevated temperature. By observing dislocation structures they observed that cells were formed during prestraining but that during stress reversal dissolution and reformation of cell walls occurred. The overall dislocation density decreased by about 16% during the Bauschinger strain portion of reverse loading and reached a minimum when the initial flow stress magnitude was reached.

Anand and Gurland [1976] conducted an extensive study of the strain hardening characteristics of spheroidized, high carbon steels. They were able to explain the double-n strain hardening behavior in terms of the back stress contribution to the overall hardening. By calculating the magnitude of the back stress from a continuum model they showed that it increases almost linearly with plastic strain up to a strain of about 3.5%, then remains approximately constant. This point where saturation was observed compares quite well with the transition in exponent for the Holloman equation. When the log of stress is plotted against the log of strain the result is two straight lines which intersect at a strain of about 4%. This seems to indicate a change in hardening mechanism which is accounted for by the saturation of the back stress contribution.

Results similar to Anand and Gurland [1976] were presented by Chang and Asaro [1978] for two high carbon steels. They noted a double-n strain hardening behavior

with the transition occurring at a plastic strain of 3 to 5% which corresponds to the saturation of the back stress. The back stress accounted for approximately 20% of the total strain hardening at these strain levels in these steels. The back stress was modeled as arising from the residual internal stresses developed around the second phase particles caused by plastic incompatabilities between the elastic particles and the elastic-plastic matrix. A continuum model was developed which described this quite well.

D. J. Lloyd [1977] carried out reverse loading tests on polycrystalline aluminum: Al-6% Ni and Al-7.6% Ca. He found that the permanent softening increased rapidly with plastic strain then saturated at 7-8% strain. He also noted that the saturation permanent softening is sensitive to microstructure and orientation of the particles and the extruded grains. The **Bauschinger effect ratio** (B.E.R.) was defined as the ratio of the permanent softening back stress to the total hardening. This is just one half of Ibrahim and Embury's [1975] Bauschinger effect parameter. For the Al-6% Ni the B.E.R. was about 0.2 to 0.3 and showed a gradual decrease with plastic strain. For the Al-7.6% Ca the B.E.R. was about 0.7 at 1% plastic strain but at larger strains was a constant 0.3 . This decrease of the B.E.R. with strain is expected if the back stress saturates in the strain region being investigated. After saturation the back stress remains constant but the total amount of hardening can increase leading to a decrease in the B.E.R.

In 1980, Uko, Sowerby and Embury [1980] reported results of reverse flow studies on two types of steels: plain carbon steels having from 0.15 to 0.95% carbon and high strength, low alloy steels. This study shows the importance of the back stress in engineering materials which have been used extensively by industry. They found

that initially the permanent softening back stress increased rapidly with plastic strain but tended toward a saturation behavior at the largest strains they tested (8%). The back stress also increased with higher carbon content. The Bauschinger effect parameter decreased with increasing prestrain towards a limit at around 8-10% strain. All of these results agree well with the description of the Bauschinger effect which has come out of the previous experimental studies.

The studies that have been cited above primarily were done with reversed uniaxial loading. Supporting evidence for the conclusions seen in such tests is also available from biaxial experimentation. The review of these tests by Hecker [1976] has been cited previously.

In a recent paper, Helling et al. [1986] examined the yield loci of 1100-O aluminum, 70:30 brass and 2024-T7 aluminum as a function of prestrains that ranged up to 32%. The results were, again, sensitive to the definition of yield. They determined the expansion, translation and distortion of the surfaces of small offset strain definition of yield. For both 1100-O and 2024-T7 the translation increases rapidly with prestrain and saturates at a strain of about 8%. For brass the translation had not yet saturated at a strain of 30% but was approaching saturation. The size of the translation measures the strength of the Bauschinger effect. Even though these results were for small offset yield the same trends are seen as for the permanent softening of the unidirectional studies.

There is a severe shortcoming with most of the results discussed so far. Based upon a paper by D.V. Wilson [1965] most investigators have estimated the back stress contribution to strain hardening on the basis of the observed permanent softening. Referring to Figure 2.1, the permanent softening is defined as the flow

stress difference between reversed and continued forward flow measured after the curves have reached parallelity. The assumption is made that:

$$\sigma_b{}^{pe} = \frac{1}{2}\Delta\sigma_o,$$

where $\sigma_b{}^{pe}$ is a tensile value of back stress determined from the permanent softening. Most theories employing back stress requires it to be a deviatoric tensor, B, ($trB = 0$). Here we would have $B_{11} = \frac{2}{3}\sigma_b{}^{pe}$.

The result determined by Wilson [1965] and confirmed by Wilson and Bate [1986] is that the internal lattice stress is *not* well related in this way. Rather, the internal stress in the ferrite matrix is better measured from the difference in forward and reverse flow stress measured at the reverse strain in which the internal lattice stress goes to zero.

Wilson and Bate [1986] made detailed measurements of internal stress using X-ray diffraction techniques. They measured the internal stress components in the ferrite matrix. By diffracting x-ray beams with the material they could infer the directional components of stress by the displacement of the diffracted beam. The nondirectional (isotropic) component was inferred by the broadening of the diffracted beam. They followed the directional internal stress in the matrix as a function of plastic strain. They found that upon reversing the straining direction the internal directional stress decreases rapidly, going to zero after a couple of percent reverse strain. It then changes sign and increases to become equal in magnitude to the value that it had before unloading but with opposite sign. Figure 2.4 shows their result containing the variation of internal, residual lattic strain with reverse strain. Notice that the results for two prestrains are given: 5% and 10%. The internal directional lattice strains (from which the residual stresses are computed) are

relatively independent of that prestrain magnitude. The magnitude and variation of that internal lattice directional stress is the quantity that should be physically modeled by the back stress variable. This is not what most of the researchers have been using as their back stress. They have been modeling the back stress with the permanent softening. The results of Wilson and Bate show the proper variation of the back stress with reverse strain and lend a much better idea of what occurs during reverse flow.

The variation of the back stress with reverse plastic flow as detemined from yield surface experiments is presented by Liu and Greenstreet [1976]. They determined the back stress from the center of the experimentally measured yield surfaces (small offset definition of yield) and plotted how it varied during reverse flow. Figure 2.5 shows that their results are very similiar to the x-ray results of Wilson and Bate (Figure 2.4). The back stress rapidly decreases to zero then increases more gradually to the magnitude it had achieved during prestraining but in the opposite direction.

In addition to modeling the directional internal stress Wilson and Bate [1986] also made estimates of the nondirectional (or isotropic) component of stress from the X-ray line broadening. This gives some insight into what happens to the isotropic component of hardening. Wilson and Bate found that the nondirectional component of stress decreases during the early portion of reverse flow to a minimum then begins to increase. *The reverse flow causes a recovery of the isotropic component as dislocations annhilate. They found that the directional component of internal stress had little effect on the permanent softening, rather, the permanent softening is caused by the recovery of the isotropic hardening during the early reverse flow.* The directional component rapidly changes sign and quickly goes to the magnitude

that it had in forward flow. This experimental result is both new and startling.

These results are supported by Hasegawa, Yako and Karashima [1975] who conducted TEM studies of the dislocation substructure during reverse flow after a 4.5% forward strain in aluminum. They observed a decrease in total dislocation density of 16% during the reverse flow. Their results are summarized in Figure 2.6 . Notice the change in dislocation structure during reverse flow. The dislocation density decreases during the first percent or so of the reverse flow then increases again. This agrees very well with the behavior of the nondirectional hardening component observed by Wilson and Bate [1986]. Marukawa and Sanpei [1971] also noted a decrease of dislocation density within the cell walls in copper single crystals after stress reversal.

The results of Deak [1962] (discussed earlier in this section) for the behavior of specimens which had been annealed after the prestrain support these observations. Reverse flow has the same effect on the flow stress level as does annealing. They both lead to a reduction in dislocation density.

2.3 Summary

To summarize these results we note that much experimental work has been conducted on uniaxial, reverse loading tests. Unfortunately, the results are generally presented in terms of the permanent softening. Most authors attribute the permanent softening to an internal back stress and model it as such. Observations of internal structure and X-ray diffraction demonstrate that this is not the case. The permanent softening is more closely related to softening of the isotropic component of hardening. The nondirectional component of stress actually *decreases* during the

early stages of reverse flow. The internal stress reverses sign very quickly after the straining direction is changed. It then achieves the same magnitude it had before unloading. It reaches this level as the reverse and forward loading curves become parallel.

These results lead to very important considerations when choosing the proper method of modeling the back stress. These considerations will be considered in Chapter 5 as a new constitutive model is constructed.

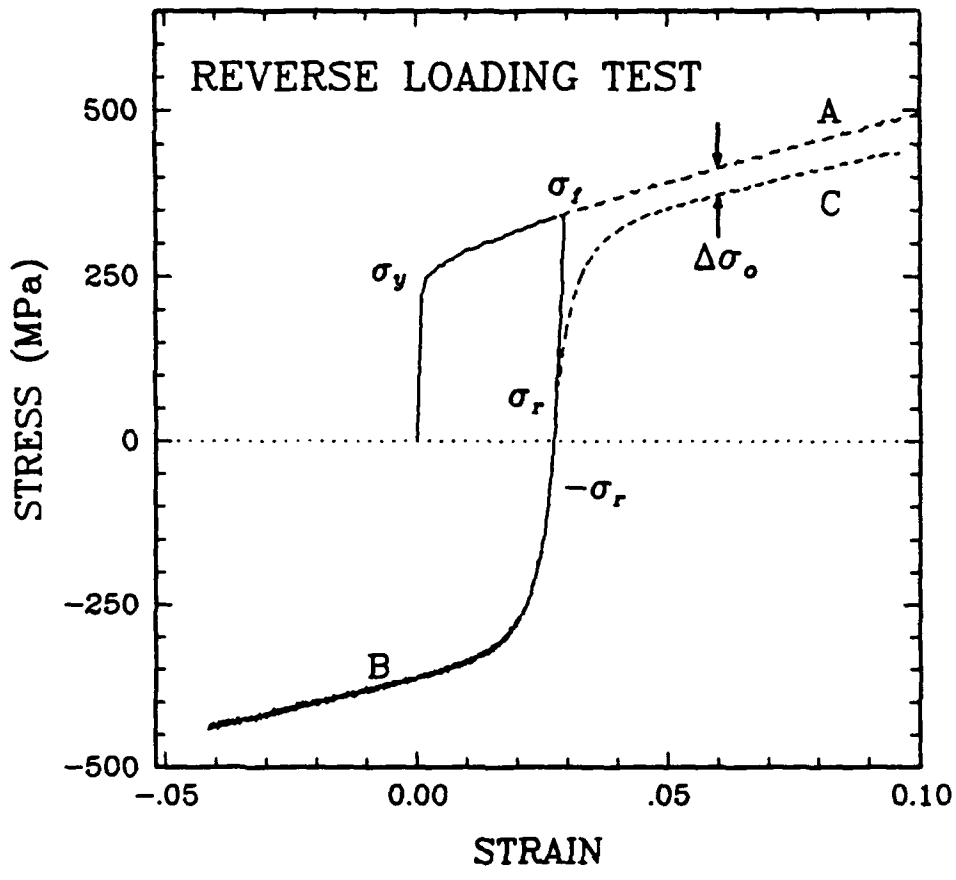

Figure 2.1 Schematic representation of reverse loading test (solid line) and the rotation of the reversing portion into the first quadrant (lower dashed line). The upper dashed line shows the monotonically loaded result for comparison.

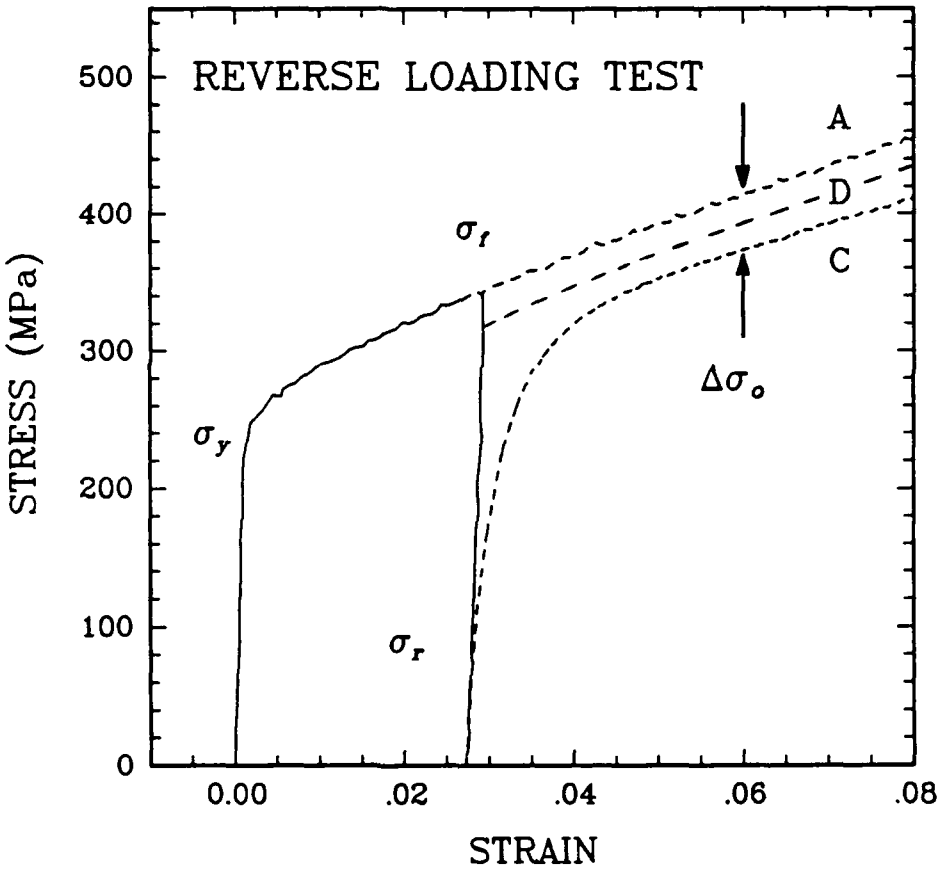

Figure 2.2 Schematic representation of experiments of Deak [1962]. Curve A is the forward loading response. Curve C is the reverse loading response. Curve D shows the predicted response for both reverse and continued forward loading if the back stress were removed.

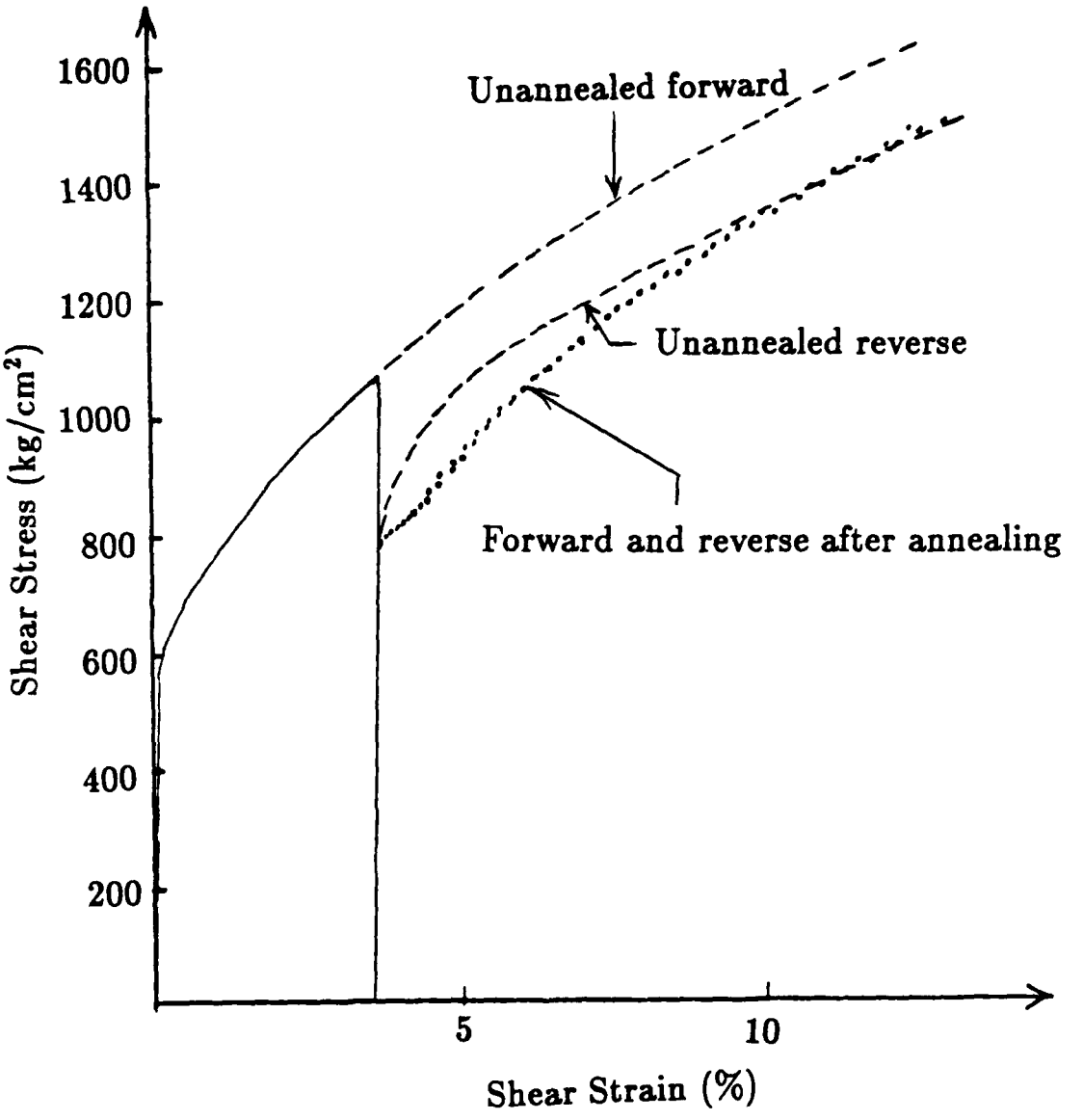

Figure 2.3 Results of Deak [1962] for reverse and continued loading of steel after annealing at $700°C$ for 1 hour. Unannealed forward and reverse curves are shown for comparison.

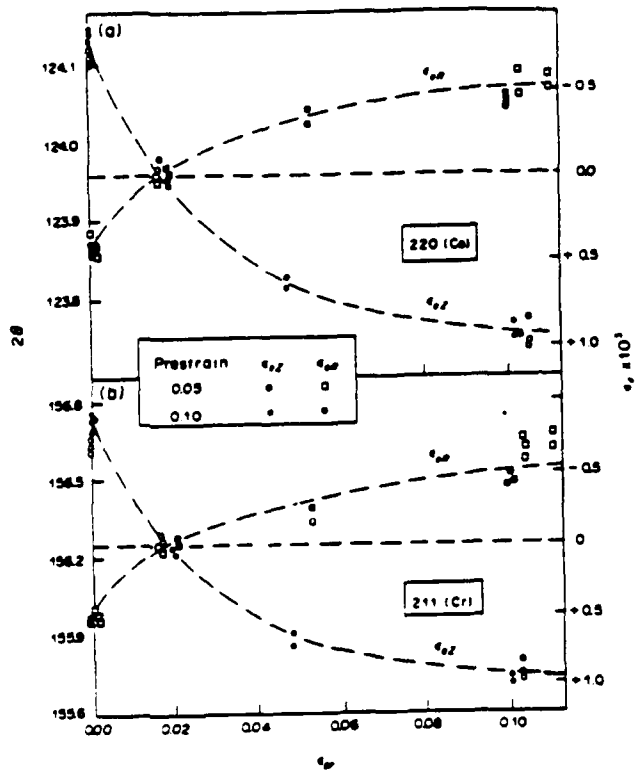

Figure 2.4a X-ray diffraction line results of Wilson and Bate [1986] for the directional component of residual strain as a function of plastic strain after reversing. The left ordinate axis shows the displacements of the 220 and 211 X-ray diffraction lines. These are converted to residual elastic strain in the matrix on the right ordinate axis. The internal residual stress is found from above using the elastic constants. It shows the same trend.

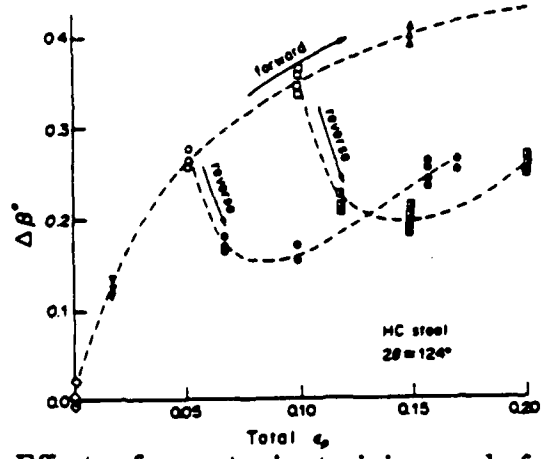

Figure 2.4b Effects of monotonic straining, and of reverse straining after prestrains of 0.05 and 0.10 on the width ($\Delta\beta^o$), of the 220 diffraction line. Increase in line width indicates an increase in nondirectional residual stress (isotropic component) in matrix. Wilson and Bate [1986].

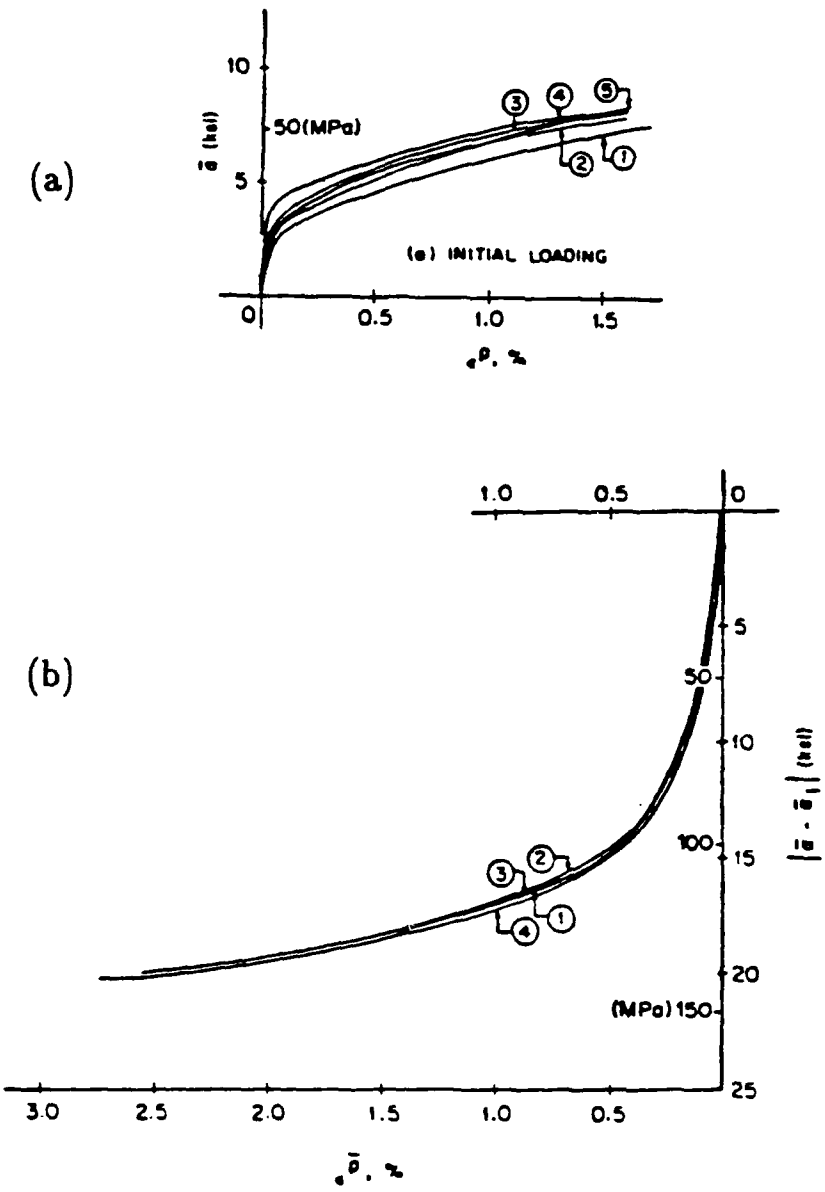

Figure 2.5 Results of Liu and Greenstreet [1976] for the back stress evolution during (a) forward and (b) reverse loading.
In (b) the change in back stress from the forward loading value is plotted.

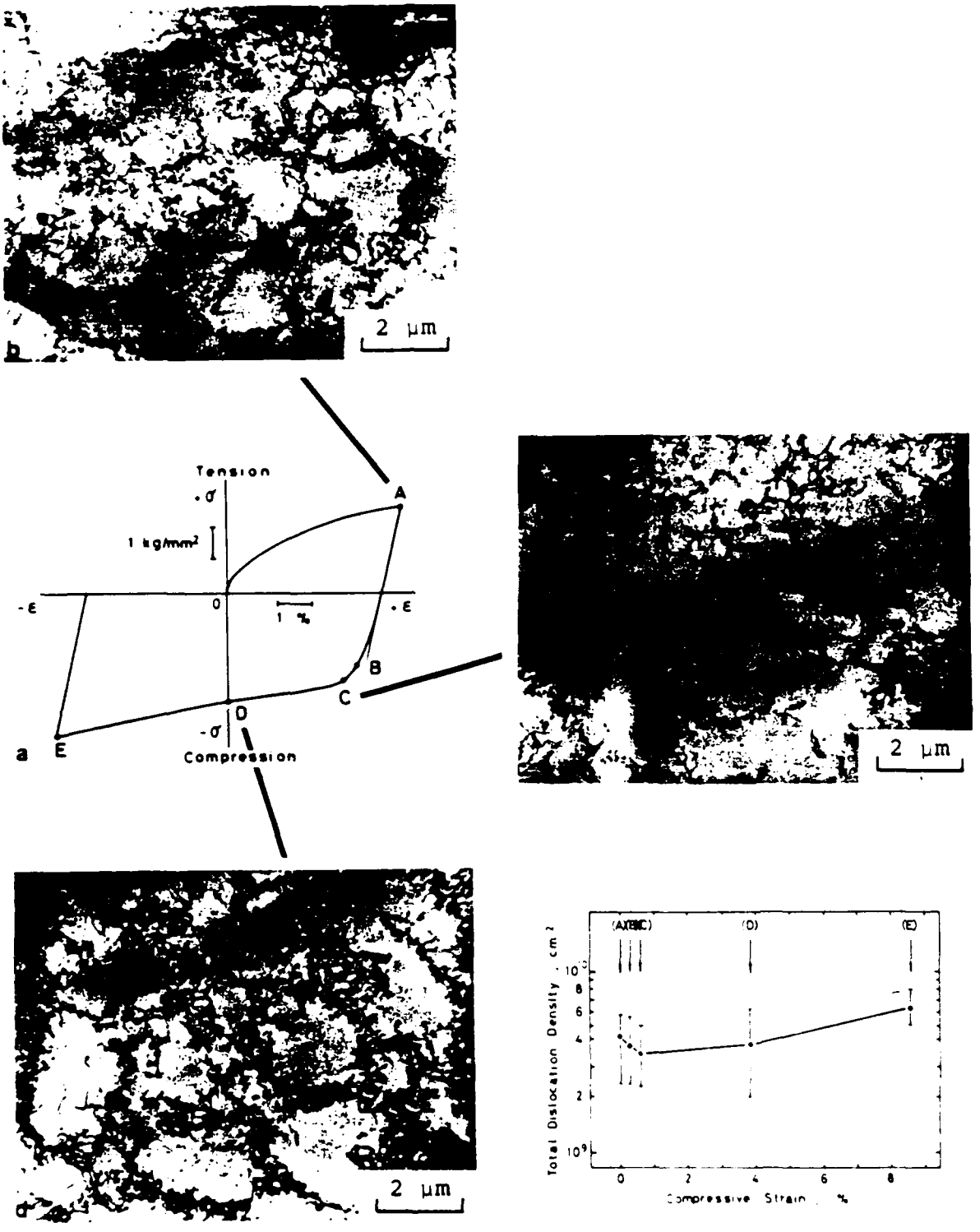

Figure 2.6 Evolution of dislocation structure during reverse loading in aluminum. Hasegawa, Yakou and Karashima [1975].

Chapter 3

Micromodeling of a Particle-Hardened Alloy Using the Finite Element Method

In modeling reverse plasticity the concept of a *back stress* or *internal stress* is widely used to explain why yield occurs at a lower macroscopic stress in the reverse direction. It is postulated that straining in the forward direction induces a local residual stress in the material. This residual stress acts to aid plastic flow in the reverse direction. At least nominally, scientists would like to attribute the back stress variable used in modeling with an actual residual stress in the material.

This is a difficult connection to make since the residual stress in the material must be very local and thus difficult to measure. The material must contain a residual stress distribution which equilibrates itself over a small size scale since the manifestation of the back stress is still seen for a zero macroscopic stress. This differs from the macroscopic residual stresses associated with, for instance, material processing where the residual stress fluctuates over the length scale of the part.

The back stress is believed to result from the inhomogeneity of plastic flow on the microscale. A local system of internal stresses is set up which is manifested as

the back stress.

In this chapter, the development of a local residual stress field caused by the interaction of an elastic particle with a surrounding elastic-plastic matrix is studied. The residual stress stress-strain response of the system, particularly the observed Bauschinger effect, is examined. This study is intended to model the deformation of a particle hardened alloy.

The particle is modeled as purely elastic with the elastic constants for cementite given by Laszelo and Nolle [1959]: $E = 29.042 \times 10^6 \text{psi}, \nu = 0.361$. The matrix material is modeled as ferrite. It has both elastic and plastic strain hardening properties. The elastic constants for ferrite were also taken from Laszelo and Nolle [1959]: $E = 30.174 \times 10^6 \text{psi}, \nu = 0.283$. The yield and small-strain hardening modulus were taken from Morrison [1966]. The modulus at strains greater than 25% was arbitrarily chosen low to give perfect or near perfect plasticity at large strain. The actual input stress strain curves are shown in the next sections. The matrix was modeled as hardening by classical isotropic hardening. This was chosen to examine if the back stress could be developed by the particle-matrix interaction and not by assuming kinematic hardening of the matrix. This is in accordance with dislocation based models of the back stress.

Two finite element models were used in this study. The first uses an axisymmetric unit cell to approximate a three dimensional array of spherical particles. The second uses a plane strain unit cell modeling an array of cylindrical particles. The axisymmetric model gives a more realistic comparison with the actual three-dimensional distribution of particles in a material. The plane strain model has, however, the utility of allowing nonaxisymmetric loading such as simple shear.

This will be presented in detail below.

3.1 Axisymmetric Unit Cell Model

This model of the material system follows recent finite element studies of Tvergaard [1982] and Needleman [1987]. Consider a material containing a periodic array of elastic particles. This array is formed by stacking planes having particle spacings shown in Figure 3.1a. The repeating unit in the plane is the hexagonal cell containing the particle at its center. In considering this boundary value problem we replace the hexagonal unit cell boundary with a circular one. This is a close approximation. If we now stack these cells so that the particles are directly above one another we obtain the cylindrical geometry of Figure 3.1b. This represents an axisymmetric column of particles. The most basic block that we can consider is one quarter of the axisymmetric unit cell. This is illustrated in Figure 3.1c.

This region is divided into a finite element mesh which models both the particle and the matrix. Figure 3.2 shows two meshes of this region. The mesh of Figure 3.2a contains 170 4-node axisymmetric elements (188 nodes). This is the basic model used for this analysis. The total number of degrees-of-freedom for this model is 330.

In order to verify whether this mesh is fine enough to capture the desired behavior a second mesh (shown in Figure 3.2b) was used in some comparison calculations. This second model has 600 elements (631 nodes) and 1180 degrees-of-freedom.

The boundary value problem that was solved with the axisymmetric model consisted of various combinations of uniaxial tension and compression. Referring to Figure 3.1b, the boundary conditions applied to each face were as follows: (f_i rep-

resents the traction force in the i direction, and u_i is the displacement in the i direction)

- On the bottom face ($X_3 = 0$)

  $u_3 = 0$

  $f_1 = 0$

- On the left face ($X_1 = 0$)

  $u_1 = 0$

  $f_3 = 0$

- On the right face ($X_1 = R$)

  $f_3 = 0$

  u_1 = constant. Where the constant is determined such that there is zero radial force on the face, $\int_0^b f_1 \, dy = 0$.

- On the top face ($X_3 = b$)

  $f_1 = 0$

  u_3 =constant. Where the constant vertical displacement was applied to the entire face to simulate tensile or compressive loading.

Across the particle-matrix interface the displacements were continuous. The cell had an equal radius and height, $A_o = B_o$ in Figure 3.1b. The ratio of the particle radius to the cell radius was 0.5759 . This gives an approximate particle volume fraction of 12.7 %.

All simulations were conducted with the ABAQUS finite element code allowing finite geometry changes. The code was run on a VAX 11-785 computer.

The *total* reaction force and displacement of the top face of the model were used to derive the "macroscopic" true stress-true strain behavior of the system. They were processed the same way that experimental load cell and extensometer signals would be handled.

The input matrix plastic stress-strain curve is shown in Figure 3.3 . The results from Morrison [1966] only extended to about 25% strain so the matrix material was assumed to be perfectly plastic above that.

Figure 3.4 shows the macroscopic stress-strain result for each of the two meshes. The agreement is so close that the curves lie virtually on top of one another. Because of this close agreement the more coarse mesh (Figure 3.2a) was determined to be detailed enough for the present study. All of the following axisymmetric calculations were conducted with this mesh.

In Figure 3.5 the uniaxial stress-strain curve is shown out to 15% strain. Notice the gradual yield region and nearly linear hardening. This is compared in Figure 3.6 with the input hardening curve for just the matrix. This plot shows a comparison of the flow stress of the system with and without the particles. The presence of the elastic particles provides increased strain hardening as expected. Since the particles only deform elastically the plastic strain is concentrated in the matrix. For a given deformation, the matrix has then strain hardened more than it would have if the particles were not present.

When the unit cell model is subjected to tensile straining followed by compressive straining a stress-strain response exhibiting the Bauschinger effect is seen. An

example of this simulation is shown in Figure 3.7. Notice the gradual reyield in compression.

In order to compactly compare the reversing results for a number of these prestrains the data is plotted in a standard way. For the reversing portions of the curves only, the compressive region is shown but it is displayed in the first quadrant by plotting the absolute value of stress against an accumulated strain where the total accumulated plastic strain is added to the elastic strain. This effectively rotates the compressive stress-strain data by 180° about the zero stress point. Displaying the data this way allows easy comparison of how the reverse yield has been lowered and the extent of rounding during reverse flow. It also is convenient for displaying the results of many tests.

In Figure 3.8 the simulations of six reversing tests are shown along with the tensile loading curve. Each of the reversing curves exhibits the gradual reyield at a lower stress magnitude than had occured during forward loading. The curves all have a similar shape. The only difference between the features of these numerical simulations and experiments is the *absence of permanent softening.* All of the simulations go back to the forward loading flow stress level. It was extensively discussed in Chapter 2 how real materials exhibit an isotropic softening during reverse flow. The dislocations annhilate reducing the strength level. It is the isotropic softening that gives the phenomenological feature of permanent softening. This finite element model does not allow for isotropic softening. The matrix isotropic flow stress is a monotonically increasing function of plastic strain. No mechanism has been included to allow it to recover. This does not limit the model's ability to simulate particle-matrix interaction during loading including back stress development. What

it does limit is the ability of the finite element model to correctly simulate isotropic hardening after reverse plastic flow. This is not a severe limitation for our goal of investigating back stress development.

One of the difficult determinations to make from a stress-strain curve like Figure 3.8 is what to use as the magnitude of the reverse yield in separating out the isotropic and kinematic (back stress) portions of hardening.

The important issue is determining what position along the reverse loading curve to use as the reverse yield point. This is difficult to resolve from just a stress-strain curve due to the smooth reyielding behavior during reverse loading. If the reverse yield point is known then the one dimensional elastic region is known and the shift of the yield surface during the initial straining is known. The hardening during forward loading can then be separated into isotropic and kinematic components (neglecting yield surface distortion).

The back stress determined from the stress strain curve should have a physical connection with the residual stress left in the material after forward loading. In order to explore this connection, the stress distribution in the finite element model after prestraining and unloading to zero macroscopic stress was examined. An example of the residual stress component in the direction of prestraining is shown in Figure 3.9a. Here the σ_{22} stress in the matrix is shown for a simulation that was given a tensile prestrain of 6% in the 2 direction. Only the residual stress for the matrix is shown here. The calculations were only conducted for the $\frac{1}{4}$ unit cell shown in Figure 3.1c but are displayed using symmetry for a whole field of particles macroscopically strained 14.5%. This corresponds to the stress distribution in a plane passing through the particles. Notice that the residual stress between the

particles in the direction of loading is tensile while the residual stress in the rest is compressive. Equilibrium requires there be both tensile and compressive stress which balance out over the whole cell.

The distribution of the residual stress lends insight into the mechanism of the Bauschinger effect. The system can be viewed as columns of one type of material (the stacking columns of the particles with the matrix separating them) contained in an annulus of another material (purely matrix). When the system is strained the annulus develops a greater averaged plastic strain (the particles can contain larger elastic strains). Once the extenal force is released, the annulus holds the particles apart creating tensile residual stress between them. The system is analogous to two springs which have been strained different amounts. One is placed in tension and the other in compression. This is the type of phenomena that the *mechanical sublayer model* was constructed to model. For the particle-matrix unit cell loaded along the particle row direction we can think of a sublayer model having two elements. Unlike that model there is extensive interaction between the two elements since neither deforms homogeneously. Here we clearly see that there is an internal stress field because of the inhomogeneous deformation of the system.

The accumulated equivalent plastic strain distribution is shown in Figure 3.9b. The macroscopic plastic strain in the direction of straining for the cell was 0.0598. This distribution shows that the strain is concentrated above the particle but the gradation is quite gradual except near the particle-matrix interface.

In a physical experiment there can be slight nonuniformity of deformation in the gauge region due to specimen geometry or loading alignment. This can cause the proportional limit of the stress-strain curve to differ somewhat from the point

where plastic flow first occurs throughout the specimen. This is not the case in our numerical experiment. Plastic flow initiates nonuniformly within the unit cell but is representative of yield occuring simultaneously in all of the repeating cells.

By taking the proportional limit as the reverse yield for the numerical stress-strain curves we can determine the back stress as the center of that elastic region. This back stress value correlates well with the residual stress distribution (at zero macroscopic load) in the matrix. The tensile back stress determined from the stress-strain result for the prestraining of 14.5% shown in Figure 3.10 was 21,000 psi. If we tried to select one number from the residual stress field of Figure 3.9c as representing its *average* then 21,000 psi would be reasonable.

This demonstrates a correspondance between the back stress determined from a small strain offset yield definition (in the numerical case an offset of zero) and the actual residual stress in the material system. It is important to have this connection. Otherwise the back stress is just a modeling variable not in touch with reality. A physical correspondance is needed when examining deformations having material rotation. We need to properly model the back stress for this region. In the literature, this has not been carried out.

Using the proportional limit definition of reverse yield, the results of Figure 3.8 were separated into isotropic and back stress components. The summary of this separation is shown in Figure 3.10 . Notice how the back stress initially rises quickly but has nearly saturated by 6% plastic strain. The isotropic part continues to rise nearly linearly with plastic strain throughout this region. These results are in agreement with experimental observations.

This result shows how the back stress increases with plastic strain for forward

straining from the virgin condition. We are also interested in how the back stress evolves during reverse plastic flow. To look at that, the model was prestrained in tension to about 6%. It was then reversed to a certain strain. Finally, it was again pulled in tension. This was done for 5 different amounts of reverse straining. By plotting the position of the center of the elastic region determined from the reloading branches, the evolution of the back stress during reversing could be traced. The reversing and reloading branches are all shown together in Figure 3.11 . Each reloading branch represents a separate test. The back stress evolution from this is shown in Figure 3.12. The tensile back stress value is plotted against the accumulated strain during the reversing branch. The initial back stress value was 17.3 ksi. During reversing it rapidly decreases to zero and tends toward the value it had prior to reversing. The back stress rapidly changes sign and becomes negative during this reverse flow. This is in close agreement with the results of Wilson and Bate [1986]. Compare Figure 3.12 with Figure 2.4. They also show this same trend from their x-ray measurements.

This same behavior is seen by Liu and Greenstreet [1976] who plotted yield surfaces during reverse flow and took their centers as the back stress. The same rapid decrease, change of sign and gradual increase in magnitude of the back stress was also noted in their work.

In Figure 3.11, The final, tensile loading branch crosses the prestress point at a higher stress value. For small enough hysteresis loops this is not seen experimentally but rather the reloading undershoots, slightly, the prestress point. This also is a result of the isotropic softening that takes place in the material but is not modeled with this calculation.

The final simulation with the axisymmetric unit cell model involves a fixed strain amplitude, cyclic test. The cell was cycled through 5 cycles of $\pm 2\%$ strain cycling. The stress-strain results are displayed in Figure 3.13. Even after 5 cycles the response is toward a stable, symmetric, saturated, hysteresis loop. This shape is typical of experimental results also. The saturation is achieved and the flow strength is limited because the input flow stress for the matrix material saturates at 100 ksi.

From this axisymmetric model many of the uniaxial, experimental results can be qualitatively reproduced. The back stress evolution both in forward and reverse flow is correctly simulated. The back stress is shown to roughly correspond to the residual stress in the matrix annulus surrounding the particles. The experimental feature that is not reproduced by the numerical model is permanent softening. If the ideas of Chapter 2 are appropriate then this is not a suprise. Permanent softening results from the reduction of the isotropic component during reversing. Since classical isotropic hardening was used for the matrix material then this is not possible with the current model.

3.2 Plane Strain Unit Cell Model

The axisymmetric model is only useful for axisymmetric loading geometries. having symmetry about the same axis. For the important case of simple shear, the boundary conditions are nonsymmetric. In order to model particle-matrix interaction with a two dimensional mesh geometry we consider a plane strain analysis.

Considering the mesh shown in Figure 3.14, the particle is modeled as a cylinder whose axis is perpendicular to the plane of the paper. The matrix surrounds the

particle as before. Notice that the full unit cell is modeled and not just one quarter of it as was done with the axisymmetric model. The elastic properties are identical to those used for the axisymmetric model but the matrix flow stress level is slightly different. The stress-plastic strain curve input for the matrix is identical to Figure 3.3 up to a plastic strain of 25% but then instead of being perfectly plastic above that it continues to harden at a reduced modulus up to a plastic strain of 500% (see Figure 3.15). Above this the model is perfectly plastic. The reason for continuing hardening to larger strains is that the plane strain model was to be used to larger strains.

The mesh contains approximately the same level of detail as the axisymmetric model. It has 711 nodes, 720 elements and 1403 degrees-of-freedom. The four outer surfaces of the mesh are all constrained to remain in straight lines. The ratio of the diameter of the particle to the cell width is 0.402 . That gives a particle volume fraction of 12.7% which is the same as for the axisymmetric model although the particle geometry is different.

3.2.1 Tensile Loading

In order to get baseline results for comparison, the model was first loaded to simulate tensile loading. The bottom edge of the model was restrained against vertical motion. The left and right sides were forced to remain straight and vertical with zero horizontal force. The top edge was displaced vertically to simulate tensile straining. Referring to Figure 3.14, the boundary conditions applied to each face were as follows: (f_i represents the traction force in the i direction, and u_i is the displacement in the i direction)

- On the bottom face ($X_2 = 0$)

$u_2 = 0$

$f_1 = 0$

- On the left face ($X_1 = 0$)

  $u_1 = 0$

  $f_2 = 0$

- On the right face ($X_1 = L$)

  $f_2 = 0$

  u_1 = constant. Where the constant is determined such that there is zero horizontal force on the face, $F_1 = 0$.

- On the top face ($X_2 = L$)

  $f_1 = 0$

  u_2 =constant. Where the constant vertical displacement was applied to the entire face to simulate tensile loading.

In Figure 3.16 the macroscopic stress-strain result for the model is shown up to a macroscopic true strain of just over 40%. The deformed mesh at this level of deformation is also displayed in Figure 3.16a. This represents the upper limit to which this mesh can be pushed without the need to remesh due to distortion. Notice the decrease of the hardening modulus. The nearly linear hardening region observed for the macroscopic result of the axisymmetric model (Figure 3.4) is also observed here for strains below 10%. Between 10 and 20% strain the macroscopic result shows a transition to a lower hardening modulus. This corresponds to a large

portion of the matrix hardening to beyond the *knee* of the input stress-strain curve (local strain of 25% in Figure 3.15). The macroscopic result *follows* the matrix hardening behavior.

3.2.2 Simple Shear

In order to simulate the simple shear deformation mode, new boundary conditions are applied to the plane strain model which has been described above. The main idea is to hold the bottom edge of the model fixed and to horizontally displace the top face. Referring to Figure 3.14, the boundary conditions applied to each face were as follows: (f_i represents the traction force in the i direction, and u_i is the displacement in the i direction)

- On the bottom face ($X_2 = 0$)

  $u_1 = 0$

  $u_2 = 0$

- On the left face ($X_1 = 0$)

  u_1 and u_2 enforced to remain on a line connecting the top left and bottom left corner nodes.

- On the right face ($X_1 = L$)

  u_1 and u_2 enforced to remain on a line connecting the top right and bottom right corner nodes.

- On the top face ($X_2 = L$)

  $u_2 = 0$

u_1 =constant. Where the constant horizonal displacement was applied to the entire face to simulate simple shear.

During large strain simple shear, not only does a shear force develop but a normal force is also required to keep the shearing faces held at a constant distance apart. By measuring the reaction forces on the top row of nodes required to enforce the above displacements we derive the macroscopic stress response shown in Figure 4.17. In Figure 4.17 we also see the deformed mesh at a shear strain of $\gamma = 0.5$. The corresponding stress-strain response is shown in Figure 3.17b. The axial stress shown in the plot is the σ_{22} component on the top face. As the model deforms it develops a compressive, vertical, normal stress. This is in qualitative agreement with the experimental literature [Montheillet, Cohen and Jonas, 1984]. If no particles were present then the predicted normal stress would be approximately -158 MPa. This is insignificant when compared with the result of -2148 MPa predicted here with the particle. The shear stress behavior shown here is in agreement with the shape of the plane strain tension result of Figure 3.16. Here we see that the finite element model is able to qualitatively give the correct behavior for large strain simple shear.

Micromodeling using finite elements shows great promise for understanding the deformation behavior of particle hardened alloys. The interaction between the different phases can be properly taken into account and give qualitatively correct results for the macroscopic behavior of Bauschinger effect and large shear tests.

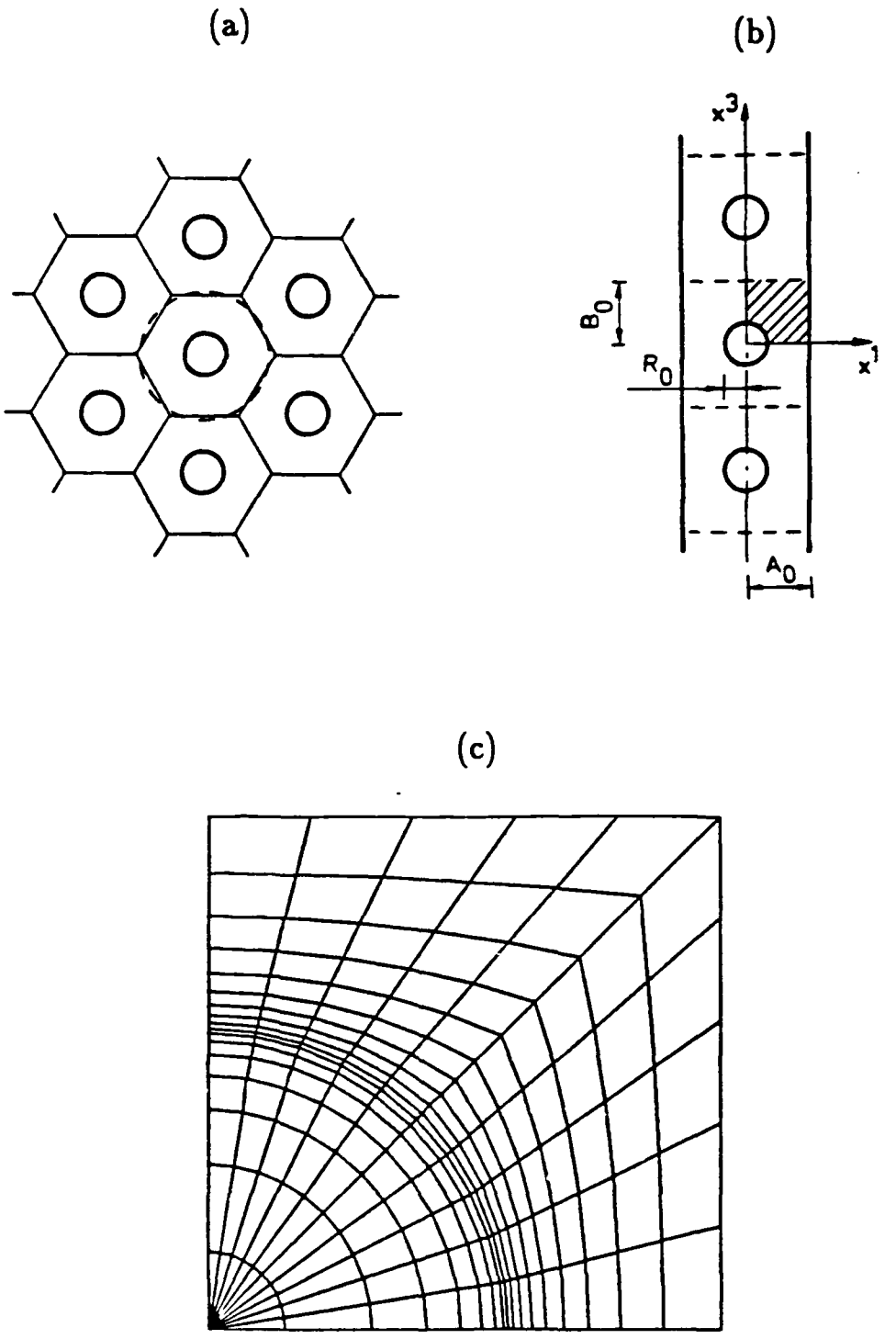

Figure 3.1 Modeling of a doubly periodic array of spherical, elastic particles in an elastic-plastic matrix. a) Hexagonal cell boundaries are approximated as circles. b) The cylindrical columns can be modeled using $\frac{1}{4}$ of the unit axisymmetric cell. c) The finite element discretization of the basic region.

(a)

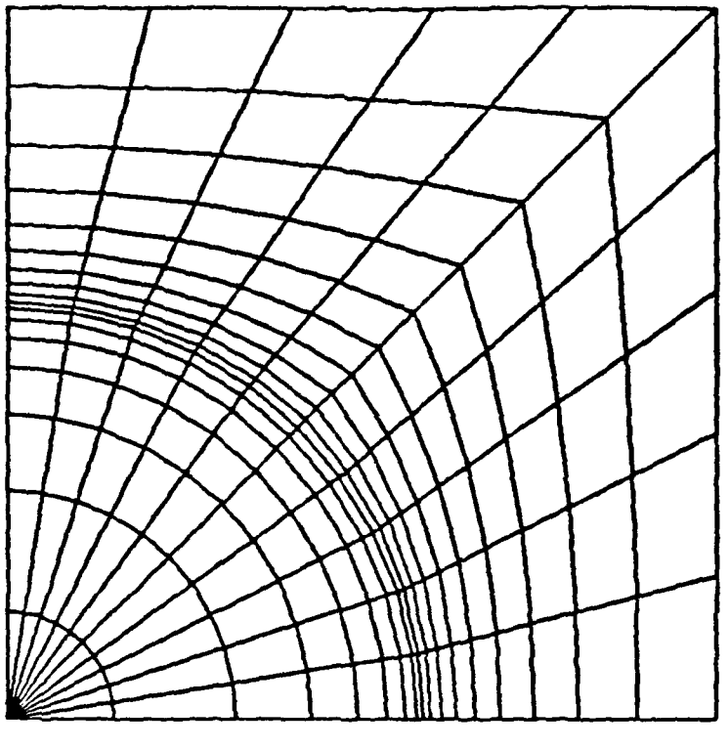

(b)

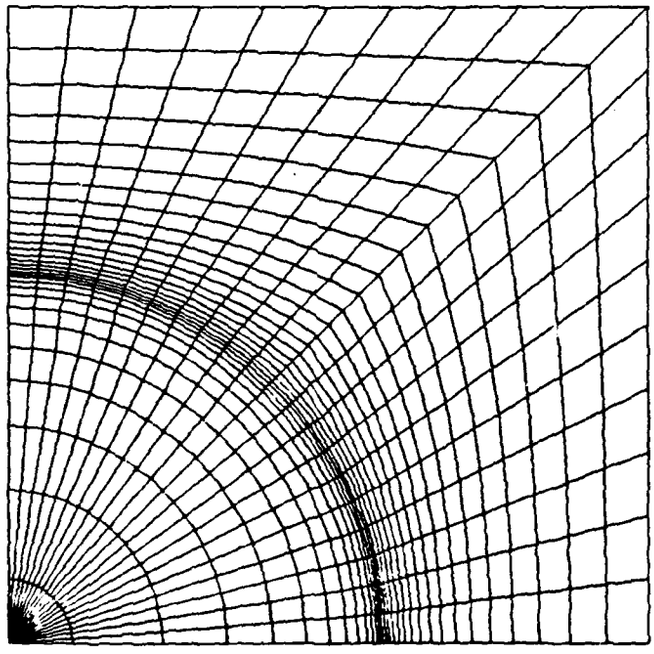

Figure 3.2 Two finite element discretizations of the axisymmetric $\frac{1}{4}$ cell. a) Mesh used for axisymmetric calculations. It contains 170 elements. b) Finer mesh used for convergence comparison. It contains 600 elements.

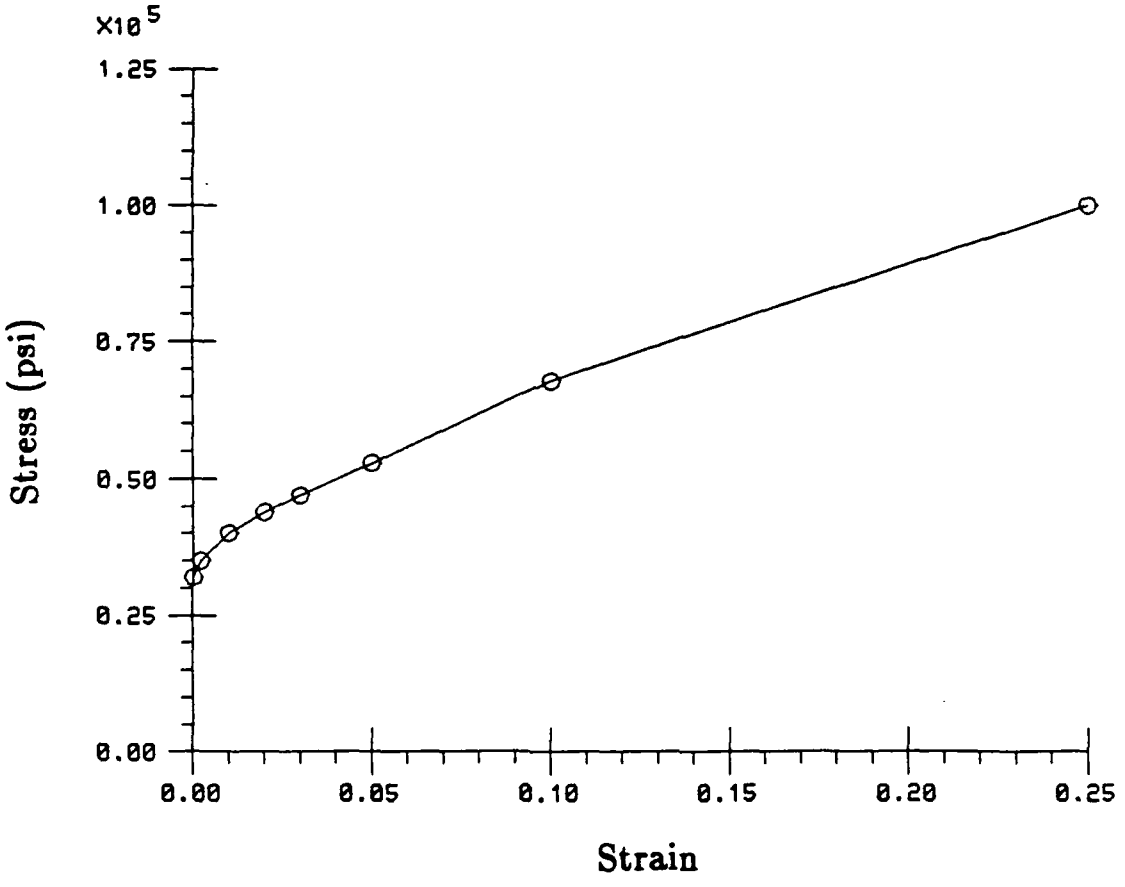

Figure 3.3 Input stress-plastic strain curve for matrix material, from Morrison [1966].

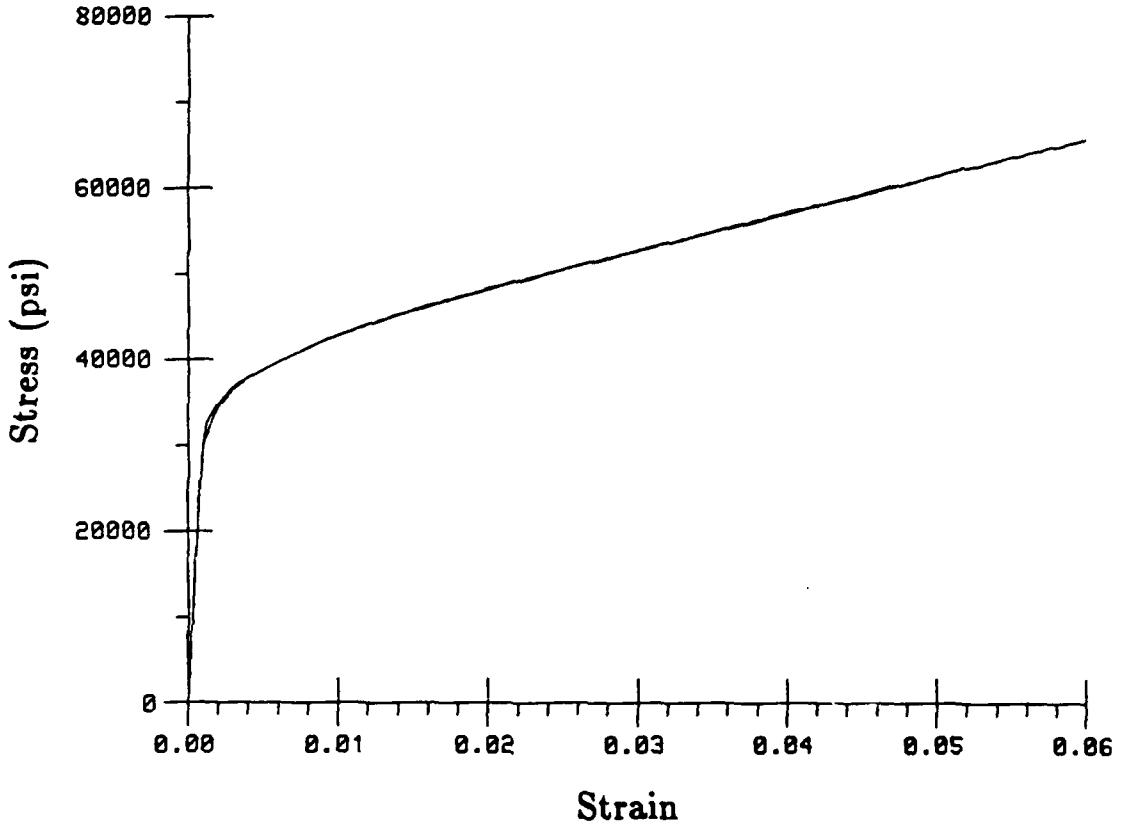

Figure 3.4 Comparison of macroscopic stress-strain result for unit cell pulled in tension using both the coarse mesh and the fine mesh of Figure 3.2.

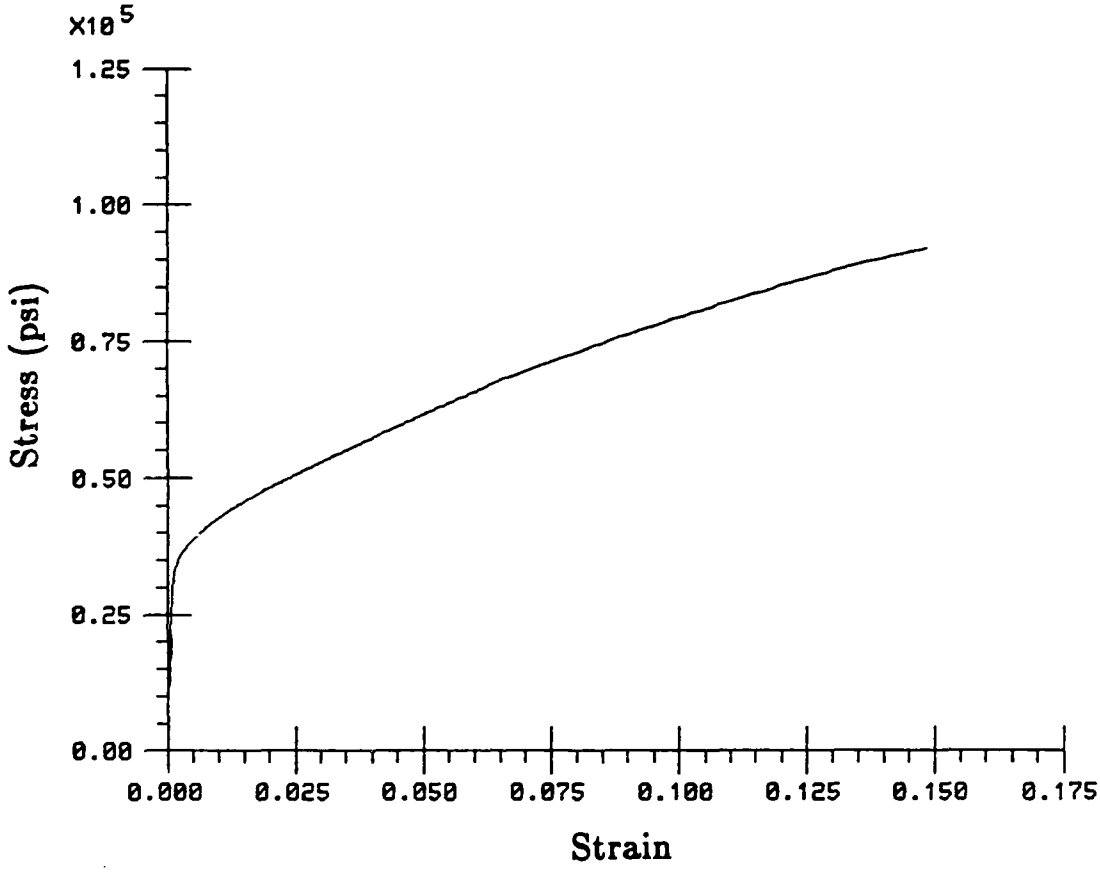

Figure 3.5 The macroscopic stress-strain result for the unit cell to 15% strain.

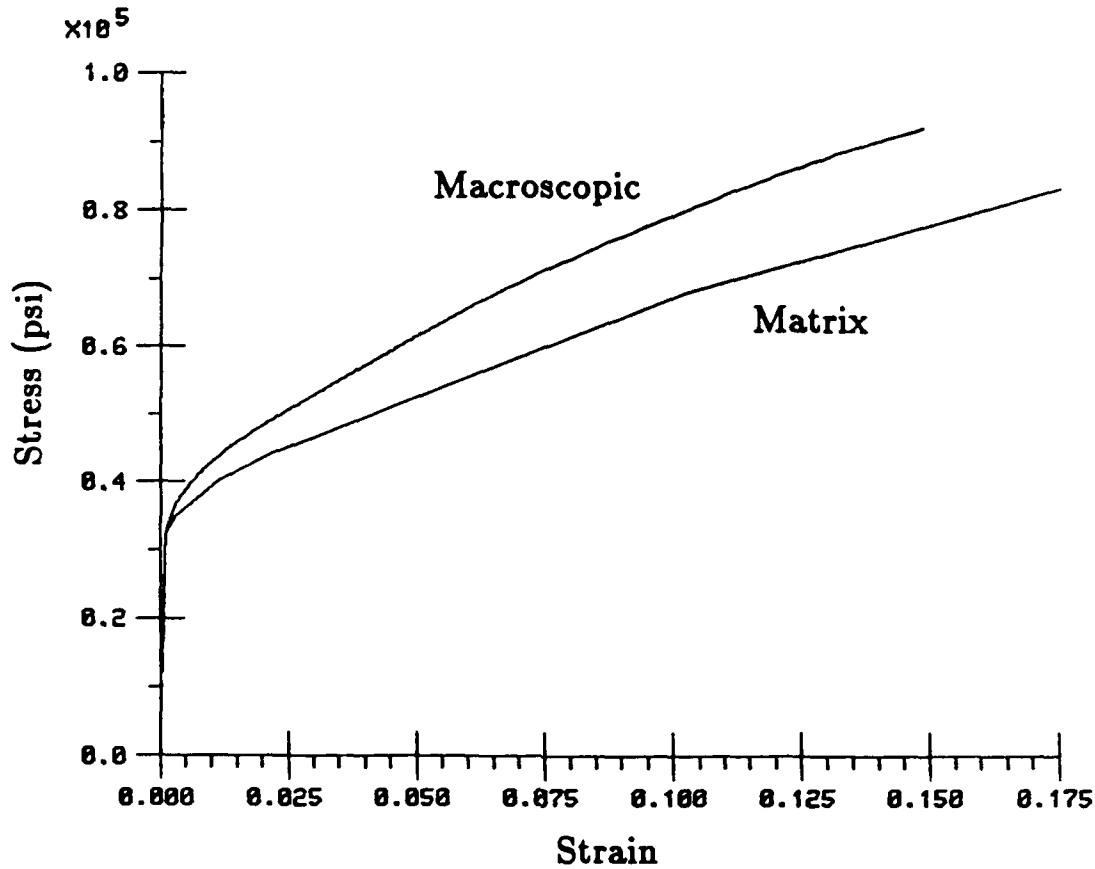

Figure 3.6 Comparison of macroscopic stress-strain result for the cell with the input stress-strain curve of the matrix.

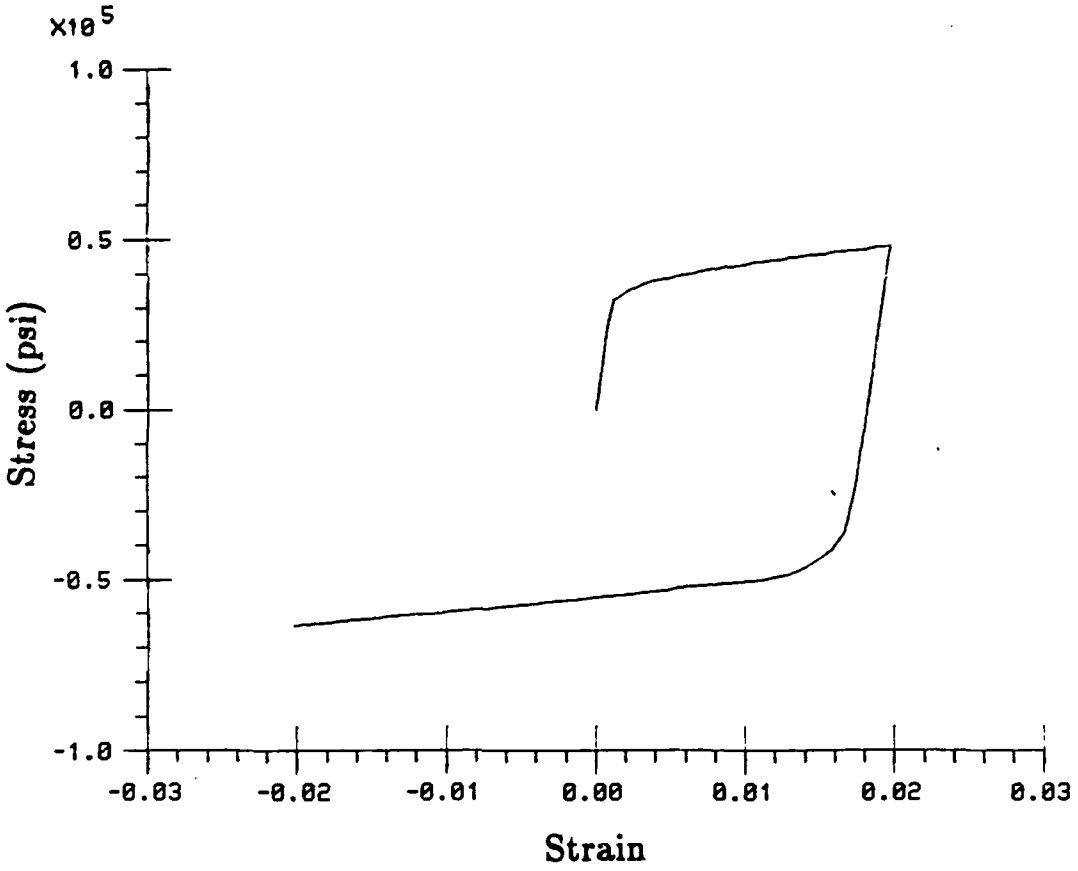

Figure 3.7 Example of the response of the cell for loading in tension followed by loading in compression.

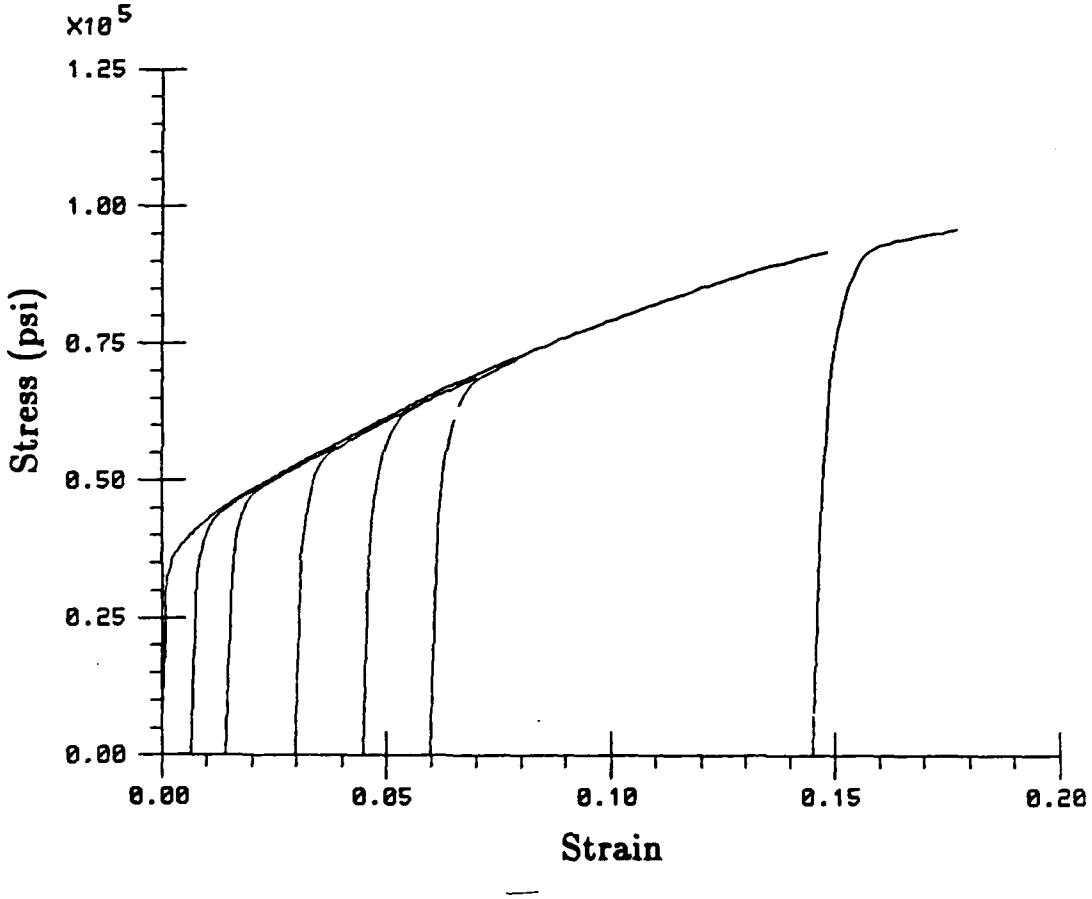

Figure 3.8 The reversing branches of 6 numerical simulations of tension-compression applied to the unit cell. The compressive results are rotated into the first quadrant for compactness.

(a)

Contour	Stress (ksi)
1	-50
2	-40
3	-30
4	-20
5	-10
6	0
7	+10
8	+20
9	+30
10	+40
11	+50

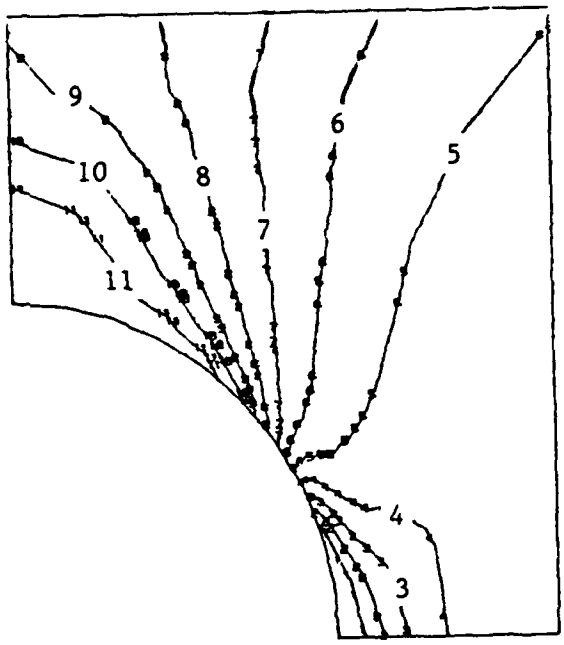

(b)

Contour	Plastic Strain
1	0
2	0.025
3	0.050
4	0.075
5	0.100
6	0.125
7	0.150
8	0.175

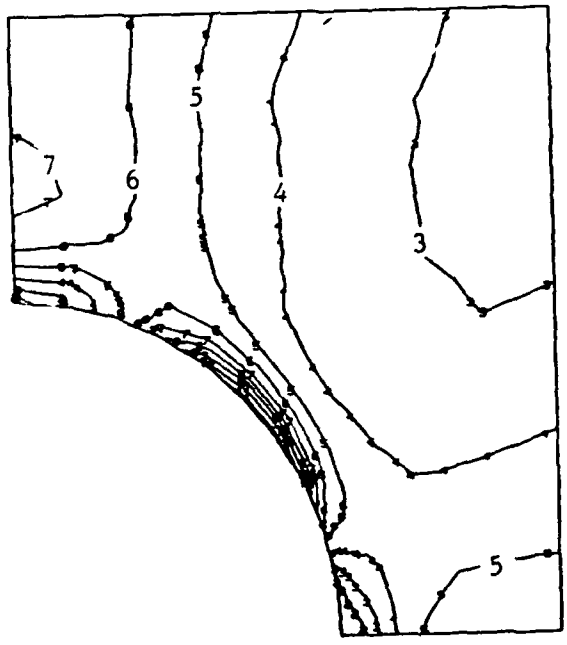

Figure 3.9 Contours for residual state in cell obtained by uniaxial loading to $\tilde{\epsilon} = 6\%$ followed by unloading to zero external load. a) Contours of residual vertical, normal stress σ_{22}. b) Contours of accumulated equivalent plastic strain.

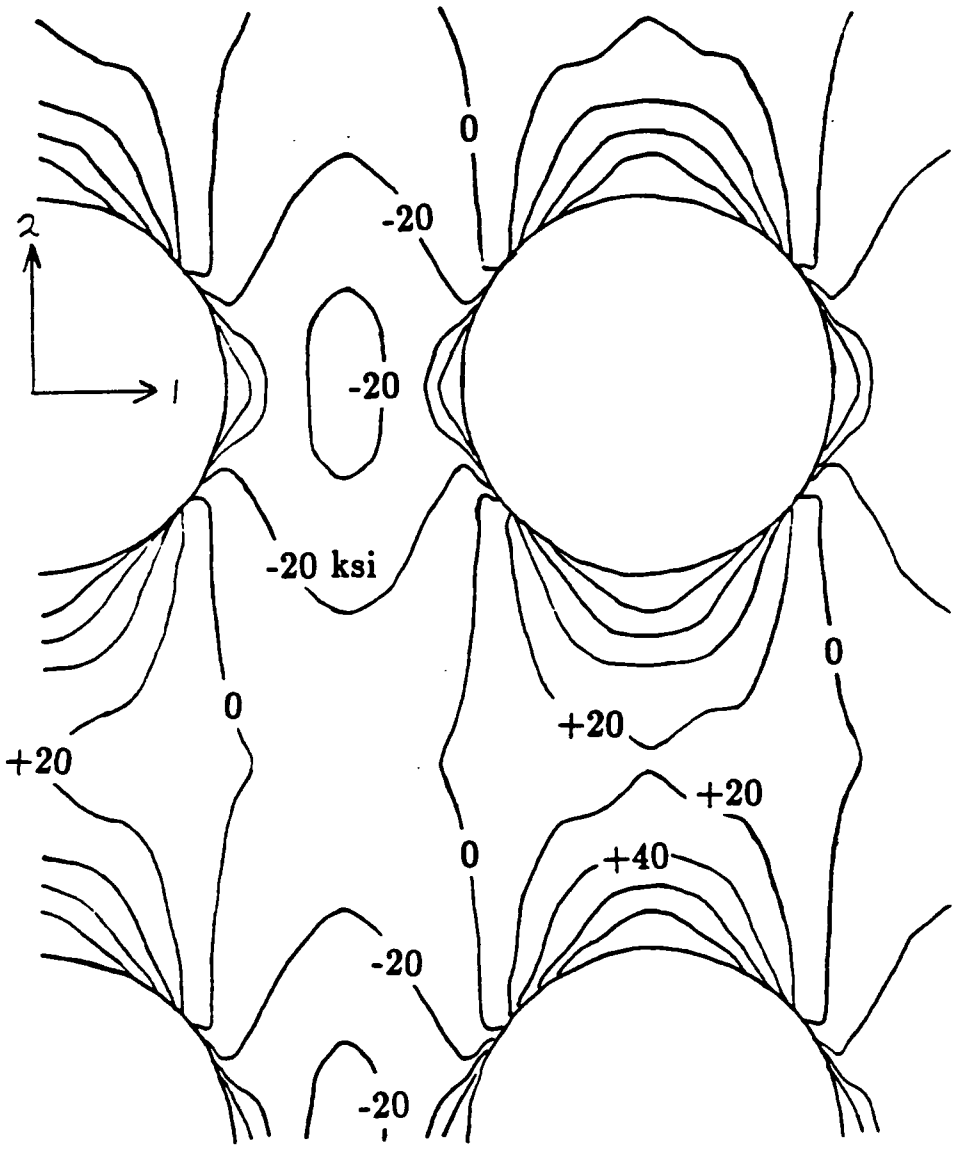

Figure 3.9c Distribution of residual stress σ_{22} for plane passing through particles. Prestrain was to 14.5% strain.

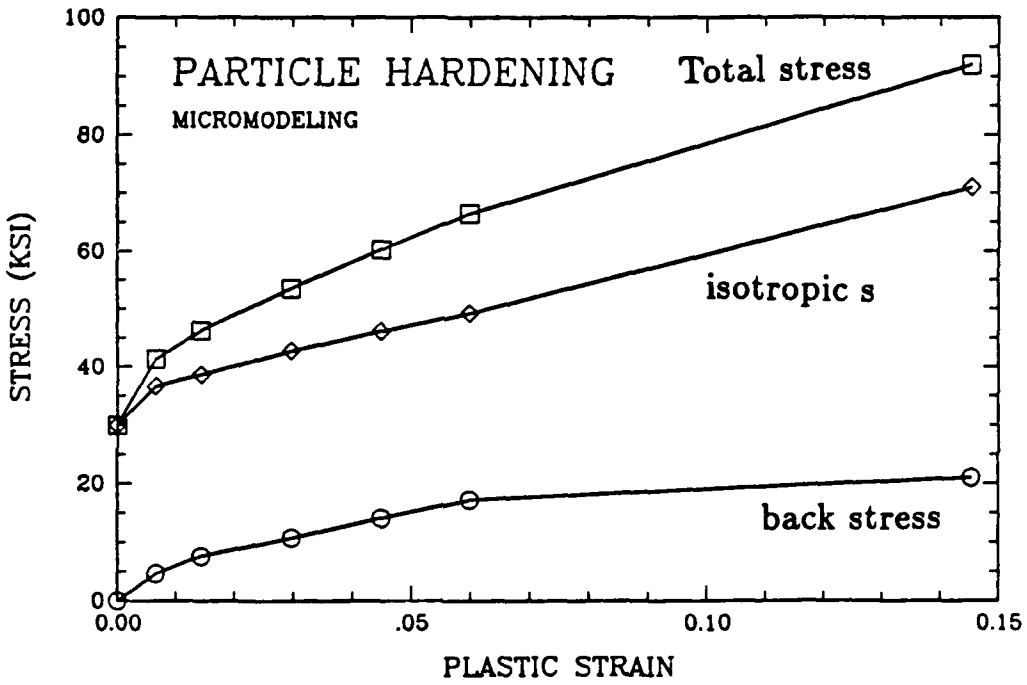

Figure 3.10 Separation of macroscopic, uniaxial loading curve into isotropic and back stress components.

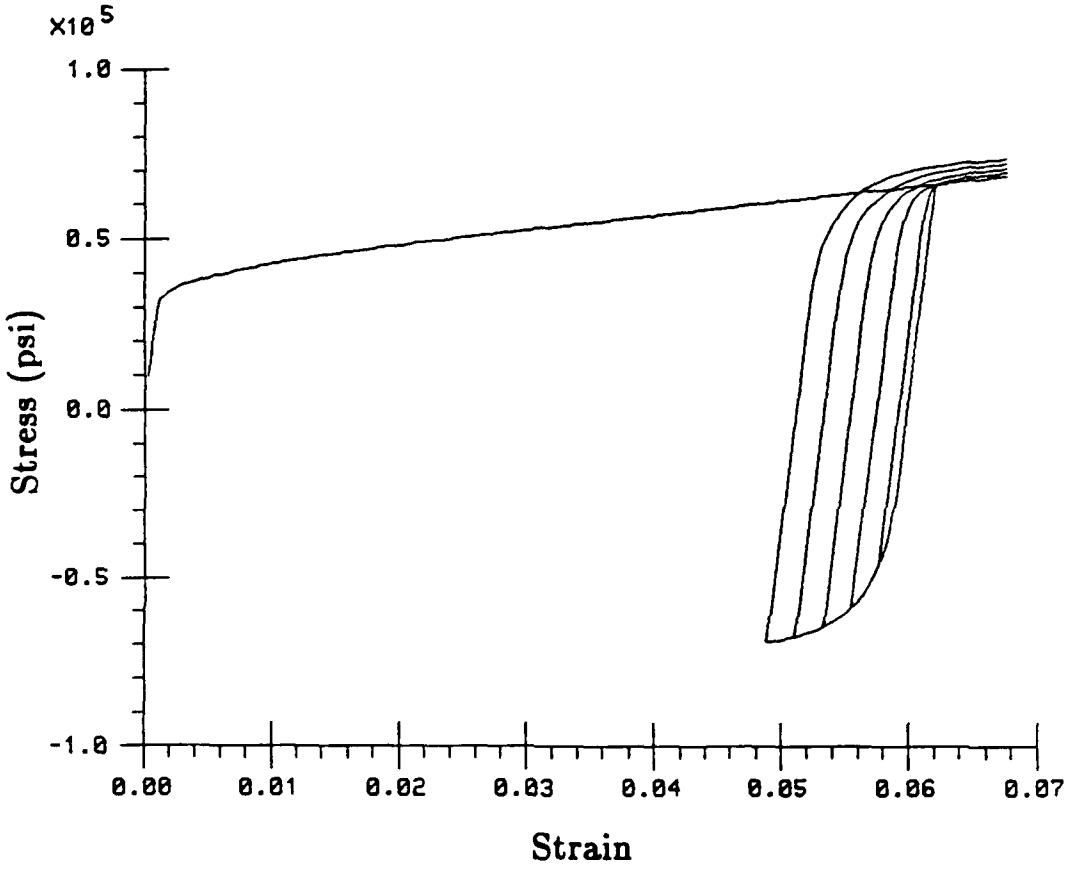

Figure 3.11 Macroscopic stress-strain results for forward loading followed by different amounts of reverse strain which is then followed by forward loading. Five different reloading branches are shown.

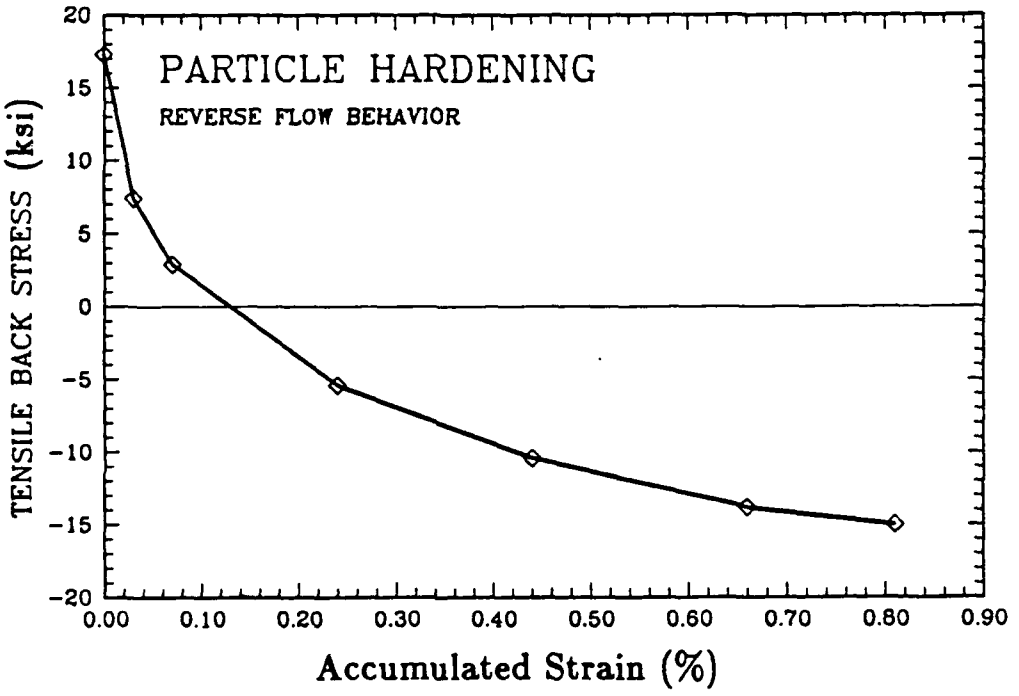

Figure 3.12 Evolution of the back stress with accumulated strain determined from the simulations of Figure 3.11.

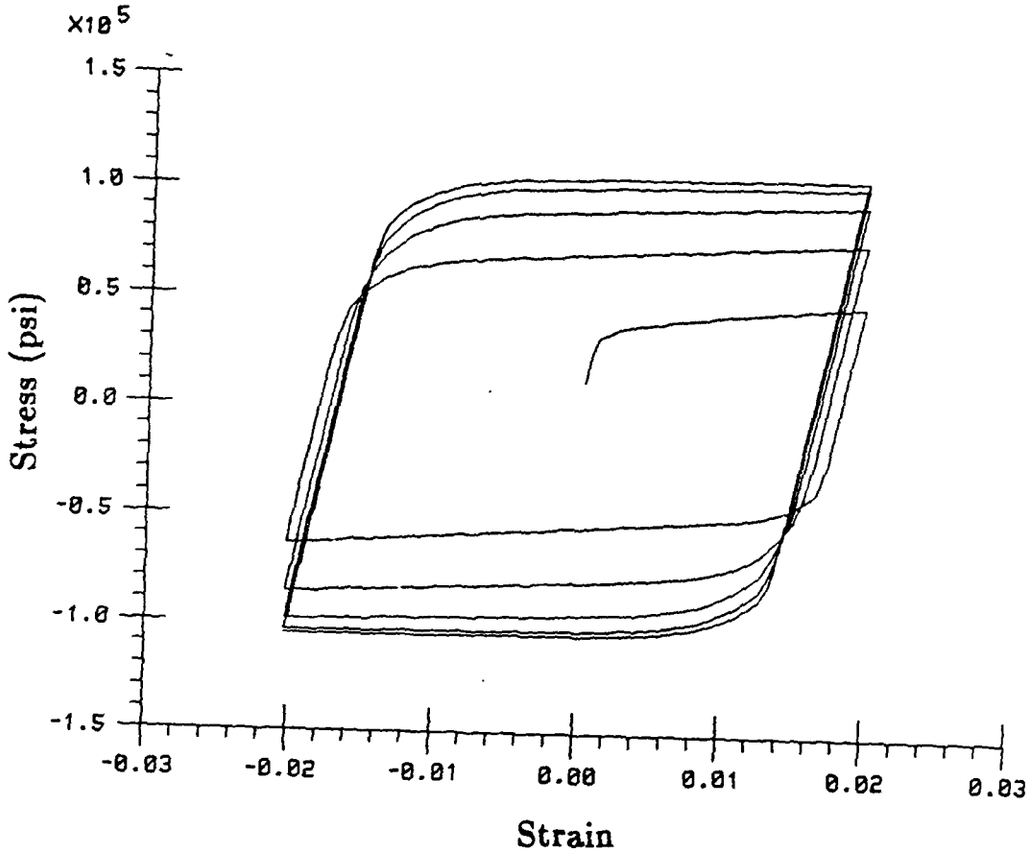

Figure 3.13 Cyclic stress-strain results for 5 cycles of $\pm 2\%$ strain cycling.

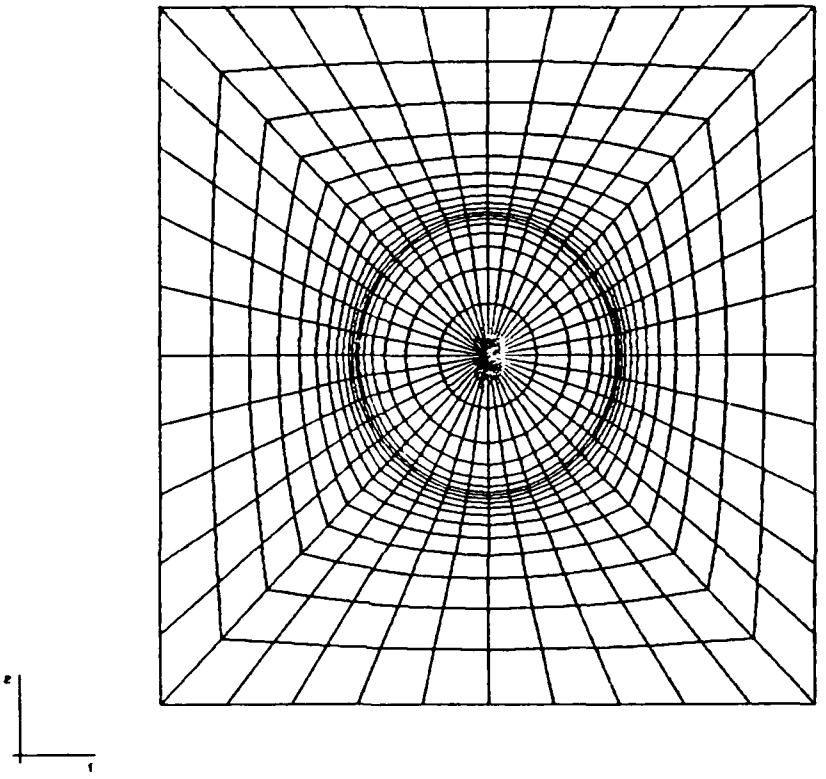

Figure 3.14 Finite element mesh used for unit cell of plane strain model.

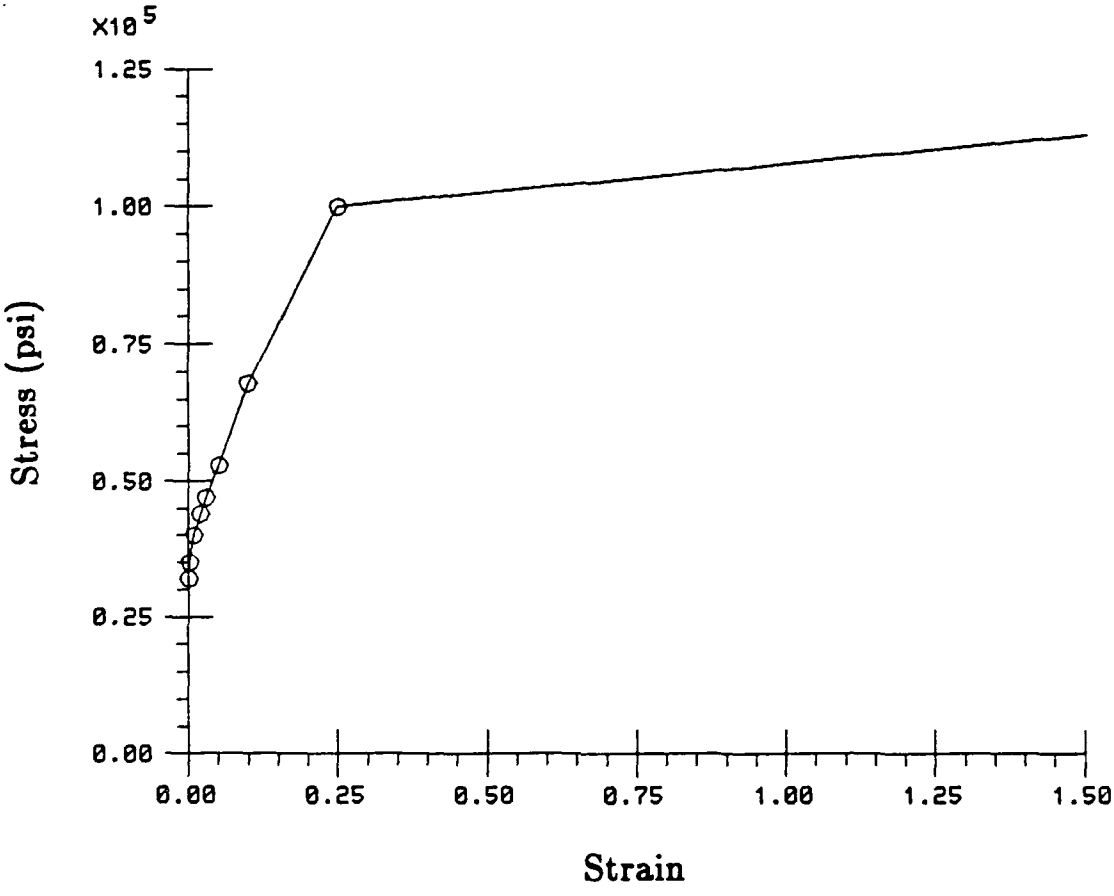

Figure 3.15 Input stress-strain curve used for modeling the matrix material for the plane strain simulation.

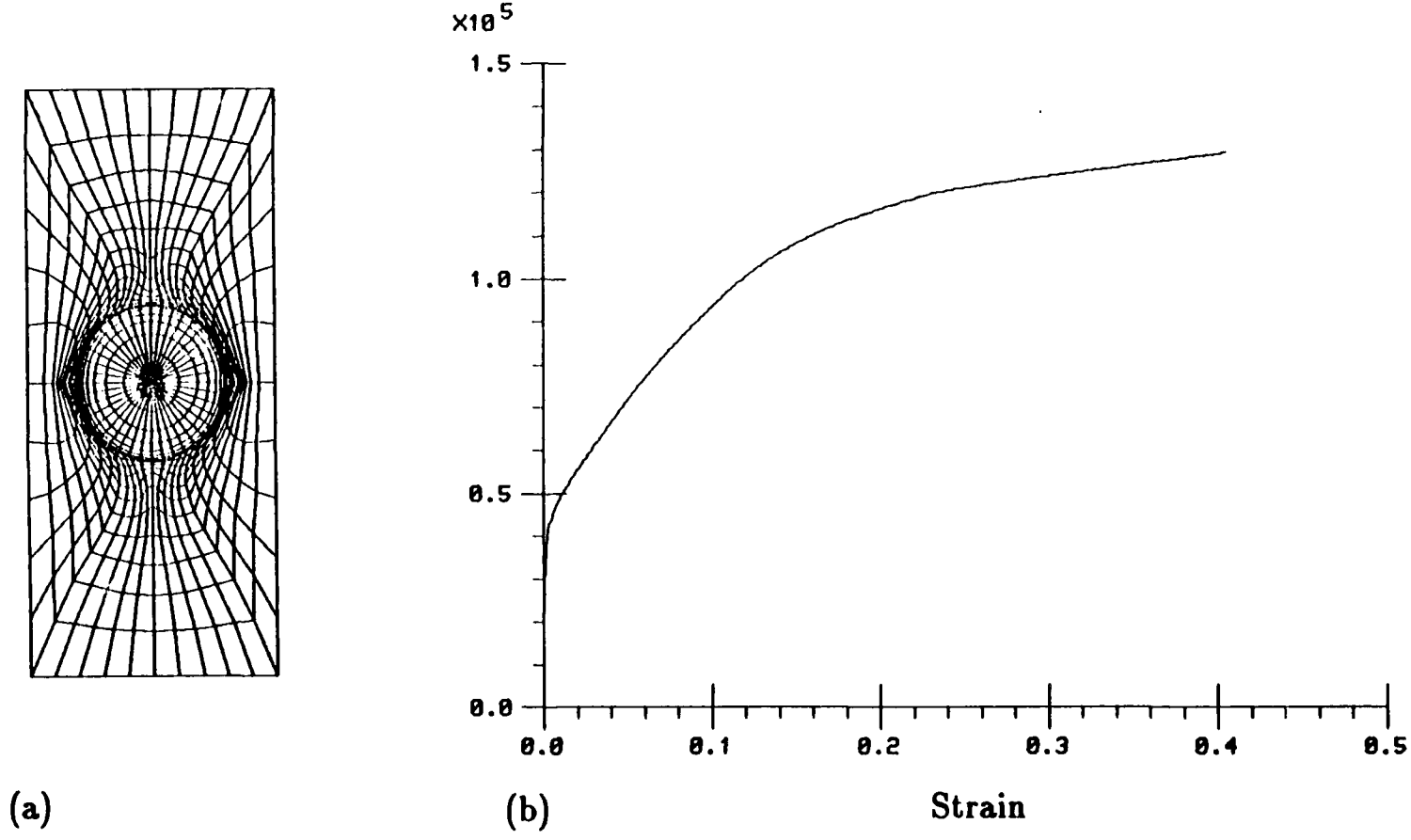

Figure 3.16 Tension test simulation using plane strain model. a) Deformed mesh after true strain of cell to 40%. b) Macroscopic stress-strain result of cell.

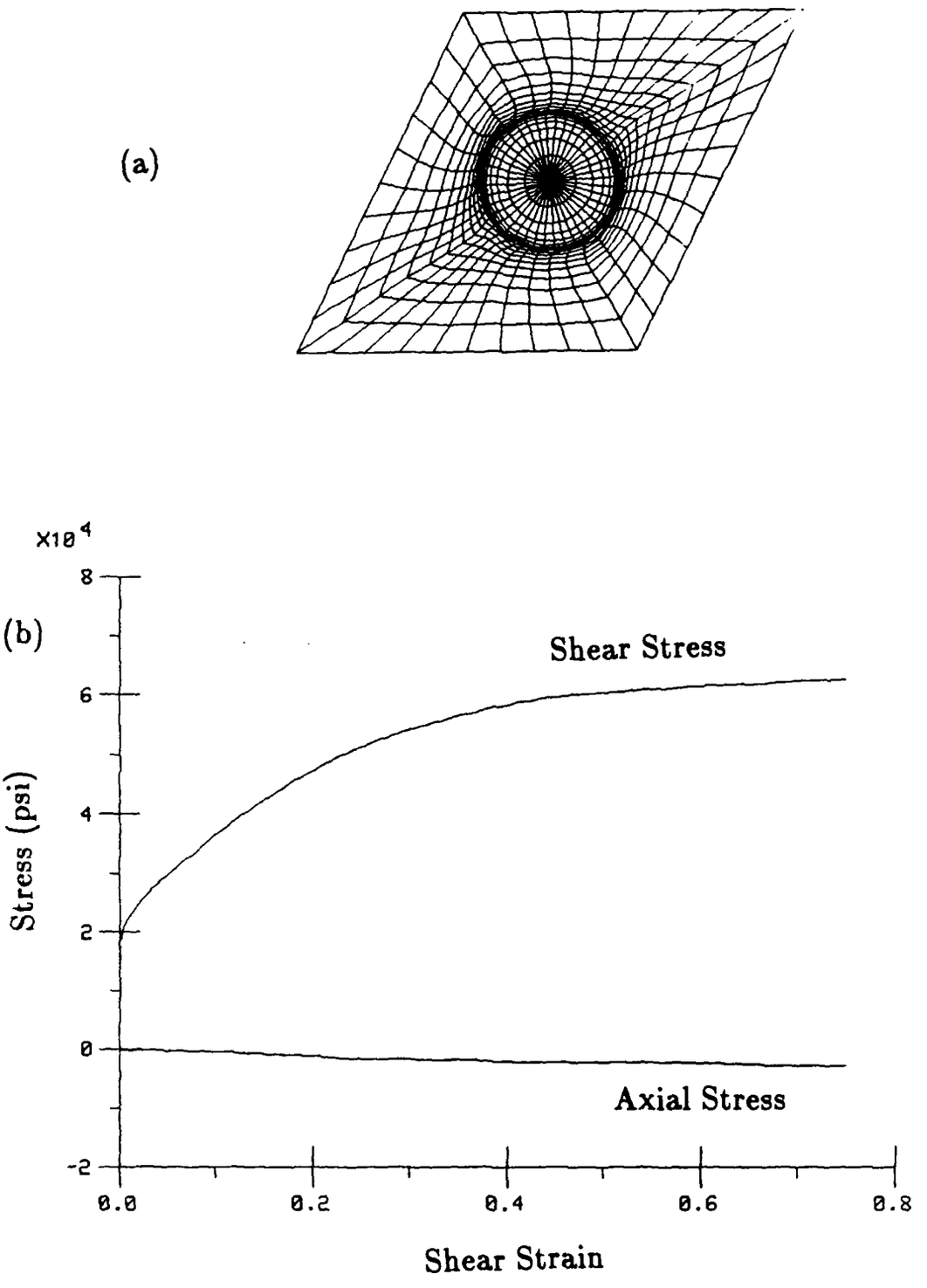

Figure 3.17 Simple shear results for plane strain cell. a) Deformed mesh for $\gamma = 0.5$. b) Macroscopic shear stress and vertical normal stress results.

Chapter 4

Review of Plasticity Modeling

In this chapter the relevant, published work is surveyed to guide constitutive modeling. This work is reviewed with the goal of extracting the important behavior to be modeled as well as the sufficiency of the current constitutive models to predict this behavior.

First, the experimental literature is briefly reviewed to identify the important behavior. The prominent areas of experimental research in metal plasticity investigated are: large strain experiments (primarily unidirectional), and cyclic plasticity (many stress reversals, both proportional and nonproportional).

In order to develop a model which can unite these classes of behavior the constitutive models particular to each of these classes were also summarized: large strain and cyclic modeling. From this review we will be able to identify several phenomena which have not been previously modeled but which lend great insight into the material behavior.

4.1 Experimental Review

4.1.1 Large Strain

Experimental studies of metals deformed to large strain have been conducted extensively over the last century. Different testing modes and test techniques have been developed and used with varying degrees of success. In this section only major trends and behavior are summarized. A more detailed discussion of large strain, experimental plasticity is presented in Appendix A.

The following list displays some of the important observed material behavior:

1. Initial yield and strain hardening are generally the same as observed in small strain experiments.

2. Strain hardening continues to many hundred percent strain. This is unlike elevated temperature testing which shows a stress saturation.

3. The equivalent stress during plastic flow is deformation mode dependent. For the same equivalent strain, torsional deformation occurs at a lower equivalent stress than tensile or compressive deformation.

4. For torsional deformation substantial axial, normal stress is developed at large strain when the specimen is restrained from axial displacement. If the specimen is unrestrained in the axial direction then axial strain accumulates with plastic deformation (the Swift effect).

This list is quite short because, even though there have been many large strain experiments, they have generally been restricted to one dimensional, monotonic loading. A useful model also needs to be able to adequately predict and represent

multiaxial, nonmonotonic loading conditions. To better understand the material response in these regimes we examine the cyclic plasticity literature as a guide to complex material response.

4.1.2 Cyclic Plasticity

Cyclic material response can vary quite markedly from pure monotonic behavior. Often the cyclic behavior of a metal is represented by a single cyclic stress-strain curve formed by connecting the tips of saturated hysteresis loops of various widths. Of course, this information alone does not properly represent all of the possible cyclic responses. There is a rich variety of phenomena for the many different types of cyclic loading. The cyclic results in the literature are limited to small strain.

This section will present some of the important behavior from the literature and draws largely from several review-type papers: Dolan [1965], Drucker and Palgen [1981], Dafalias [1984b], and Chaboche [1986]. First, behavior from uniaxial, cyclic tests will be discussed. This will be followed by results of multiaxial, nonproportional loading tests.

The most fundamental cyclic test in one in which the specimen is uniaxially cycled between constant strain limits centered on zero strain. The material will either show progressive hardening with each cycle or progressive softening depending upon the prior history of the material. Generally, an annealed material will harden and a cold-worked material will soften. Eventually the material responds with a saturated hysteresis loop, symmetric about the stress axis, that does not change with increasing numbers of cycles. For most materials, this steady state loop depends much more strongly upon the magnitude of the cyclic strain then it does upon the

prior strain history [Morrow and Tuler, 1965].

If a specimen is cycled between two strain limits which are not centered on zero then the first cycle will show a nonzero mean stress (mean of the maximum and minimum stress in the cycle). As cycling continues, the specimen will relax as the mean stress tends toward zero and a stable, symmetric hysteresis loop is formed. Again the cyclic strain range being most important in the size of the stress range. The cycle shows *mean stress relaxation.*

A specimen that is cycled between stress limits not centered on zero stress will show *cyclic creep.* With each cycle a small mean plastic strain will accumulate in the direction of mean stress. For many cycles this can give a substantial accumulation of plastic strain.

An example of this cyclic creep was given by Feltner [1963] for near pure aluminum. He measured the cyclic creep and compared that with the dislocation cell structure developed after various numbers of cycles. A very interesting result was that the dislocation density and cell structure was essentially unchanged from the first half cycle to more than 3400 cycles when a creep strain of more than 30 % had accumulated, see Figure 4.1. This is very different from monotonic loading where the dislocation density monotonically increases with plastic strain. Feltner cited two possible explanations for this behavior. The first would be that during a cycle few dislocations are generated but the existing ones move relatively long distances. The second explanation would be that during a cycle many new dislocations are created, move a short distance, and are annhilated. For the constancy of dislocation loop density that was observed there would have to be a balance between the dislocations that are created and those that are annhilated during each cycle.

Since the dislocation loop density is largely unchanged over many cycles, the difference between monotonic and cyclic behavior is substantiated on the microscopic as well as macroscopic scale. Cyclic behavior does not show the dramatic structural changes seen in monotonic loading.

In a recent paper Trampczynski [1988] conducted back stress evolution studies on two steels using a partial, successive unloading technique. He used a 0.05% offset definition for reverse yield. His results reinforce many of the observations made above:

- The general shape of the back stress path is established during the first loop of cyclic loading and changes only slightly for further cycles.
- The cyclically stable maximum values of back stress and isotropic component depend upon plastic strain amplitude.
- After prestrain in one direction, cyclic loading causes the isotropic component to soften.

The experimental results for **nonproportional** cyclic straining contain even more material phenomena which lend insight as well as require modeling. A summary of the most important differences of nonproportional cycling compared to proportional is presented below.

In 1978, Lamba and Sidebottom [1978a] conducted multiaxial experiments on tubular specimens of OFHC copper. They first recognized the main features of multiaxial, cyclic plasticity. The results for stable, hysteresis loops cycled between symmetric strain limits showed that there is one cyclic stress-strain curve for proportional loading whether conducted in tension/compression, torsion, or in-phase

tension/torsion. Plotting the maximum Mises equivalent stress against the maximum equivalent plastic strain range gave one curve independent of the loading direction as long as that direction remained constant throughout the test.

A dramatic result was seen when the combined tension/torsion straining was changed so that it was no longer proportional but 90° out-of-phase. This type of loading consists of cycling the axial strain and the shear strain where one lags the other by 90°. The material showed continued hardening *above* that for a uniaxial test. It formed a stable hysteresis loop at a stress level 40 % higher than that at the same maximum plastic strain range in the proportional (or in-phase) test. This level was independent of whether the specimen was initially cycled uniaxially or not.

This *additional hardening* due to out-of-phase straining has been noted more recently by other researchers also conducting tests of this type. Kanazawa, Miller and Brown [1979] have noted it in a 1% Cr-Mo-V steel. Krempl and Lu [1984] observed it type 304 stainless steel at room temperature. Cailletaud, Kaczmarek and Policella [1984], and Benallel and Marquis [1987] have studied the additional hardening in 316 stainless steel. The amount of additional hardening is strongly influenced by the degree of nonproportionality in the loading. The maximum hardening is seen for a 90° out-of-phase test where, for instance, a sinusoidal input is given to the axial and torsional strain controllers with the torsional signal lagging the axial one by 90°. The stress response for such a test is shown in Figure 4.2. Notice the hardening to a saturation stress magnitude. The final, multiaxial hysteresis loop is symmetric about the stress origin.

Additional hardening is seen, not only for out-of-phase cycling but for any change

in cycling direction. Benallel and Marquis [1987] note increased stress levels when changing from tension-compression to torsional cycling.

A final observation for multiaxial, cyclic loading concerns the loss of the additional strength when uniaxial cycling is resumed. A specimen that has saturated at the higher stress level due to out-of-phase cycling will soften if uniaxial cycling is added having the same maximum strain range. The additional hardening fades slowly with the cycling. This was observed by Lamba and Sidebottom [1978a] (they noticed that the additional hardening could be *erased*) and Cailletaud, Kaczmarek and Policella [1984].

Trampczynski [1988] also observed that additional hardening is caused by the isotropic component. Resuming uniaxial cycling causes the isotropic component to soften back to the unique value associated with that strain amplitude.

Lu [1986] presented data for 90° out-of-phase stress cycling of 6061-T6 aluminum alloy. Unlike with strain controlled cycling here strain is the response to the stress input. The stress rate is always perpendicular to the stress direction. Lu's results showed that the plastic strain rate does not have the same direction as stress for this loading. It bends toward the loading direction.

Several authors have also presented data for general, nonproportional loading blocks. It is not clear what specific phenomena can be cited from these tests but they do provide data to be used for general evaluation of cyclic models. These results are in [Lamba and Sidebottom, 1978b], [Cailletaud et al., 1984] and [McDowell, 1985].

4.2 Review of Constitutive Modeling

The previous section contained a description of the important material behavior to be modeled. This section examines the current constitutive modeling ideas in light of these phenomena.

A review of plasticity's early beginnings is not included here since that information is readily available elsewhere [Hill, 1950]. The constitutive model that has proven most useful for small strain plasticity is commonly referred to as the Prandtl-Reuss equations.

$$\mathrm{d}\epsilon' = \frac{\mathrm{d}\mathbf{T}'}{2\mathrm{G}} + \frac{3\,\mathrm{d}\sigma}{2\sigma H}\mathbf{T}',$$

$$\mathrm{d}\epsilon_{ii} = \frac{3\mathrm{d}\sigma_{ii}}{K},$$

where σ is the equivalent stress ($\sigma = \{\frac{3}{2}\mathbf{T}' \cdot \mathbf{T}'\}^{\frac{1}{2}}$), H is the slope of the equivalent stress-plastic strain curve, K is the bulk modulus and G is the elastic shear modulus. This is the plasticity theory most commonly found in computer codes today.

The other most significant small strain theory is due to Prager [1956] with modification due to Ziegler [1959]. This is referred to as *kinematic hardening*. The yield surface does not expand in stress space but rather translates. The translation of the yield surface center, **B**, is given by

$$\mathrm{dB} = C\,\mathrm{d}\epsilon^p,$$

where C is a scalar.

4.2.1 Large Strain Extensions of Previous Theories

The extension of constitutive theories valid for small amounts of deformation to ones suitable to describe finite deformation is not a straightforward process. Both

the kinematics of large deformation and the issues of material objectivity need to be addressed.

Around 1970 Budiansky [1970] proposed an extension of the Prandtl-Reuss equations in which he used the Cauchy stress measure with the kinematics defined in terms of the curvilinear coordinates. This theory was used by Needleman [1972] to study the growth of voids. Hutchinson [1973] modified the theory by replacing tne Cauchy stress with the Kirchhoff stress. This involved very little change to the theory for metals where the bulk modulus is much greater than the applied stress level. The benefit of this replacement is that it makes the finite element implementation easier since it leads to a symmetric formulation. Hibbitt, Marcal and Rice [1970] and also McMeeking and Rice [1975] were involved in concurrent extensions of the small strain Prandtl-Reuss equations.

Analogous to the way that the isotropically hardening theories developed in the small strain regime the large strain version of kinematic hardening was proposed in 1978 by Tvergaard [1978]. He used this theory to analyze biaxial necking. Calculations of bifurcation loads and strain levels have always been overestimated by models based on purely isotropic hardening. Tvergaard found that the softer transverse response of kinematic hardening better predicted the stress levels of localization but still overestimated the strains where localization occurred. Tvergaard's model generalized the Prager-Ziegler evolution law for the back stress by replacing the material time derivative with the Jaumann derivative.

$$\overset{\nabla}{\boldsymbol{B}} = \dot{\boldsymbol{B}} - \boldsymbol{W}\boldsymbol{B} + \boldsymbol{B}\boldsymbol{W} = \mu(\boldsymbol{\tau} - \boldsymbol{B})$$

where $\boldsymbol{B}$ is the back stress, $\boldsymbol{W}$ is the spin (= skew part of the velocity gradient), $\boldsymbol{\tau}$ is the Kirchhoff stress ($=\mathbf{T}\frac{\rho}{\rho_o}$), $\mathbf{T}$ is the Cauchy stress.

This substitution seemed natural from the mathematical viewpoint of formalism required to make the equation objective.

The formulation of a model which combines the features of isotropic and kinematic hardening was proposed by Key, Biffle and Krieg [1977] and used to calculate metal forming processes by Key, Krieg and Bathe [1979]. Since material data is not generally available in the literature to partition the hardening into realistic percentages of kinematic and isotropic components they chose to model their material as purely kinematically hardening.

The extension of the notion of kinematic hardening from small strain to large strain by the substitution of the objective Jaumann stress rate for the material stress rate in the equations of Prager-Ziegler was severely challenged in a presentation at a workshop held at Stanford University in 1981 by Nagtegaal and deJong [1982]. They showed that if this extension is used, then if the material is subjected to simple shear, such as in the fixed end torsion test, stress oscillations are predicted for both the shear and normal stresses. This response was unexpected for a monotonic loading condition.

This result sparked much interest in finite strain constitutive modeling. Simple shear is unlike many of the loading conditons that had been considered for model verification. The tensor stretching component is equal in magnitude to the continuum spin (skew symmetric portion of the velocity gradient). Lee, Mallett and Wertheimer [1983] explained that use of the Jaumann derivative in the back stress evolution equation leads to a back stress tensor that continues to rotate in stress space even though the deformation is bounded. They proposed using the spin of a material line element that instantaneously coincides with direction of the eigen-

vector corresponding to the largest back stress eigenvalue in a corotational stress rate.

$$\overset{\nabla}{B}{}^{L} = \dot{B} - W^{L}B + BW^{L},$$

where W^{L} is the spin of the material line coincident with the direction of the largest eigenvalue of the back stress.

This choice of stress rate does remove the oscillations for a sufficiently large hardening modulus but does not produce a monotonic shear stress response if the hardening modulus is low or, especially, if the hardening modulus decreases with strain (Reed and Atluri [1985]).

A number of different choices for the spin to be used in a corotational type rate have been proposed. Among them are the Green-Naghdi rate proposed by Dienes [1979,1986] and Johnson and Bamman [1984] and the "elastic" or "accomodating" spin of Dafalias [1984c], Loret [1983], and Anand [1985].

The use of tensor representation theorems to construct constitutive relations for the total velocity gradient, not just the symmetric part, has been pursued by Dafalias [1984c], Loret [1983], and Anand [1985]. Lee [1969] had proposed decomposing the deformation gradient, $\mathbf{F}$, into elastic and plastic parts,

$$\mathbf{F} = \mathbf{F}^{e}\mathbf{F}^{p}.$$

Dafalias, Loret and Anand have taken the approach that F^{p} is defined in an analogous way to one dimensional, small plastic strain. Consider unloading the body that has been deformed, then orienting the material elements, with respect to a spatial reference frame, to the identical orientation they had in the original configuration. The F^{p} is then just that transformation which takes the original configuration to this specially oriented, relaxed configuration.

This is not the only way to prescribe the partitioning of the $F^e F^p$ decomposition. Fardshisheh and Onat [1974] and Parks et. al. [1985] require that F^e be a pure straining such that $F^e = F^{eT}$. They embed the plastic spin in a skew symmetric expression which is prescribed without additional constitutive modeling. Loret [1983] and Dafalias [1984c] presented the general forms for representing a skew symmetric tensor such as spin by using the representation theorems of C.C. Wang [1970]. By using the lowest order generator which is derivable from two symmetric tensors they propose a constitutive law containing one scalar material function. Loret [1983] and Dafalias [1984a, 1984c, 1985] examine the response of this type of model for simple shear. They show that for proper choice of the scalar parameter the stress oscillations predicted by the kinematic hardening model can be removed. Also they showed that the magnitude of the normal stress which develops during large simple shearing can be controlled by this parameter. Without attempting to match experiments they have demonstrated that including plastic spin in the material model provides better qualitative predictions.

Dafalias has also applied the inclusion of plastic spin into an illustration of a transversely isotropic material (Dafalias [1984c]). Here the significant material directions can be more easily visualized than with kinematic hardening.

Anand [1985] applied a full state variable representation to finite, elastoviscoplasticity. He shows the construction of a phenomenological theory, the form of which follows from the use of Wang's tensor representation theorems. By proper simplification the traditional plastic stretching flow rule is recovered. This form is equivalent to that proposed by Dafalias and Loret for rate-independent plasticity.

Paulun and Pecherski [1985,1987] argue for a particular choice of the constitutive

function for the plastic spin. Their choice is equivalent to the spin of the material line element initially perpendicular to the shear direction. This selection also gives monotonic behavior in simple shear.

In reviewing this flurry of stress rate proposals, Reed and Atluri [1985] reexamine the simple shear results of classical (Jaumann rate) kinematic hardening, that of the "Green-McInnis" rate presented by Dienes [1986], and the rate of Lee et al. [1983]. They point out that none of these stress rates predict normal stresses having the proper order of magnitude for the limited torsion results from the literature. This author would like to point out that no material has been shown to harden entirely by kinematic translation of the yield surface either. Reed and Atluri correctly assert that the discrepancy in stress rates can be absorbed on the right hand side of the equations by modifying the constitutive form. They suggest that any objective stress rate can be used for the evolution of the back stress if an additional "damping" term is used,

$$\overset{\nabla}{\mathbf{B}} = C\mathbf{D}^p - F(\mathbf{B}\cdot\mathbf{D}^p)\mathbf{B}.$$

This idea was also proposed by Nagtegaal and deJong [1982] and is discussed in this document in terms of modeling cyclic plasticity. Haupt and Tsakmakis [1986] examined several classes of evolution equations having damping terms. They showed that, for linear hardening, none of their damping forms eliminated nonmonotonic behavior in simple shear. This suggests that proper choice of an objective stress rate is necessary to obtain correct material response.

4.2.2 Theories for Cyclic Plasticity

The theories for large strain plasticity have often ignored the details of material response upon a change in loading direction. The constitutive models developed for cyclic plasticity, on the other hand, have paid considerable attention to that situation. Here the main classes of these theories are reviewed with an eye toward simplicity yet retaining the essential features of the material behavior.

The accurate modeling of the reverse loading behavior observed in metals has proven elusive. In 1886 Bauschinger [1886] observed that a metal specimen which had been plastically deformed in tension showed a decrease in the magnitude of yield upon subsequent compression. This asymmetry of deformation across the stress space has been the subject of many experimental studies and much analytical modeling. This section examines the modeling concepts and analytical formulations postulated to describe reverse loading behavior.

Recent reviews by Chaboche [1986], Dafalias [1984b] and Drucker and Palgen [1981] are available so the objective here is to briefly present a list of the observed phenomena to be reproduced and to describe how the various modeling concepts apply to them. The models to be considered include:

1. Prager-Ziegler kinematic hardening
2. Mechanical sublayer model
3. Mroz model
4. Two surface model
5. Evanescent hardening

6. Endocronic theory.

Some experimental phenomena to be modeled in cyclic plasticity have been given by Drucker and Palgen [1981] and discussed by Dafalias [1984] . A list of items applicable to modeling for large strain applications should include the following.

1. After deformation in one stress direction an excursion across the yield surface should show a reduced stress magnitude when yielding occurs again.

2. There should be a smooth transition from elastic to elastic-plastic behavior when crossing the yield surface in the reverse direction from the previous loading.

3. The plastic modulus should gradually decrease as plastic flow recommences and achieves the value it had prior to unloading after 2-10 % subsequent strain.

4. After reverse flow when the plastic modulus achieves the value it had prior to unloading there may be a permanent softening where the flow stress magnitude is less than it would have been in unidirectional loading at the same equivalent strain.

5. Under symmetric stress or strain cycles, metals and alloys will cyclically harden or soften to a stable hysteresis loop.

6. Asymmetric stress cycles will cause cyclic creep (or ratchetting) in the direction of the mean stress.

7. Asymmetric strain cycles will cause progressive relaxation of the mean stress to zero.

8. Multiaxial, proportional, cyclic loading behaves similar to uniaxial cycling when the equivalent stress and equivalent strain are used for comparison.

9. Increased hardening is observed for multiaxial, nonproportional cycling. Higher saturation stress levels are obtained for cycling to the same maximum strains. The largest increase in hardening is seen for 90° out-of-phase cycling.

A review of these observations shows that the first four items relate to deformation having few changes in loading direction while the next three are observed during cyclic deformation. The last two items relate specifically to multiaxial cycling. It has not been explicitly stated but it is assumed that a specimen unloaded into the elastic region then reloaded in the original loading direction will have a sharp reyield and continue plastically deforming as if the elastic excursion had never taken place. This is a very good assumption for room temperature deformation of most structural alloys.

Since the vast majority of the experiments and the modeling have been applied to uniaxial cycling, it will be considered first, followed by multiaxial applications of the models.

A common feature of all of the models considered is their use of a "back stress" to account for the stress space asymmetry. The differences arise from the way the back stress develops. These models can be characterized by the evolution laws for the back stress and the models evaluated in terms of how well they can represent the conditions described above. A brief summary of the models listed above is given in Appendix B. The highlights of their suitability to model the above mentioned phenomena is also considered.

When considering these cyclic plasticity models concentration is given to the

back stress evolution, or kinematic portion. In modeling cyclic behavior these particluar models have been used with certain assumptions about the isotropic hardening component. The isotropic hardening is the nondirectional component of hardening that can be thought of as giving the radius of the yield surface. In some applications no isotropic hardening is used [Mroz, 1967] but for most of these models a monotonic increase in the yield surface radius is allowed. The evolution of the isotropic variable s can be written by

$$\dot{s} = h_I \dot{\tilde{\epsilon}}^p.$$

Here h_I is the isotropic hardening modulus which can be a constant or often is a decreasing function of s or $\tilde{\epsilon}^p$.

As discussed by Chaboche [1986] in the application to cyclic hardening combined with, for instance, the evanescent back stress law s must go to a saturation level s^* for the model to predict a stabilized cyclic loop. An example of an evolution equation that yields such behavior [Brown, 1987] is

$$\dot{s} = h_0 \left(1 - \frac{s}{s^*}\right)^q \dot{\tilde{\epsilon}}^p,$$

where h_0, q and s^* are material constants. The difficulty with such a formulation is that for every cyclic strain range the same saturated value of $s(= s^*)$ would be predicted. Experimentally, this is not seen [Chaboche, 1986]. Cycling at larger strain ranges should give larger values of stress saturation. Also cycling the same specimen at two different strain levels shows an effect of the first strain level on the saturation achieved at the second. This has been termed the maximum plastic strain memory effect. Chaboche [1986] has taken this effect into account in an ad hoc way by making s^* a function of the maximum plastic strain amplitude.

The models which impose the restraint that $h_I = 0$ for a stable cyclic loop are too restrictive. What is really necessary is just that the change in s over a closed cycle by equal to zero.

$$\oint \dot{s} = 0.$$

This condition is less restrictive although to date no author has seemed to realize that or employ it. The implications of this will be discussed when the new model is presented in Chapter 5.

As discussed above, and in Appendix B, each of the models used for cyclic plasticity has certain strengths and weaknesses. The choice of a model depends in part upon the phenomena most important for a given application. The Mroz, two surface, and evanescent models give qualitatively similar modeling capabalities. The two surface model has the advantage of specifying a smooth elastoplastic transition and a better simulation of random-type loadings and ratchetting effects (Chaboche [1986]). The evanescent hardening model has the advantage of easier numerical implementation and connection with internal variable theories.

The modeling of the **nonproportional hardening** phenomena has not been as systematically investigated. The comparison with experiment, to date, has largely been application of the models listed above.

Lamba and Sidebottom [1978b] compared three constitutive models with results from a highly nonproportional strain path test. The models they compared were:

Prager kinematic hardening with a Mises yield surface.

Ziegler kinematic hardening with a Tresca yield surface.

Mroz type hardening with Tresca yield and limit surfaces.

These were all purely kinematic hardening theories. There was no isotropic expansion assumed. They found that all three models gave qualitatively correct results. The Mroz-Tresca model gave better quantitative results. For this reason they came out in support of Mroz type models. They did not try to match the additional hardening observed in [Lamba and Sidebottom, 1978a] with any theory. None of the above would have been able to do it.

Nouailhas et al. [1985] examine several different models in comparison to their 316 stainless steel out-of-phase data. They saw that Prager hardening produces a softening during out-of-phase loading compared with the uniaxial cyclic response. This is a nonphysical prediction when compared with experiment. The evanescent hardening does not give this softening but it does not predict any additional hardening either.

They also incorporated a new memory parameter which tracks the maximum plastic strain range. This was introduced and is discussed by Chaboche et al. [1979]. This model did give an additional hardening of 50 MPa which is far below their observed magnitude of 300 MPa.

Nouailhas et al. [1985] also considered a model which did not retain the same yield surface shape during deformation but deformed from a Mises circle into an ellipse. The yield surface distortion was a function of the back stress developed. This surface was incorporated with both Prager and evanescent hardening. It allowed large amounts of additional hardening with its additional free parameter.

Tseng and Lee [1983] proposed a two surface model for cyclic plasticity. Their model retained much of the same machinery as that of Dafalias and Popov [1976] with one major exception. The direction of the stress rate influences the translation

of the inner surface (back stress evolution). The yield surface translates more in the stress rate direction than a Mroz type evolution law would predict. This was justified on the basis of translating yield surface experiments of Phillips and Lee [1979]. This model does not predict additional hardening for out-of-phase strain cycling but did a good job correlating the nonproportional tests of Lamba and Sidebottom [1978b].

McDowell [1987] compared a number of theories, including that due to Tseng and Lee, with nonproportional test data obtained for type 304 stainless steel at room temperature [McDowell, 1985]. He found that the Mroz, Tseng-Lee, and evanescent hardening rules were all superior to Prager-Ziegler type hardening. He also showed that the Tseng-Lee model was more accurate than the others for correlating his test data.

Chu [1987] applied a generalized Mroz model to some of the nonproportional test results in the literature ([Phillips and Lu, 1984], [Lamba and Sidebottom, 1978 a and b]). She reported reasonable results for these experiments. This is expected from the other results that have been presented.

Megahed [1988] compared a number of the models mentioned above with the nonproportional experiments of Kaneko, Ogawa and Iwata [1982]. In these tests a sharp corner was made in the stress loading path for type 304 stainless steel. The comparisons showed that the Mroz nesting surface model and a memory surface model were capable of predicting the behavior but not the two surface model [Dafalias and Popov, 1976] or the classical isotropic or kinematic hardening models. The observation was made of the importance of the isotropic component in successful plasticity theories.

The large additional hardening observed in out-of-phase cycling has been attributed to an increase in isotropic hardening. More isotropic hardening is considered to have occurred if the principal strain directions change during deformation. It is felt that more slip systems become activated. A number of proposals have been made to increase the amount of isotropic hardening by making it a function of the nonproportionality.

Benallel and Marquis [1987] make the isotropic radius saturation level a function of the angle between the back stress and its rate. For 90° out-of-phase cycling the maximum additional hardening is indeed predicted.

McDowell [1987] defined a variable reperesentative of the averaged noncollinearity of plastic strain. He made the isotropic saturation state a function of this history dependent parameter. Other measures of nonproportionality are also being considered based upon angles between various stress or strains and/or their rates.

All of these approaches start with the uniaxial isotropic hardening as the baseline material behavior. They then add something based upon the degree of nonproportionality.

In summarizing the application of cyclic plasticity models to multiaxial, nonproportional loading we note several things. First, for experiments with sharp changes in loading paths the Mroz, two surface, and evanescent hardening theories all capture the correct qualitative behavior. The Prager-Ziegler back stress evolution does not capture the behavior as well. Second, the isotropic hardening needs to be reexamined. In light of the inadequacy of the models to predict additional hardening for the out-of-phase tests, new ideas for modeling isotropic hardening are needed. The effect this would have on the previously drawn conclusions about the back stress

evolution laws is unknown but could be significant.

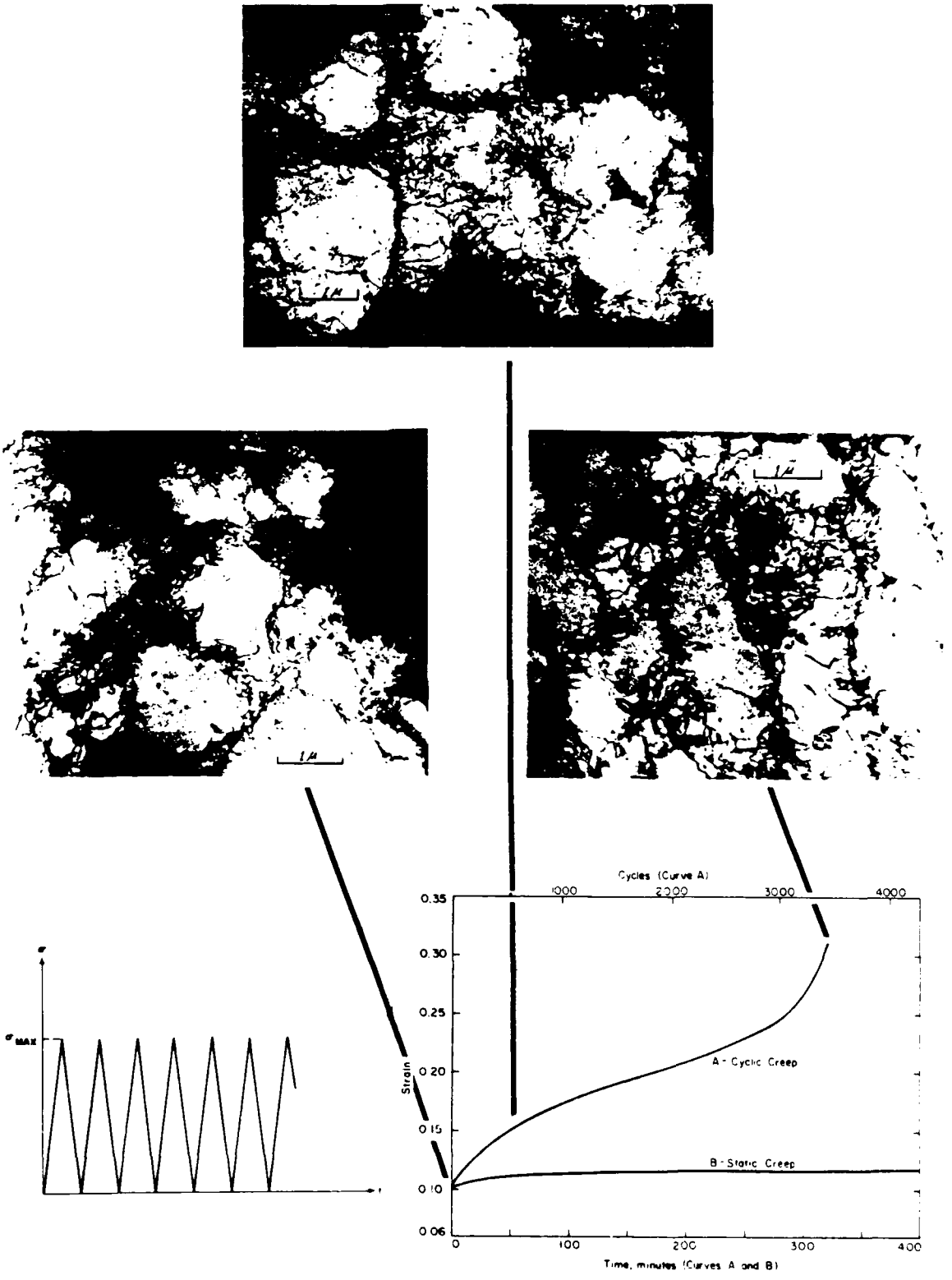

Figure 4.1 Evolution of dislocation structure during cyclic creep. Micrographs of aluminum are shown at indicated points in the deformation history. [Feltner, 1963].

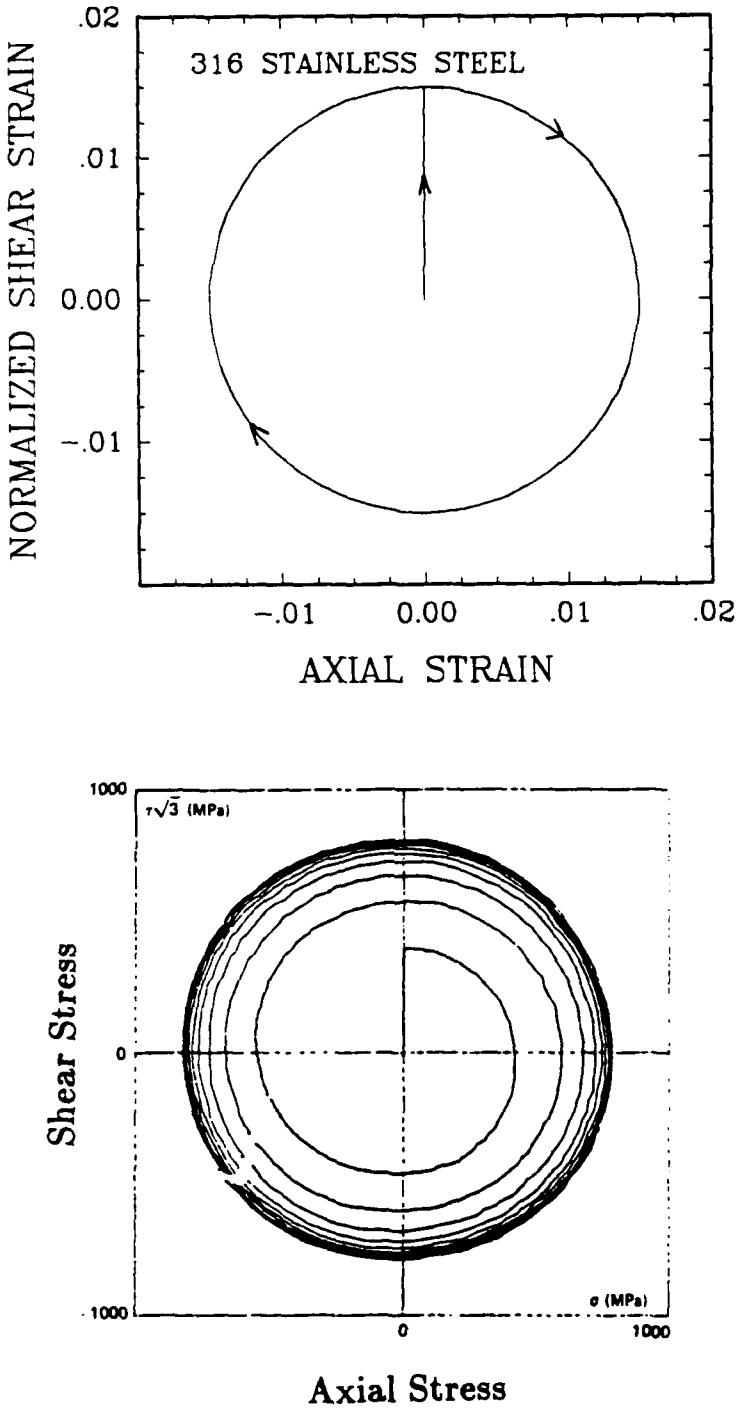

Figure 4.2 Out-of-phase cycling. a) Input strain history. b) Stress response. [Cailletaud et al., 1984].

Chapter 5

Constitutive Equations for Rate-Independent, Elastic-Plastic Solids

5.1 Overview

This chapter develops a procedure for expressing the finite deformation of elastic-plastic, rate-independent solids. The general framework is developed, including kinematics, then is simplified to focus on the observed behavior of metals. Finally, some constitutive forms are proposed and experiments suggested to evaluate the material parameters.

5.2 Finite Deformation

The kinematical framework for finite deformation metal plasticity has been vigorously debated in recent years [Fardshisheh and Onat, 1974], [Lee, Mallett and Wertheimer, 1983], [Dafalias, 1987], [Boyce et al., 1988]. Central to the discussion is the factorization of the deformation gradient, $\mathbf{F}$, into an "elastic" part, $\mathbf{F}^e$, and a "plastic" part, $\mathbf{F}^p$ [Lee, 1969].

$$\mathbf{F} = \mathbf{F}^e\mathbf{F}^p.$$

By using this decomposition and the other usual approximations of metal plasticity such as small elastic stretches Anand [1985] reduced a general constitutive framework to one applicable to viscoplasticity. Here, we take as our starting point that framework except as it is applied to rate independent plasticity.

$$\mathbf{L} = \mathbf{D} + \mathbf{W},$$

$$\mathbf{D} = \mathbf{D}^e + \mathbf{D}^p,$$

$$\mathbf{W} = \mathbf{W}^e + \mathbf{W}^p,$$

where $\mathbf{L}$ is the velocity gradient, $\mathbf{D}$ the stretching which has elastic ($\mathbf{D}^e$) and plastic ($\mathbf{D}^p$) parts. $\mathbf{W}$ is the spin. It has accomodating ($\mathbf{W}^e$) and plastic ($\mathbf{W}^p$) parts.

The objective rate $(\,)^{\nabla e}$ is defined by

$$(\,)^{\nabla e} \equiv \dot{(\,)} - \mathbf{W}^e(\,) + (\,)\mathbf{W}^e.$$

The constitutive equations can be written in the current, loaded configuration.

1. The stress equation becomes

$$\mathbf{T}^{\nabla e} = \mathcal{L}[\mathbf{D} - \mathbf{D}^p]. \tag{5.1}$$

2. The yield condition

$$f = \frac{3}{2}\mathbf{T}'^* \cdot \mathbf{T}'^* - s^2 \leq 0. \tag{5.2}$$

Here $\mathbf{T}'^* \equiv \mathbf{T}' - \mathbf{B}$.

3. The flow rule

$$\mathbf{D}^p \;=\; \Psi\,\frac{1}{H}(\mathbf{n}\cdot\mathbf{T}^{\nabla e})\,\mathbf{n} \quad \text{where} \quad \mathbf{n} \;=\; \frac{\mathbf{T}'^*}{\sqrt{\frac{2}{3}}s}, \tag{5.3}$$

$$\mathbf{W}^p \;=\; \Psi\,\frac{\eta}{H}(\mathbf{n}\cdot\mathbf{T}^{\nabla e})\,\mathbf{\Omega}^p \quad \text{where} \quad \mathbf{\Omega}^p \;=\; \frac{\mathbf{B}\mathbf{T}'^* - \mathbf{T}'^*\mathbf{B}}{\frac{2}{3}\sigma_b s}. \tag{5.4}$$

The parameter Ψ provides the switching condition for plastic flow

$$\text{if } f = 0 \text{ and } \mathbf{n}\cdot\mathcal{L}[\mathbf{D}] > 0 \text{ then } \Psi = 1,$$

$$\text{if } f < 0 \text{ or } \mathbf{n}\cdot\mathcal{L}[\mathbf{D}] \leq 0 \text{ then } \Psi = 0.$$

4. The evolution equations

$$\mathbf{B}^{\nabla e} \;=\; C_1\,\mathbf{D}^p \;-\; C_2\,\dot{\bar{\epsilon}}^p\,\mathbf{B}, \tag{5.5}$$

$$\dot{s} \;=\; H_{iso}\,\dot{\bar{\epsilon}}^p. \tag{5.6}$$

Next we will turn our attention to functional forms to use for the scalar constitutive functions C_1, C_2, H, H_{iso} and η. First, we can take advantage of the consistency condition to relate C_1, C_2, H_{iso}, and H. The yield condition must be satisfied throughout active plastic flow. We can write that by

$$\dot{f} \;=\; 3(\mathbf{T}' - \mathbf{B})\cdot(\mathbf{T}'^{\nabla e} - \mathbf{B}^{\nabla e}) \;-\; 2s\dot{s} \;=\; 0. \tag{5.7}$$

If we substitute from the constitutive equations above (eqs. 6.35 to 6.38) and simplify then we obtain the relation

$$H \;=\; \frac{2}{3}\,H_{iso} \;+\; C_1 \;-\; \sqrt{\frac{2}{3}}\,C_2\,\mathbf{B}\cdot\mathbf{n}. \tag{5.8}$$

In physical terms, this merely states that the total hardening is the sum of that due to the isotropic expansion and that due to the kinematic translation. There are differing views in the literature as to which of the material functions should be the dependent one. If the emphasis of a model is on determining the evolution equations then H is the dependent function and is determined from the evolution equation functions via Equation 6.40 . Dafalias [1984b] discusses these issues and stresses the importance for correctly determining the plastic modulus H. In the present work we view correctly choosing functions that can be experimentally verified as of prime importance. Since, as we shall see, H can be directly determined from a uniaxial experiment we will consider it an independent function and use the consistency condition to infer one of the evolution equation functions.

5.3 Function Dependence

The general model presented in the previous section (Equations 6.33 to 6.38) is similar to ones presented in the literature. It contains five constitutive scalar functions (four of which are independent).

H: the plastic hardening modulus,

H_{iso}: the isotropic hardening modulus,

C_1: the back stress hardening modulus,

C_2: the back stress recovery modulus,

η: the plastic spin factor.

Various models in the literature can be fit into the above framework.

- Classical Isotropic Hardening

$$H = \frac{2}{3} H_{iso}$$

$$H_{iso} = \hat{H}_{iso}(\tilde{\epsilon}^p)$$

$$C_1 = C_2 = \eta = 0$$

- Prager Kinematic Hardening

$$H = C_1$$

$$H_{iso} = 0$$

$$C_1 = \hat{C}_1(\tilde{\epsilon}^p)$$

$$C_2 = 0$$

$$\eta = 0$$

- Krieg Combined Hardening

$$H = \hat{H}(\tilde{\epsilon}^p)$$

$$H_{iso} = \frac{3}{2} \beta H$$

$$C_1 = (1 - \beta) H$$

$$C_2 = \eta = 0$$

- Loret Model

$$H = \hat{H}(\tilde{\epsilon}^p)$$

$$H_{iso} = \hat{H}_{iso}(\tilde{\epsilon}^p)$$

$$C_1 = \hat{C}_1(\tilde{\epsilon}^p)$$

$$C_2 = \hat{C}_2(\tilde{\epsilon}^p)$$

η = constant

- Dafalias Model

  $H = C_1$

  $H_{iso} = 0$

  C_1 = constant

  $C_2 = 0$

  η = constant

- Chaboche Model

  $H = \frac{2}{3}\hat{H}_{iso} + C_1 - C_2\mathbf{B}\cdot\mathbf{n}$

  $H_{iso} = \hat{H}_{iso}(s)$

  C_1 = constant

  $C_2 = \hat{C}_2(\tilde{\epsilon}^p)$

  $\eta = 0$

- Mroz [1983] Model

  $H = \frac{2}{3}H_{iso} + C_1 - C_2\mathbf{B}\cdot\mathbf{n}$

  $H_{iso} = \hat{H}_{iso}(B_a, B_{max})$

  $C_1 = \hat{C}_1(\tilde{B})$

  $C_2 = \hat{C}_2(\tilde{B})$

  $\eta = 0$

  with $\tilde{B}, B_a$, and B_{max} defined below.

This summary presents the simplified forms that various authors have used to apply their models (often just for illustration). Here we need to consider the actual material behavior and describe how proper dependence of these material functions can model that behavior.

In continuing the state variable approach to modeling, we require that the scalar material functions must be functions of the scalar list derivable from the state variables $\mathbf{T}, \mathbf{B}$ and s. Notice from above that many models require the various moduli to depend upon the accumulated plastic strain. Since $\tilde{\epsilon}^p$ is not a state variable, we do not use it.

A general scalar list of invariants for constructing tensor representation functions is given by Wang [1970] and applied to anisotropic hardening by Loret [1983]. The reduced list we want to consider here is drawn from that work with one addition.

$$\ell = \{\tilde{\sigma}, \tilde{B}, s, B_{max}\},$$

where

$\tilde{\sigma}$ is the effective equivalent stress $\tilde{\sigma} = \{\frac{3}{2}(\mathbf{T}' - \mathbf{B}) \cdot (\mathbf{T}' - \mathbf{B})\}^{\frac{1}{2}}$,

$\tilde{B}$ is the effective back stress, $\tilde{B} = \{\frac{3}{2}\mathbf{B} \cdot \mathbf{B}\}^{\frac{1}{2}}$,

s is the isotropic variable,

B_{max} is the maximum value that $\tilde{B}$ has achieved over the history of deformation and is given by $B_{max} = sup[\tilde{B}]$.

The introduction of the variable B_{max} is motivated by the observation that during stress reversal the hardening transient is limited to the time that it takes for the back stress to reverse and achieve the same magnitude that it had prior to

unloading [Wilson and Bate, 1986]. The material *remembers* its previous extreme state. This variable was first used by Mroz [1983]. He also allowed the possibility for a material to cyclically soften by postulating an asymptotically limiting value of the isotropic variable s. This limiting value was a function of B_{max} as well as a certain accumulated back stress measure B_a.

This scalar variable list can be reduced for rate-independent plasticity. In this case, whenever we are in a plastic loading situation contact with the yield surface is required ($\tilde{\sigma} = s$). We reduce the list to

$$\ell = \{s, \tilde{B}, B_{max}\}.$$

Note that for viscoplasticity this reduction is not required or, in general, possible.

5.4 Functional Dependence

We can now synthesize the experimental observations from the literature that were discussed in detail in Chapters 2 and 4 with the model framework established this far in this chapter.

5.4.1 Back Stress Evolution

The back stress should increase monotonically under uniaxial, monotonic loading until it reaches its saturation value. This can be achieved by having C_1 and C_2 be constants. The problem with that is the reversing behavior is generally not matched well. In this model C_2 sets the time constant for transition as the back stress increases monotonically as well as the rate of transition during reverse flow. Generally, the reverse transient occurs much more quickly than the initial build up. Chaboche and Rousselier [1983] added several back stress variables having different

C_2's to account for this (see Section 2.2.3). Mroz [1983] proposed using a different C_1 for reverse loading than had been used for the monotonic build up.

The approach taken here is to take advantage of the fact that the variable B_{max} can be thought of as defining a surface in back stress space. This is similar in form to the yield surface in stress space. The surface can be defined by

$$f_B = \{\frac{2}{3}\mathbf{B}\cdot\mathbf{B}\}^{\frac{1}{2}} - B_{max} = 0.$$

Similar to isotropic hardening plasticity, the surface just expands without translation or distortion. B_{max} is not a state variable for which there is a separate evolution equation postulated. It merely tracks the maximum of $\tilde{B}$ obtained during deformation. By introducing this surface we have an easy way of delimiting when the material is experiencing a reversing event ($\mathbf{B}$ inside of f_B) and when the reversing transient is over ($\mathbf{B}$ returns to f_B). Use of a surface provides for multiaxial application. This concept is illustrated in Figure 5.1 .

The moduli during the reversing event should depend upon the position of $\mathbf{B}$ within f_B. In some ways this can be reminiscent of the two surface plasticity models where the moduli depend upon the relative positions of the two surfaces. In those models elaborate updating procedures are required for determining the current and initial distance measurements upon which the moduli depend. Here a simple measure is used. It is the fractional distance that the back stress has moved across the maximal back stress surface. In Figure 5.1 this fraction is illustrated as g ($g = \frac{a}{a+b}, 0 \leq g \leq 1$). At the beginning of reverse flow $g = 0$ and as the reversing transient ends $\mathbf{B}$ goes to the surface f_B and g goes to 1.

A reverse loading event begins when $\sigma_b = B_{max}$ and $\mathbf{B}\cdot\mathbf{D}^p < 0$. It continues while $\sigma_b < B_{max}$ and concludes when $\sigma_b = B_{max}$.

Not all loading paths will be direct, straight line traverses of the maximal back stress surface. For that reason g is defined as an instantaneous measure where the assumed direction of traverse is given by $\mathbf{D}^p$. In the general case, g is determined by taking the current back stress point and passing a line through it which is collinear with $\mathbf{D}^p$. The fraction g is found from intersecting this line with f_B. Then g is given by the fraction of the distance that $\mathbf{B}$ is on this line going in the direction of $\mathbf{D}^p$. This definition satisfactorily describes how to handle changes in loading direction during reverse loading.

In general g can be given by $g = \frac{a}{a+b}$, where a is found by solving the quadratic,

$$a^2 - 2\,a\,\mathbf{B}\cdot\mathbf{n} - (\frac{3}{2}{B_{max}}^2 - \mathbf{B}\cdot\mathbf{B}) = 0.$$

Here $\mathbf{n} = \frac{\mathbf{D}^p}{|\mathbf{D}^p|}$. The value of b is given by

$$b = a - 2\,\mathbf{B}\cdot\mathbf{n}.$$

The value for g can change instantaneously with an instantaneous change in straining direction. That implies that the moduli can instantaneously change too. It is only the back stress $\mathbf{B}$ itself that must be continuous.

It is expected that the isotropic hardening will have some influence upon the back stress evolution. If we consider the hardening to come from a dislocation field, some of the dislocations will be polarized due to the previous plastic flow. They may be pinned by a concentration of particles or immobile dislocations. When the flow is reversed some of these dislocations will glide in the reverse direction until they again reach a sufficient obstacle field. During the reverse flow, interaction with the *uniform* dispersion of dislocations should be expected. There needs to be allowance in a model for the back stress evolution moduli to be influenced by the

nondirectional level of hardening of s. As s increases, the resistance to back stress reversing should also increase.

The dependence on $\tilde{B}$ is absorbed by the introduction of the variable g through the maximal back stress surface f_B. Further, the assumption is made that C_2 is a constant.

$$C_1 = \hat{C}_1(s, g, B_{max}),$$

$$C_2 = \text{constant}.$$

To be consistent with the results from the literature we observe that $\hat{C}_1$ should decrease as g increases. $\hat{C}_1$ should be large for $g = 0$ and then gradually decrease as g increases during crossing the maximal back stress surface. A smooth elastic-plastic transition during reversing can be accomodated by allowing $\hat{C}_1$ to be infinite at $g = 0$.

5.4.2 Isotropic Hardening

The classical notions of isotropic hardening need to be reevaluated in light of the observations from Chapter 2 that the isotropic variable can *decrease* during reverse flow. As shown by Wilson and Bate [1986] , the isotropic variable shows a rapid decrease during the initial reverse plastic flow. The rate of isotropic hardening returns to its original value after a reverse strain roughly corresponding to that required for the back stress to fully reverse. The isotropic variable is softened by this reversing transient. Clearly classical isotropic hardening can not predict this behavior. It has H_{iso} as a constant or decreasing (but positive) function of plastic strain. Thus it predicts that s monotonically increases with plastic strain regardless of the loading history.

The way to model the observed behavior is to let H_{iso} incorporate both hardening and softening. This can be done by writing

$$H_{iso} = h_1 - h_2,$$

where h_1 is the hardening function and h_2 is the softening function. What is intended here is not softening due to thermally assisted static recovery such as found in viscoplastic models but rather dynamic recovery during reverse flow. The reverse flow erases some of the previous hardening. This can be envisioned from a mechanism such as dislocation annhilation.

This softening is a new concept but it follows very logically from the experimental results of Wilson and Bate [1986], Hasegawa et al. [1975], Marukawa and Sanpei [1971], and Feltner [1963]. Lowe and Miller [1983,1984] also made the observation that during a large strain ($\pm 15\%$ strain) hysteresis loop the isotropic component softens slightly. They introduce a new scalar and a new tensor internal variable to model this softening.

By separating H_{iso} additively we present a competition between two mechanisms, one for hardening and one for softening. Some of the implications of this will be discussed later.

The softening function is only operative during a reversing event. It is zero for monotonic loading histories. Thus h_1 can be determined from simple tensile or compressive experiments. Here we let h_1 be a function only of s, the isotropic variable.

$$h_1 = \hat{h_1}(s).$$

This is sensible if we envision the isotropic resistance arising mainly from dislocation interaction. The creation and tangling (or forest hardening) of dislocations provides

the main nondirectional increase in resistance to flow. The function $\hat{h_1}$ should decrease as s increases to give the normal stress-strain law behavior.

The softening function is operative during reverse flow. The softening modulus should depend upon the reversing event. This can be accomodated in the general multiaxial situation using the back stress positional variable g. This variable was introduced to be a monotonic measure of the reversing event. The complicated model of Lowe and Miller [1984] is only applied in one dimension and it does not restrict the softening to only operative during the reversing of the back stress.

The amount of softening should also depend upon s and B_{max}. More softening can occur if more dislocations have been introduced. The softening may depend upon B_{max} since there should be some coupling between the back stress reversal and isotropic softening if both involve dislocation rearrangement.

$$h_2 = \hat{h_2}(s, g, B_{max}).$$

The variable dependence of the evolution equations can be summarized by:

$$\mathbf{B}^{\nabla e} = \hat{C_1}(s, g, B_{max})\mathbf{D}^p - C_2\dot{\bar{\epsilon}}^p\mathbf{B}, \tag{5.9}$$

$$\dot{s} = \hat{h_1}(s)\dot{\bar{\epsilon}}^p - \hat{h_2}(s, g, B_{max})\dot{\bar{\epsilon}}^p. \tag{5.10}$$

These evolution equations contain three scalar material functions: $\hat{C_1}, \hat{h_1}, \hat{h_2}$, and one constant C_2. The plastic spin is also implicitly included in $\mathbf{B}^{\nabla e}$. Although for general loading there is a coupling between these functions, each can be related to a specific phenomenon of a simple experiment. The experimental program described in Chapter 6 is designed to isolate and measure these functions.

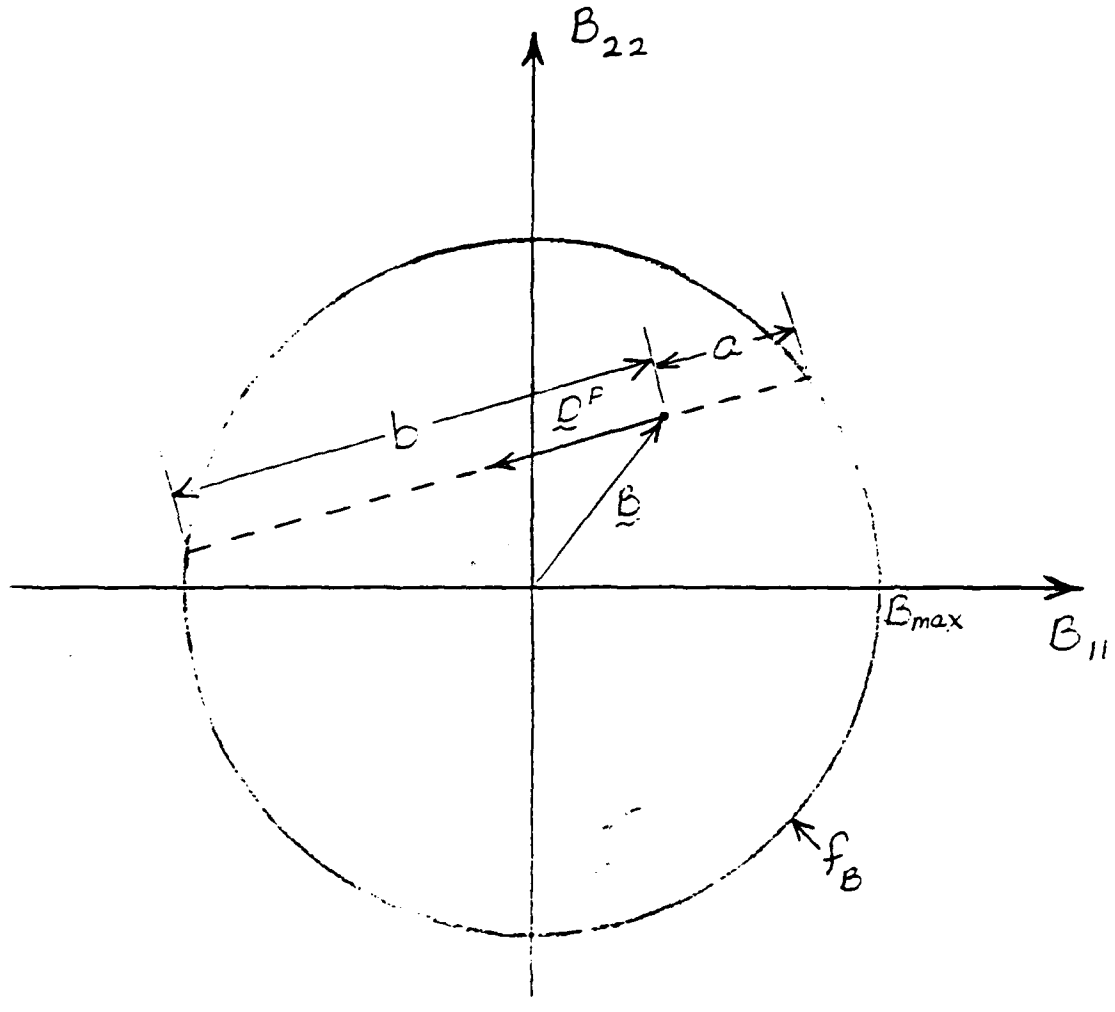

Figure 5.1 Maximal back stress surface f_B. Illustration of the definition of g. $g = \frac{a}{a+b}$.

Chapter 6

Experimental Program

6.1 Types of Experiments

In order to evaluate the multiaxial response of any material a variety of experiments is needed. This is to assure that the results are not testing mode dependent. For example, the uniaxial behavior of certain high strength steels depends upon whether the testing is done in tension or compression (strength differential effect). If a model is intended to apply to both of those loading environments then adequate data must be available about both modes to allow construction of the model.

In this current program the following tests were conducted: tensile testing, large strain compression testing, reverse strain testing, cyclic testing, and large strain torsion testing. These tests were chosen to display as much of the phenomena of rate-independent plasticity as possible. We can associate the observed phenomena with approximate strain regimes. Evaluation of yield point and initial hardening modulus are restricted to the first percent or two of strain and can be evaluated from the uniaxial tensile test. The generation of back stress and development of permanent softening upon strain reversal are associated with the first 10 to 15 percent strain. This regime can be studied by reverse strain and cyclic testing.

The decrease of the hardening modulus with plastic strain is evaluated from the large strain compression test. Finally, more complex interactions of finite strains and rotations causing nonproportional loading can be investigated using the torsion test. Each of these testing types will be discussed in more detail below.

6.2 Materials Tested

Two metals were chosen for evaluation: 1100-O aluminum and 316 stainless steel. Complete data, generated from the types of tests outlined above, are not available in the literature for any material. These two were chosen since they would be expected to span a variety of behaviors in other metals.

The 1100-O aluminum is a relatively simple, high stacking fault, face centered cubic metal which is known to harden primarily by cell formation. It is not expected to generate a large back stress since it has many slip systems to distribute the deformation. The material was received from ALCOA in $1\frac{1}{2}$ inch diameter rods in the "F" condition. It was then annealed at $500°C$ for 1 hour and allowed to air cool. The 1100 aluminum that was tested came from two separate batchs although both were annealed. The compression and torsion specimens came from one batch (batch A). The reverse loading specimens came from another batch (batch B). The final grain structure is shown in Figure 6.1. The grains were equiaxed with an approximate diameter of 70 microns.

The AISI 316 stainless steel belongs to the class of austenitic stainless steels so it also has an FCC crystal structure but with a relatively low stacking fault energy ($78\frac{MJ}{m^2}$) (Peckner and Bernstein [1977]). The low stacking fault energy inhibits cross slip and can be expected to generate a larger back stress. The material was received

in $1\frac{3}{4}$ inch diameter rods. It was annealed in air at $1075°C$ for 1 hour then air cooled. The final grain structure is shown in Figure 6.2.

6.3 Experimental Apparatus

All of the experiments were conducted at ambient conditions. The equivalent strain rate was nominally $\dot{\bar{\epsilon}} = 1 \times 10^{-3}\text{sec}^{-1}$ for all of the tests. These materials are reasonably rate insensitive at room temperature and slow strain rate.

The experiments were conducted primarily using two servohydraulic test machines manufactured by Instron Corp. The uniaxial tests (tension, compression, reverse straining, cyclic) were run on a 1331 testing machine controlled by an 8000 series computer based controller. The machine capacity was 100 KN (22,500 lbf). Two load cells were used depending upon the experiment. A 10 KN cell was used for the tensile and reversed loading tests of the 1100-O aluminum and a 100 KN cell for all of the other tests.

The torsion experiments were conducted on an Instron 1323 biaxial test machine located at the U.S. Army Materials Technology Laboratory in Watertown, Mass. This machine has a capacity (and load cell) of 50,000 lbf thrust and 25,000 in-lbf torque. The machine was controlled using its analog function generator.

The data collection for both machines was via IBM personal computer based systems using Metrabyte conversion boards. The collection for the torsion machine used Keithley software while the system for the uniaxial machine used the Unkelscope program developed by Prof. W. Unkel at M.I.T. Approximately 500-1000 data points were collected for the uniaxial tests and 1000-2000 data points for the torsion tests. All data were transferred to a Data General MV 10,000 supermini-

computer for reduction and comparison with theory.

6.4 Compression Testing

The use of compression tests to obtain large strain flow stress results has been well documented [ASTM Standard E209-65; Chait and Papirno, 1983]. This testing mode offers resistance to the necking geometric instability of the tension test although it has special considerations of its own.

A circular cylindrical specimen is compressed between parallel flat platens. Proper lubrication between platen and specimen is necessary to prevent barrelling of the specimen. Homogeneous deformation can be achieved by proper selection of the lubricant and the specimen geometry. In this study sheets of 0.003 inch thick teflon were used to provide lubrication between polished steel platens and the specimen. The specimen was simply a right, solid circular cylinder having smooth ends. With certain lubricants, some investigators have grooved the ends of their specimens to capture the lubricant [Brown 1987]. Grooving was used here during some preliminary testing when Molydisulfide was being considered as the lubricant but better results were obtained with smooth-end specimens and two layers of the teflon sheets as the lubricant.

The aluminum compression tests were all conducted at a true strain rate of $\dot{\epsilon} = 1 \times 10^{-3} \text{sec}^{-1}$. This was achieved using an analog function generator designed by M. Haghi [Haghi, 1987]. The actuator was controlled to move with an exponentially decaying velocity to keep the logarithmic strain rate constant ($\frac{\dot{l}}{l}$). The 316 stainless steel compression tests were conducted both controlling the logarithmic strain rate and controlling engineering strain rate ($\frac{\dot{l}}{l_o}$). No differences were observed in the

material response to the two controlling methods.

Another experimental difficulty with the compression test is the tendency for the specimen to shear. When the gauge length is too long or the platens are not in good alignment the specimen will not deform uniformly but will shear. This mode is reminescent of simple shear between the platens with evidence of some rollover at diagonally opposite corners of the specimen. This unfavorable condition was avoided by using specimens with an aspect ratio (original length divided by original diameter) of 1.5 or less. For the tests run here the specimen dimensions were:

Table 6.1 Compression Specimen Dimensions

Material	Diameter (mm)	Length (mm)
1100-O aluminum	11.3	17.6
316 stainless steel	6.4	9.0

The loads were directly measured from the load cell. The strains were determined from the displacement of the actuator with proper account taken for system compliance. For the 1100 aluminum results the actuator displacement was taken from the LVDT output of the actuator position. A nonlinear load train compliance was measured by loading up the system without having a specimen in place. The strains determined from this procedure matched well with results where a specimen was strain gauged and tested. The strain gauge popped off after a small amount of strain (5%) but provided an independent check that the strain measurements from the actuator position were reasonable.

For the 316 stainless steel tests, instead of using the actuator LVDT output a 20% extensometer was placed across portions of the platens. This gave a stiffer system for displacement measurement. Some platen compliance still had to be subtracted off but it could be considered to have constant stiffness at the load levels

of the test.

The compression tests were successfully run to large strain with the above precautions. A strain of almost 95% was reached for the aluminum and 65% for the stainless steel.

6.5 Reverse Straining Testing

In order to model the Bauschinger effect and general cyclic behavior of the materials a certain number of reverse loading tests is required. These tests have typically been done either by twisting a cylindrical specimen in one direction then reversing the direction of twist or by loading in tension followed by compression. In this study, tension/compression loading was used.

The proper measurement of reverse loading phenomena requires care in system alignment. When a specimen is taken from tension to compression or vice-versa, system backlash and misalignment can cause spurious results.

The testing system used was one designed for reverse loading and low cycle fatigue. An Instron 1331 servohydraulic test machine was mounted with a Wood's metal grip for system alignment. The specimen was a threaded, cylindrical sample having a short gauge length, see Figure 6.3. The reduced gauge section was necessary to prevent plastic buckling during compression. The specimen was threaded into the top grip which was attached to the load cell. The specimen was firmly locked in place using a differential nut assembly which preloaded the specimen threads. With the specimen secure in the top assembly the alignment with the actuator axis was checked using a dial gauge. The bottom of the specimen was threaded into the Wood's metal grip assembly which was locked onto the actuator.

The grip allows for good alignment because it has two parts. One firmly attaches to the actuator. The other attaches to the specimen, preloading the threads using a differential nut. When installing the specimen the two components are free to rotate and move relative to each other. Once the specimen is threaded into the grip a low melting point liquid metal is allowed to cool and solidify locking the components together without introducing bending moments to the load train. Thus the specimen is securely fixed between the load cell and actuator, without bending moments, and in line with the actuator axis.

The specimens deformed maintaining good alignment overall. Some of the 1100 aluminum specimens showed a shear across the gauge section at later parts of the compressive loading. The data for this continued deformation after alignment was lost has not been used.

The deformation was measured by attaching a 20% axial extensometer across the gauge section. The loads were measured directly from the load cell and the results converted to true stress and true strain based upon the extensometer output.

The reverse loading tests were limited in strain range to +20% and -5% so separate tensile tests were run to expand this strain range. The tensile tests were run with the same setup as was used for reverse loading. The only difference was that the specimens were modified to have longer gauge lengths. The gauge length for the stainless steel specimen was 29.2 mm (1.15 in) and for the aluminum specimen was 38 mm (1.5 in).

6.6 Finite Element Analysis of Reverse Straining Specimen

The choice of specimen design for the reverse straining tests was based upon experience in the literature with specimens that could be used both for tensile and compressive loading. In the course of analyzing the reverse straining results it was noticed that the uniaxial loading flow stress level was higher for each of the reverse tests than for the tension test having a longer gauge section. In order to investigate the uniformity of stress and strain in the reverse loading specimen a finite element analysis was conducted of the stainless steel specimen. The specimen dimensions are shown in Figure 6.3.

Only one quadrant of the axisymmetric specimen was examined due to symmetry. The region was divided up into 260 elements (4 node, bilinear, quadrilaterals), Figure 6.4. The bottom row of nodes was fixed. The centerline row of nodes (on the left in Figure 6.4) was restrained against radial displacement and the nodes at the top were displaced vertically to simulate loading. The model had 594 degrees of freedom. The material was treated as elastic-plastic with a Young's Modulus of 30 x 10^6 psi, Poisson's ratio $\nu = 0.3$, yield stress of 41,000 psi and a constant plastic hardening modulus of 2.63 x 10^5 psi. The classical, isotropic hardening plasticity relations were used. The analysis was conducted with the ABAQUS finite element code using the nonlinear geometry option [ABAQUS, 1984].

One intent of the analysis was to compare the stress and strain distribution inside the specimen gauge region with the homogeneous states assumed in reducing the test data. In Figure 6.5 is plotted contours of constant vertical normal stress. This is the stress that is assumed to be constant over the gauge section in the simple

1-D analysis. Notice the stress gradient along the specimen length in the shoulder region. There is an area of elevated stress along the specimen axis approximately one radius below the shoulder/gauge section transition. Across the very center of the gauge section (the bottom of Figure 6.5) the vertical stress is fairly uniform here being approximately 60 ksi for this moderate deformation.

The simple experimental analysis would take the total force on the specimen and divide it by the average cross sectional area of the gauge section to give the applied stress. Here we can see that the true stress is not constant throughout the gauge region by varies due to the presence of other stress components. Along the specimen central cross section the vertical stress is quite uniform so on this plane the simple analysis would be a reasonable estimation of the vertical normal stress.

In Figure 6.6 the contours of constant accumulated plastic strain are shown. Notice the continued gradient along the specimen length throughout the gauge section. Experimentally an axial extensometer was used to determine the average strain across the entire gauge section. The nominal gauge length of the extensometer was 0.5 inch. For the realistic deformation level shown here that means averaging over strains that vary from about 3% to 9%. That gives a rough estimate of the strain level. A better experimental technique would be to use a diametral extensometer mounted at the center of the gauge section. Across this plane the strain varies from 7% to less than 10%, a much tighter range than over the entire gauge region although this is still less uniform than would be hoped. This is an important experimental improvement. *A diametral extensometer provides more accurate behavior for these short gauge length specimens.*

In order to compare the real material behavior with that which would be exper-

imentally determined from this specimen the finite element results were used. The displacement of the node corresponding to the extensometer measured displacement and the reaction forces corresponding to the load cell output were used as though they were experimental data and the stress-strain behavior was computed.

Figure 6.7 shows the curve of equivalent stress versus equivalent strain. The base curve is the elastic-plastic behavior input into the finite element model. This is the material law seen at each point in the specimen. The curves marked *Extensional* and *Diametral* show the average specimen behavior that would have been determined experimentally using either an extensional or diametral extensometer, respectively. The extensional curve lies well above the true material behavior and even the diametral results are high. This is mainly due to the way the strain measurement was necessarily averaged over the nonuniform gauge region using an extensometer.

In this experimental program the results that were observed are consistent with this analysis. The flow curve for all of the tests run with this specimen design having a short gauge length were higher than the results for a tensile test with a longer, more uniform, gauge length. To compensate for this elevation in *apparent* flow stress the reverse loading stresses were reduced to agree with the tensile data. The procedure used was as follows:

1. The forward flow stress σ^f at the point of reversing the straining direction, ϵ^f, was determined.

2. The flow stress from the tensile test was evaluated at the same strain level σ^{ten}.

3. The stress multiplier was defined by $SMULT = \frac{\sigma^{ten}}{\sigma^f}$.

4. The stresses for the entire data set from that reverse loading experiment were multiplied by $SMULT$.

This brings all of the reverse loading curves to a common basis. This procedure not only accounts for the stress nonuniformity in an approximate way but it also removes any systematic experimental error from the flow stress measurements. Types of error that this would correct include: load cell calibration variability, specimen geometry variability, and material differences between specimens.

From the results in Figure 6.7 we can see that a better way to use this type of specimen design would be with a diametral extensometer. The stress and strain are more nearly uniform across the central cross section than they are throughout the whole gauge section. Future testing should be conducted this way.

6.7 Torsion Testing

The torsion test holds a number of advantages for determining material behavior at large strain. These advantages are discussed elsewhere but some of the main points are again summarized here:

1. No large changes in the geometry of the specimen.
2. Multiaxial stress states are obtainable with both normal and shear stresses.
3. Constant strain rates can be achieved with simple ramp type control signals.
4. A deformation field having equal stretching and spin components is achieved.
5. There is noncoaxiality between the stress deviator and the back stress.

Torsion of cylindrical testpieces has been commonplace for a long time. Generally tests conducted on solid rods have been used. These produce nonuniform stress and strain fields which vary in the specimen with radial position. The required torque to produce a certain twist angle is generally the output of this type of test. Various techniques have been used to convert the torque/twist behavior to stress-strain curves ([Dieter 1976, p. 381], [Canova, Shrivastava, Jonas and G'Sell, 1982], [Shrivastava, Jonas and Canova, 1982]). These assume certain constitutive restrictions and neglect the production of axial normal stresses and their interaction with the shear deformation fields. At best, the results from solid rod testing represents an averaged flow stress magnitude.

To circumvent these limitations Lindholm et al. [Lindholm, Nagy, Johnson and Hoegfeldt, 1980] used a cylindrical specimen having a thin walled, tubular gauge section. This allows a nearly uniform stress and strain distribution in the gauge section. As long as the wall thickness is much less than the specimen's radius the gauge region can be treated as a plane stress sheet. This design has been extensively used for small strain, multiaxial testing but suffers plastic buckling when compressed or twisted to large strain. Lindholm et al. reduced the gauge length of their specimen and were able to obtain results up to shear strains of 700%. Since that time this specimen design has received much attention but without extensive experimental usage.

The feature of this specimen that is most striking is that it has a massive shoulder very close to the gauge region. This restricts the axial deformation that the specimen can be used for since an axial strain would also produce a hoop strain which would be resisted at the shoulder. This would produce a large strain gradient since the

shoulder has such a small transition region close to the gauge section. This specimen is best suited for a pure torsion test where the crosshead is fixed so that the axial strain is zero and the deformation is nearly simple shear. This produces a simple deformation field.

$$\mathbf{F} = \begin{bmatrix} 1 & \gamma & 0 \\ 0 & 1 & 0 \\ 0 & 0 & 1 \end{bmatrix},$$

where γ is the (engineering) shear strain in the gauge section.

$$\gamma = \frac{\bar{r}}{l}\Delta\Phi,$$

where $\bar{r}$ is the mean radius of the gauge section, l is the gauge length, and $\Delta\Phi$ is the angle that the crosshead has twisted through. Note that is is important to fix the crosshead against axial motion to ensure that the gauge section maintains uniform deformation. Lipkin et al. [Lipkin, Chiesa and Bammann, 1987] have conducted a finite element analysis of a Lindholm type specimen. For their constitutive model of 304L stainless steel and particular specimen geometry they found that the shear stress and shear strain were quite uniform through the wall thickness although deformation was not constrained to just the gauge section but did extend somewhat into the shoulder transition region at shear strains above $\gamma = 2.0$. Also they found that the gauge length did change somewhat even when they fixed the shoulders against axial motion away from the gauge section.

The torsion tests conducted in this study also utilized Lindholm type specimens. Figure 6.8 shows the geometries used for both the 1100 aluminum and the 316 stainless steel tests. The specimen dimensions are given in Table 6.2.

Table 6.2 Torsion Specimen Dimensions

Material	Gauge Length (mm)	Inside Diameter (mm)	Outside Diameter (mm)	Shoulder Diameter (mm)
1100 Alum	7.9	27.76	30.30	38.0
316 SS	5.9	19.05	20.52	38.1

For the aluminum specimen a larger diameter and thicker wall was allowed for the same total applied torque for both materials. For the stainless steel the ratio of outside diameter to wall thickness is $\frac{OD}{t} = 28$. The thin wall approximation is appropriate for this ratio. The aluminum specimen had $\frac{OD}{t} = 24$. This also is quite good. Values for this ratio common in the literature are around 16 [Lipkin, Chiesa and Bammann, 1987].

The specimens were gripped in an hydraulic collet pair of grips mounted on the Instron 1323 biaxial test machine. Into the ends of each specimen were inserted mild steel plugs that were match machined for tight fit. These plugs were inserted into the specimen ends and extended approximately $\frac{1}{3}$ to $\frac{1}{2}$ of the way down the shoulder region. Their purpose was to provide an extra support when the hydraulic collets closed on the outside of the shoulder regions. The desire was to have the clamping forces of the grips supported as much as possible by radial stress transmitted to the plug and as little as possible by hoop stresses in the specimen which could more easily influence the gauge region.

These grips were aligned in the loading frame when installed by dial gauges and strain gauged solid rod specimens. The grips are very massive as seen in Figure 6.9 and were never used to their rated capacity. No slipping or backlash was observed at any time with this set-up.

It is extremely important to have a gripping system which can hold good alignment throughout the test. For the large angles that the actuator is twisted through any eccentricity of the specimen is greatly amplified. Also it is important to be able

to transmit both torque and axial force with no slippage or cross talk. Early in our testing program we tried a gripping arrangement where the specimens were held by cross pins. This was abandoned because the position where the pin and holes contacted would change during loading as the ratio of torque to axial force changed. This changed the axial position of specimen end and introduced an applied axial normal strain.

The hydraulic collet grips did not suffer from the above problems and served well as our method of gripping.

The torsion tests were conducted as follows:

1. The axial position of the actuator was held constant. The axial control channel of the feedback system was set to maintain a constant axial position of the actuator as measured by its LVDT.

2. The rotary motion of the actuator was controlled to maintain a constant rate of twist. That twist rate was selected to give an equivalent strain rate in the gauge section of $\dot{\bar{\epsilon}} = \sqrt{3}\ \dot{\gamma} = 10^{-3}\text{sec}^{-1}$. The standard analog function generator was used, and it satisfactorily controlled this motion.

3. The rotary position, axial force and torque were digitally recorded.

In reducing the data, this test was assumed to simulate simple shear. The system was stiff and had massive grips and shoulders so all of the deformation was assumed to occur in the gauge region. The strain and stresses were then given by:

$$\gamma = \frac{r_m}{l}\Delta\Phi,$$

$$T_{12} = \frac{M}{\pi(r_o^2 - r_i^2)r_m},$$

$$T_{22} = \frac{F}{\pi(r_o^2 - r_i^2)},$$

where l is the gauge length, $\Delta\Phi$ the twist angle of the actuator, r_i, r_o the inside and outside radii of the gauge section, r_m the mean radius ($r_m = \frac{1}{2}(r_i + r_o)$), M the measured torque, and F the measured axial force.

Lipkin et al. [Lipkin, Chisea and Bammann, 1987] have questioned this type of analysis for their specimen. They maintain that the proper strain state in the gauge section may not be properly represented when the plastic deformation extends into the transition region. For their tests this begins to be important at shear strains around 2.0 . In our work the largest shear strains to which we tested were around 1.6 . Post test observation of the specimens did not show any permanent strain in the transition region so these objections were set aside until after analysis of the test results.

6.8 Experimental Results

In this section the results of the experimental program outlined above are presented. These experiments were all completed at M.I.T. with the exception of the torsion tests, as described above. The results are presented in terms of Cauchy stress and true (logarithmic) strain.

Figure 6.10 shows the tensile test results for the type 316 stainless steel. The material shows a rather abrupt yield with nearly linear hardening. Here we see the substantial hardening rate persists even to the maximum strain of the test (38%). This alloy has good tensile elongation due to its large ductility and resistance to necking from its high hardening.

The 1100-O aluminum tensile results are displayed in Figure 6.11. Notice the

gradual yield and continually decreasing hardening modulus. The test was run to a strain of 17%. The curve shapes and strength levels for both materials are consistent with literature values.

The compression results are displayed in Figure 6.12 for the 316 s.s. and in Figure 6.13 for the 1100 aluminum. The stress and strain *magnitudes* are plotted. In compression both the stress and strain are negative in sign. That will be assumed to be understood.

The stainless steel compression results show the same shape as the tensile test. The hardening is almost linear in the range of 5% to 35% strain and decreases slightly thereafter. This test achieved a strain of 64%. The appearance of the specimen after the test is shown in Figure 6.14. Notice that the specimen was reduced in height but maintained its cylindrical shape. The end of the specimen showed a shiny rim around the outer edge. This was attributed to the polishing of that surface by the platen as the teflon sheets were pinched off. In order to evaluate whether lubrication was lost as the specimen expanded radially during compression, a test was run where the deformation was interrupted and new teflon sheets were inserted. The test was relubricated this way three times during the deformation. The comparison of the interrupted and continuous tests are shown in Figure 6.15. The results were very close. This indicates that lubrication was not significantly lost during deformation.

The aluminum compression results also show the same shape as the tensile test results. A gradual and continuous reduction of the hardening rate is seen with strain. The aluminum results present a more rounded curve than the stainless steel.

Aluminum is known to show a small amount of rate sensitivity at room temperature. To assess its importance, a compression test was conducted at $\dot{\epsilon} = 10^{-1}\text{sec}^{-1}$.

This is two orders of magnitude larger than the standard stain rate used throughout this test program of $\dot{\epsilon} = 10^{-3}\text{sec}^{-1}$. The comparison of the different strain rate results is shown in Figure 6.16. The strain rate hardening is measurable but not beyond what was expected. Using these two curves, the strain rate sensitivity, m, is 0.012 ($\sigma = C\dot{\epsilon}^m$). This value is small but it is in the expected range for aluminum [Hasford and Caddell, 1983]. Care was taken to conduct all of the other experiments at the same equivalent strain rate (10^{-3}sec^{-1}).

The results of the tension and compression tests are plotted together in Figure 6.17. Notice that the compression result lies above the tensile test result. The difference between the two curves is approximately a constant 60 Mpa. This is a significant difference. The curves have the same general hardening characteristics but at different flow stress levels.

At first glance this might appear to be the result of a strength differential effect where the flow stress depends upon the mean hydrostatic stress. This was investigated using one of the reverse loading specimens which can be loaded in both tension and compression. A specimen that was initially loaded in compression was compared with the ones that were initially loaded in tension. When comparing these results, there is little difference in material response, see Figure 6.18. This difference is comparable with the specimen to specimen variation seen in the tensile results. The yield and hardening behavior were independent of loading direction.

A more plausible explanation for this difference is that it is due to variations in heat treatment. All of the 316 s.s. was subjected to the same nominal annealing

schedule but not all of the material was treated simultaneously. Variations in the furnace, cooling rates, specimen volume, etc. could have contributed to the difference. Since the hardening behavior is the same but only the flow stress level differs we can perhaps view this as a difference in initial dislocation density. This would be primarily seen as a difference in yield stress. All of the tension/reverse loading specimens were annealed together. They give very consistent yield values and flow curves. The compression material was annealed separately and could, perhaps, have cooled much faster (they were all air cooled) than the 15 rods for the reversing specimens. The volume of compression material was much less.

One additional possible explanation should be considered and that is that there is a specimen geometry effect. The shape and gripping of the two specimens is vastly different. The tension specimen has a uniform gauge section which transitions to shoulders having threaded grips. The compression specimen is a squat, cylinder which is squeezed between platens. If there was a lubrication breakdown, then the compression results should be artificially high since friction would also need to be overcome. That trend would be in the direction consistent with our data. The problem with this explanation is that there was no evidence of improper lubrication.

The reverse loading tests were all conducted by first loading in tension followed by reversing into compression. The only exception was the stainless steel test prestrained to 5%. That test had compression followed by tension.

An example of the full stress-strain response for one of these reversing tests is shown in Figure 6.19. All of the features commonly seen in reverse testing are displayed: the linear unloading region, gradual reyield and return to the same hardening modulus seen prior to unloading. Presenting the data as shown in Figure

6.19 does not bring out one of the important features of reverse testing though. Often permanent softening is observed where the final flow stress after reversing is smaller in magnitude than the continued forward loading would be. In order to emphasize this, as well as compactly present the results from a number of tests, we adopt a standard way to present the reversing data. For the reversing portions of the curves only the compressive region is shown. It is displayed in the first quadrant by plotting the absolute value of stress against an accumulated strain measure where the elastic strain is added to the accumulated, effective plastic strain. This effectively rotates the compressive stress-strain data by 180° about the point during unloading, of zero stress. Displaying the data this way allows easy comparison of how the reverse yield has been lowered, the extent of rounding during reverse flow, and the permanent softening.

There was small specimen to specimen variation in the forward loading flow curves. this was compensated for by normalizing all of the reverse loading tests to the tensile test. The procedure for this is discussed in section 3.6.

The reverse loading data are presented in Figure 6.20 for stainless steel and Figure 6.21 for the 1100 aluminum. The data show the trends that would be expected. The permanent softening first increases and then is fairly constant with prestrain. This has been extensively noted in the literature (see Chapter 2). There also is no abrupt yield during reversing.

One cyclic test was conducted. That involved 5 cycles of $\pm 5\%$ strain controlled cycling. The resulting stress-strain response is shown in Figure 6.22. The material quickly hardens to a saturation stress amplitude of about 750 MPa.

The final testing mode was in fixed end torsion of thin-wall tubular specimens.

The specimens were twisted to large strain while the axial position of the grips was held fixed. The resulting torque and axial force were monitored and converted to shear and axial normal stresses using the thin-wall approximation as discussed in section 3.7. the torsion results for the type 316 stainless steel is shown in Figure 6.23. The suprising feature of this test is the magnitude of the axial stress. It is of the same order of magnitude as the shear stress. The shape of how it develops is in accord with expectations from the literature but the magnitude is larger than a second order effect. At a shear strain of $\gamma = 1.4$ the axial stress is about -190 MPa.

The aluminum results are shown in Figure 6.24. Here we see that, relative to the shear stress response, the axial stress is much smaller than with the stainless steel. This is more in accord with expectations.

The level of deformation achieved in these torsion tests is comparable to the strain reached in the compression tests. Figure 6.25 shows a torsion specimen after testing. The black line in the gauge section was initially parallel with the specimen axis but has rotated due to the shear deformation.

These experiments represent the first collection of data over this range of deformation for the same material. This gives a qualified data base to use in constructing constitutive models and also in verifying their predictions.

6.9 Comparison of Some Existing Theories with the Experiments

The application of current material models to the experiments of this study provides a manner for evaluation of their predictive capability. In this section three simple, kinematic type laws are applied to the experiments performed on the type 316 stainless steel: Prager-Ziegler kinematic hardening, Krieg combined isotropic-

kinematic hardening, and the Mroz [1967] model. The Prager-Ziegler theory and Krieg theory [Key, Biffle, and Krieg, 1977] can be written in the following form,

$$\mathbf{D}^p = \frac{1}{H}\frac{\mathbf{T}'^{\nabla} \cdot (\mathbf{T}' - \mathbf{B})}{\frac{2}{3}s^2}(\mathbf{T}' - \mathbf{B}),$$

$$\mathbf{B}^{\nabla} = (1-\beta)H\mathbf{D}^p,$$

$$\dot{s} = \beta\frac{3}{2}H\dot{\bar{\epsilon}}^p.$$

The back stress evolves with a Prager-type rule. The relative magnitudes of the isotropic and kinematic parts is given by the constant β. It is assumed to be constant throughout deformation. For Prager-Ziegler hardening $\beta = 1$. In the Krieg model the permanent softening is a function of the back stress. The value of β is chosen to match the permanent softening.

The material functions are H, the plastic hardening modulus, and β the isotropic hardening ratio. The material flow curve was fit using the following expression for H,

$$H = \frac{2}{3}\frac{d\bar{\sigma}}{d\bar{\epsilon}^p} = \frac{2}{3}h_0(1 - \frac{\bar{\sigma}}{\sigma^*})^q.$$

This gives H as a function of the equivalent stress $\bar{\sigma}$. The constants h_0, σ^*, q and the yield stress σ_y were fit for both the reverse loading specimens and the large strain compression experiments. For reverse loading: $\sigma_y = 262.$ MPa, $\sigma^* = 1300.$ MPa, $h_0 = 3757.2$ MPa, and $q = 1.304$. For compression: $\sigma_y = 340.$ MPa, $\sigma^* = 1400.$ MPa, $h_0 = 2797.1$ MPa, and $q = 0.7151$.

The predictions of the reverse loading stress response for Prager-Ziegler hardening is given in Figure 6.25 . Notice that the theory does not match either the permanent softening or the elastic-plastic transition region. The theory gives predictions of quite small reverse flow stress levels.

In the Krieg theory, the introduction of isotropic hardening allows better match of the reversing behavior. The isotropic ratio was chosen by predicting one of the reversing curves and adjusting β to match the permanent softening. A value of $\beta = 0.88$ gave satisfactory agreement as shown in Figure 6.26 . This partitioned the hardening to 88% isotropic and 12% kinematic. The application of this to the rest of the reverse curves is shown in Figure 6.27 . The permanent softening is well matched but the transition is ignored and the gradually changing slope is replaced with a sharp reverse yield.

The prediction from this model of the cyclic test is shown in Figure 6.28 . A very "box like" response is predicted which saturates at a stress of 1300 MPa($= \sigma^*$). This does not agree with experiment.

Finally, the prediction of the torsion test is also examined in Figure 6.29 . The agreement with experiment is still not close. The shear stress is overpredicted and the normal stress is underpredicted.

The Krieg model can be made to match the permanent softening of a single reverse by treating the back stress as a phenomenological fitting parameter. This provides a reasonably good estimate of the reverse flow stress after several percent reverse strain. This neglects the physics of the deformation as developed in the main body of this work. The transition region is not modeled and it predicts that all symmetric strain controlled cycling will saturate at the same stress level, σ^*.

The Mroz [1967] model is briefly described in Appendix B. It consists of nested yield surfaces each of which has a different plastic modulus associated with it. This model was applied to the type 316 s.s. experiments by segmenting the first 30% strain from the tension test into 10 linear segments. This 10 surface model was used

to predict the reverse loading experiments. Figure 6.30 shows these results.

The Mroz model does not match the experiments very well. The permanent softening is vastly overpredicted. The reverse predictions do not show the gradual elastic-plastic transition because tensile test stress-strain behavior shows nearly linear hardening. Since there is not much of a knee region during initial loading then there can not be much of one during reverse loading using the Mroz model.

Here we have seen that none of these theories does a satisfactory job describing the basic experiments. The next chapter applies the new modeling ideas developed in this work to these experiments.

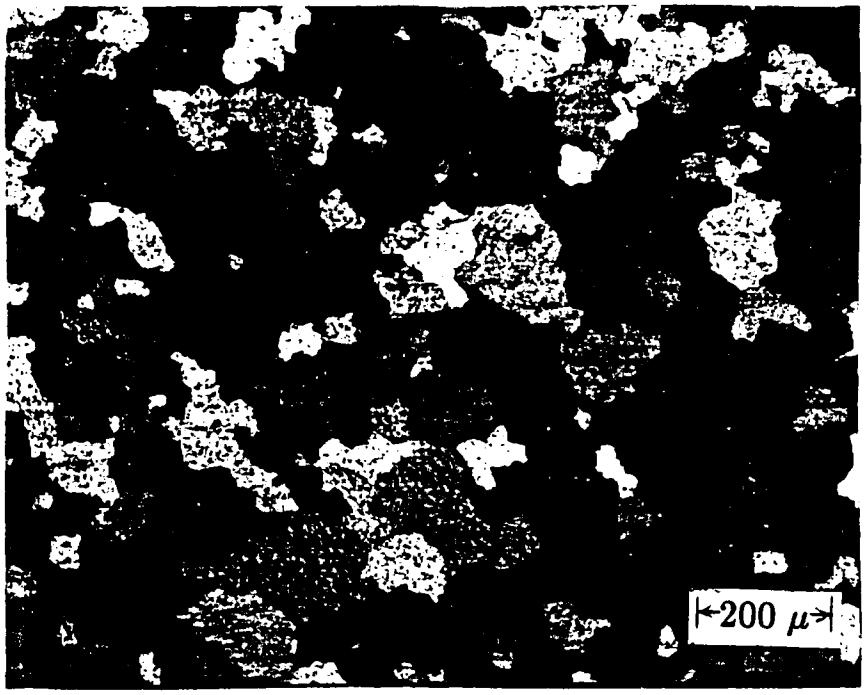

Figure 6.1 Micrograph of 1100-O aluminum after annealing showing grain structure.

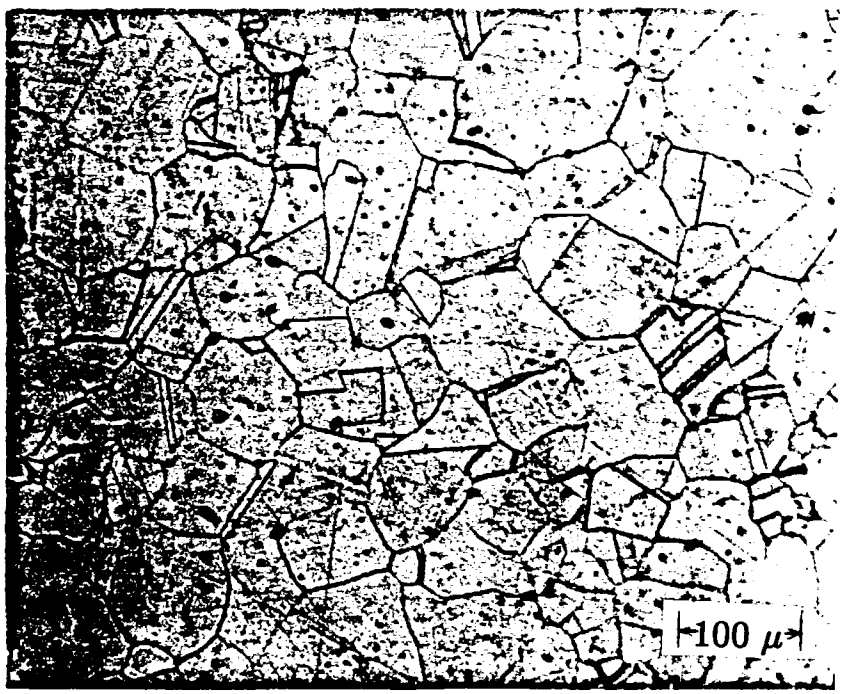

Figure 6.2 Micrograph of type 316 stainless steel after annealing showing grain structure.

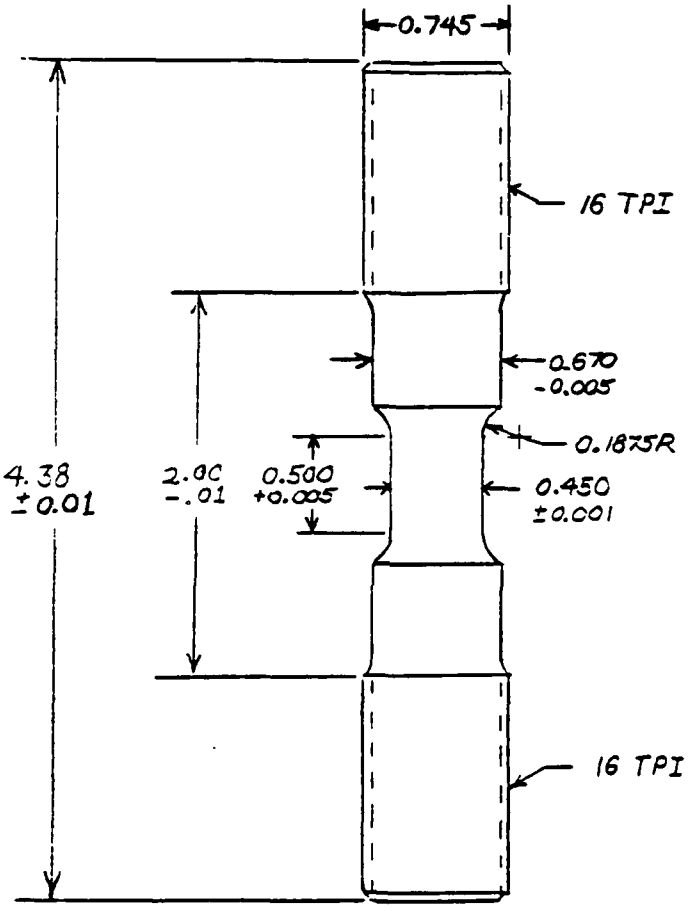

Figure 6.3 Reverse loading specimen design for 316 s.s. Dimensions in inches.

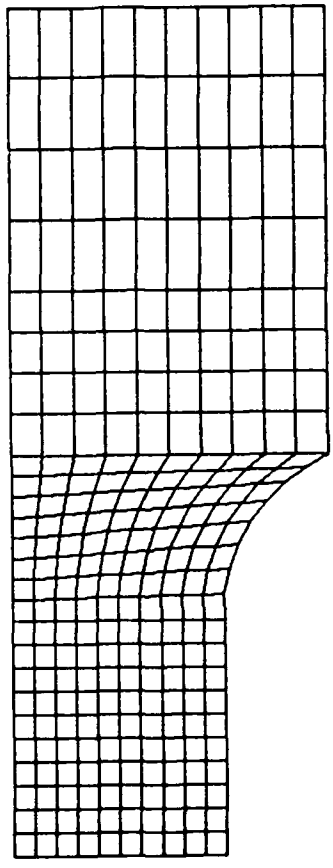

Figure 6.4 Finite element mesh used to model the reverse loading specimens. It contains 260 4-node elements.

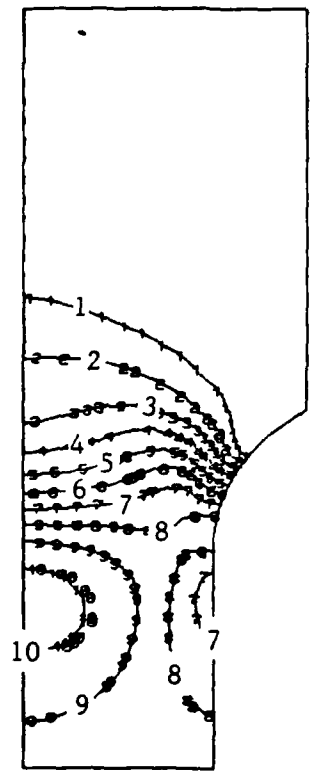

Contour	Stress (ksi)
1	30
2	34
3	38
4	42
5	46
6	50
7	54
8	58
9	62
10	66
11	70

Figure 6.5 Contours of vertical normal stress during loading of the reverse loading specimen.

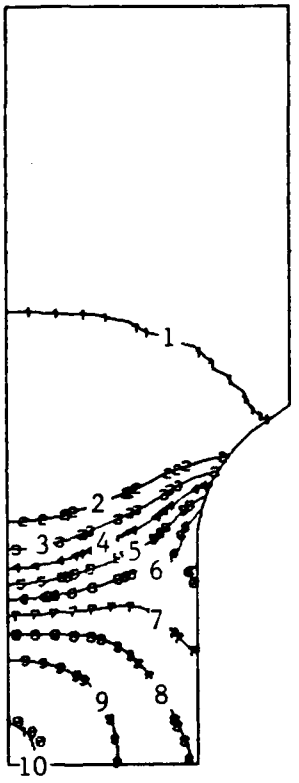

Contour	Plastic Strain
1	0
2	0.01
3	0.02
4	0.03
5	0.04
6	0.05
7	0.06
8	0.07
9	0.08
10	0.09
11	0.10

Figure 6.6 Contours of accumulated equivalent plastic strain during the vertical loading of the reverse loading specimen.

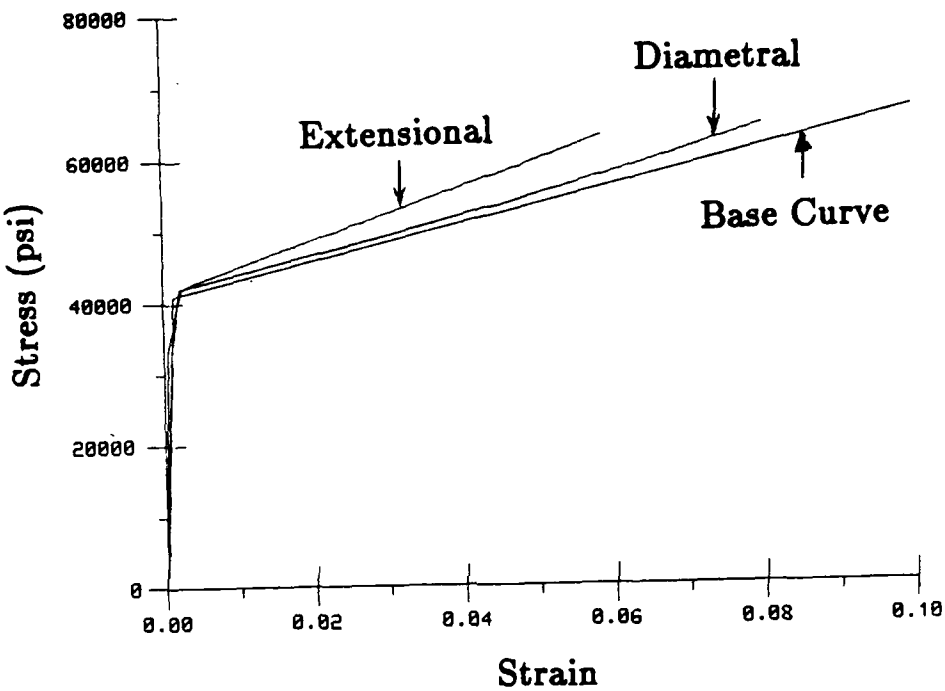

Figure 6.7 Plot of average stress against average strain for the specimen using different extensometer measures of strain.

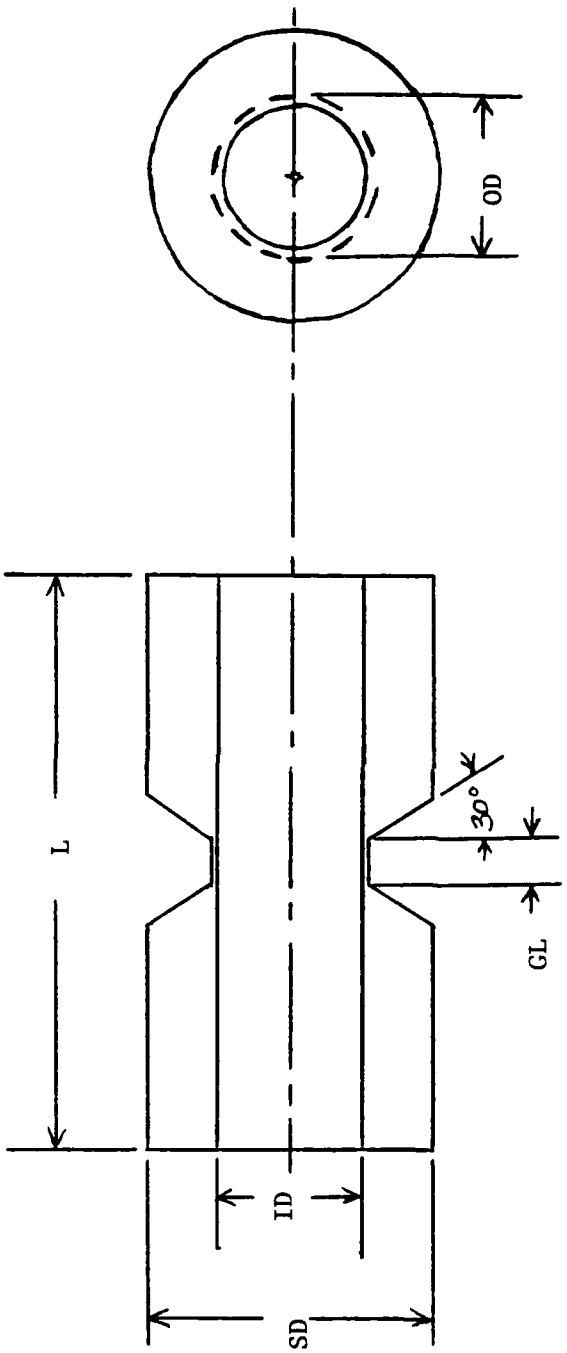

Figure 6.8 Geometry of the torsion specimens.

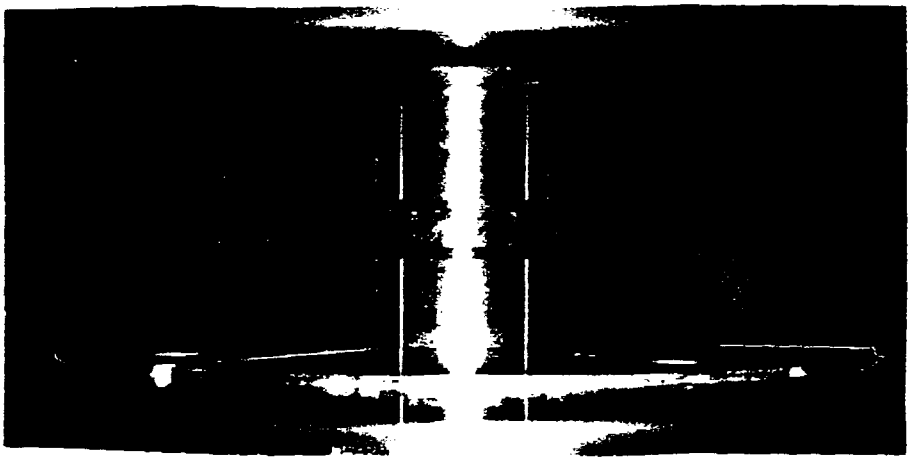

Figure 6.9 Photograph of torsion specimen in hydraulic collet grips.

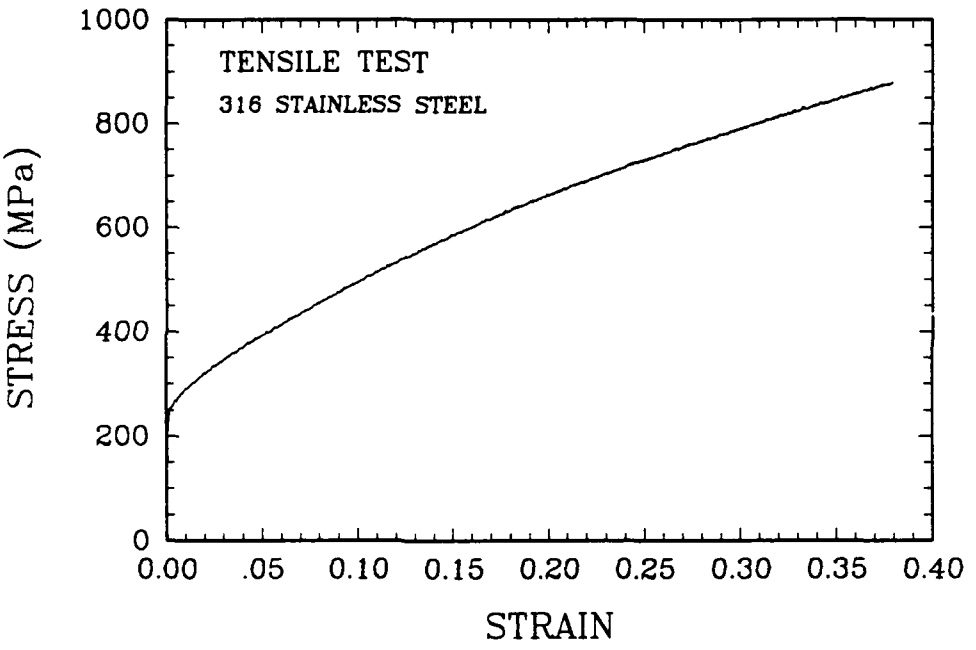

Figure 6.10 Experimental stress-strain result for tensile test of type 316 stainless steel.

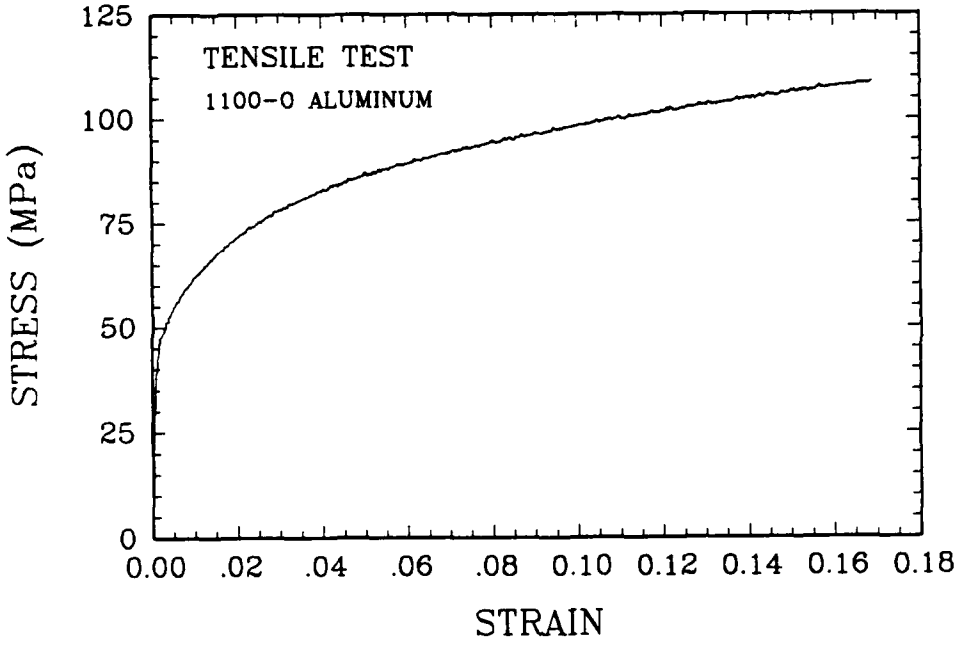

Figure 6.11 Experimental stress-strain result for tensile test of 1100-O aluminum.

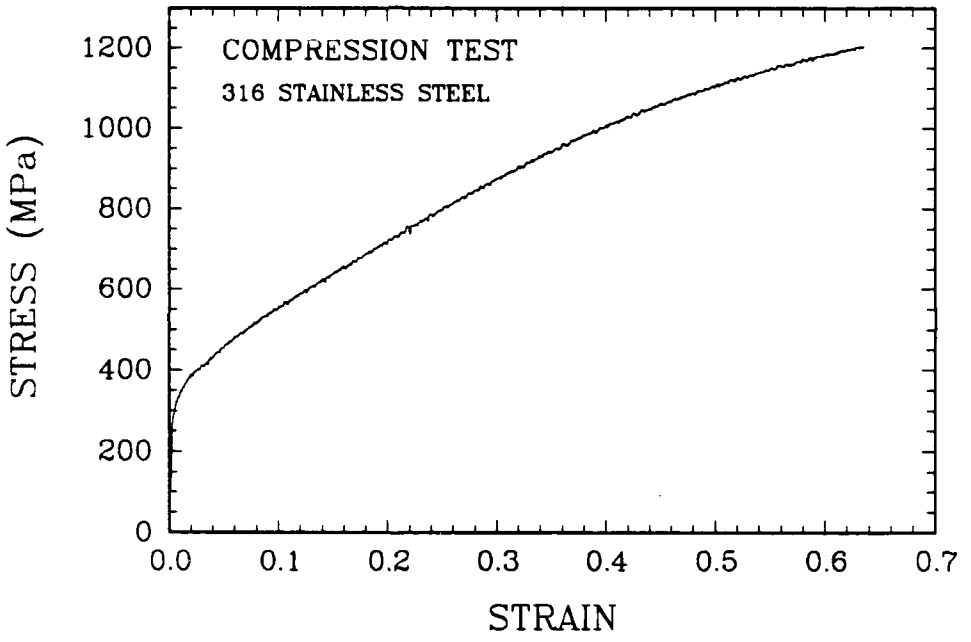

Figure 6.12 Experimental stress-strain result for compression test of type 316 stainless steel.

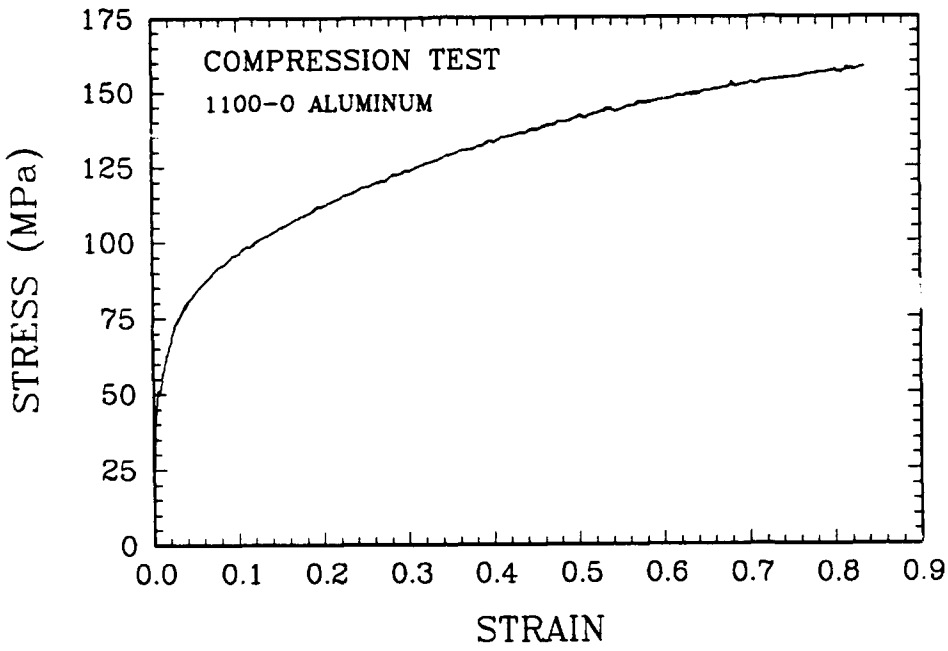

Figure 6.13 Experimental stress-strain result for compression test of 1100-O aluminum.

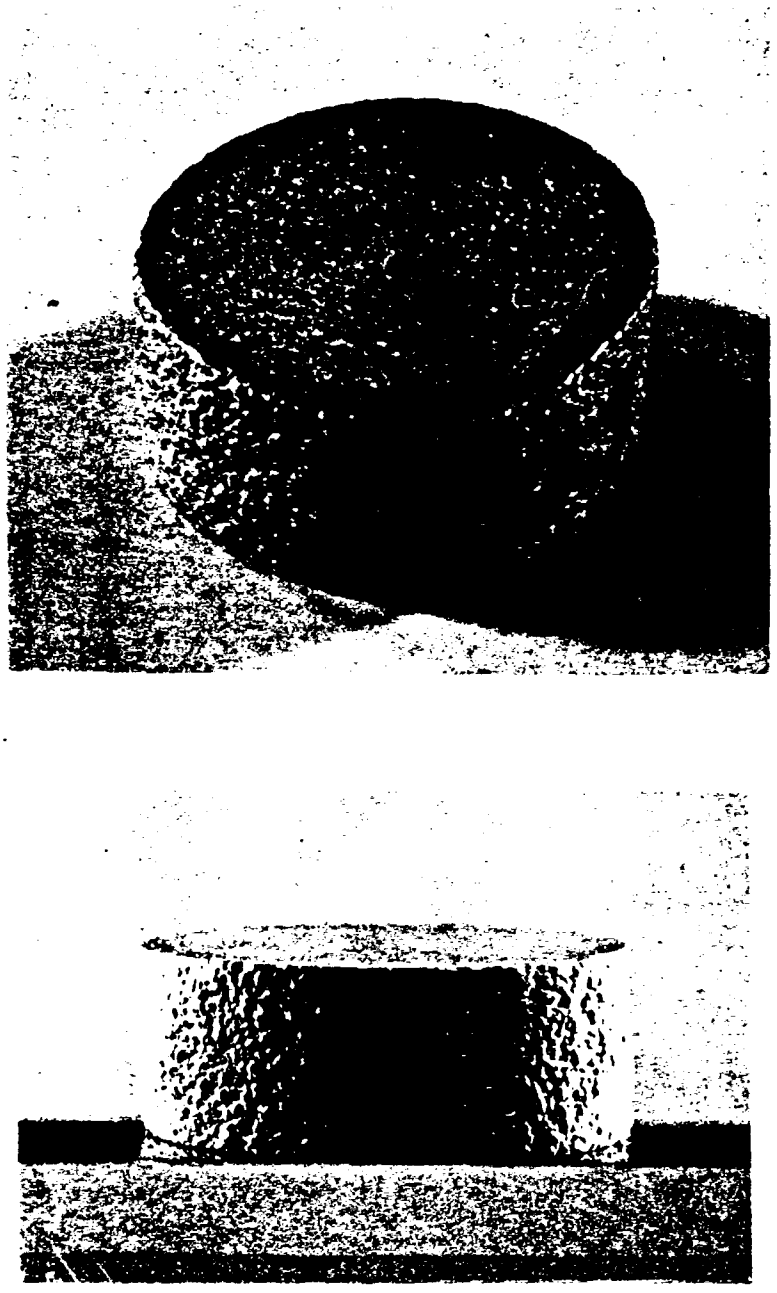

Figure 6.14 Photograph of deformed compression specimen of 1100-O aluminum. Final plastic equals -0.9 .

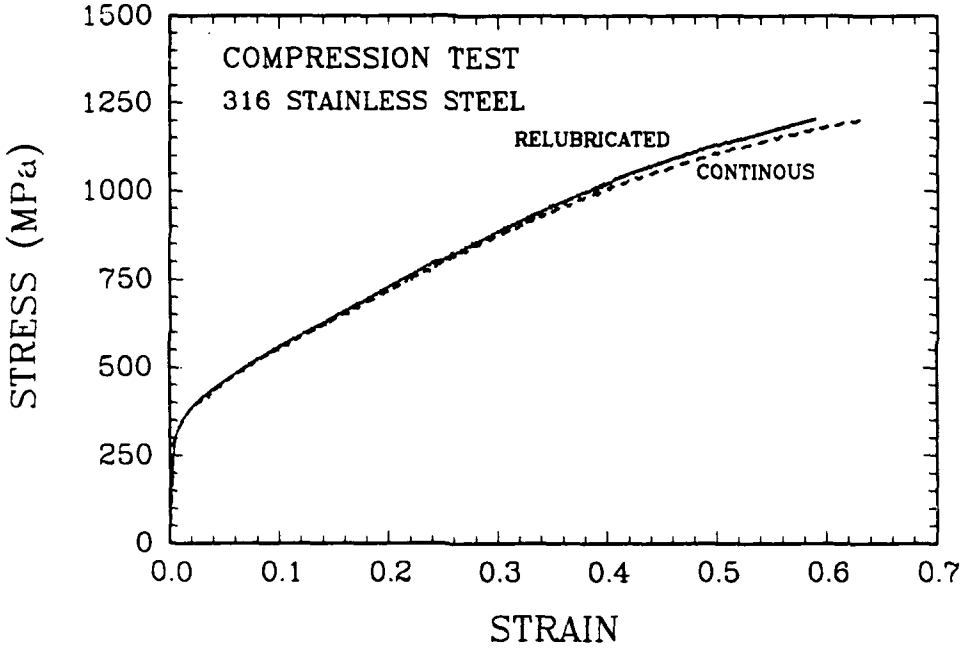

Figure 6.15 Comparison of compression results for two tests of type 316 stainless steel. One test was run continuously using just the initial teflon lubrication between specimen and platens. The other test was interrupted two times to relubricate the specimen-platen interface.

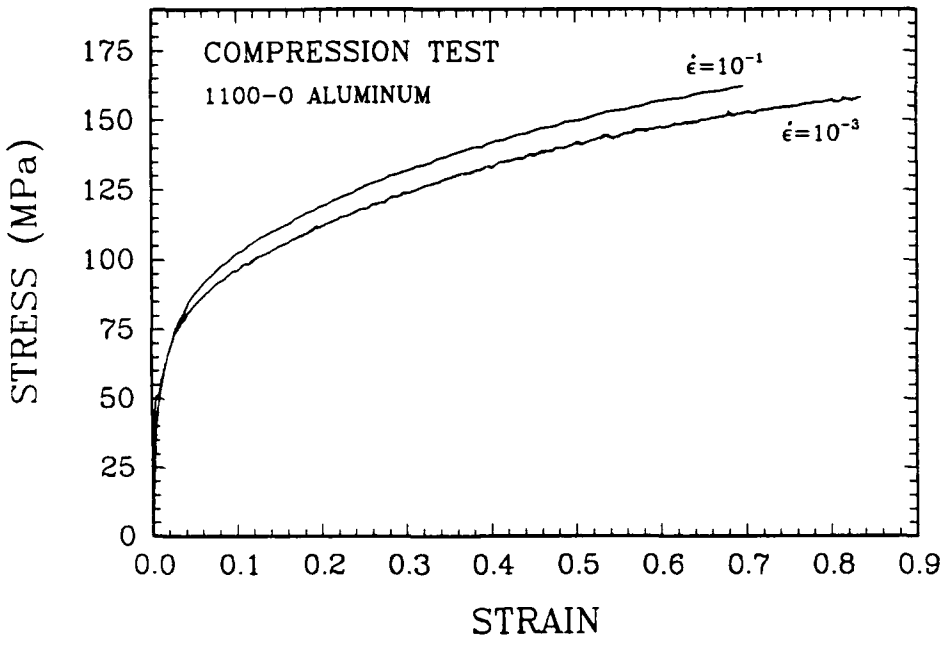

Figure 6.16 Comparison of compression test of type 316 stainless steel run at two different logarithmic strain rates (sec^{-1}).

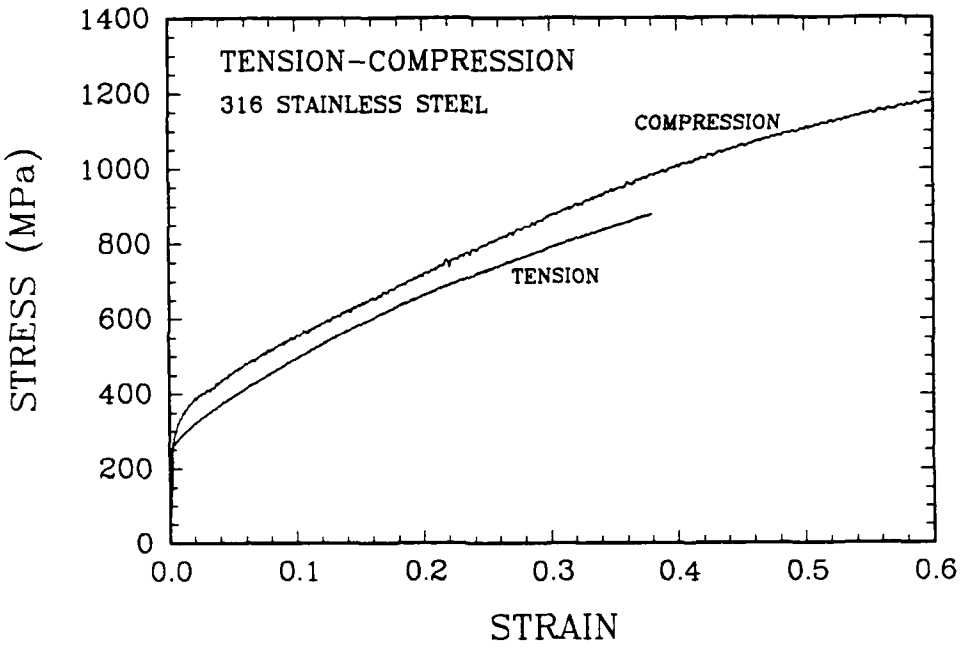

Figure 6.17 Comparison of flow stress levels for tensile results from reverse loading specimen with compression results from compression specimen.

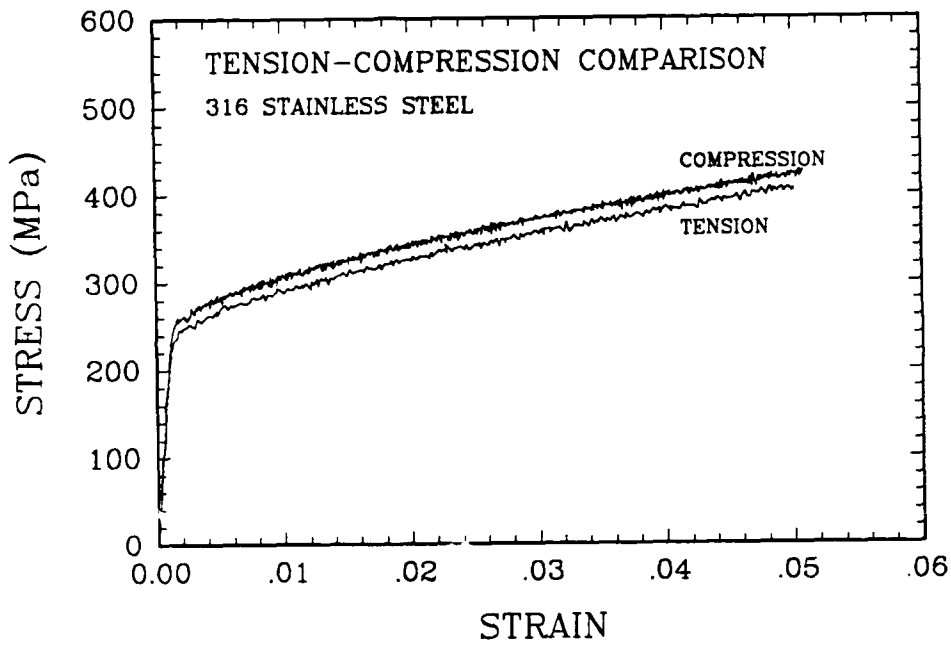

Figure 6.18 Comparison of flow stress levels for two reverse loading specimens: one initially loaded in tension, the other initially loaded in compression.

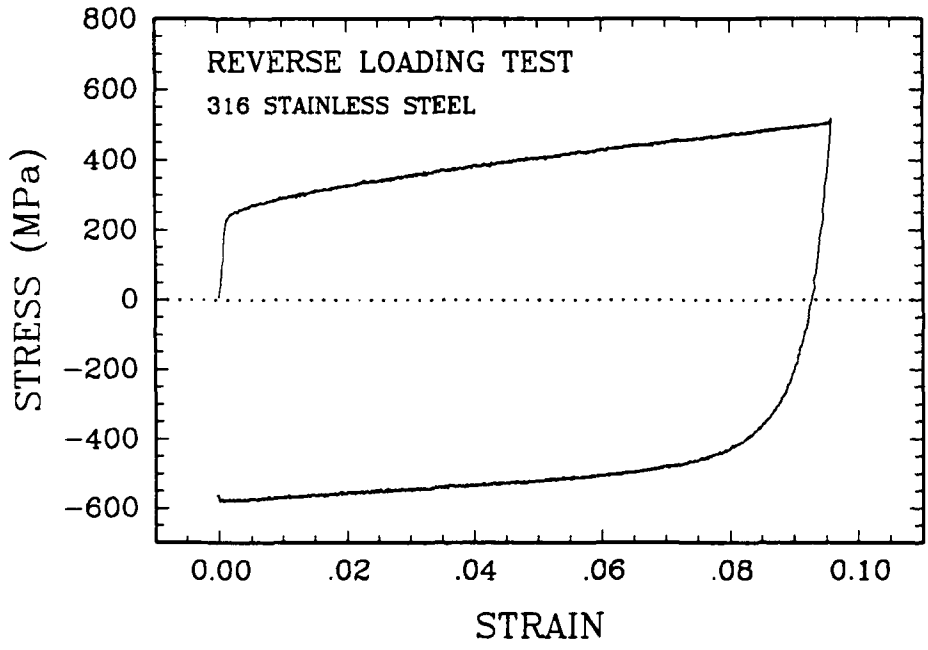

Figure 6.19 True stress-true strain result for type 316 stainless steel loaded in tension followed by compression.

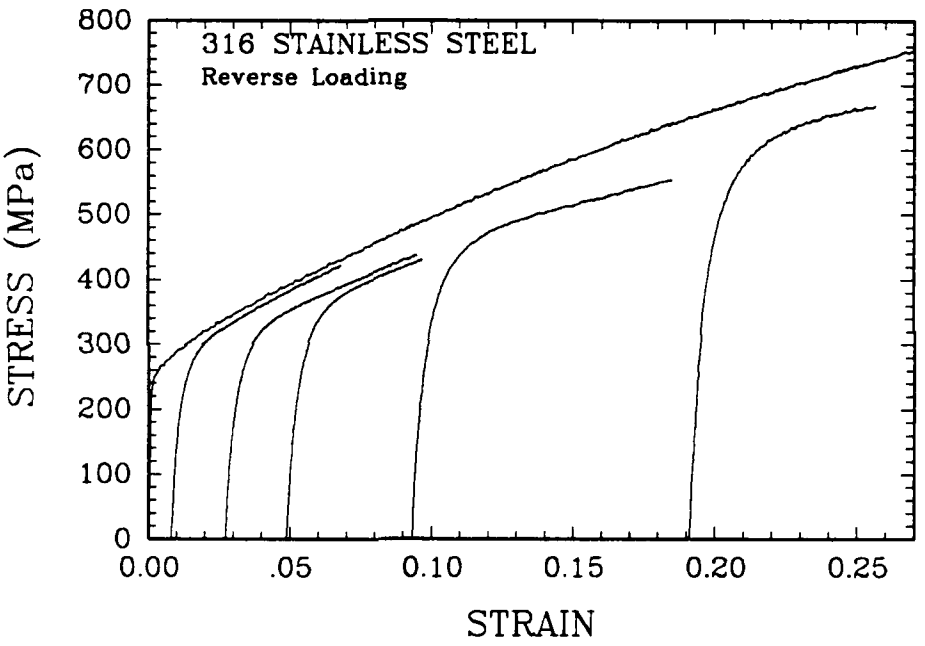

Figure 6.20 Composite figure showing the reversing branches of the reverse loading tests of type 316 stainless steel. All of the reversing branches have been rotated into the first quadrant. The tensile curve is also plotted for comparison of flow stress levels.

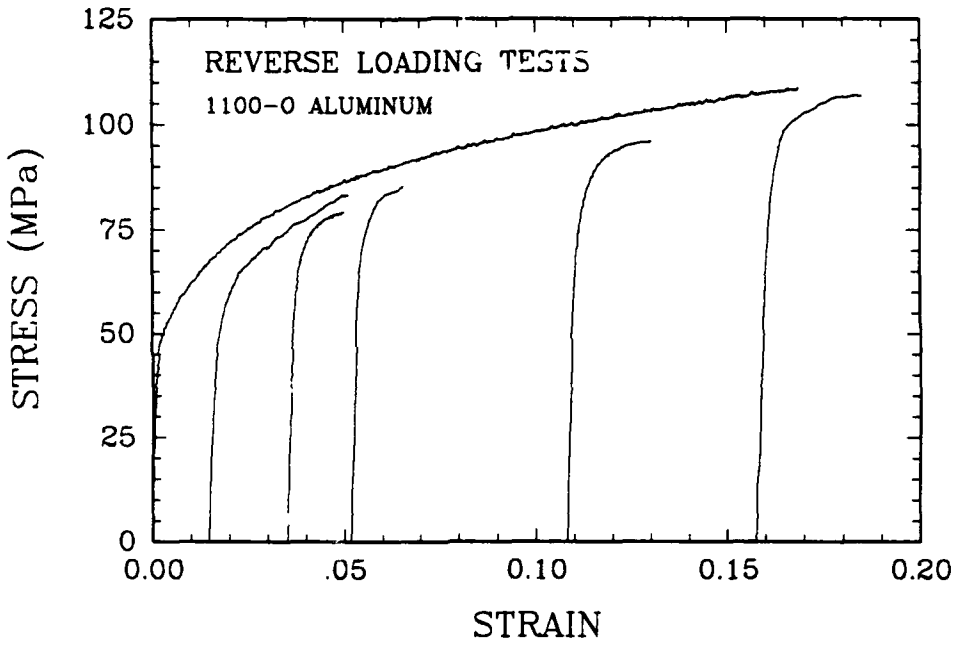

Figure 6.21 Composite figure showing the reversing branches of the reverse loading tests of 1100-O aluminum. All of the reversing branches have been rotated into the first quadrant. The tensile curve is also plotted for comparison of flow stress levels.

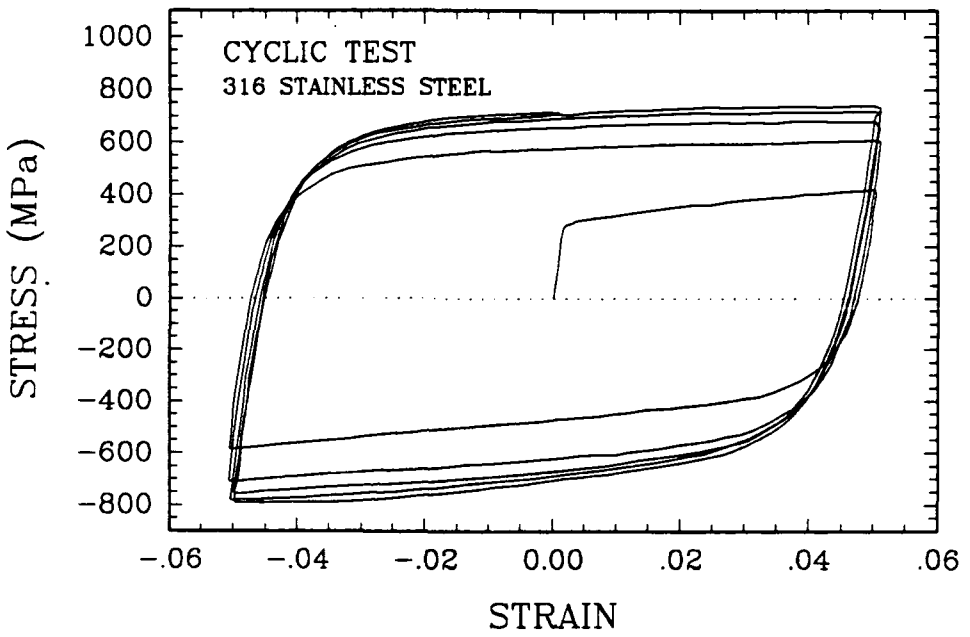

Figure 6.22 Stress-strain result for cyclic loading of type 316 stainless steel. Specimen was cycled under strain control for 5 cycles at ±5% strain.

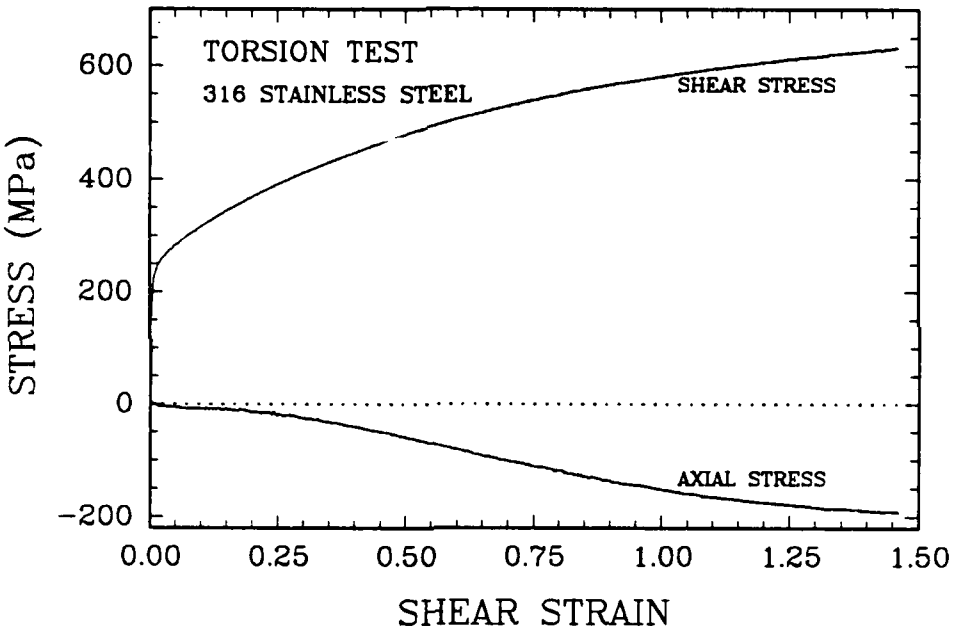

Figure 6.23 Torsion test result for type 316 stainless steel. Shear stress and axial normal stress are plotted as a function of engineering shear strain.

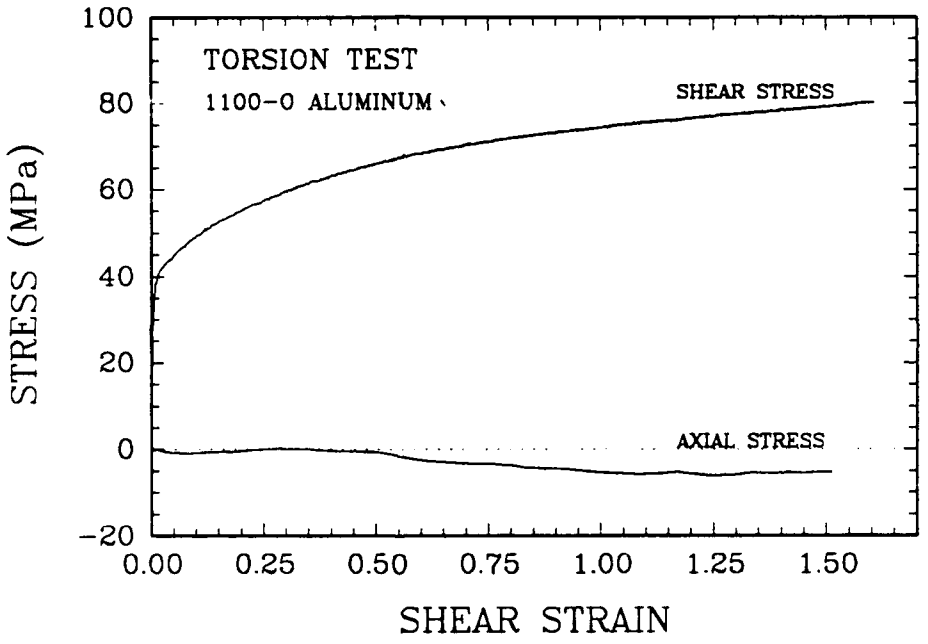

Figure 6.24 Torison test result for 1100-O aluminum. Shear stress and axial normal stress are plotted as a function of engineering shear strain.

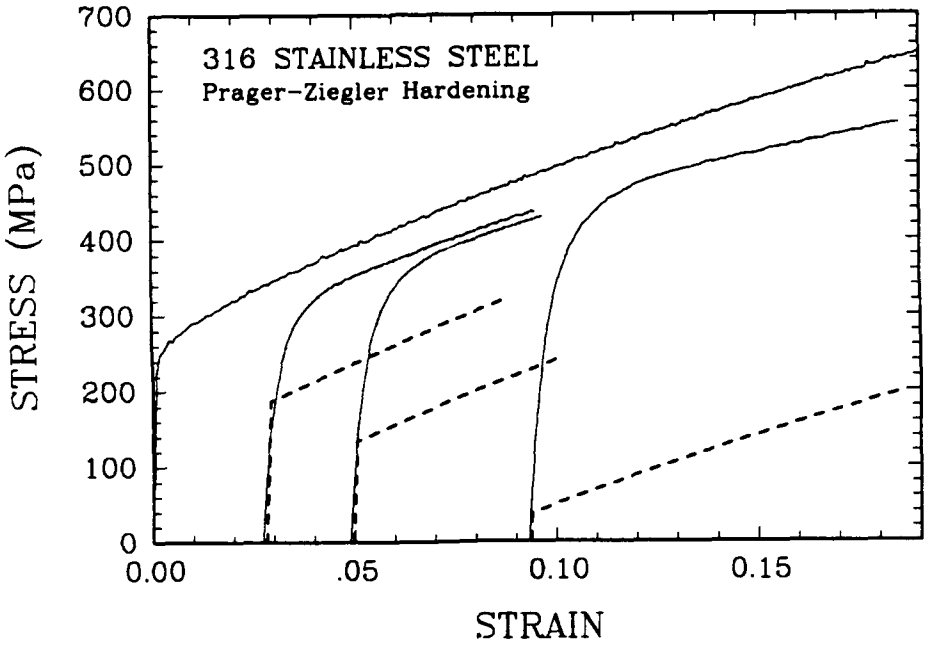

Figure 6.25 Prediction of the reverse loading results for type 316 stainless steel using the Prager-Ziegler theory. Solid curve is experiment, dashed curve is theory.

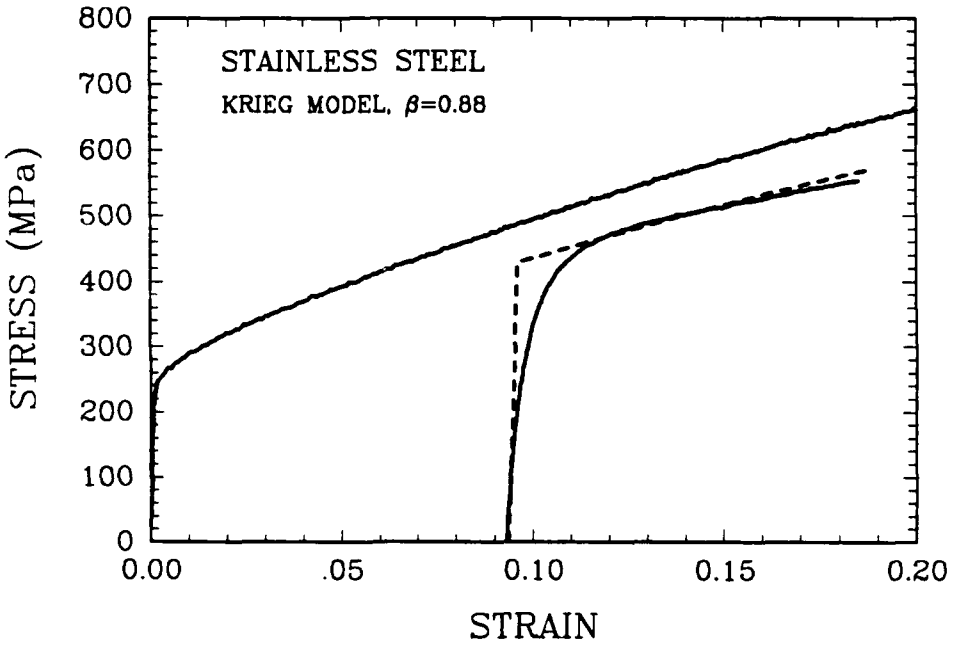

Figure 6.26 Match of reverse loading test using the Krieg theory with $\beta = 0.88$. Solid curve is experiment, dashed curve is theory.

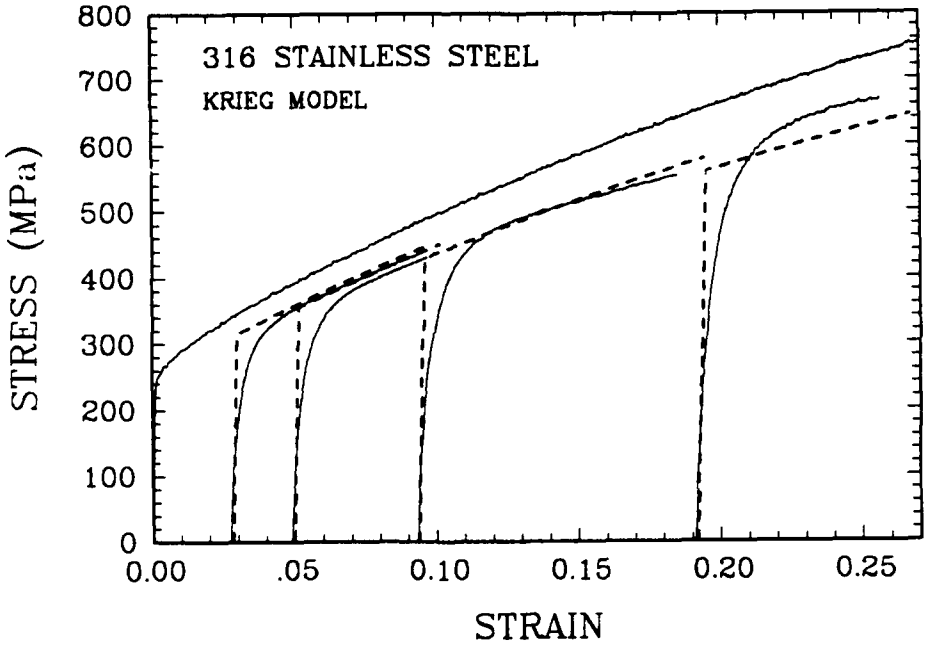

Figure 6.27 Prediction of reverse loading tests using the Krieg theory. Solid curves are experiments, dashed curves are theory.

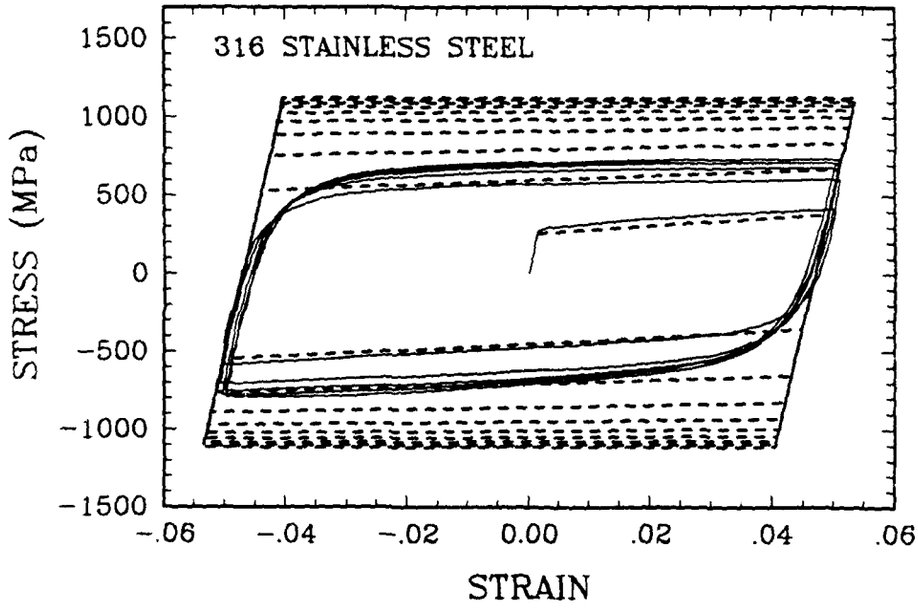

Figure 6.28 Prediction of cyclic test using the Krieg theory. Solid curve is experiment, dashed curve is theory.

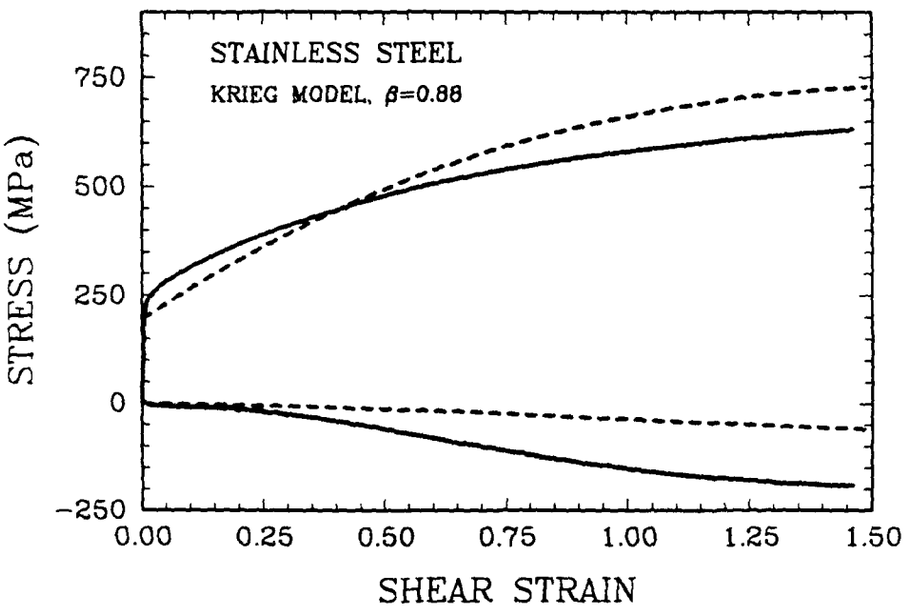

Figure 6.29 Prediction of torsion test using the Krieg theory. Solid curve is experiment, dashed curve is theory.

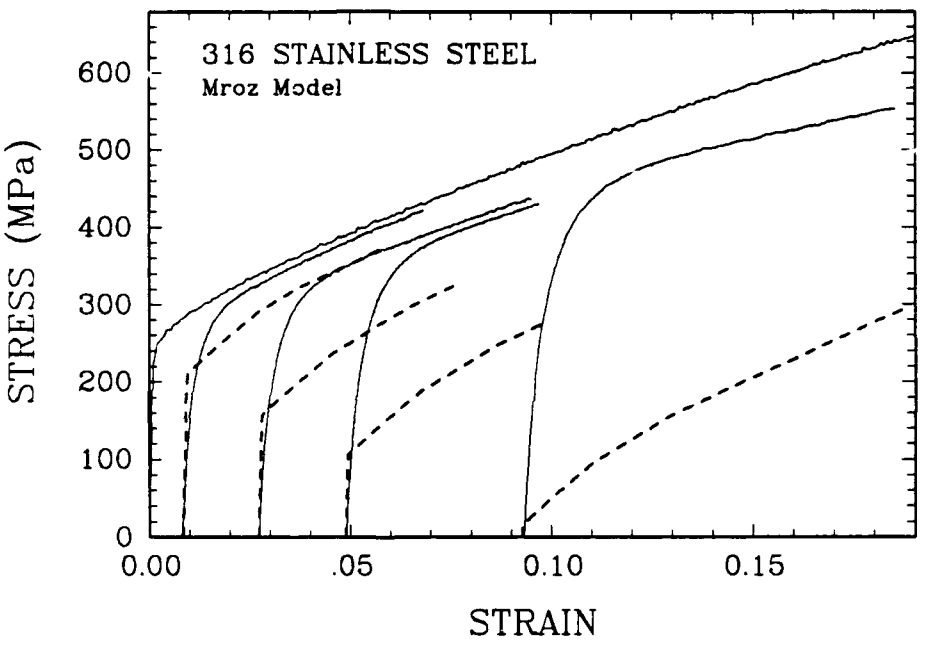

Figure 6.30 Prediction of the reverse loading tests using the Mroz [1967] model. Solid curves are experiments, dashed curves are theory.

Chapter 7

Comparison of Theory with Experiments

In this chapter the theoretical framework developed in Chapter 5 is applied to the experiments of Chapter 6. Simple material functions are chosen for the materials studied. The correlation that these give with the basic experiments as well as predictions of the more complicated experiments are presented. The specific functions presented are not intended to be final, general forms applicable to all materials. Rather, simple forms are chosen which are consistent with the criterion given in Section 5.4.

7.1 Specific Material Functions Employed

Referring to the equations 5.1-5.4 and eqs. 5.9 and 5.10, we note the need to postulate material functions for η, C_1, C_2, h_1, and h_2. In Chapter 5 it was shown that C_1 and h_2 could be functions of $\{s, g, B_{max}\}$ where g and B_{max} were defined as the fractional distance transversed of the maximal back stress surface and the size of that surface. C_2 will be considered a constant and h_1 a function only of s. The plastic spin coefficient, η, is also considered a constant. These dependencies

are summarized as:

$$C_1 = \hat{C}_1(s, g, B_{max}),$$

$$C_2 = \text{constant},$$

$$h_1 = \hat{h_1}(s),$$

$$h_2 = \hat{h_2}(s, g, B_{max}),$$

$$\eta = \text{constant}.$$

The plastic hardening modulus, H, was determined from the consistency condition (Equation 5.8).

A universal form was employed for $\hat{h_1}(s)$ for all of the materials investigated:

$$\hat{h_1}(s) = h_{10}(1 - \frac{s}{s^*})^q. \tag{7.1}$$

This material function has proven effective in modeling stress-strain results having a stress saturation [Brown, 1987] and also those without a measurable saturation state [Bronkhorst, 1988]. This function has three parameters h_{10}, s^*, and q. The value of s^* determines the saturation level, q controls how quickly that is reached, and h_{10} sets the hardening level. A material that shows no saturation in the strain range of interest is modeled by choosing s^* and q such that the predicted saturation is well outside of the working range. Linear isotropic hardening is achieved by setting s^* to a very large value or by setting q to zero.

In choosing a function for $\hat{h_2}(s, g, B_{max})$ it is necessary to satisfy the conditions: $\hat{h_2} \to 0$ as $s \to s_o$ (s_o is the annealed value of s), $\hat{h_2}$ increases monotonically with both s and B_{max}, and $\hat{h_2} \to 0$ as $g \to 1$ (the back stress has fully reversed in 1-D). A simple function that satisfies these conditions is

$$\hat{h_2}(s, g, B_{max}) = h_{20}\, B_{max}\, (s - s_o)\, (1 - g). \tag{7.2}$$

This function has a linear dependence on each of the variables and one coefficient, h_{20}, which is used to match the experiments. This particular function, although quite simple, was used for all of the materials investigated in this study.

The remaining constitutive function is the back stress coefficient $\hat{C_1}(s, g, B_{max})$. For monotonic loading $\hat{C_1}$ should be constant so that standard evanescent hardening is recovered. During reversing there should be a coupling between $\hat{C_1}$ and $\hat{h_2}$. This is expected if it is the same mechanism responsible both for the isotropic softening and the back stress hardening. Also $\hat{C_1}$ is expected to increase with B_{max}. The simple form chosen for $\hat{C_1}$ is

$$\hat{C_1} = C_{10} + K\, B_{max}(1 - g)\; +\; \frac{2}{3}\hat{h_2}. \tag{7.3}$$

It was necessary to include the $\hat{h_2}$ term in $\hat{C_1}$ to ensure that during uniaxial, reverse flow the tangent modulus is continuously decreasing. This function contains one reverse hardening coefficient, K, as well as the back stress constant C_{10}.

The evolution equations containing the particular constitutive functions used in this study are presented below. Note that these particular functions are not presented as *the* universal functions, rather they are simple expressions consistent with the constitutive restrictions outlined above.

$$\mathbf{B}^{\nabla e} \;=\; \{C_{10} \;+\; KB_{max}(1 - g) \;+\; \frac{2}{3}\hat{h_2}\}\, \mathbf{D}^p \;\; - \;\; C_2\dot{\epsilon}^p\mathbf{B}, \tag{7.4}$$

$$\dot{s} \;=\; h_{10}\,(1 - \frac{s}{s^*})^q\,\dot{\epsilon}^p \;\; - \;\; h_{20}B_{max}(s - s_o)(1 - g)\dot{\epsilon}^p. \tag{7.5}$$

The constants needed to completely specify the material are: $C_{10}, K, C_2, h_{10}, s^*, q, h_{20}$, the annealed value of s, (s_o), and the spin factor, η.

7.2 Simple Example of Model Components

Before applying the evolution equations developed in Section 7.1 (eqs. 7.4 and 7.5) to the experiments let us first examine the behavior of the model for a single reversing event. This proves very illustrative for visualizing the effects of the different parts of the model.

Figure 7.1 shows the stress-strain response for uniaxial loading in tension followed by compression. The stress response is given by the solid line. The stress is given by the sum of the isotropic and kinematic (back stress) components.

$$T_{11} = \frac{3}{2}B_{11} \pm s.$$

Here we are only examining one stress component. The plus sign applies during tensile straining and the negative sign during compressive strain increments. Figure 7.1 also plots these components of the total stress. The back stress initially rises to saturation during forward straining. Upon reversal it quickly changes sign and saturates in reverse at the same magnitude. The isotropic component starts at its initial value and increases monotonically during forward loading. Here the hardening is shown as linear, $q = 0$. Upon reversal the magnitude of s initially decreases. Once B_{11} has fully reversed then s again shows the same rate of growth as before reversal.

In Figure 7.1 the effects of the different model parameters are shown. The constants C_{10} and C_2 control the back stress growth during monotonic loading. C_{10} gives the initial slope and the ratio $\frac{C_{10}}{C_2}$ gives the saturation magnitude. During reversing, it is primarily the value of K that determines how quickly B_{11} reverses. K controls the sharpness of the reversing knee of the back stress evolution curve.

The isotropic softening variable, h_{20}, primarily controls the decrease in s immediately after reversing the direction of loading. It influences the permanent softening but not the stress response immediately after yield due to the presence of the $\hat{h}_2$ term in $\hat{C}_1$.

The influence that the constants C_{10}, C_2, K, h_{10}, and h_{20} have on the stress-strain response can be seen from Figure 7.1 since the stress response is a sum of the isotropic and kinematic components. The next section will consider how these parameters are chosen.

7.3 Procedure for Determining Constants

Whenever a theory is considered for a particular application care must be taken to prescribe how the theory will be fit to that material and range of strain rate and temperature. A rational method for determining the material parameters must be chosen or the theory is of no practical use. The experiments that are required need to be clearly specified.

In this section a methodology for determining the material parameters is given and applied to the materials under consideration. The experiments that were required to completely specify the constants consisted of the uniaxial monotonic (tension or compression) test, the uniaxial single reverse tests, and the large strain torsion test. The material model was completely specified by these tests. They are the *model construction* tests. The cyclic and nonproportional tests are the *model verification* tests and are used only to investigate the predictive capability of the model.

The strategy used to determine the material parameters is as follows. The

back stress constants C_{10} and C_2 are determined from the reversing experiments by looking at the reverse yields. Once they are known the back stress evolution under monotonic loading can be predicted. The tension or compression test is then used to find the constants in $\hat{h_1}$. For monotonic radial loading the back stress is known. Its contribution to the total stress can be subtracted out leaving just the isotropic variable. For monotonic loading $h_2 = 0$ so the function $\hat{h_1}$ can be fit to the isotropic variable evolution.

The transient reverse hardening and isotropic softening are both manifested in the reverse loading tests. The values of K and $\hat{h_{20}}$ are chosen to match to the reversing portions of the tests. The value of K controls the sharpness of the *knee* of the reverse loading curve and h_{20} controls the permanent softening.

From these tests the proper effects can be isolated to determine the material constants. From the strategy outlined above, the following methodology was used to select the parameters of the model for the materials considered in this study.

1. **Determine the back stress evolution from the reverse loading tests.** From the stress-strain results for reverse loading find the reverse yield stress σ_r. This is determined using a certain offset definition for the reverse yield. This offset is in the approximate range of 0.05% to 0.3% strain. The tensile equivalent back stress is then determined as $\sigma_b = \frac{1}{2}(\sigma_f + \sigma_r)$ where σ_f is the forward flow stress achieved before reversing. Note that σ_r can be positive or negative in sign. Since the back stress tensor $\mathbf{B}$ is deviatoric ($tr\mathbf{B} = 0$) the component in the direction of loading of the experiment is

$$B_{11} = \frac{2}{3}\sigma_b = \frac{1}{3}(\sigma_f + \sigma_r). \tag{7.6}$$

The constants C_{10} and C_2 are chosen from the evolution of B_{11} with plastic strain ${\epsilon_{11}}^p$.

$$B_{11} = \frac{C_{10}}{C_2}(1 - e^{-C_2 {\epsilon_{11}}^p}). \tag{7.7}$$

The ratio $\frac{C_{10}}{C_2}$ is chosen to match the saturation value of B_{11} achieved at large strain. The value of C_2 is then chosen to match the time constant or rise time of the results.

This procedure gives a systematic manner of selecting C_{10} and C_2. Figure 7.2 shows this fitting for type 316 stainless steel.

2. **Determine the isotropic hardening constants.** From equation 7.7 the back stress evolution for uniaxial, monotonic loading can be predicted. The evolution of the isotropic variable s for monotonic loading is found by subtracting the back stress from the total stress. For each point on the stress-strain curve the value of s is given by

$$s = \sigma - \frac{3}{2}B_{11}, \tag{7.8}$$

where B_{11} is given by equation 7.7. This is illustrated in Figure 7.3 for the compression of type 316 stainless steel. Once the curve of s versus plastic strain is known the material constants can be fit. For monotonic loading $h_2 = 0$ so:

$$\dot{s} = h_{10}\left(1 - \frac{s}{s^*}\right)^q \dot{\epsilon}^p, \tag{7.9}$$

is the functional form to be fit. Integration of equation 7.9 [Brown, 1987] yields

$$s = s^* - [(s^* - s_o)^{(1-q)} + (q-1)\{h_{10}(s^*)^{-q}\}\tilde{\epsilon}^p]^{\frac{1}{(1-q)}}, \tag{7.10}$$

where s_o is the initial value of s and h_{10}, s^*, and q are the material parameters.

This function has four parameters. Theoretically they could all be determined using a four parameter least squares fit. In practice, s_o and s^* correspond to the initial and saturation values of s so they can be chosen or inferred by extrapolation from the results of s versus plastic strain. Nonlinear fitting for h_{10} and q was performed with an IMSL numerical subroutine ZXSSQ which provides for minimization of a nonlinear function on the basis of a least squares residue. For type 316 s.s. in compression this fit is shown in Figure 7.4.

This procedure yields consistent values of the parameters and provides a check on the choice of offset reverse yield definition. We make the assumption that, for monotonic loading from the annealed state, the value of s should also increase monotonically. *If too small of an offset yield definition is used this does not hold.* The inferred curve of s versus plastic strain then shows an initial dip. This is not consistent with the initial annealed state of the materials tested in this study. We expect that s should show a monotonic increase with plastic strain. Choice of reverse yield defined by a 0.05% to 0.3% offset strain satisfies this requirement.

3. **Determine the Reversing Coefficient K and the Isotropic Softening Coefficient h_{20}.** Using the previously determined values of $C_{10}, C_2, h_{10}, s^*, s_o$, and q the reverse loading experiments are simulated with different values of K and h_{20}. To select the appropriate values, first set $h_{20} = 0$ then simulate one of the reverse loading tests for various values of K. The test to be matched

should be one which has the back stress well developed ($\epsilon_f^p \sim 0.1$). The simulation will have no permanent softening for $h_{20} = 0$ but choice of K should be made to match the initial steeply rising portion of the reversing curve.

Once the order of magnitude of K is known then isotropic softening is added by increasing h_{20}. This will be seen as an increase in permanent softening. As h_{20} is changed, K will also need to be changed to provide good agreement with the rising portion of the reverse curve. There is a coupling of the effect of h_{20} and K on the reverse flow curve. In a few trials K and h_{20} can be selected to give good agreement.

When K and h_{20} have been selected from the one reverse test they should next be used in simulating all of the reverse tests. If good agreement is not obtained for all of the tests then different functional forms are needed for $\hat{h}_2$ and $\hat{C}_1$. These can be modified and new values for the coefficients selected using the same procedure.

The procedure which has been described in this section uses just two types of experiments (uniaxial monotonic and single reverse) to select all of the material parameters of the proposed combined kinematic-isotropic model.

Table 7.1 Material Constants

material	C_{10}	C_2	h_{10}	q	s_o	s^*	K	h_{20}
1100 alum (t)	500	25	39,619	13.619	47.	200	600	10
1100 alum (c)	500	25	276	1.015	53	150	600	10
316 s.s. (t)	1780	17.8	1600	0.3189	240	1100	200	1.5
316 s.s. (c)	1780	17.8	1752	0.3345	290	1200	200	1.5
1020	5233.3	50	19,256	7.7106	175	1217	150	1
1045	5600	40	8255	5.361	350	1414	150	3
1095	6934	40	39,825	5.249	442	1000	100	10

The one remaining parameter, the plastic spin factor, is considered by examining the large strain torsion response. Calculations of the model for different values of η are directly compared with the experimental shear stress and normal stress response. The question of the importance of plastic spin can be addressed by this approach. If it is important, the choice of η from this matching completes the model. If it does not matter, or it the value of $\eta = 0$ provides the best match to the experiment, then plastic spin is not important for this application.

7.4 Correlation of Theory with Base Experiments

In section 7.3 the procedure for choosing the constants in the theory was discussed. Appropriate values for the coefficients were chosen from the set of base experiments. In this section the comparisons of the theory with these tests are presented. These results do not show the predictive capability of the model but rather how well it correlates the tests. In section 7.5 the predictive capabilities will be examined.

These experiments used for model construction include tension, large strain compression, and single reverse tests for the following materials: type 316 stainless steel, 1100-O aluminum, and three spherodized carbon steels (1020, 1045, 1095). The carbon steel data are from the studies of Bronkhorst [1988].

The reversing tests were used to determine the back stress evolution during monotonic loading. The constants C_{10} and C_2 were used to predict this growth. Figure 7.5 shows the correlation of the model with the experimentally inferred data points. Notice that the theory predicts a saturating, decaying exponential behavior.

$$B_{11} = \frac{C_{10}}{C_2}(1 - e^{-C_2\bar{\epsilon}^p}). \tag{7.11}$$

The experimental back stresses were determined using various percent offset def-

initions for reverse yield, as discussed in section 7.3. The offsets that were used were: 0.3% for type 316 s.s., 0.05% for 1100-O aluminum , 0.3% for 1020, 1045, 1095 carbon steel. These offsets were chosen to ensure a monotonically increasing isotropic component during forward loading as discussed above.

After the back stress evolution was chosen, the isotropic component was fit and the tension and compression curves were simulated. These are shown in Figures 7.6 to 7.12. The simulation of these results is very close as expected.

The reverse loading experiments were also used to select the level of isotropic softening and additional back stress stiffening. The correlation of these experiments with the model is shown in Figures 7.13 to 7.17. The proper trends are captured by the model for each material. The initial high stiffening during reversing is well matched. The permanent softening trends are also well represented. Better correlation could be obtained if different functions for $\hat{h}_2$ and $\hat{C}_1$ were chosen for each material. The ones that were chosen were intended to be simple, having few parameters, yet retaining the proper constitutive restrictions. In that light the correlation is quite good.

This section has presented the comparisons of the model with the base experiments used to determine the evolution equations. The correlation is quite satisfactory as five materials are modeled with the same simple constitutive forms.

7.5 Evaluation of the Predictive Capability of the Model

The true test of a constitutive model comes not from its accuracy in modeling the tests that were used to construct the model. Rather, a model should be evaluated according to its ability to predict the behavior of different types of experiments. In

this section, the proposed constitutive model is used to predict the response under different types of loading than were experienced in Section 7.4.

The tests that were predicted were:

Symmetric, strain-controlled, cyclic tests of 316 s.s. and the carbon steels.

Unsymmetric, strain-controlled, cyclic tests of the carbon steels.

Unsymmetric, stress-controlled, cyclic test of 1045 carbon steel.

90° out-of phase strain-controlled cyclic test of 316 s.s.

Large strain, fixed end, torsion tests of 316 s.s. and 1100-O aluminum.

Using the material parameters determined in the base experiments described in Section 7.4, the experimental data and model predictions are compared. For each test it is the stress response that is examined.

7.5.1 Symmetric Strain Cycling

The model has been derived from mainly monotonic type loading. The single reverse experiments were used but not cyclic tests. A type of experiment that is a good test for the model is symmetric strain cycling. This test is important because it can be cycled to achieve a stable, saturation loop. If a model does not do a closely match the state after one reversal then the errors are accentuated with many cycles. In Figures 7.18 to 7.21 the experimental results and model predictions are presented for the symmetric strain cycling of four materials. Notice that the model does a good job of matching not only the final stress level but also the rate of buildup of stress. For each of these materials the response was cyclic hardening since they had

initially been in the annealed condition. For each test the nominal cycling range was $\pm 5\%$ strain.

In predicting this behavior the model behaves differently than most of the models in the literature. During each half cycle the isotropic component initially softens, then hardens. In the more classical models the isotropic component is always monotonically increasing with strain. At the cyclically stable state, these models predict that the isotropic component has its maximum saturation value, the value that it would achieve at large strain in a compression test. The new model predicts that the stable cycle is reached when the hardening and softening occuring during each half cycle just balance each other out. The maximum value of the isotropic component reached in the stable cycle depends upon the strain limits. For a larger hysteresis loop, a greater amount of hardening takes place and the isotropic component is larger. This means that for predicting cyclic plasticity, the isotropic component of stress depends upon the strain limits. This is just what is observed experimentally. For monotonic loading the isotropic component can reach a much greater value than for small to moderate strain cyclic plasticity. Modeling this behavior is an important feature for a general model for the small to large strain regimes.

7.5.2 Unsymmetric Strain Cycling

The symmetric cyclic tests give cyclic hardening. The results of Bronkhorst [1988] include unsymmetric strain cycling tests which show cyclic softening and mean stress relaxation for the three carbon steels. In Figures 7.22 to 7.24 the experiments and predictions are compared. For all three materials the tests consisted of a forward prestrain to approximately 9% strain followed by strain controlled cycling between 7% and 9% strain. The tests show cyclic softening as the hysteresis loops get

continuously smaller with cycling and approach a stable loop. The loops shrink mainly by a reduction in stress of the positive loading half cycle. The compression half cycle maintains the same stress.

The model predicts the stress softening (through the softening of the isotropic component) and the correct, stable hysteresis loop. What the model does not do as well is follow each cycle as it gradually softens to the stable state in about 5 cycles. The model achieves the final state in 1 or 2 cycles. This is not a major shortcoming. The characteristic features of this test are well predicted. The size of the stable loop is largely set by the value of s_o for cyclic softening conditions. The back stress merely alternates but s decreases. The factor $(s - s_o)$ in $\hat{h}_2$ is necessary to prevent s from softening below its annealed value. Figures 7.22 to 7.24 show that physically this is what limits the softening.

For the 316 s.s. an unsymmetric strain cycling test was conducted that consisted of forward loading to a strain of 19%, reverse straining to 17%, then forward straining. Figure 7.25 shows the prediction of the theory against the experiment. The model does an adequate job predicting the response here as with the unsymmetric strain cycling of the carbon steels.

7.5.3 Unsymmetric Stress Cycling

The experiments of Bronkhorst [1988] include unsymmetric stress cycling results of the carbon steels. Here we predict the behavior for the case of unsymmetric cycling of 1045 carbon steel. The specimen was cycled between stress limits of +490 Mpa in tension and -430 Mpa in compression. The results of both simulation and experiment are shown in Figure 7.26 .

The model correctly reproduces the hysteresis loop seen in the experiment. The

correct width and shape are predicted. The model does not do as well predicting the actual amount of cyclic creep. After $4\frac{1}{2}$ cycles the experiment has accumulated about 4% plastic strain but the model predicts about $5\frac{1}{2}$% accumulated plastic strain. When considering how other models do at predicting cyclic creep this is quite reasonable. The model does not do better due to the very low tangent modulus to the stress-strain curve at this level of strain. A small discrepancy is the stress prediction is magnified by the strain response. Overall, the model captures the correct behavior.

7.5.4 90^o Out-of-Phase Cycling

The predictions of the two types of tests described above very heavily activate the isotropic softening function $\hat{h}_2$ but do not test the tensorial nature of the constitutive equations since they involve uniaxial loading. One of the types of experiments that is not so limited involves cycling in the tension-torsion subspace. This involves radial loading in either the tension or shear direction to a certain prestrain then cycling by following a circular trajectory in strain space keeping the equivalent strain constant. These types of experiments have been cited frequently in the literature as a basic test of nonproportional, cyclic plasticity [Lamba and Sidebottom, 1978b], [Cailletaud, et al., 1984]. The experiments of Cailletaud et al. [1984] were for type 316 stainless steel. Although this material was heat treated differently than the annealed type 316 tested in this study, a simulation was conducted using the material constants developed here.

Figures 7.27a and b show the experimental results of Cailletaud and a simulation of this test with the current model. Notice that the same features are observed for both: a spiraling outward stress trajectory that saturates. The level of this

saturation stress value is higher than the corresponding saturation stress for uniaxial cycling at the same maximum strain range. The experimental results shown in Figure 7.27a are for a total imposed strain range of $\pm 1.5\%$. The out-of-phase stablization stress is 800 MPa. This compares with 550 MPa for the uniaxial stabilization stress for the same maximum strain cycling range. The simulation of Figure 7.27b predicts a stablization stress of 1105 Mpa. This compares with a model prediction of the uniaxial stablization stress of 496. Mpa. Notice that the additional hardening which is seen experimentally is picked up by the model. *This is a natural consequence of the physics of isotropic recovery limiting the uniaxial stress but not the out-of-phase cycling.* The other models which attempt to model this well known behavior do so by increasing the isotropic hardening modulus or making the isotropic saturation value depend upon some measure of nonproportionally [McDowell, 1987], [Benallel and Marquis, 1987], [Lindholm et al., 1985]. In the model presented here, additional hardening is a natural consequence except it is a misnomer to call it additional hardening. Really, it is the uniaxial cycling tests that show *reduced* hardening.

For uniaxial, symmetric cycling it was observed that the stabilization stress depended upon the competition between h_1 and h_2. For out-of-phase cycling, the back stress remains on its maximal surface during all of the deformation except right after the initial strain corner going from preloading to cycling. Thus s is not limited by softening and increases to its saturation value of s^*. So s^* is the important parameter determining the saturation stress level. There are important differences between uniaxial and out-of-phase cycling but the new constitutive model is able to predict them well.

7.5.5 Fixed End Torsion Tests

The deformation mode with the biggest interest in recent years has been simple shear. This deformation not only involves nonproportional loading but also material rotation at large deformation. The fixed end, torsion test of thin-walled tubular material provides the best experimental measure of simple shear.

Figure 7.28 presents the composite results of the 316 stainless steel torsion test. Both shear and normal (axial) stresses are shown as a function of engineering shear strain. The predictions of the model for simple shear are also displayed. For all of the torsion test predictions, the material constants reduced from the compression tests were used. This gave slightly different isotropic hardening parameters than if the tensile curve was used but more reliable large strain predictions since less extrapolation was required. The predictions in Figures 7.28 and 7.29 have $\eta = 0$, no plastic spin.

Notice that even without using plastic spin, the predicted stresses do not show any oscillations or inflections. The predicted normal stresses are also quite small, much smaller than those that were observed. Both of these result from the evanescent back stress evolution law. The value of C_2, the evanescent term, determines the importance of the evanescent or damping term. When C_2 is chosen large enough to properly model the back stress growth during uniaxial loading it does not allow for much buildup of normal stress during simple shear. The axial normal stress monotonically increases to a saturation value which, for small elastic strain and $C_2 >> 1$ yields,

$$T_{22}^{sat} = \frac{1}{2}\frac{T_{12}^2}{\mu} + \frac{3}{2}\frac{C_1}{C_2^2}.$$

The first term gives the elastic contribution and the second gives the plastic con-

tribution to the normal stress. For realistic values of C_2 (15-50) the plastic term is quite small and for metal plasticity the elastic term is also quite small. Substantial normal stresses are not predicted using the evanescent evolution law.

The effect of η is unimportant with these material constants. The effect that η has on the stress response is to decrease the magnitude of the normal stress and increase the shear stress. That would lead to slightly worse results here. For an evanescent law with realistic choices of C_1 and C_2 the plastic spin is unimportant. The new model does not predict an oscillatory sterss response even without activating the plastic spin.

The comparison of the shear stress result is not much better than the normal stress. The shear stress does not harden nearly as much in the experiment as the theory predicts.

These same trends are seen in Figure 7.29 for the torsion test of 1100-O aluminum. Here the experimental normal stresses are smaller in relative magnitude than for the 316 s.s. but are still well underpredicted by the theory. The shear stress prediction is also higher than the experiment.

Figure 7.30 shows the simple shear prediction of 1100-O aluminum carried out to very large shear strain (500%). Notice that for the realistic choice of material constants that no stress oscillation is seen. The shear stress approaches an asymptotic value. It is not necessary to include plastic spin to have monotonic stress response.

The proposed constitutive model works well for the cyclic tests (both proportional and nonproportional) but not as well for the large strain torsion test. The evanescent nature of the back stress evolution equation captures the cyclic response.

Even the out-of-phase tension-torsion cycling shape is well represented. In fact, the C_2 term in the evolution equation is necessary to center the stress hysteresis spiral on the stress origin. *The often debated question of the importance of plastic spin becomes moot for an evanescent back stress law with realistic constants.*

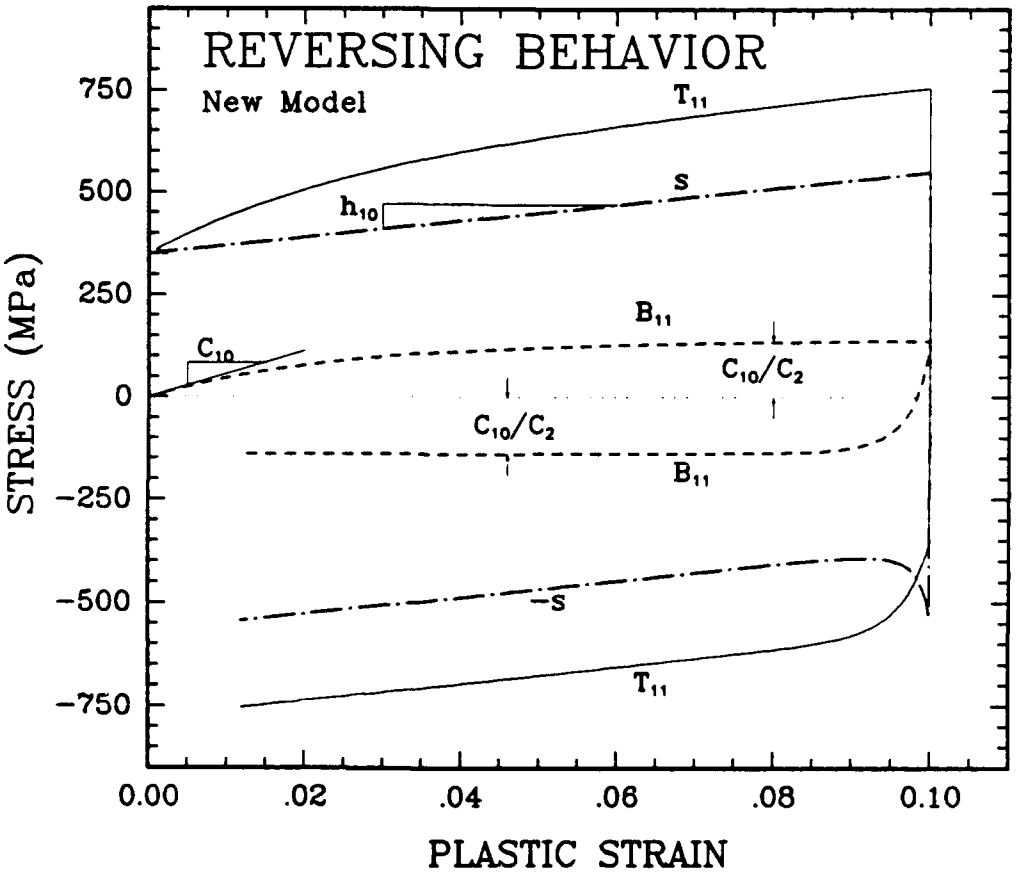

Figure 7.1 Schematic diagram of the new constitutive model simulating a uniaxial, single reversing test. The back stress component B_{11}, the isotropic component s, and the total stress T_{11} are shown to illustrate their behavior. The reversing coefficient K affects the sharpness of the knee of the B_{11} response immediately after strain reversal. The isotropic softening coefficient h_{20} affects the softening of the s response curve immediately strain reversal.

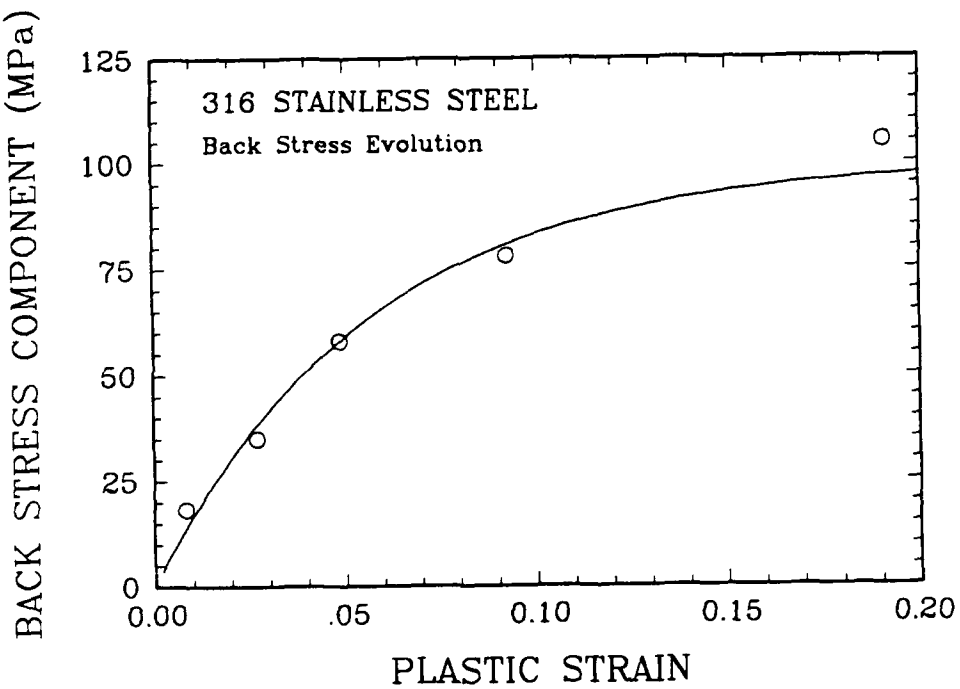

Figure 7.2 Comparison of experimentally determined back stress with fit. $C_{10} = 1780., C_2 = 17.8.$

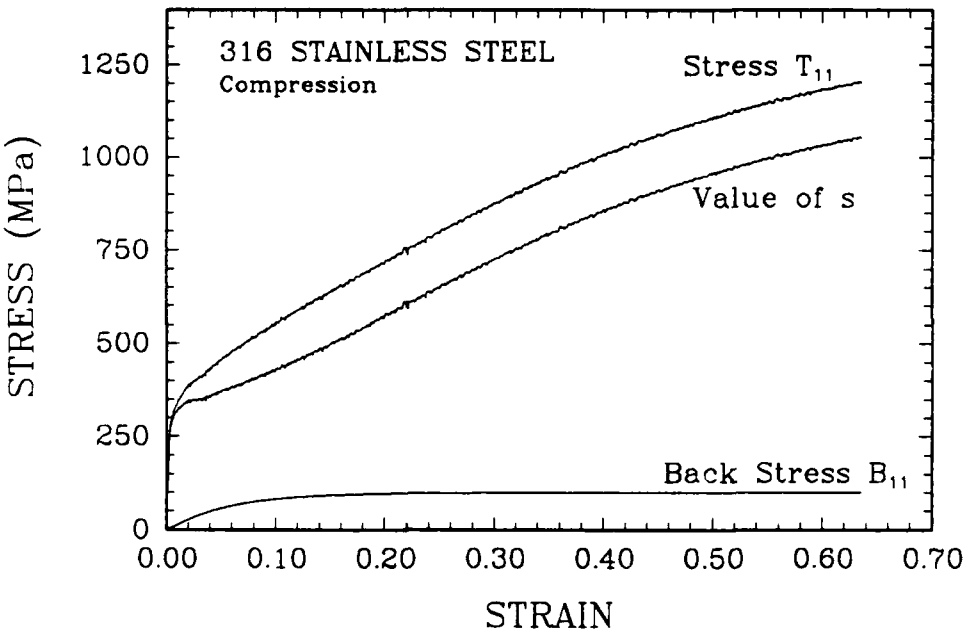

Figure 7.3 Decompostion of uniaxial stress-strain by subtracting back stress component from total stress to determine isotropic *s*.

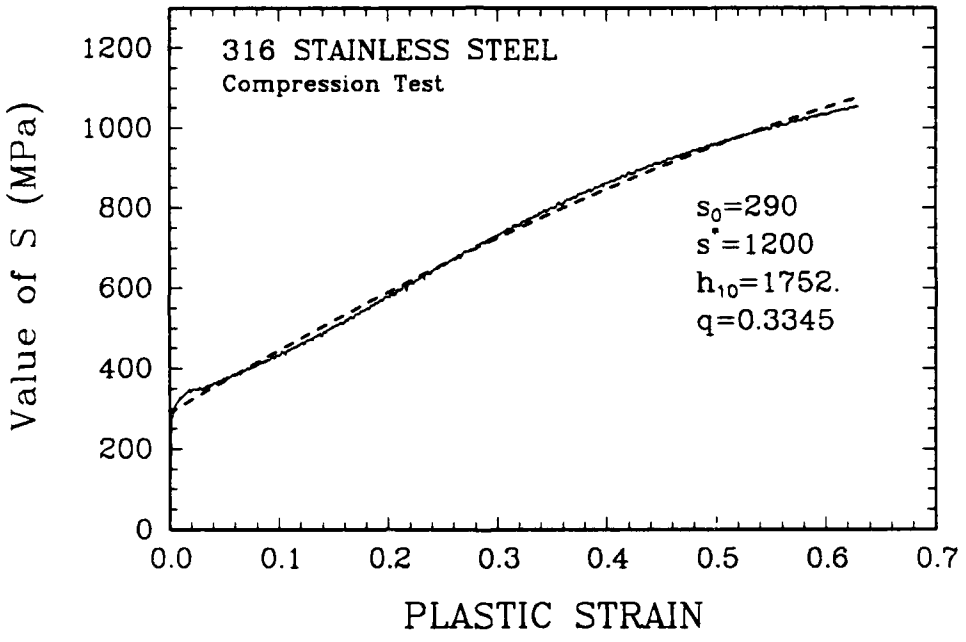

Figure 7.4 Fit of isotropic hardening function to inferred curve of s. Solid curve is experiment, dashed curve is fit.

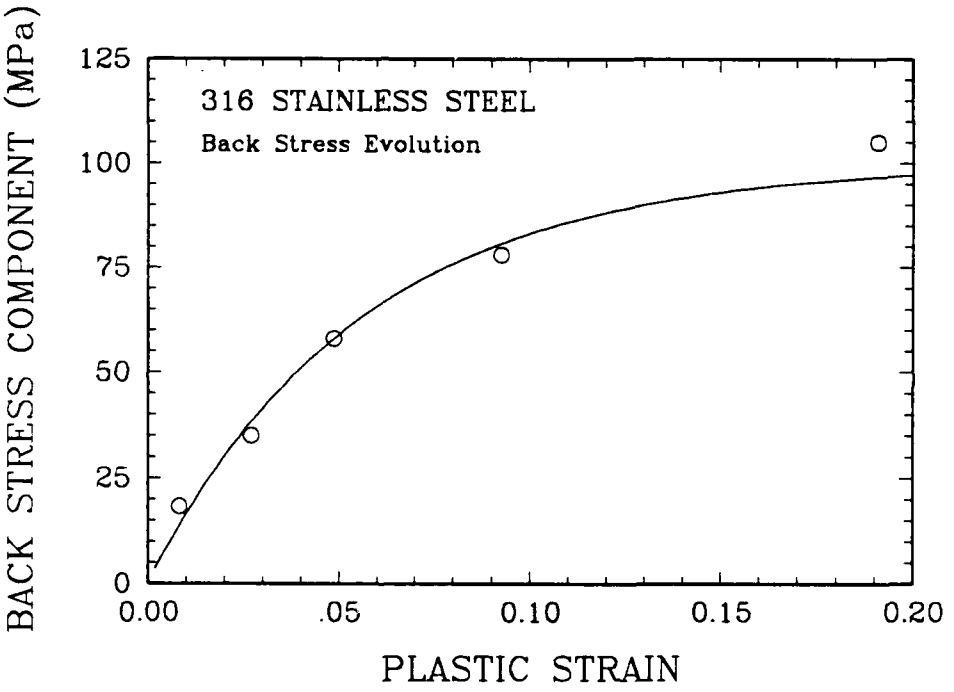

Figure 7.5a Back stress evolution for type 316 stainless steel.

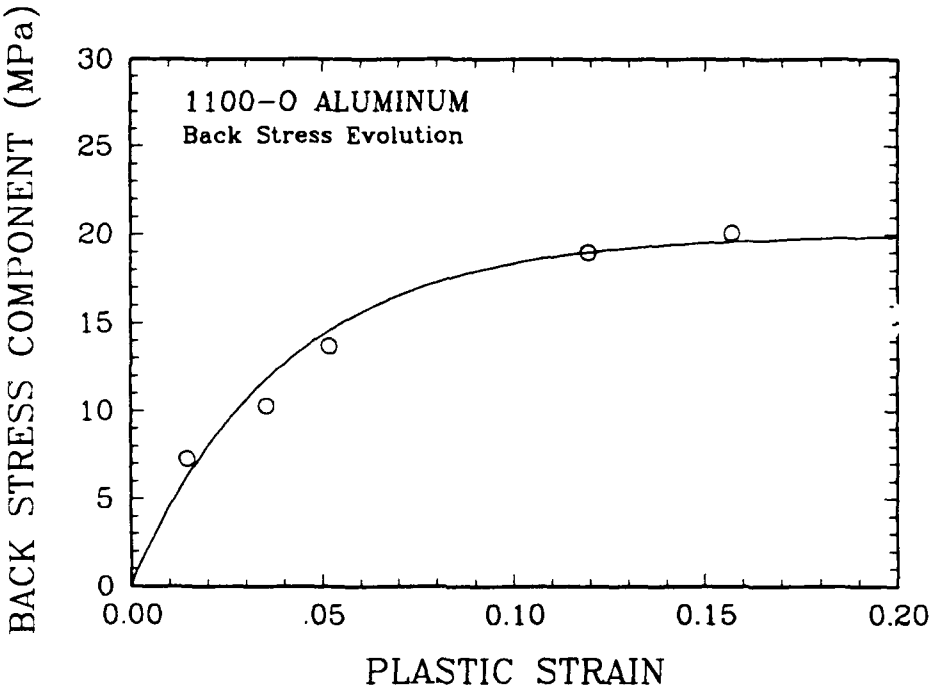

Figure 7.5b Back stress evolution for 1100-O aluminum.

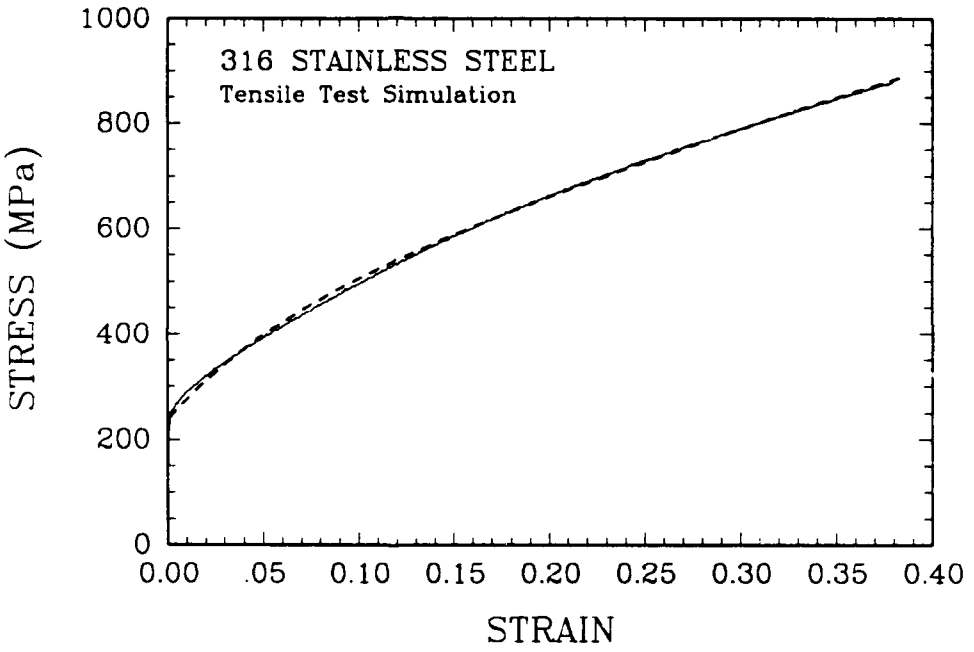

Figure 7.6 Comparison of tensile test with model fitting for type 316 stainless steel. Solid curve is experiment, dashed curve is model.

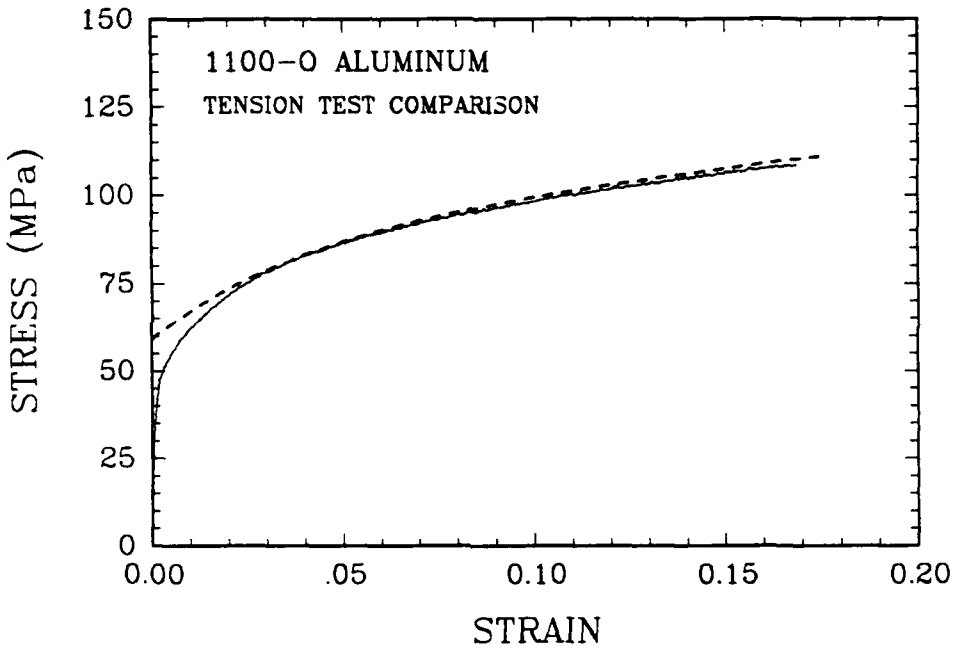

Figure 7.7 Comparison of tensile test with model fitting for 1100-O aluminum. Solid curve is experiment, dashed curve is model.

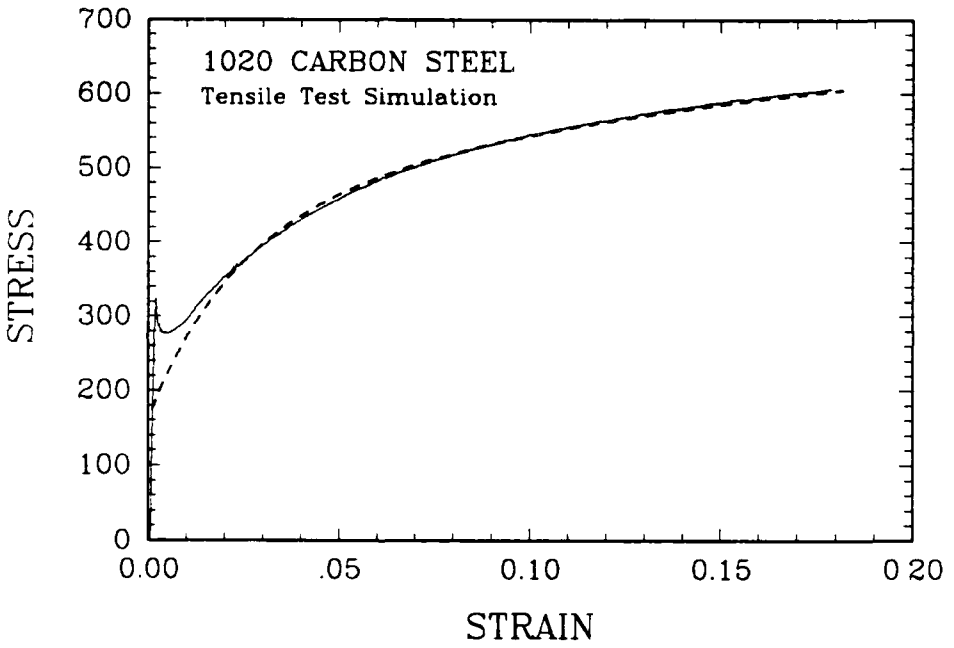

Figure 7.8 Comparison of tensile test with model fitting for 1020 carbon steel. Solid curve is experiment, dashed curve is model.

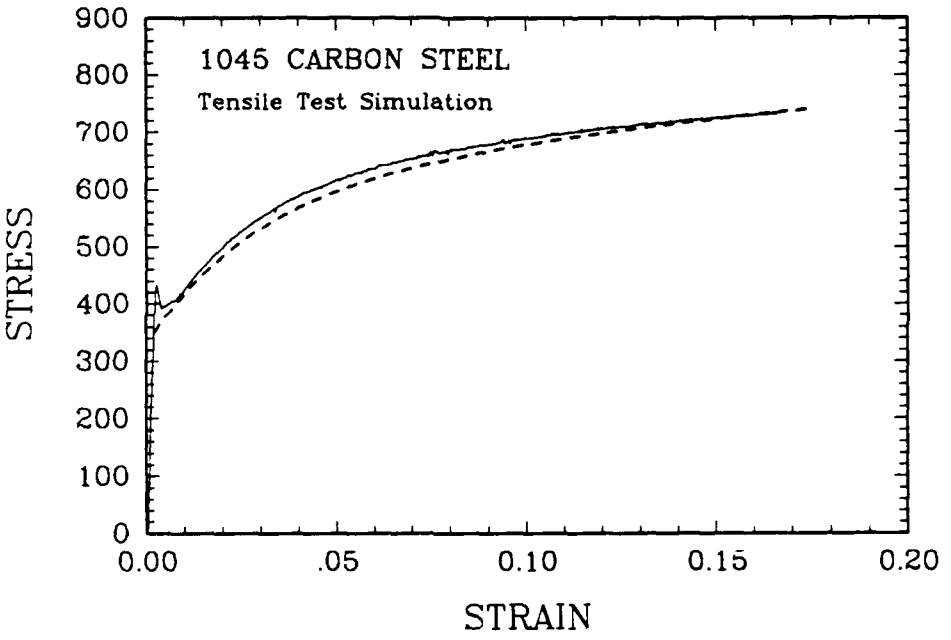

Figure 7.9 Comparison of tensile test with model fitting for 1045 carbon steel. Solid curve is experiment, dashed curve is model.

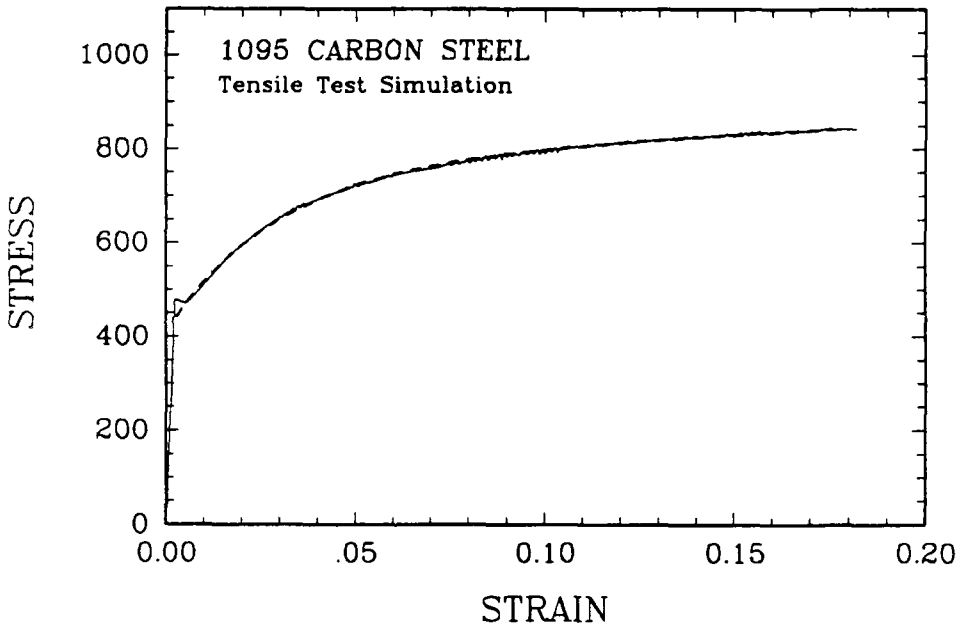

Figure 7.10 Comparison of tensile test with model fitting for 1095 carbon steel. Solid curve is experiment, dashed curve is model.

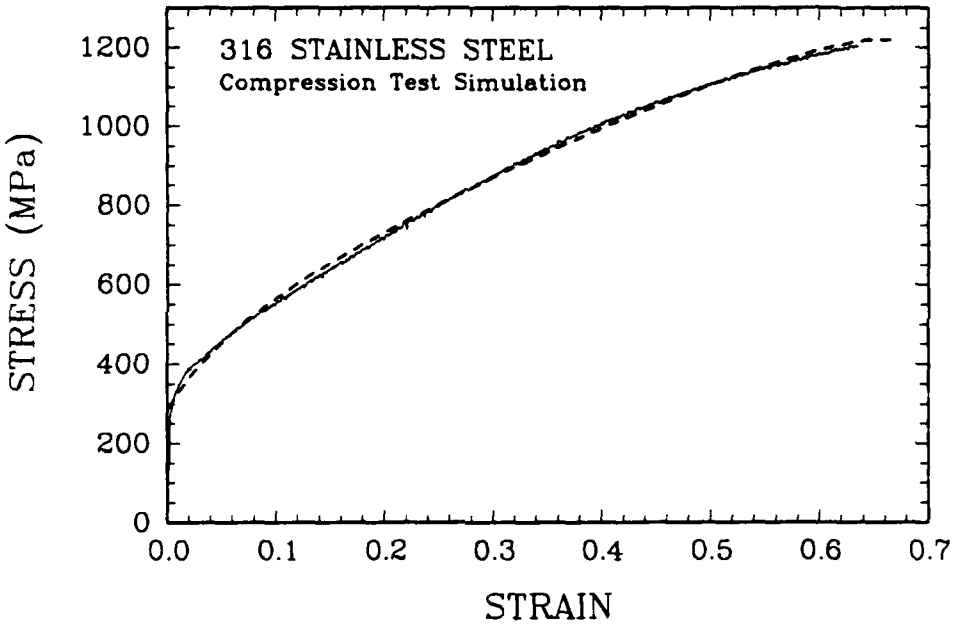

Figure 7.11 Comparison of compression test with model fitting for type 316 stainless steel. Solid curve is experiment, dashed curve is model.

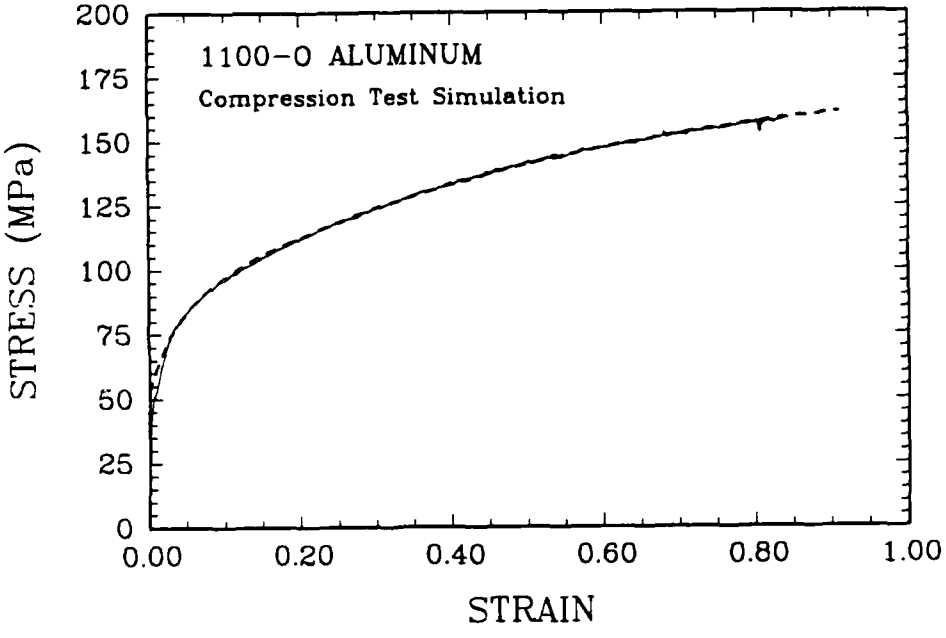

Figure 7.12 Comparison of compression test with model fitting for 1100-O aluminum. Solid curve is experiment, dashed curve is model.

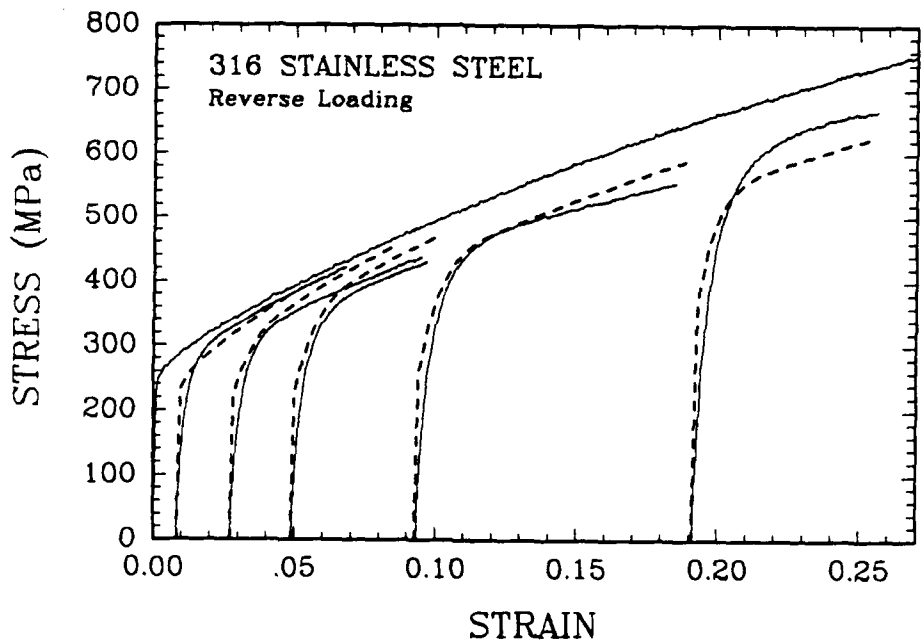

Figure 7.13 Comparison of model with reverse loading results for type 316 stainless steel. Solid curve is experiment, dashed curve is model.

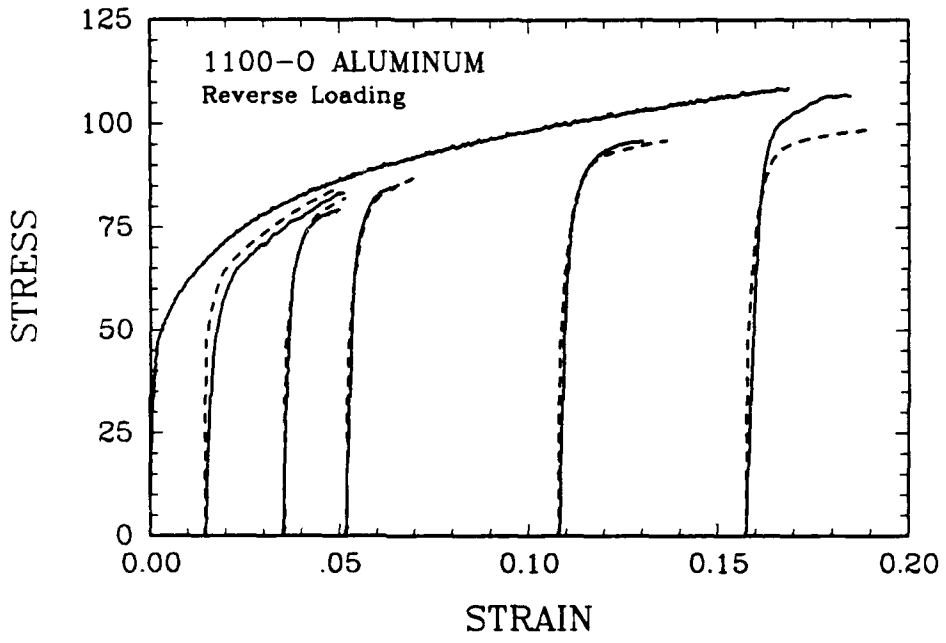

Figure 7.14 Comparison of model with reverse loading results for 1100-O aluminum. Solid curve is experiment, dashed curve is model.

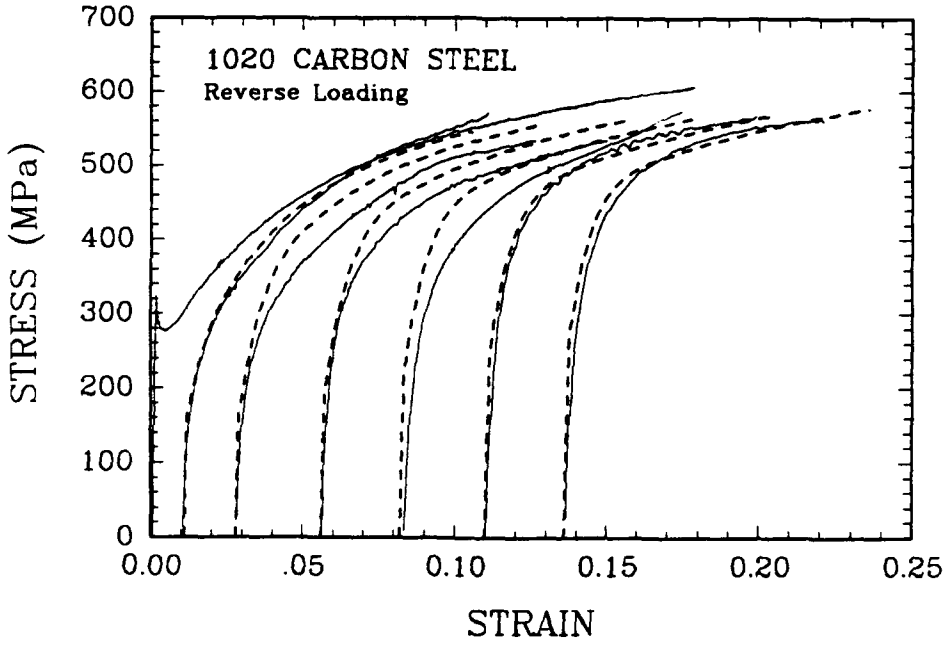

Figure 7.15 Comparison of model with reverse loading results for 1020 carbon steel. Solid curves are experiments, dashed curves are model.

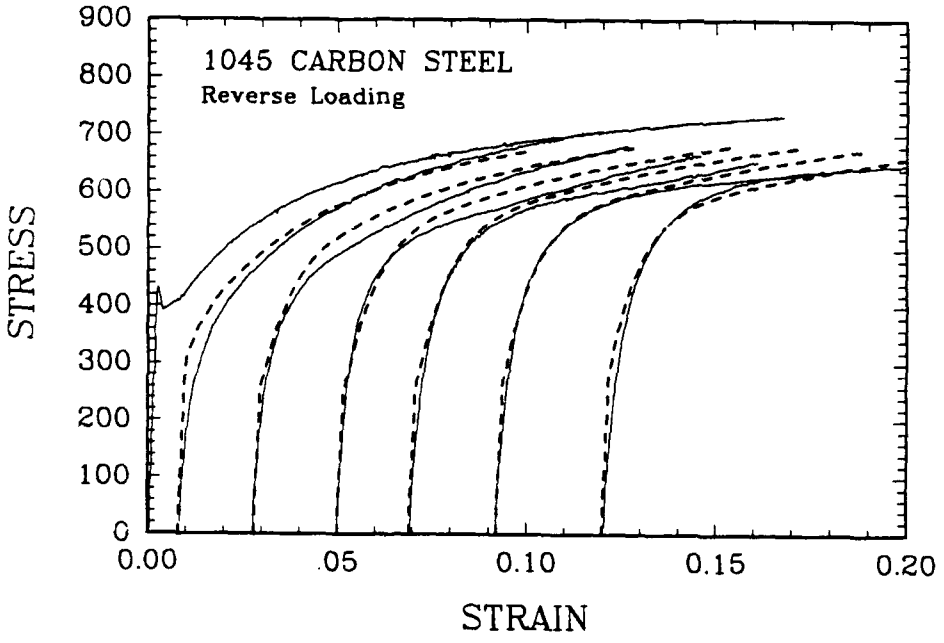

Figure 7.16 Comparison of model with reverse loading results for 1045 carbon steel. Solid curves are experiments, dashed curves are model.

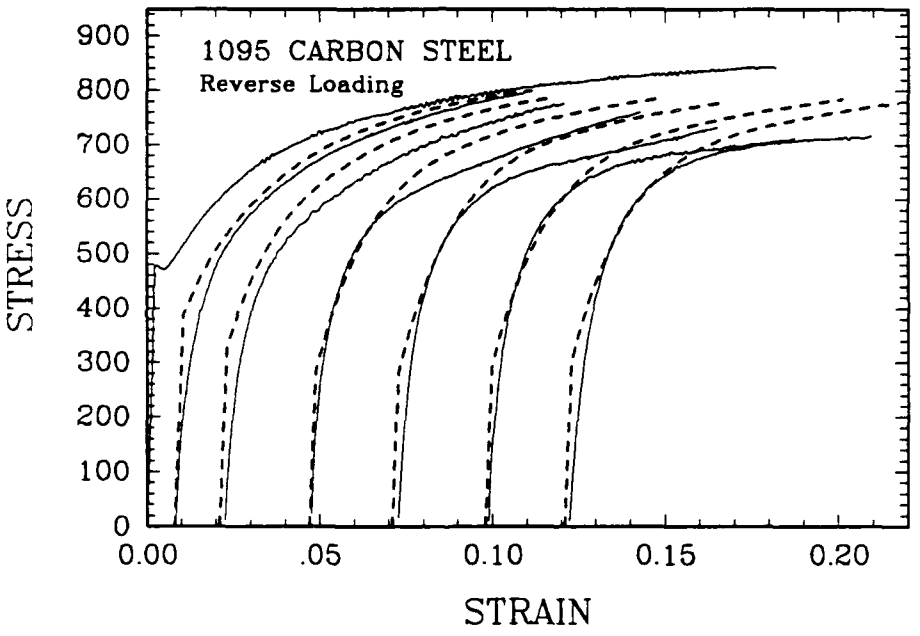

Figure 7.17 Comparison of model with reverse loading results for 1095 carbon steel. Solid curves are experiments, dashed curves are model.

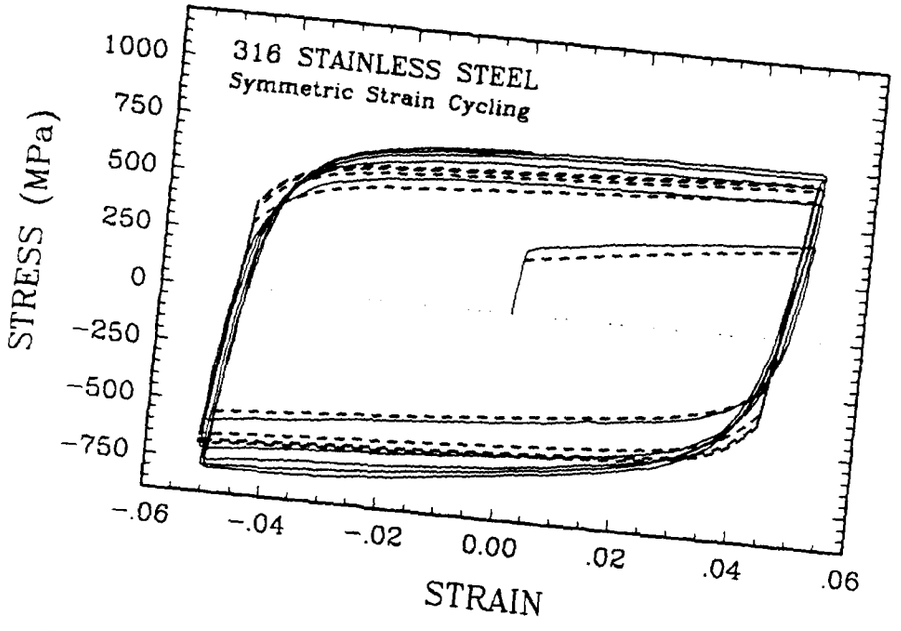

Figure 7.18 Comparison of model prediction and experimental results for $\pm 5\%$ symmetric strain cycling of 316 stainless steel. Solid curve is experiment, dashed curve is model.

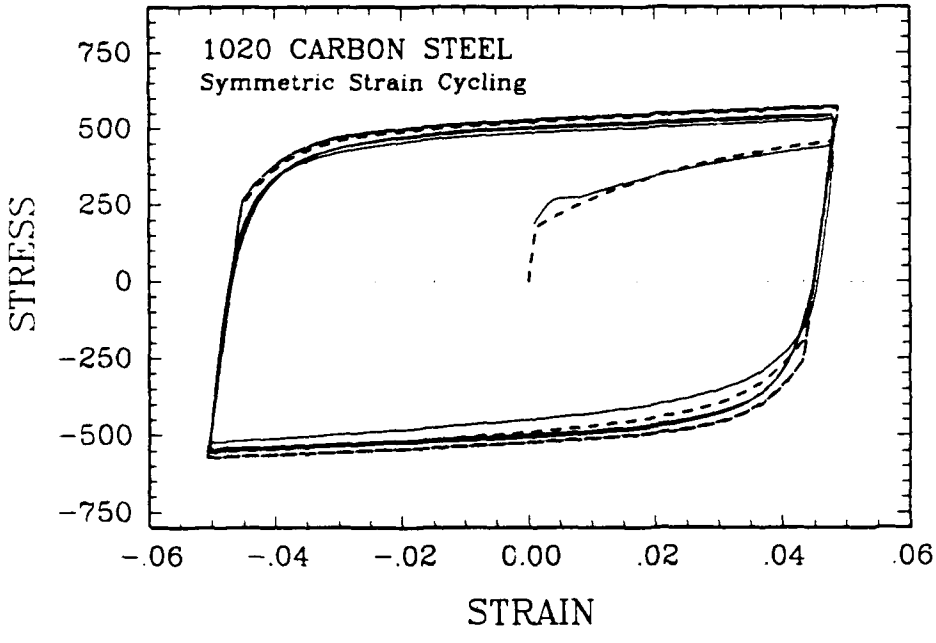

Figure 7.19 Comparison of model prediction and experimental results for ±5% symmetric strain cycling of 1020 carbon steel. Solid curve is experiment, dashed curve is model.

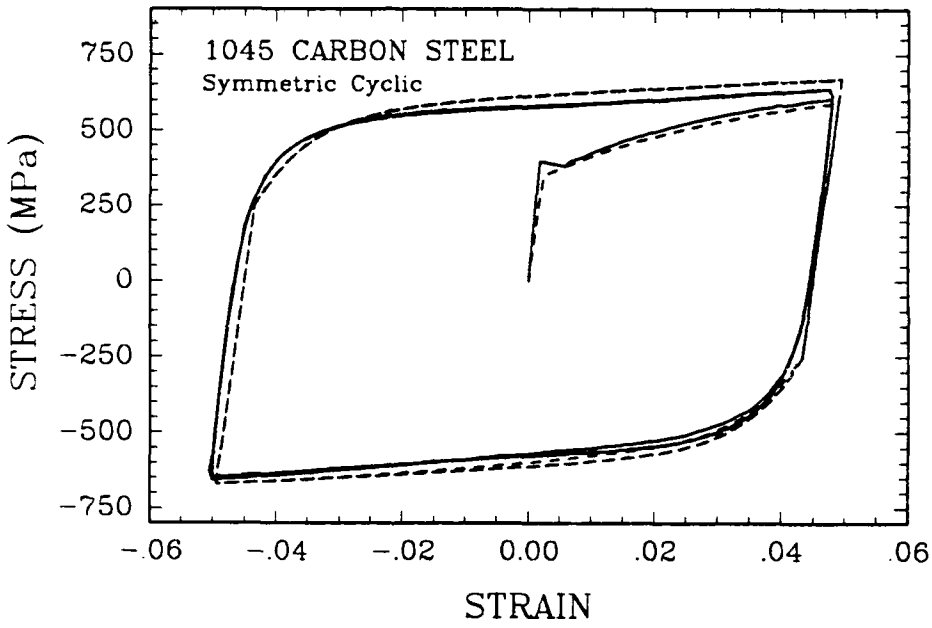

Figure 7.20 Comparison of model prediction and experimental results for ±5% symmetric strain cycling of 1045 carbon steel. Solid curve is experiment, dashed is model.

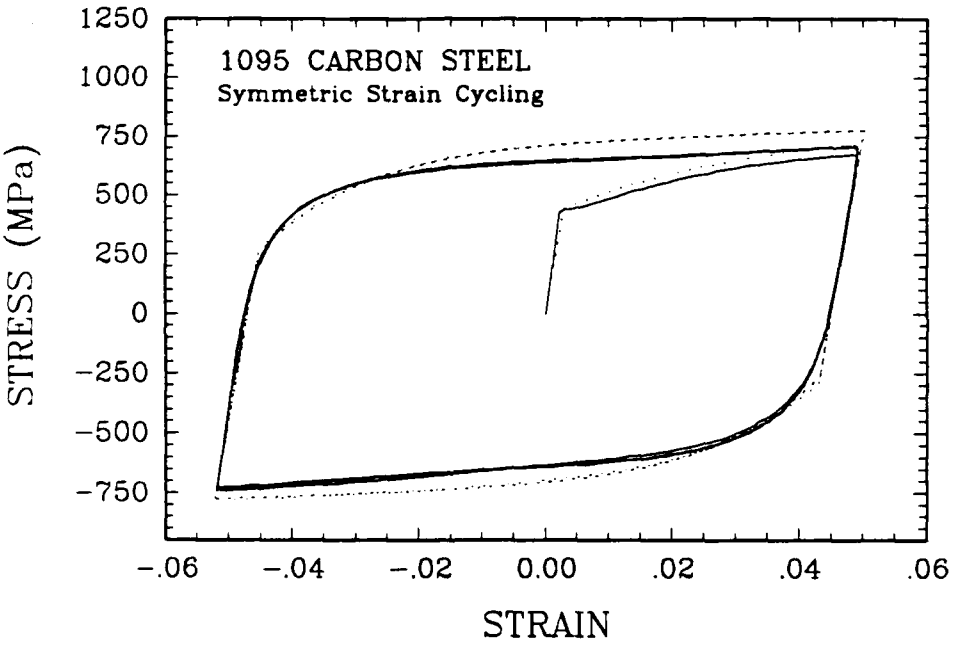

Figure 7.21 Comparison of model prediction and experimental results for ±5% symmetric strain cycling of 1095 carbon steel. Solid curve is experiment, dashed is model.

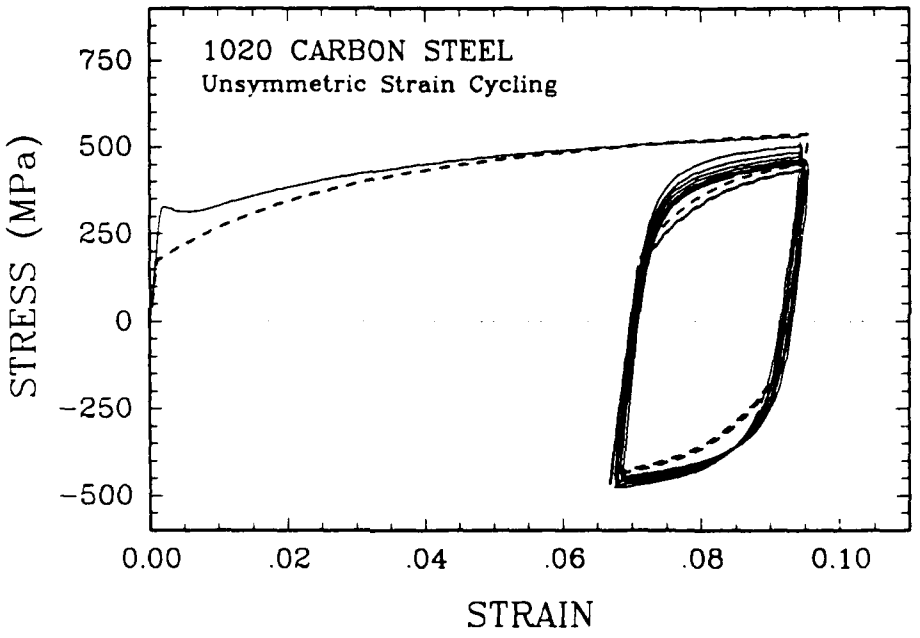

Figure 7.22 Comparison of model prediction and experimental results for unsymmetric strain cycling of 1020 carbon steel. Solid curve is experiment, dashed is model.

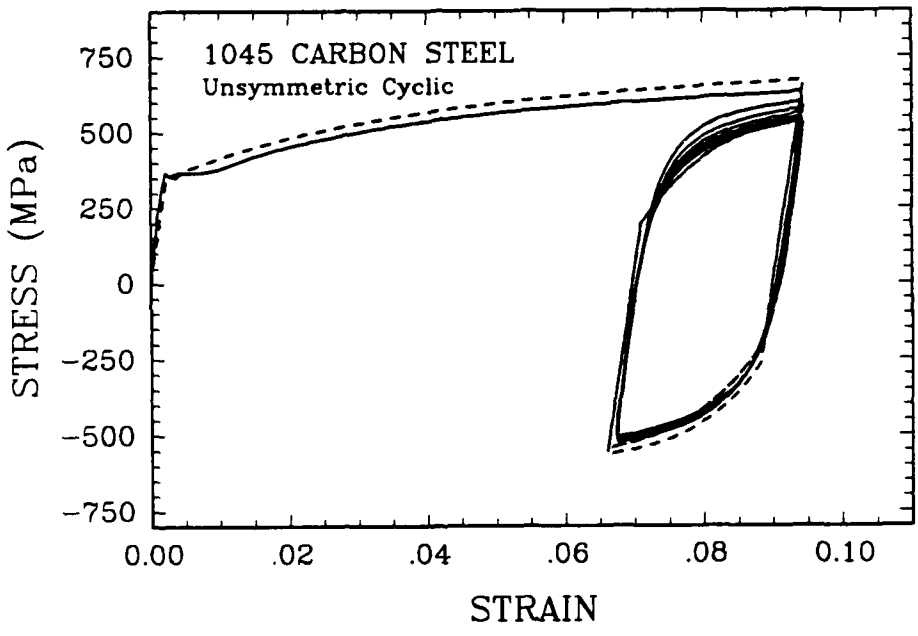

Figure 7.23 Comparison of model prediction and experimental results for unsymmetric strain cycling of 1045 carbon steel. Solid curve is experiment, dashed is model.

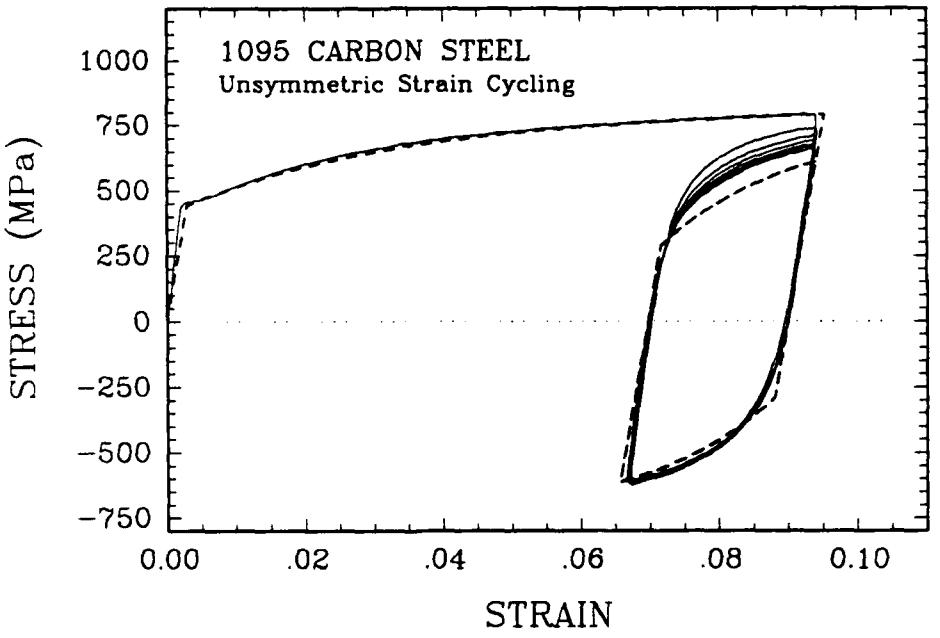

Figure 7.24 Comparison of model prediction and experimental results for unsymmetric strain cycling of 1095 carbon steel. Solid curve is experiment, dashed is model.

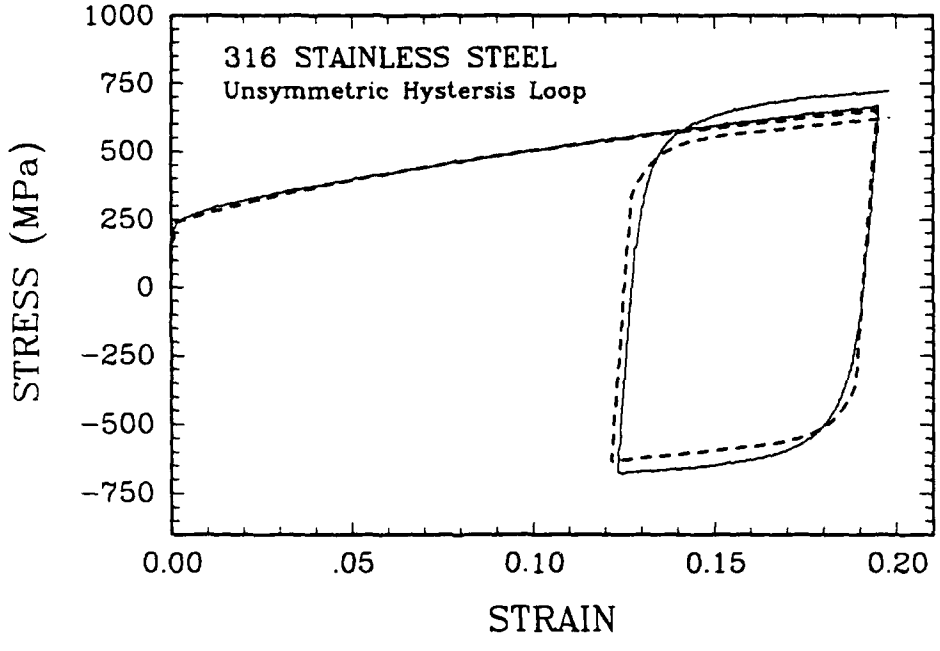

Figure 7.25 Comparison of model prediction and experimental results for unsymmetric hysteresis loop of type 316 stainless steel. Solid curve is experiment, dashed is model.

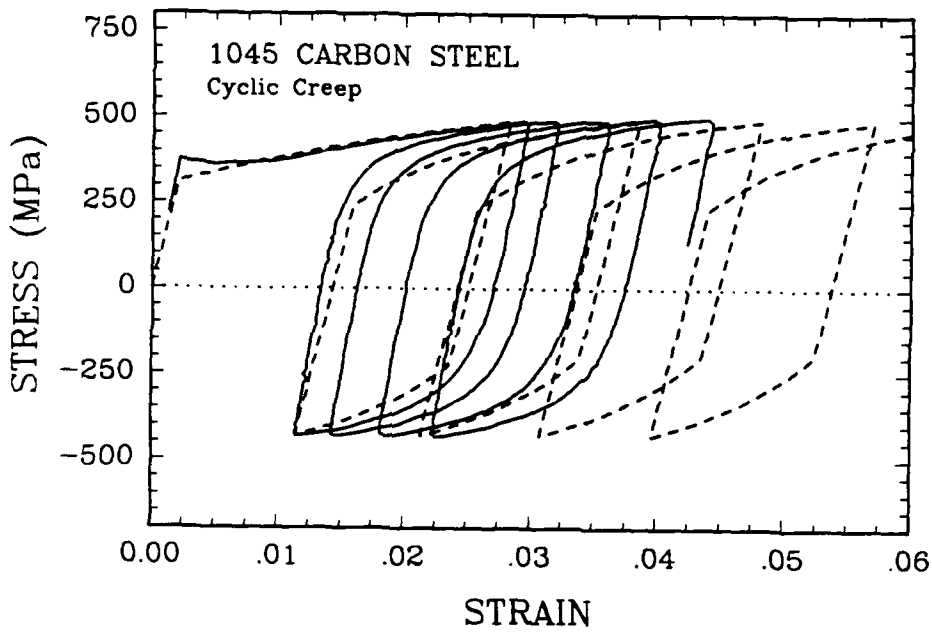

Figure 7.26 Comparison of model prediction and experimental results for unsymmetric stress cycling. Specimen was cycled between +490 Mpa and -430 Mpa. Solid curve is experiment, dashed curve is model.

(a)

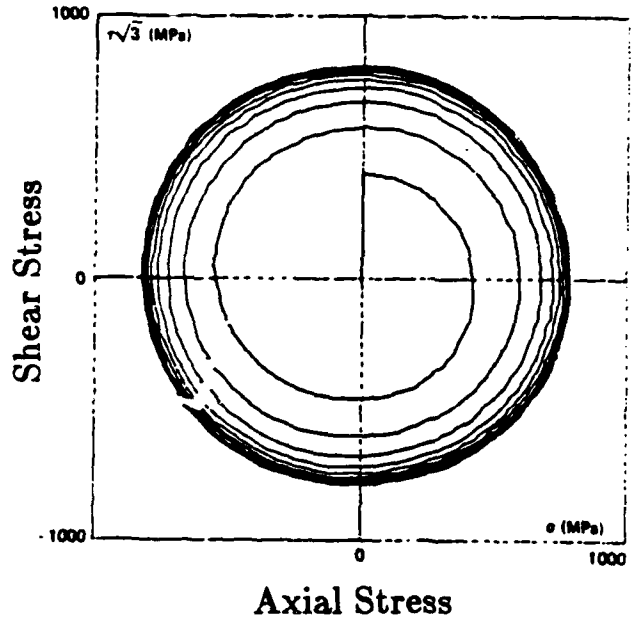

(b)

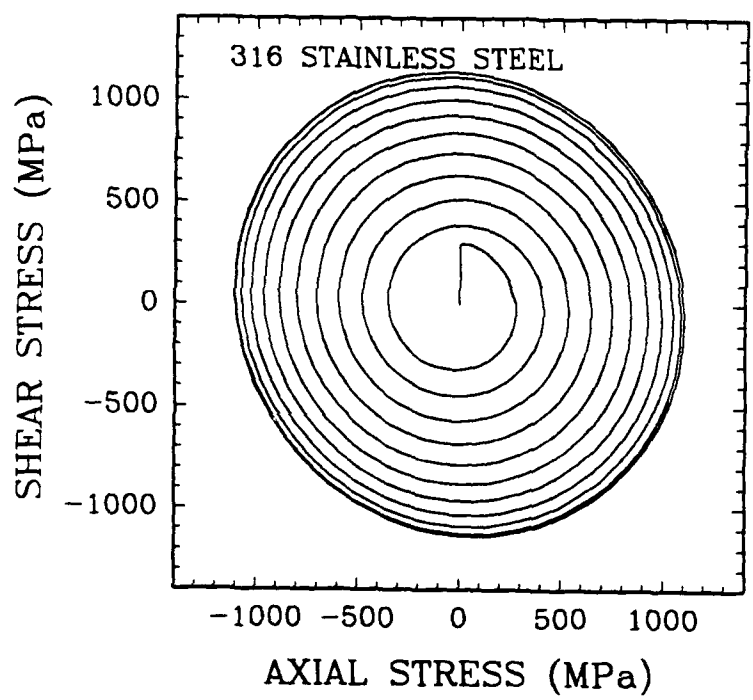

Figure 7.27 Stress response for 90° out-of-phase tension-torsion cycling of 316 stainless steel. a) Experimental results of Cailletaud et al. [1984]. b) Prediction of new model.

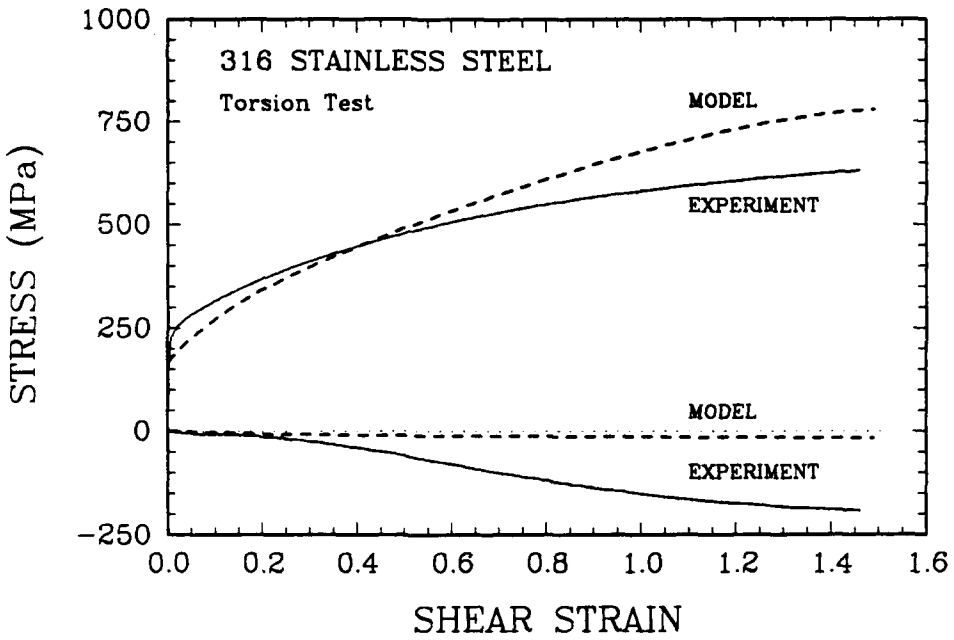

Figure 7.28 Comparison of model prediction and experimental results of the shear and normal stresses developed in a torison test of type 316 stainless steel. Solid curves are experiments, dashed curves are model.

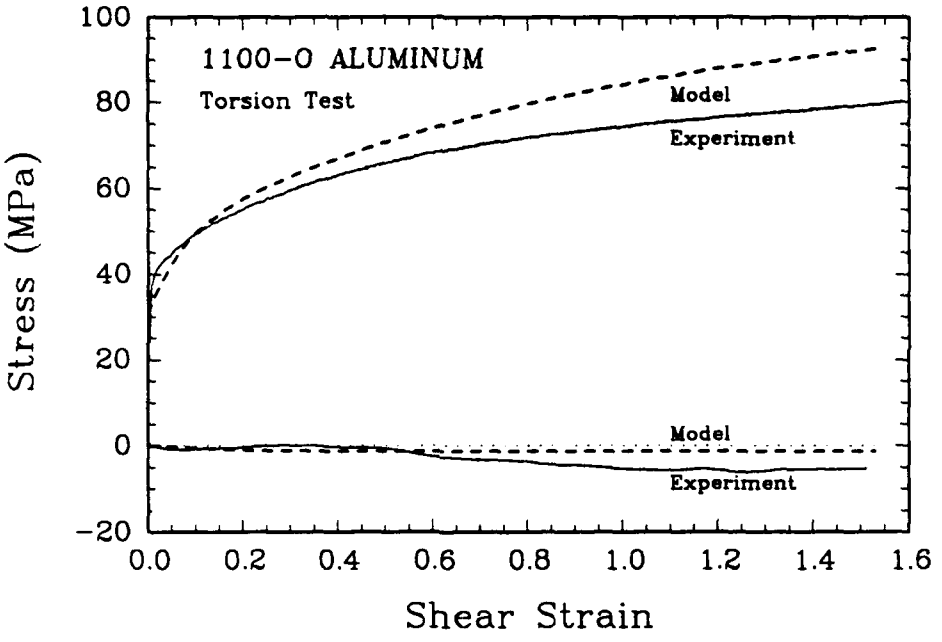

Figure 7.29 Comparison of model prediction and experimental results of the shear and normal stresses developed in a torsion test of 1100-O aluminum. Solid curves are experiments, dashed curves are model.

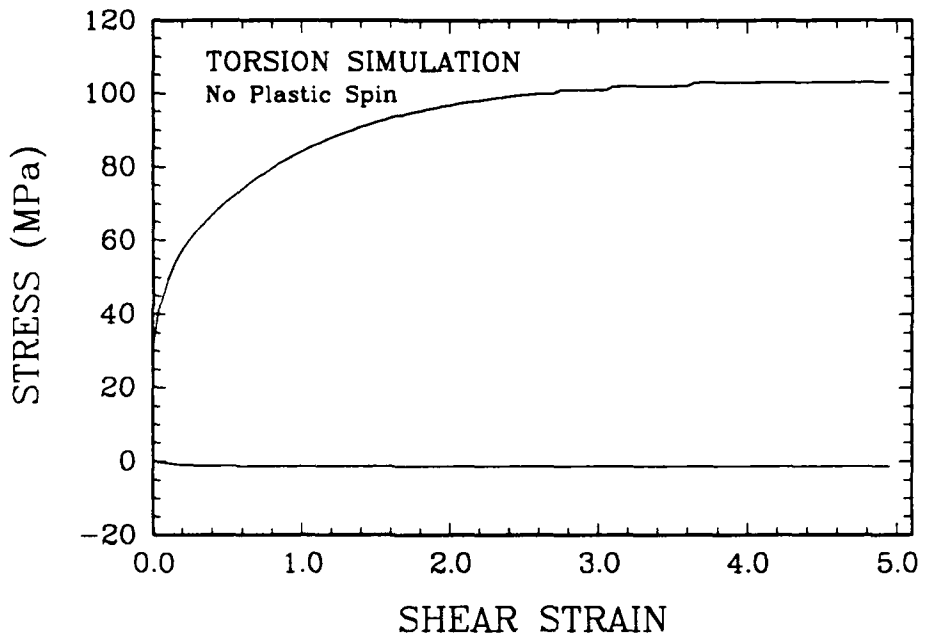

Figure 7.30 Prediction of new model for very large simple shear deformation. Constants simulate 1100-O aluminum (zero plastic spin).

Chapter 8

Conclusions

The major results of this study include: fundamental data from critical experiments, crucial observations of material behavior extracted from the literature, and a particular new constitutive model. The main new results are summarized below.

1. **Experimental results.** The experimental program has produced a variety of results from different types of tests. Two materials, 1100-O aluminum and 316 stainless steel were tested. The following experiments were performed: tension tests, large strain compression tests, single reverse tests, and large strain torsion tests. Additionally the 316 s.s. was tested in $\pm 5\%$ strain cycling and in a single unsymmetric hysteresis loop. This is a larger variety of tests for the same materials than have previously been available for constitutive modeling.

2. **Definition of the back stress variable.** The back stress variable, used so often in phenomenological modeling, can be connected to the residual stress due to plastic deformation on the microscopic scale. The residual stress is directly related to the reduced yield stress during load reversal, not to the observed "permanent softening". The back stress should be measured from a

small offset definition of yield (0.05 to 0.3 %) and not from back extrapolation of the linear portion of the reverse curve. Monotonicity of the isotropic hardening during forward loading limits how small the offset definition can be.

3. **Behavior of the back stress variable during reversing.** The back stress builds up quickly during uniaxial loading and approaches a saturation value at plastic strains on the order of 5% to 10%. The form of this build up can be approximately modeled by a decaying exponential. The initial build up actually occurs slightly more quickly than this. Upon reversal in the direction of the plastic strain rate, the back stress quickly reverses sign and approaches the same magnitude it had achieved during forward loading. The back stress reversal occurs more quickly than the initial build up and can not be adequately modeled by a simple evanescent evolution equation with constant coefficients.

4. **Behavior of the isotropic component.** The isotropic variable increases monotonically during proportional, monotonic loading. During a strain reversal the isotropic component exhibits softening. It decreases during the beginning of reverse plastic flow, goes through a minimum, then begins to increase again. This softening feature has not been previously investigated in plasticity modeling. *The permanent softening seen in single reverse tests is a result of isotropic softening* and not of the back stress in the material retaining its original direction as so often assumed. This behavior has been modeled using an isotropic softening function that is only active during a reversing event. The implications of this behavior are far reaching, especially for cyclic

plasticity. The stabilized cyclic loop reached in uniaxial cycling is a result of competition between the isotropic hardening and softening functions. This explains the strain amplitude dependence of the stabilized loop as well as the additional hardening observed in out-of-phase tension-torsion cycling.

5. **A new constitutive model.** The model developed in this thesis follows the trend of current plasticity modeling (decomposing into isotropic and kinematic portions, evanescent-type back stress evolution equation) with two important departures. The first is the introduction of the maximal back stress surface. This a surface defined by the maximum norm of the back stress that has occurred over the prior history of the deformation. This implies that the maximum back stress that has been achieved still affects the material response after the back stress has decreased. Its affect is erased once the back stress again increases to that previous value. This maximal back stress surface is used to define a "reversing event". During a reversing event the back stress modulus is variable and the isotropic component softens, as discussed above. This model captures a large variety of the observed experimental behavior involving cycling and load reversal. The only behavior that this model does not predict well is the large strain torsion results. The model overpredicts the shear stress and underpredicts the normal stress. For simple shear deformation this model reduces to a simple evanescent rule with isotropic hardening.

   The new model was applied to the experimental results using simple material functions. These can be seen in the evolution equations,

$$\mathbf{B}^{\nabla e} = \{C_{10} + KB_{max}(1-g) + \frac{2}{3}\hat{h}_2\}\,\mathbf{D}^p - C_2\,\dot{\bar{\epsilon}}^p\,\mathbf{B}, \tag{8.1}$$

$$\dot{s} = h_{10}(1 - \frac{s}{s^*})^q \dot{\epsilon}^p - \hat{h_2} \dot{\epsilon}^p, \tag{8.2}$$

where $\hat{h_2} = h_{20} B_{max}(s - s_o)(1 - g)$.

In summary, the model accurately reproduces the uniaxial behavior. Both for cyclic and montonic loading the model captures the material deformation. For out-of-phase cycling in tension-torsion the model also gives the correct qualitative results. It is only in large strain torsion that the model fails to well represent the behavior. This is attributed to the inadequacy of the evanescent term to model this very large strain behavior. However, with the constitutive model even for $\mathbf{W}^p = \mathbf{0}$ the shear stress does not oscillate at large shear strain.

Areas of fruitful future research can be identified. The first is to investigate the back stress behavior in large strain torsion. This can be done using reverse loading tests after various prestrains. These reversing tests are needed at large strain. This is not possible in tension-compression testing due to the geometry changes and inherent instability.

The material functions that were used in the correlations and predictions in this thesis were the simplest possible which retained the correct dependence on the independent variables. Other functions should be investigated to provide better fit to the shape of the reversing curves.

The effects of crystallographic texture have been ignored in this work. They become important at large enough levels of deformation. The limit of theories based upon isotropic functions should be investigated.

The effect of plastic spin could not be properly evaluated since the back stress behavior to large shear strain was not known with precision. Once the back stress

behavior at large shear strain is better known the importance of plastic spin can be addressed.

References

1864 TRESCA, H., *Memoire sur L'ecoulement des Corps Solides Soumis a des Fortes Pressions*, C. Rend. Paris, **59**, pp. 754.

1886 BAUSCHINGER, J., *On the change of the elastic limit and hardness of Iron and Steels through extension and compression, through heating and cooling, and through cycling*, Mitteilung aus dem Mechanisch , Technischen Laboratorium der K. Technische Hochschule in Munchen, **13**, Part 5, p. 31.

1923 MASING, G., Wiss. Ver. a. d. Siemens-Konzern, **3**, p. 231.

1926 MASING, G. and W. MAUKSCH, Wiss. Ver. a. d. Siemens-Konzern **5**, p. 142.

1927 SACHS, G. and H. SHOJI, *Bauschinger Effect in Brass*, Z. Physik, **45**, pp. 776-796.

1931 NADAI, A., **Plasticity**, McGraw-Hill, N.Y.

1943 BRIDGMAN, P.W., Transactions of the American Society of Metals, **32**, 1943, pp. 553.

1947 SWIFT, H.W., Engineering, **47**, pp. 253-257.

1950 HILL, R., **The Mathematical Theory of Plasticity**, Oxford University Press.

1950 RAHLFS, P. and G. MASING, Zeit f. Metallkunde, **41**, p. 454.

1953 BESSLING, J.F., *A Theory of Elastic, Plastic and Creep Deformation of an Initially Isotropic Material Showing Anisotropic Strain Hardening, Creep Recovery and Secondary Creep*, ASME Journal of Applied Mechanics, **25**, pp. 529-536.

1953 WOOLEY, R.L., *The Bauschinger Effect in Some Face-Centered and Body-Centered Cubic Metals*, Phil. Mag., **44**, pp. 597-618.

1956 PRAGER, W., *A New Method of Analyzing Stresses and Strains on Work-Hardening Plastic Solids*, ASME Journal of Applied Mechanics, **23**, pp. 493-496.

1958 WU, T.-M., Master of Science Thesis, Department of Mechanical Engineering, Massachusetts Institute of Technology, Cambridge, MA.

1959 LASZELO, F. and H. NOLLE, *On Some Physical Properties of Cementite*, Journal of the Mechanics and Physics of Solids, **7**, pp. 193-208.

1959 OROWAN, E., *auses and Effects of Internal Stresses*, **Internal Stresses and Fatigue in Metals**, General Motots Symposium, Elsevier, Amsterdam, pp. 59-80.

1959 ZIEGLER, H., *A Modification of Prager's Hardening Rule*, Quarterly of Applied Mathematics, **17**, pp. 55-65.

1960 CANAL, J.R., Master of Science Thesis, Department of Mechanical Engineering, Massachusetts Institute of Technology, Cambridge, MA.

1962 DEAK, G., *A Study of the Causes of the Bauschinger Effect*, Sc. D. Thesis, Department of Mechanical Engineering, Massachusetts Institute of Technology, Cambridge, MA.

1963 FELTNER, C.E., *Dislocation Arrangements in Aluminum Deformed by Repeated Tensile Stresses*, Acta Metallurgica, **11**, pp. 817-828.

1964 WILSON, D.V. and Y.A. KONNAN, *Work Hardening in a Steel Containing a Coarse Dispersion of Cementite Particles*, Acta Metallurgica, **12**, pp. 617-628.

1965 DOLAN, T.J., *Nonlinear Response Under Cyclic Loading Conditions*, **Proceedings of the Ninth Midwestern Mechanics Conference**, Madison, Wisconsin, pp. 3-21.

1965 MORROW, J. and F.R. TULER, *Low Cycle Fatigue Evaluation of Inconel 713C and Waspaloy*, ASME Series D, **87**, p. 275.

1965 WILSON, D.V., *Reversible Work Hardening in Alloys of Cubic Metals*, Acta Metallurgica, **13**, pp. 807-814.

1966 ABEL, A. and R.K. HAM, *The Cyclic Strain Behavior of Crystals of Aluminum-4 Wt % Copper - I. The Bauschinger Effect*, Acta Metallurgica, **14**, pp. 1489-1494.

1966 ARMSTRONG, P.J. and C.O. FREDERICK, *A Mathematical Representation of the Multiaxial Bauschinger Effect*, Central Electrical Generating Board Report RD/B/N 731.

1966 MORRISON, W.B., *The Effect of Grain Size on the Stress-Strain Relationship in Low Carbon Steel*, Transactions of the ASM, **59**, pp. 824-846.

1967 MROZ, Z., *On the Description of Anisotropic Workhardening*, Journal of the Mechanics and Physics of Solids, **15**, pp. 163-175.

1969 LEE, E.H., *Elastic-Plastic Deformations at Finite Strains*, Journal of Applied Mechanics, **36**, pp. 1-6.

1970 BUDIANSKY, B. Unpublished work.

1970 HIBBITT, H.D., MARCAL, P.V. and J.R. RICE, *A Finite Element Formulation for Problems of Large Strain and Large Displacement*, International Journal of Solids and Structures, **6**, pp. 1069-1086.

1970 WANG, C.C., *A New Representation Theorem for Isotropic Functions: An Answer to Professor G.F. Smith's Criticism of My Paper on Representations for Isotropic Functions*, **36**, pp. 198-223.

1971 MARUKAWA, K. and T. SANPEI, *Stability of the Work Hardened State Against Stress Reversal in Copper Single Crystals*, Acta Metallurgica, **19**, pp. 1169-1176.

1972 ABEL, A. and H. MUIR, *The Bauschinger Effect and Discontinuous Yielding*, Phil. Mag., **26**, pp. 489-504.

1972b ABEL, A. and H. MUIR, *The Bauschinger Effect and Stacking Fault Energy*, Phil. Mag., **26**, pp. 585-594.

1972 BAILEY, J.A., HAAS, S.L. and K.C. NAWAB, *Anisotropy in Plastic Torsion*, ASME Journal of Basic Engineering, March 1972, pp 231-237.

1972 NEEDLEMAN, A., *Void Growth in an Elastic-Plastic Medium*, ASME Journal of Applied Mechanics, pp. 964-970.

1973 HUTCHINSON, J.W., *Finite Strain Analysis of Elastic-Plastic Solids and Structures*, **Numerical Solution of Nonlinear Structural Problems**, R.F. Hartung ed., pp. 17-29.

1973 KISHI, T. and T. TANABE, *The Bauschinger Effect and its Role in Mechanical Anisotropy*, Journal of the Mechanics and Physics of Solids, **21**, pp. 303-315.

1973 TANAKA, K. MATSUOKA, S., SUZUKI, H. and T. NAKAMURA, *The Work Hardening Rate of Pearlitic Steel*, Scripta Metallurgica, **7**, pp. 799-802.

1974 ATKINSON, J.D. BROWN, L.M. and W.M. STOBBS, *The Work-Hardening of Copper-Silica IV. The Bauschinger Effect and Plastic Relaxation*, Phil. Mag. , **30**, pp. 1247.

1974 FARDSHISHEH, F. and E.T. ONAT, *Representation of Elastoplastic Behavior by Means of State Variables*, **Problems of Plasticity**, Sawczuk, A. ed., Leyden: Noordhoff, pp. 89-115.

1974 GOULD, D., HIRSCH, P.B. and F.J. HUMPHREYS, *The Bauschinger Effect, Work-Hardening and Recovery in Dispersion Hardened Copper Crystals*, Phil. Mag., pp. 1353-1377.

1974 HASEGAWA, T. and T. YAKOU, *Region of Constant Flow Stress During Compression of Aluminum Polycrystals Prestrained by Tension*, Scripta, Metallurgica, **8**, pp. 951-954.

1974 PHILLIPS, A., TANG, J.-L. and M. RICCIUTI, Acta Mechanica, **20**, pp. 23-39.

1974 STOLTZ, R.E. and R.M. PELLOUX, *Cyclic Deformation and Bauschinger Effect in Al-Cu-Mg Alloys*, Scripta Metallurgica, **8**, pp. 269-276.

1975 HASEGAWA, T., YAKOU, T. and S. KARASHIMA, *Deformation Behavior and Dislocation Structures Upon Stress Reversal in Polycrystalline Aluminum*, Material Science and Engineering, **20**, pp. 267-276.

1975 IBRAHIM, N. and J.D. EMBURY, *The Bauschinger Effect in Single Phase B.C.C. Materials*, Materials Science and Engineering, **19**, pp. 147-149.

1975 KRIEG, R.D., *A Practical Two Surface Plasticity Theory*, ASME Journal of Applied Mechanics, **47**, pp. 641-646.

1975 McMEEKING, R.M. and J.R. RICE, *Finiet-Element Formulations for Problems of Large Elastic-Plastic Deformation*, International Journal of Solids and Structures, **11**, pp. 601-616.

1975 MORI, T. and K. NARITA, *Decrease of Back Stress and Softening of Work Hardened Copper-Silica Crystals by Recovery*, Acta Metallurgica, **23**, pp. 85-91.

1976 ANAND, L. and J. GURLAND, *Strain-Hardening of Spheroidized High Carbon Steels*, **24**, pp. 901-909.

1976 DAFALIAS, Y.F. and E.P. POPOV, *Plastic Internal Variables Formalism of Cyclic Plasticity*, ASME Journal of Applied Mechanics, **43**, pp. 645-651.

1976 DIETER, G.E., **Mechanical Metallurgy**, 2nd Edition, McGraw-Hill.

1976 HECKER, S.S., *Experimental Studies of Yield Phenomena in Biaxially Loaded Metals*, **Constitutive Equations in Viscoplasticity**, ASME AMD Vol. 20, pp. 1-33.

1976 LIU, K.C. and W.L. GREENSTREET, *Experimental Studies to Examine Elastic-Plastic Behaviors of Metal Alloys Used in Nuclear Structures*, **Constitutive Equations in Viscoplasticity**, ASME AMD Vol. 20, pp. 35-56.

1976 MROZ, Z. SHRIVISTAVA, H.P. and R.N. DUBEY, *A Non-Linear Hardening Model and Its Application to Cyclic Loading*, Acta Mechanica, **25**, pp. 51-61.

1977 KEY, S.W., BIFFLE, J.H. and R.D. KRIEG, *A Study of the Computational and Theoretical Differences of Two Finite Strain Elastic-Plastic Models*, **Formulations and Computational Algorithms in Finite Element Analysis**, Bathe, Oden and Wunderlich, eds., Massachusetts Institute of Technology.

1977 LLOYD, D.J., *The Bauschinger Effect in Polycrystalline Aluminum Containing Coarse Particles*, Acta Metallurgica, **25**, pp. 459-466.

1977 PECKNER, D. and I.M. BERNSTEIN, **Handbook of Stainless Steels**, McGraw-Hill.

1978 CHANG, Y.W. and R.J. ASARO, *Bauschinger Effects and Work-Hardening in Spheroidized Steels*, Metal Science, pp. 277-284.

1978a LAMBA, H.S. and O.M. SIDEBOTTOM, *Cyclic Plasticity for Nonproportional Paths: Part 1 - Cyclic Hardening, Erasure of Memory, and Subsequent Strain Hardening Experiments*, ASME Journal of Engineering Materials and Technology, **100**, pp. 96-103.

1978b LAMBA, H.S. and O.M. SIDEBOTTOM, *Cyclic Plasticity for Nonproportional Paths: Part 2 - Comparison With Predictions of Three Incremental Plasticity Models*, ASME Journal of Engineering Materials and Technology, **100**, pp. 104-111.

1978 TVERGAARD, V., *Effect of Kinematic Hardening on Localized Necking in Biaxially Stretched Sheets*, International Journal of Mechanical Science, **20**, pp. 651-658.

1979 CHABOCHE, J.L., DANG VAN, K. and G. CORDIER, *Modelization of the Strain Memory Effect on the Cyclic Hardening of 316 S.S.*, SMIRT5, Div. L Berlin.

1979 CHRISTOFFERSEN, J. and J.W. HUTCHINSON, *A Class of Phenomenological Corner Theories of Plasticity*, Journal of the Mechanics and Physics of Solids, **27**, p. 465.

1979 DIENES, J.K., *On the Analysis of Rotation and Stress Rate in Deforming Bodies*, Acta Mechanica, **32**, pp. 217-232.

1979 KANAZAWA, K., MILLER, K.J. and M.W. BROWN, *Cyclic Deformation of 1% Cr-Mo-V Steel Under Out-of-Phase Loads*, Fatigue of Engineering Materials and Structures, **2**, pp. 217-228.

1979 KEY, S.W., KRIEG, R.D. and K.-J. BATHE, *On the Application of the Finite Element Method to Metal Forming Processes - Part I*, Computer Methods in Applied Mechanics and Engineering, **17/18**, pp. 597-608.

1979 PHILLIPS, A. and C.W. LEE, *Yield Surfaces and Loading Surfaces, Experiments and Recommendations*, International Journal of Solids and Structures, **15**, pp. 715-729.

1979 SOWERBY, R., UKO, D.K. and Y. TOMITA, *A Review of Certain Aspects of the Bauschinger Effect in Metals*, Materials Science and Engineering, **41**, pp. 43-58.

1980 LINDHOLM, U.S., NAGY, A., JOHNSON, G.R. and J.M. HOEGFELDT, *Large Striain, High Strain Rate Testing of Copper*, ASME Journal of Engineering Materials and Technology, pp. 376-381.

1980 UKO, D., SOWERBY, R. and J.D. EMBURY, *Bauschinger Effect in Structural Steels and Role in Fabrication of Line Pipe: Part 1 Analysis of Bauschinger Effect in Structural Steels*, Metals Technology, pp. 359-371.

1980 VALANIS, K.C., *Fundamental Consequence of a New Instrinsic Time Measure - Plasticity as a Limit of the Endocronic Theory*, Archives of Mechanics, pp. 171-191.

1980 WENG, G.J., *Constitutive Equations of Single Crystals and Polycrystalline Aggregates Under Cyclic Loading*, International Journal of Engineering Science, **18**, p.1385.

1981 DRUCKER, D.C. and L. PALGEN, *On Stress-Strain Relations Suitable for Cyclic and Other Loading*, ASME Journal of Applied Mechanics, **48**, pp. 479-485.

1981 MROZ, Z., *On Generalized Kinematic Hardening Rule with Memory of Maximal Prestress*, Journal de Mechanique Appliquee, **5**, pp. 241-259.

1981 PEDERSEN, O.B., BROWN, L.M. and W.M. STOBBS, *The Bauschinger Effect in Copper*, Acta Metallurgica, **29**, pp. 1843-1850.

1982 CANOVA, G.R., SHRIVASTAVA, S., JONAS, J.J., and C. G'SELL, *The Use of Torsion Testing to Assess Material Formability*, ASTM STP 753, pp. 189-210.

1982 GIL-SEVILLO, J., VAN HOUTTE, P. and E. AERNOUT, *Large Strain Work Hardening and Textures*, **Progress in Material Science**, Chrsitian, Haasen, and Massalski, eds., **25**, pp. 69-412.

1982 HECKER, S.S., STOUT, M.G. and D.T. EASH, *Experiments on Plastic Deformation at Finite Strains*, **Plasticity of Metals at Finite Strain: Theory, Experiment and Computation**, E.H. Lee and R.L. Mallett, eds., Proceedings of Research Workshop held at Stanford University, June 29 - July 1, 1981, pp. 162-205.

1982 KANEKO, K., OGAWA, K. and K. IWATA, *Evaluation of Inelastic Constitutive Models for Breeder Reactor Design Practices - Part I: Plasticity Models*, ASME PVP Special Publication, Orlando, Florida.

1982 NAGTEGAAL, J.C. and J.E. DEJONG, *Some Aspects of Non-Isotropic Workhardening in Finite Strain Plasticity*, Proceedings of the Workshop on Plasticity of Metals at Finite Strain: Theory, Experiment and Computation, E.H. Lee and R.L. Mallett, eds., Stanford University, pp. 55.

1982 SHRIVASTAVA, S.C., JONAS, J.J. and G. CANOVA, *Equivalent Strain in Large Deformation Torsion Testing: Theoretical and Practical Considerations*, Journal of the Mechanics and Physics of Solids, **30**, pp. 75-90.

1982 TVERGAARD, V., *On Localization in Ductile Materials Containing Spherical Voids*, International Journal of Fracture, **18**, pp. 237.

1983 ASARO, R.J., *Micromechanics of Crystals and Polycrystals*, **Advances in Applied Mechanics, 23**, p. 1.

1983 CHABOCHE, J.L. and G. ROUSSELIER, *On the Plastic and Viscoplastic Constitutive Equations. Part I: Rules Developed with Internal Variable Concept. Part II: Application of Internal Variable Concepts to the 316 Stainless Steel*, ASME Journal of Pressure Vessel Technology, **105**, pp. 153-164.

1983 CHAIT, R. and R. PAPIRNO, **Compression Testing of Homogeneous Materials and Composites**, ASTM STP 808.

1983 HOSFORD, W.F. and R.M. CADDELL, **Metal Forming, Mechanics and Metallurgy**, Prentice-Hall.

1983 LEE, E.H., MALLETT, R.L. and T.B. WERTHEIMER, *Stress Analysis for Anisotropic Hardening in Finite-Deformation Plasticity*, ASME Journal of Applied Mechanics, **50**, pp. 554-560.

1983 LORET, B., *On the Effect of Plastic Rotation in the Finite Deformation of Anisotropic Elastoplastic Materials*, Mechanics of Materials, **2**, pp. 287-304.

1983 LOWE, T.C. and A.K. MILLER, *The Nature of Directional Strain Softening*, Scripta Metallurgica, **17**, pp. 1177-1182.

1983 MROZ, Z., *Hardening and Degradation Rules for Metals Under Monotonic and Cyclic Loading*, ASME Journal of Engineering Materials and Technology, **105**, pp. 113-118.

1983 TSENG, N.T. and G.C. LEE, *Simple Plasticity Model of Two-Surface Type*, ASCE Journal of Engineering Mechanics, **109** , pp. 795-810.

1984 ABAQUS Theory Manual, version 4.6, Hibbitt, Karlsson and Sorensen, Inc., Providence, RI.

1984 BELL, J.F., **Mechanics of Solids: Volume 1, The Experimental Foundations of Solid Mechanics**, Germany, Springer-Verlag.

1984 CAILLETAUD, G., KACZMAREK, H. and H. POLICELLA, *Some Elements on Multiaxial Behavior of 316L Stainless Steel at Room Temperature*, Mechanics of Materials, **3**, pp. 333-347.

1984a DAFALIAS, Y.F., *A Missing Link in the Formulation and Numerical Implementation of Finite-Transformation Elastoplasticity*, **Constitutive Equations: Macro and Computational Aspects**, William, K.J., ed., ASME, pp.25-40.

1984b DAFALIAS, Y.F., *Modelling Cyclic Plasticity: Simplicity Versus Sophistication*, **Mechanics of Engineering Materials**, C.S. Desai and R.H. Gallagher, eds., Wiley.

1984c DAFALIAS, Y.F., *The Plastic Spin Concept and a Simple Illustration of Its Role in Finite Plastic Transformations*, Mechanics of Materials, **3**, pp. 223-233.

1984 JOHNSON, G.C. and D.J. BAMMAN, *A Discussion of Stress Rates in Finite Deformation Problems*, International Journal of Solids and Structures, **20**, pp. 725-737.

1984 KREMPL, E. and H. LU, *The Hardening and Rate-Dependent Behavior of Fully Annealed AISI Type 304 Stainless Steel Under Biaxial In-Phase and Out-of-Phase Strain Cycling at Room Temperature*, ASME Journal of Engineering Materials and Technology, **106**, pp. 376-382.

1984 LOWE, T.C. and A.K. MILLER, *Improved Constitutive Equations for Modeling Strain Softening - Part I: Conceptual Development*, ASME Journal of Engineering Materials and Technology, **106**, pp. 337-342.

1984 MONTHEILLET, F., COHEN, M. and J.J. JONAS, *Axial Stresses and Texture Development During the Torsion Testing of Al, Cu and α-Fe*, Acta Metallurgica, **32**, pp. 2077-2089.

1984 PHILLIPS, A. and W.-Y. LU, *An Experimental Invegation of Yield Surfaces of Pure Aluminum with Stress-Controlled and Strain-Controlled Paths of Loading*, ASME Journal of Engineering Materials and Technology, **106**, p. 349.

1985 ANAND, L., *Constitutive Equations for Hot-Working of Metals*, International Journal of Plasticity, **1**, pp. 213-232.

1985 CANOVA, G.R., KOCKS, U.F., TOME, C.N. and J.J. JONAS, Journal of the Mechanics and Physics of Solids, **33**, p. 371.

1985a DAFALIAS, Y.F., *The Plastic Spin*, ASME Journal of Applied Mechanics, **52**, pp. 865-871.

1985b DAFALIAS, Y.F., *A Missing Link in the Macroscopic Constitutive Formulation of Large Plastic Deformations*, **Plasticity Today**, Sawxzuk, A., Bianchi, G., eds., Elsevier.

1985 MCDOWELL, D.L., *An Experimental Study of the Structure of Constitutive Equations for Nonproportional Cyclic Plasticity*, ASME Journal of Engineering Materials and Technology, **107**, pp. 307-315.

1985 NOUHAILHAS, D., CHABOCHE, J.L., SAVALLE, S. and G. CAILLETAUD, *On the Constitutive Equations for Cyclic Plasticity Under Nonproportional Loading*, International Journal of Plasticity, **1**, pp. 317-330.

1985 OGAWA, K., *Mechanical Behavior of Metals Under Tension-Compression Loading at High Strain Rate*, International Journal of Plasticity, **1**, pp. 347-358.

1985 PAULUN, J.E. and R.B. PECHERSKI, *Study of Corotational Rates for Kinematic Hardening in Finite Deformation Plastictiy*, Archives of Mechanics, **37**, pp. 661-677.

1985 REED, K.W. and S.N. ATLURI, *Constitutive Modeling and Computational Implementation in Finite Strain Plasticity*, International Journal of Plasticity, **1**, pp. 63-87.

1985 STOUT, M.G., MARTIN, P.L., HELLING, D.E. and G.R. CANOVA, *Multiaxial Yield Behavior of 1100 Aluminum Following Various Magnitudes of Prestrain*, International Journal of Plasticity, **1**, pp. 163-174.

1985 SWEARENGEN, J.C. and J.H. HOLBROOK, *Internal Variable Models for Rate-Independent Plasticity: Analysis of Theory and Experiment*, Res Mechanica, **13**, pp. 93-128.

1986 BATE, P.S. and D.V. WILSON, *Analysis of the Bauschinger Effect*, Acta Metallurgica, **34**, pp. 1097-1105.

1986 CHABOCHE, J.L., *Time-Independent Constitutive Theories for Cyclic Plasticity*, International Journal of Plasticity, **2**, pp. 149-188.

1986 DIENES, J.K., *A Discussion of Material Rotation and Stress Rate*, Acta Mechanica, **65**, pp. 1-11.

1986 HAGHI, M., *Deformation Behaviour of Iron Based ODS Superalloy MA956*, Master of Science Thesis, Massachusetts Institute of Technology, Cambridge, MA, June, 1986.

1986 HAUPT, P. and C. TSAKMAKIS, *On Kinematic Hardening and Large Plastic Deformations*, International Journal of Plasticity, **2**, pp. 279-293.

1986 HELLING, D.E., MILLER, A.K. and M.G. STOUT, *An Experimental Investigation of the Yield Loci of 1100-O Aluminum, 70:30 Brass, and an Overaged 2024 Aluminum Alloy After Various Prestrains*, ASME Journal of Engineering Materials and Technology, **108**, pp. 313-320.

1986 LU, W.-Y., *Plastic Flow Under Multiaxial Cyclic Loading*, Experimental Mechanics, **26**, pp. 224-229.

1986 WANTANABE, O. and S.N. ATLURI, *Internal Time, General Internal Variable, and Multi-Yield-Surface Theories of Plasticity and Creep: A Unification of Concepts*, International Journal of Plasticity, **2**, pp. 37-57.

1986 WILSON, D.V. and P.S. BATE, *Reversibility in the Work Hardening of Spheroidised Steels*, Acta Metallurgica, **34**, pp. 1107-1120.

1987 AGAH-TEHRANI, A., LEE, E.H., MALLETT, R.L. and E.T. ONAT, *The Theory of Elastic-Plastic Deformation at Finite Strain with Induced Anisotropy Modeled as Combined Isotropic-Kinematic Hardening*, Journal of the Mechanics and Physics of Solids, **35**, pp. 519-539.

1987 BENALLAL, A. and D. MARQUIS, *Constitutive Equations for Nonproportional Cyclic, Elasto-Viscoplasticity*, ASME Journal of Engineering Materials and Technology, **109**, pp. 326-336.

1987 BROWN, S.B., *An Internal Variable Constitutive Model for the Hot Working of Metals*, Ph.D. Thesis, Massachusetts Institute of Technology, April, 1987.

1987 CHU, C.-C., *The Analysis of Multiaxial Cyclic Problems with an Anisotropic Hardening Model*, International Journal of Solids and Structures, **23**, pp. 569-579.

1987 DAFALIAS, Y.F., *Issues on the Constitutive Formulation at Large Elastoplastic Deformations, Part I: Kinematics*, Acta Mechanica, **69**, pp. 119-138.

1987 KOBAYASHI, H. and B. DODD, *Estimation of Errors in Torsion Testing*, Res Mechanica, **20**, pp. 163-175.

1987 LIPKIN, J., CHIESA, M.L. and D.J. BAMMANN, *Thermal Softening of 304L Stainless Steel: Experimental Results and Numerical Simulations*, Proceedings of IMPACT '87, Bremen, FRG, May, 1987.

1987 MCDOWELL, D.L., *An Evaluation of Recent Developments in Hardening and Flow Rules for Rate-Independent, Nonproportional Cyclic Plasticity*, ASME Journal of Applied Mechanics, **54**, pp. 323-334.

1987 NEEDLEMAN, A., *A Continuum Model for Void Nucleation by Inclusion Debonding*, ASME Journal of Applied Mechanics, **54**, p. 525.

1987 PAULUN, J.E. and R.B. PECHERSKI, *On the Application of the Plastic Spin Concept for the Description of Anisotropic Hardening in Finite Deformation Plasticity*, International Journal of Plasticity, **3**, pp. 303-314.

1988 ASTM Standard E209-65, American Society of Testing and Materials.

1988 BOYCE, M.C., WEBER, G.G. and D.M. PARKS, *On the Kinematics of Finite Strain Plasticity*, Submitted to the Journal of the Mechanics and Physics of Solids.

1988 BRONKHORST, C., *A Study of the Bauschinger Effect and Cyclic Plasticity in Spheroidized Steels*, Master of Science Thesis, Massachusetts Institute of Technology, Cambridge, MA, March, 1988.

1988 MEGAHED, M.M., *A Critical Examination of Nesting, Bounding and Memory Surface/s Plasticity Theories Under Nonproportional Loading Conditions*, International Journal of Mechanical Engineering Science, **30**, pp. 101-118.

1988 TRAMPCZYNSKI, W., *The Experimental Verification of the Evolution of Kinematic and Isotropic Hardening in Cyclic Plasticity*, Journal of the Mechanics and Physics of Solids, **36**, pp. 417-441.

Appendix A

Finite Strain Experimentation

Experimental results for deformation to large strain have been obtained in the past century for many different metals under a variety of deformation modes. Certainly a tremendous amount of metal working has been done over the course of human history. Many significant technological advances have been a direct result of man's increasing ability to work metal. The industrial revoltion was only made possible by iron and steel fabrication.

Metal working has also been used to try to extract material properties and behavior. Tresca [1864] postulated the yield condition that bears his name by analyzing a series of metal extrusion experiments. Unfortunately the deformation histories for most formed parts are highly nonhomogeneous and do not easily lend themselves to material stress-strain evaluation.

Homogeneous deformation modes are the most preferrable for obtaining the stress-strain response of the material. Stress is invariably inferred by taking measured loads on the specimen and dividing by an appropriate area to obtain the average stress in the specimen. Strain is similarly measured by a displacement over a certain portion of the specimen which is then normalized to give the average strain in a region. For these averaged values to be representative of the pointwise material behavior the stress and strain must be fairly uniform in the region where the measurements are made.

The most common testing modes which have a homogeneous deformation are: uniaxial tension, biaxial tension, compression, and torsion of thin-walled tubular

specimens. In each of these tests the stresses and strains are 'uniform' throughout the gauge region.

The biggest problem to obtaining useful experimental results for large strain deformation is the significant geometry changes that generally accompany flow. A discussion of many of the limitations of different testing modes is given in a recent review by Hecker, Stout and Eash [1982].

A number of inhomogeneous and indirect tests have also been used to infer large strain results. Two such tests having inhomogeneous deformation are the solid rod torsion test and the post necking tensile test. Analysis techniques are available (Bridgman [1943], Nadai [1931]) to obtain the stress-strain results but certain assumptions are made about the material behavior which are too restrictive.

Indirect tests have been used to obtain results to the very largest strains. An indirect test is one in which the specimen is deformed in some mode such as wire drawing or plate rolling to a large prestrain. It is then unloaded and the effect of the prestrain is determined by testing in a mode where the yield can easily be determined such as uniaxial tension. The locus of these yield stresses for various prestrains is plotted as a stress-strain result. This type of analysis makes many assumptions about the material behavior and is not appropriate for studying the details of that behavior.

Of the direct, homogeneous testing techniques the two which have seen the most effective use are the uniaxial compression and thin-walled torsion tests. The tensile test is by far the most widely used mechanical test to determine yield strengths but it suffers from the geometric instability of necking. Few metals can be strained in tension to even 40 or 50% strain before the localization occurs. Most metals can

not even sustain that much tensile strain. The strain hardening rate of the material controls this instability point.

Uniaxial compression is used extensively to obtain flow stress values at large strain (Brown [1987], Chait and Papirno [1983]). Solid, cylindrical specimens are compressed between smooth, flat platens in a controlled manner to obtain strains approaching 100%. This strain range can even be increased by remachining the specimens. Initially a specimen should have a length to diameter ratio of 1.5 to 1.6 . If it is larger than this plastic buckling may occur. During compression it is important to maintain adequate lubrication between the specimen and platen. This is necessary to achieve uniform straining and to prevent barrelling. The specimen undergoes large geometry changes during compression. To achieve a true (logarithmic) strain of -100% the specimen must by compressed to 37% of its original height. Nonetheless a significant amount of compression data is available in the literature (Hecker, Stout and Eash [1982]; Gil Sevillano, van Houtte and Aernoudt [1982]).

The other testing mode used to generate a significant amount of large strain data is torsion. The torsion test involves twisting a cylindrical specimen and recording the torque required as a function of twist angle. For solid specimens, as noted above, the reduction of the torque/twist to stress-strain results is very restrictive. For example it is known that when twisting a specimen to large shear strain there is a coupling between the response in the shear and axial direction. A specimen that is unrestrained in the axial direction will elongate (Swift [1947]) and a specimen prevented from elongating axially will develop either tensile or compressive stresses [Montheillet, Cohen and Jonas, 1984]. The magnitude of these axial effects are important material characterizing parameters as will be demonstrated later in this

report.

If we consider a solid rod twisted plastically but unconstrained against axial motion the specimen will tend to elongate. The amount of axial strain is a function of the shear strain that the material point has experienced. But the shear strain of a solid rod varies from zero at the centerline to a maximum at the surface. The axial strain should also vary with radial position in a similar manner. That would violate the symmetry requirements that plane cross section must remain plane. The only way that this deformation can be accomodated is for the entire cross section to experience an "average" axial strain accompained by a residual stress state that varies with radial position and sums to zero force on the cross section. The solid rod thus has a nonuniform stress in the axial direction and the axial extension it experiences is not a simple material function of the state of any single material point in the rod. This example shows how the solid rod torsion test gives ambiguous results for the free end condition and a similar argument can be made about the fixed end condition.

The torsion of a thin-walled tubular specimen does not have these limitations. If a specimen gauge length is made up of a cylindrical tubular section having a sufficiently large ratio of diameter to wall thickness then the stress and strain across the wall thickness then the stress and strain across the wall thickness will be quite uniform. For pure torsion the shear strain varies linearly with radial position, r.

$$\gamma_{\theta z} = r\frac{d\phi}{dl},$$

where $\gamma_{\theta z}$ is the engineering shear strain, and $\frac{d\phi}{dl}$ is the twist angle per unit length in the gauge section. When the wall is sufficiently thin the variation in strain is small.

$$\frac{\Delta\gamma_{\theta z}}{\gamma_{\theta z}} = \frac{\Delta r}{r},$$

so,

$$\frac{\Delta\gamma_{\theta z}}{\tilde{\gamma_{\theta z}}} \approx \frac{1}{\frac{1}{2}\frac{OD}{t}},$$

where $\tilde{\gamma_{\theta z}}$ is the strain at the mean radius $\tilde{r} = \frac{1}{2}(r_{inside} + r_{outside})$. Here $\frac{OD}{t}$ is the ratio of the outside diameter to wall thickness and is a measure of the appropriateness of the thin-wall approximation. The values of $\frac{OD}{t}$ for tests reported in the literature are often around 15. A discussion of ways to estimate errors in torsion testing is given by Kobayashi and Dodd [1987].

Not only does the thin-wall torsion test provide a relatively homogeneous deformation state but when the test is run with a fixed restraint in the axial direction the specimen's dimensions do not change. The shear strain is then directly proportional to the twist angle of the actuator and the shear and normal stresses are proportional to the torque and axial load, respectively. These tests provide a suitable method of obtaining large strains although not with uniaxial stress due to the presence on the normal stresses which are developed.

If a torsion test is run without axial restraint then the specimen will either elongate or shorten. The diameter of the specimen will also change and the simple expression used to determine shear strain is no longer valid.

One experimental difficulty in twisting tubular specimens to large strain is their tendency to buckle. This problem is one of the reasons that much of the torsion results in the literature are derived from solid specimens. Some researchers have tried to suppress buckling by inserting lubricated mandrels into the specimen centers (Helling, Miller and Stout [1986]). To circumvent this problem Bailey, Haas

and Nawab [1972] and Lindholm et al. [1980] developed a torsion specimen design having large shoulders and a short gauge section. With this design large strains are achievable on testing machines having a limited angle of rotation since the twist is concentrated in the small gauge region. This also inhibits the torsional buckling modes since the large shoulders are close to one another. The only questionable aspect of this design would be whether there is a significant stress-strain concentration where the shoulders and gauge region meet. Scribe lines used as markers on the gauge length show quite uniform shear strain in that region with an abrupt transition to rigid conditions with no localization at the shoulders. This is also verified by finite element calculations (Lipkin, Chiesa and Bamman [1987]).

For this short gauge length specimen the deformation is well approximated by simple shear. By not allowing the specimen to elongate, the volume of the tube remains constant. The thick shoulders prevent a change in specimen diameter and allow the normal stresses which are predicted in simple shear to be sustained.

This specimen should not be used as a free end test in which the length is allowed to change due to the torsion. That requires the specimen diameter to change but since the large shoulders restrain against that there would be a severe gradient along the short gauge length. The gauge section would not be seeing uniform strain and spurious behavior would result. The experimental results could not be analyzed by a homogeneous theory. Lipkin, Chiesa and Bammann [1987] have run tests of this type and note that there is little difference between the results for specimens with the free or with the fixed end conditions. One difficulty with this result is the axial compliance in their test system. Even for their constrained condition they measure quite small magnitudes of axial strain in the gauge section which would relieve the

axial stress. In reality, their 'fixed' end condition was very much closer to a free end condition than it was to being rigid.

The vast majority of large strain experimental results in torison are determined from tests on solid rods with unspecified end constraint (Dieter [1976]). These results are of limited value in detailled constitutive modeling but they do give a qualitiative idea of the flow strength level.

One effect seen consistently in large strain testing is that the equivalent stress versus equivalent strain curve determined in torsion falls beneath that determined in compression (Hecker, Stout and Eash [1982]). The equivalent stress is given by $\tilde{\sigma} = (\frac{3}{2}\boldsymbol{T}' \cdot \boldsymbol{T}')^{\frac{1}{2}}$ and the equivalent strain by $\tilde{\epsilon} = \int (\frac{2}{3}\ \boldsymbol{D}^p \cdot \boldsymbol{D}^p)^{\frac{1}{2}} dt$. In comparing different tests in this manner the implicit assumption is being made that the material can be described by a *universal* curve. This is the assumption of isotropic hardening plasticity. Much of the thinking in metal plasticity has historically been in terms of isotropic hardening.

Montheillet, Cohen and Jonas [1984] have applied the theory of crystallographic texture development to describe how axial stresses are generated in torsion at very large strains. The experiments that they compared with were conducted on solid rod specimens twisted to equivalent strains of $\tilde{\epsilon} = 4$ to 10. These strains truly are large and require accounting for crystallographic orientation. The axial stress development at these strains is attributed to a tilting of the yield surface (Canova, Kocks, Tome and Jonas [1985]). This tilting can be considered a permanent rotation of the yield surface with respect to the loading direction, or in rate form, a plastic spin of the material. The macroscopic shearing causes a small spin or rate of rotation of the underlying microstructure of the material.

The effect of a lower flow stress in torsion is seen at strains much less than these where crystallographic texture is important. This has been a major motivation for the work presented in this thesis. The traditional ideas of isotropic hardening can not account for this yet much of the large plastic deformation in manufacturing or ballistic penetration is done under a shearing action where this discrepancy is seen. A better model of these experimentally observed results is sought in this work.

Appendix B

Review of Cyclic Plasticity Modeling

Prager-Ziegler kinematic hardening has the simplest explicit evolution equation for the back stress.

$$\dot{\mathbf{B}} = C\mathbf{D}^p.$$

Here **B** is the back stress, $\mathbf{D}^p$ the plastic stretching and C is generally a constant (linear hardening). This is the most common theory employing a back stress and has been incorporated into most nonlinear finite element codes.

The significant shortcomings of this model include its failure to give a smooth elastoplastic transition during reverse loading, and its failure to develop a stable, symmetric hysteresis loop under cycling. This model has been applied to large strain deformation, often when combined with some form of isotropic hardening. For such a model, the permanent softening is a measure of the back stress prior to unloading. As discussed in section 2.2 recent work by Wilson and Bate [1986] show that this is not what is occurring physically. The permanent softening is *not* a good measure of the back stress in the lattice of the material.

Attempts have been made to generalize this model by letting C be a function of plastic strain, $C = \hat{C}(\bar{\epsilon}^p)$. This leads to inconsistencies since there then exists a unique relationship between the back stress and plastic strain [Chaboche,1986]. Other possibilities for functional dependence of C have not been generally explored. This could be a fruitful area of research. What is required is for C to be such that it gives the proper back stress increase during monotonic loading (which is a fairly slow increase) and a rapid change in back stress during reversing. Currently this

does not exist so the Prager kinematic hardening rule is generally not used for modeling cyclic behavior.

In the **mechanical sublayer model** a number of independent structural elements are deformed in parallel. Each element undergoes the same deformation but by having different flow strength and hardening (isotropic) properties a composite response is obtained. Models of this type have been proposed by Bessling [1953] and Bate and Wilson [1986]. This modeling concept does not allow the development of permanent softening although it does introduce a more gradual transition from elastic to reverse plastic flow. In order to achieve a good match with experiments many elements are required which adds many variables to the theory and increases the complexity.

The **Mroz model** [Mroz,1967] consists of a series of nested surfaces which can translate inside of one another. The plastic modulus is given as a function of the size of the active surface. The active surface is the largest surface which the stress point contacts. Once the active surface touches the next larger surface it no longer is active but just translates along with the stress point. The direction that the active surface translates in is given by the vector connecting the stress point with the point on the next larger surface having the same outward normal $\boldsymbol{n}$ as the active surface. This is illustrated in Figure B.1. This leads to a piecewise stress-strain curve with a large number of surfaces required to obtain a good fit to experiment.

For uniaxial cycling this model captures many of the important features described above (1-6) although it does poorly on the asymmetric cycling (7,8).

An important difference between the Mroz and Prager models is the direction of yield surface translation. For multiaxial loading they can be quite different. This

will be brought out in more detail when considering multiaxial, nonproportional cycling.

The two surface model was first introduced by Krieg [1975] and Dafalias and Popov [1976]. Conceptually it is similar to the Mroz model since it contains one surface (the yield surface) nested inside of the other (the bounding surface). In the Mroz model the plastic modulus equals its constant value associated with the outer active surface. In the two surface model the plastic modulus is given as a function of the distance between the yield and bounding surfaces. As illustrated in Figure B.2, when the loading direction is reversed the distance between the two surfaces is measured between points on the corresponding surfaces having the same outward normal $\mathbf{n}$. The magnitude of this distance is given as δ where δ_{in} represents this value when plastic flow is reinitiated. The direction of motion of the yield surface is given by the same rule as that of the Mroz model. That is, the direction of motion is given by the vector connecting the corresponding points on the two surfaces having the same $\mathbf{n}$.

Dafalias and Popov [1976] have chosen to represent the plastic modulus, E_p, by

$$E_p = \overline{E_p} + h(\delta_{in})\frac{\delta}{(\delta_{in} - \delta)}.$$

Here $\overline{E_p}$ represents the plastic modulus before unloading from contact with the bounding surface. Notice that this function satisfies the requirements for a smooth elastoplastic transition.

$$\delta = \delta_{in} \qquad E_p \to \infty,$$

$$\delta = 0 \qquad E_p = \overline{E_p}.$$

This model can be made to satisfy all of the criteria (1-7) although a small partial reverse load followed by reloading can cause a significant stress overshoot.

This is discussed by Dafalias [1984b] and Chaboche [1986]. The updating procedure chosen by Dafalias and Popov [1976] leads to this overshoot but it is not a necessary consequence of two surface models.

The evanscent hardening model is a phenomenological theory similar to Prager-Ziegler hardening except that the back stress evolution law is modified.

$$\dot{\mathbf{B}} = C_1 \mathbf{D}^p - C_2 \dot{\bar{\epsilon}}^p \mathbf{B}$$

Here the direction and magnitude of the motion of the yield surface are modified by the back stress. This gives a direction similar to the Mroz or two surface models. The functions C_1 and C_2 are taken to be constants or functions of plastic strain ϵ^p. This theory has been used by Armstrong and Frederick [1966], Chaboche [1983] and Nagtegaal and deJong [1982].

Here the back stress is removed more quickly during reverse flow than it builds up during monotonic loading. The plastic modulus is larger when plastic flow commences in the reverse direction than it had been during forward loading but there is not a smooth elastoplastic transition. Also the theory predicts a saturation of the back stress during uniaxial loading of $B_{11}^{sat} = C_1/C_2$ and no permanent softening. This theory then does not satisfy requirements (2) or (4).

This model has been used to model the shape of cyclic curves at one strain range, but often fails when the strain range is changed. The constant C_2 determines both how quickly the back stress builds up during monotonic loading *and* the degree of rounding of the stress-strain curve during reversing. A large value of C_2 is needed to adequately model the large stiffness during reversing but a small C_2 is required for the correct build up of back stress. Chaboche and Rousselier [1983] accomodated this by introducing *several* back stress variables, each with its own

evolution equation.

$$\mathbf{B} = \Sigma\, \mathbf{B}_i,$$

$$\dot{\mathbf{B}}_i \;=\; C_{1i}\mathbf{D}^p \;-\; C_{2i}\dot{\bar{\epsilon}}^p\mathbf{B}_i.$$

This improves the uniaxial modeling but greatly increases the complexity and storage requirements.

The work of Chaboche and his coworkers has been extensive in applying evanescent type models [Chaboche, 1986]. They have settled on a particular form where C_1 is a constant and C_2 is an increasing function of plastic strain.

A variation of the evanescent hardening rule has been proposed by Mroz [1981,1983]. In order to account for the history effect of the previous maxiamum stress, a maximal back stress surface is introduced. This keeps track of the maximum value of the equivalent back stress that has occured over the history of the deformation. For deformation occuring inside of this surface the isotropic component evolves to an asymptotic value which could involve hardening or softening. The scalars C_1 and C_2 are functions of the current, scalar equivalent back stress. Mroz claims that the new parameter (maximal equivalent back stress) is a way of taking into account the natural dependence of the Mroz model [Mroz, 1967] on the maximal back stress. In the Mroz [1967] model this dependence is incorporated through the relative configuration of the nested surfaces.

The **endocronic**, or internal time, theory of plasticity was first proposed and used by Valanis in the 1970's [Valanis, 1980]. The theory uses an internal time variable as the measure of the history of deformation. It is a measure of material memory.

Many engineers have avoided the endocronic theory because it does not resemble the more classical formulations. Plasticity laws have historically been formulated in terms of incremental or flow relationships due to the nature of the deformation process (dislocation glide in metals). The endocronic theory has been constructed using integrals over the deformation history. It has received recent attention because of its success in modeling some of the phenomena of cyclic plasticity.

Its success has derived from its flexibility of including many parameters to match experiments. At the heart of the theory lies the equation for the deviatoric stress $\mathbf{T}'$.

$$\mathbf{T}' = 2\mu \int \rho(z - z') \frac{\partial \epsilon^p}{\partial z'} dz',$$

where z is an internal time variable. The choice of the kernel $\rho(z)$ provides the flexibility of the model. Watanabe and Atluri [1986] showed that by proper choice of $\rho(z)$ the endocronic theory can be reduced , in its differential form, to any of the following: Prager-Ziegler kinematic hardening, Mroz model, two surface model, or evanescent hardening. The endocronic theory can then be seen as an overall framework for use in expressing many theories. In application, a specific kernel function must be postulated. This reduces the endocronic theory to more recognizable form.

In general then, the endocronic theory can satisfy any of the requirements of cyclic plasticity that the above models can. It does not make sense to discuss the model without specifying a particular kernel $\rho(z)$. Since the obvious kernels to use reduce to one of the above models it is logical to just analyze the models in the more recognizable flow formulation.

As discussed above, each of the models used for cyclic plasticity has certain strengths and weaknesses. The choice of a model depends in part upon the phe-

nomena most important for a given application. The Mroz, two surface, and evanescent models give qualitatively similar modeling capabalities. The two surface model has the advantage of specifying a smooth elastoplastic transition and a better simulation of random-type loadings and ratchetting effects (Chaboche [1986]). The evanescent hardening model has the advantage of easier numerical implementation and connection with internal variable theories.

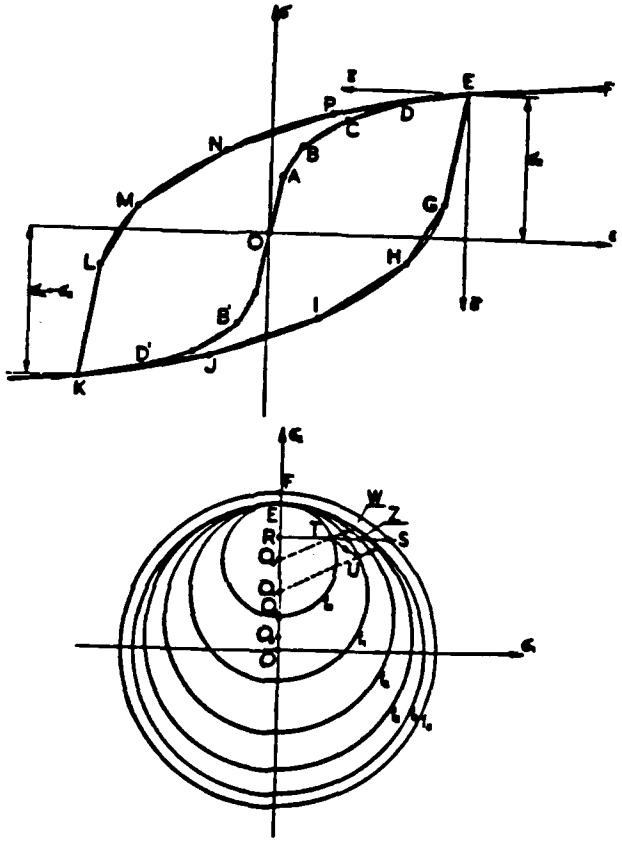

Figure B.1 Illustration of the Mroz [1967] model showing the piecewise linear approximation to the stress-strain curve and its multiaxial representation with nested yield surfaces.

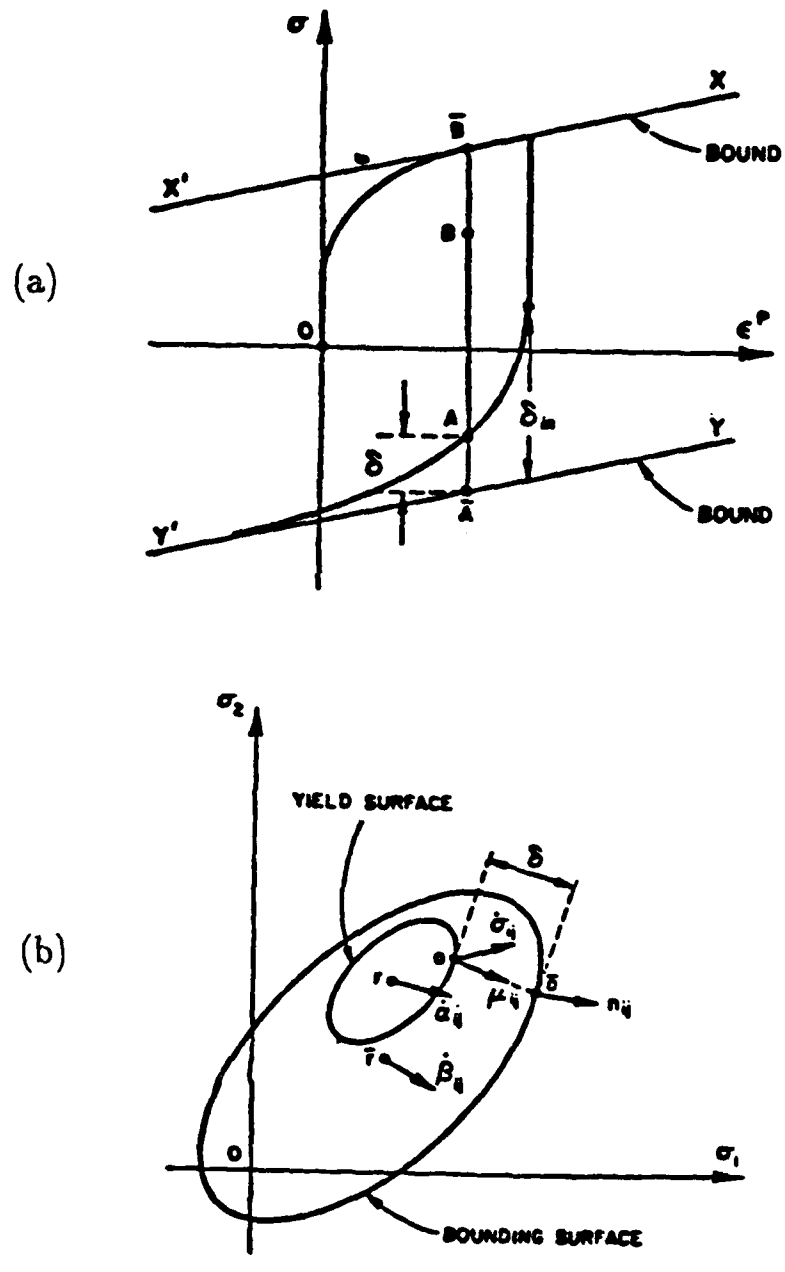

Figure B.2 Illustration of the two surface plasticity model. Both the (a) one dimensional and (b) multiaxial representations are shown.

DISTRIBUTION LIST

No. of Copies	To
1	Office of the Under Secretary of Defense for Research and Engineering, The Pentagon, Washington, DC 20301
	Commander, U.S. Army Materiel Command, 5001 Eisenhower Avenue, Alexandria, VA 22333-0001
1	ATTN: AMCLD
	Commander, U.S. Army Laboratory Command, 2800 Powder Mill Road, Adelphi, MD 20783-1145
1	ATTN: AMSLC-IM-TL
	Commander, Defense Technical Information Center, Cameron Station, Building 5, 5010 Duke Street, Alexandria, VA 22304-6145
2	ATTN: DTIC-FDAC
1	Metals and Ceramics Information Center, Battelle Columbus Laboratories, 505 King Avenue, Columbus, OH 43201
	Commander, Army Research Office, P.O. Box 12211, Research Triangle Park, NC 27709-2211
1	ATTN: Information Processing Office
	Commander, U.S. Army Electronics Technology and Devices Laboratory, Fort Monmouth, NJ 07703-5000
1	ATTN: SLCET-DT
	Commander, U.S. Army Missile Command, Redstone Arsenal, AL 35898-5247
1	ATTN: AMSMI-RD-ST
1	Technical Library
	Commander, U.S. Army Armament, Munitions and Chemical Command, Dover, NJ 07801
2	ATTN: SMCAR-TDC
	Commander, U.S. Army Natick Research, Development and Engineering Center, Natick, MA 01760
1	ATTN: Technical Library
	Commander, U.S. Army Tank-Automotive Command, Warren, MI 48397-5000
1	ATTN: AMSTA-R
	Commander, U.S. Army Engineer Waterways Experiment Station, P.O. Box 631, Vicksburg, MS 39180
1	ATTN: Research Center Library
	Director, U.S. Army Ballistic Research Laboratory, Aberdeen Proving Ground, MD 21005
1	ATTN: SLCBR-DD-T (STINFO)
1	SLCBR-IV-M, Dr. W. H. Drysdale
1	SLCBR-TB-W, Dr. J. Walter
1	SLCBR-TB-W, Dr. Thomas W. Wright
	Director, Benet Weapons Laboratory, LCWSL, USA AMCCOM, Watervliet, NY 12189
1	ATTN: AMSMC-LCB-TL
	Commander, U.S. Army Foreign Science and Technology Center, 220 7th Street, N.E., Charlottesville, VA 22901-5396
1	ATTN: AIAST-RA-ST
	Director, Eustis Directorate, U.S. Army Air Mobility Research and Development Laboratory, Fort Eustis, VA 23604-5577
1	ATTN: SAVDL-E-MOS (AVSCOM)
	Director, Langley Directorate, U.S. Army Air Mobility Research and Development Laboratory, NASA-Langley Research Center, Hampton, VA 23665
1	ATTN: Aerostructures Directorate
	Naval Research Laboratory, Washington, DC 20375
1	ATTN: Code 5830
	Office of Naval Research, 800 North Quincy Street, Arlington, VA 22217-5000
1	ATTN: Mechanics Division, Code 1132-SM

No. of Copies	To
	Naval Air Development Center, Warminster, PA 18974-5000
1	ATTN: Code 6064
1	AVCSTD/6043
	U.S. Navy David Taylor Research Center, Bethesda, MD 20084
1	ATTN: Code 172
	U.S. Air Force Office of Scientific Research, Bolling Air Force Base, Washington, DC 20332
1	ATTN: Mechanics Division
	Commander, U.S. Air Force Materials Laboratory, Wright-Patterson Air Force Base, OH 45433
1	ATTN: AFWAL/MLLN
	National Aeronautics and Space Administration, Marshall Space Flight Center, Huntsville, AL 35812
1	ATTN: EH01, Dir, M&P lab
1	Committee on Marine Structures, Marine Board, National Research Council, 2101 Constitution Avenue, N.W., Washington, DC 20418
	Director, U.S. Army Materials Technology Laboratory, Watertown, MA 02172-0001
2	ATTN: SLCMT-TML
1	Author

U.S. Army Materials Technology Laboratory,
Watertown, Massachusetts 02172-0001
A COMBINED ISOTROPIC-KINEMATIC HARDENING MODEL FOR LARGE DEFORMATION METAL PLASTICITY -
Charles S. White

Technical Report MTL TR 88-46, December 1988, 248 pp - illus-tables, D/A Project 1L2631020077

AD_____

UNCLASSIFIED
UNLIMITED DISTRIBUTION

Key Words

Plastic properties
Plastic deformation
Metals

The need for increased accuracy in material modeling has been driven in recent years by advances in computing capability and the complexity of problems which now may be analyzed. Current material models are unable to represent many of the important multi-dimensional effects of the plastic deformation of metals to large strain. These effects can become very important at the level of deformation reached in metal processing operations, shear band formation, penetration mechanisms, and crack tip processes. An experimental program was conducted to produce a number of different types of tests on several materials. The types of tests included: tension, large strain compression, symmetric cyclic, unsymmetric cyclic, single reverse and large strain torsion. Materials tested were type 316 stainless steel and 1100-0 aluminum. Also data for 3 carbon steels was analyzed. A new constitutive model for metal deformation is introduced to analyze and predict these experiments. The model contains both isotropic and kinematic hardening components but overcomes some of the shortcomings of previous such models by introducing new material functions. The two important new features are: 1) The back stress moduli depend upon the position of the back stress within a surface defined by its previous maximum norm, and 2) During a reversing event the isotropic component initially softens. The effects of these features are discussed and implemented using simple functions in the constitutive model. The model captures key features of small strain uniaxial cyclic behavior very well including the additional hardening due to nonproportional cycling in tension-torsion. The predictions of the finite torsion results are not as close. The inclusion of plastic spin does not affect these results.

U.S. Army Materials Technology Laboratory,
Watertown, Massachusetts 02172-0001
A COMBINED ISOTROPIC-KINEMATIC HARDENING MODEL FOR LARGE DEFORMATION METAL PLASTICITY -
Charles S. White

Technical Report MTL TR 88-46, December 1988, 248 pp - illus-tables, D/A Project 1L2631020077

AD_____

UNCLASSIFIED
UNLIMITED DISTRIBUTION

Key Words

Plastic properties
Plastic deformation
Metals

The need for increased accuracy in material modeling has been driven in recent years by advances in computing capability and the complexity of problems which now may be analyzed. Current material models are unable to represent many of the important multi-dimensional effects of the plastic deformation of metals to large strain. These effects can become very important at the level of deformation reached in metal processing operations, shear band formation, penetration mechanisms, and crack tip processes. An experimental program was conducted to produce a number of different types of tests on several materials. The types of tests included: tension, large strain compression, symmetric cyclic, unsymmetric cyclic, single reverse and large strain torsion. Materials tested were type 316 stainless steel and 1100-0 aluminum. Also data for 3 carbon steels was analyzed. A new constitutive model for metal deformation is introduced to analyze and predict these experiments. The model contains both isotropic and kinematic hardening components but overcomes some of the shortcomings of previous such models by introducing new material functions. The two important new features are: 1) The back stress moduli depend upon the position of the back stress within a surface defined by its previous maximum norm, and 2) During a reversing event the isotropic component initially softens. The effects of these features are discussed and implemented using simple functions in the constitutive model. The model captures key features of small strain uniaxial cyclic behavior very well including the additional hardening due to nonproportional cycling in tension-torsion. The predictions of the finite torsion results are not as close. The inclusion of plastic spin does not affect these results.

U.S. Army Materials Technology Laboratory,
Watertown, Massachusetts 02172-0001
A COMBINED ISOTROPIC-KINEMATIC HARDENING MODEL FOR LARGE DEFORMATION METAL PLASTICITY -
Charles S. White

Technical Report MTL TR 88-46, December 1988, 248 pp - illus-tables, D/A Project 1L2631020077

AD_____

UNCLASSIFIED
UNLIMITED DISTRIBUTION

Key Words

Plastic properties
Plastic deformation
Metals

The need for increased accuracy in material modeling has been driven in recent years by advances in computing capability and the complexity of problems which now may be analyzed. Current material models are unable to represent many of the important multi-dimensional effects of the plastic deformation of metals to large strain. These effects can become very important at the level of deformation reached in metal processing operations, shear band formation, penetration mechanisms, and crack tip processes. An experimental program was conducted to produce a number of different types of tests on several materials. The types of tests included: tension, large strain compression, symmetric cyclic, unsymmetric cyclic, single reverse and large strain torsion. Materials tested were type 316 stainless steel and 1100-0 aluminum. Also data for 3 carbon steels was analyzed. A new constitutive model for metal deformation is introduced to analyze and predict these experiments. The model contains both isotropic and kinematic hardening components but overcomes some of the shortcomings of previous such models by introducing new material functions. The two important new features are: 1) The back stress moduli depend upon the position of the back stress within a surface defined by its previous maximum norm, and 2) During a reversing event the isotropic component initially softens. The effects of these features are discussed and implemented using simple functions in the constitutive model. The model captures key features of small strain uniaxial cyclic behavior very well including the additional hardening due to nonproportional cycling in tension-torsion. The predictions of the finite torsion results are not as close. The inclusion of plastic spin does not affect these results.

U.S. Army Materials Technology Laboratory,
Watertown, Massachusetts 02172-0001
A COMBINED ISOTROPIC-KINEMATIC HARDENING MODEL FOR LARGE DEFORMATION METAL PLASTICITY -
Charles S. White

Technical Report MTL TR 88-46, December 1988, 248 pp - illus-tables, D/A Project 1L2631020077

AD_____

UNCLASSIFIED
UNLIMITED DISTRIBUTION

Key Words

Plastic properties
Plastic deformation
Metals

The need for increased accuracy in material modeling has been driven in recent years by advances in computing capability and the complexity of problems which now may be analyzed. Current material models are unable to represent many of the important multi-dimensional effects of the plastic deformation of metals to large strain. These effects can become very important at the level of deformation reached in metal processing operations, shear band formation, penetration mechanisms, and crack tip processes. An experimental program was conducted to produce a number of different types of tests on several materials. The types of tests included: tension, large strain compression, symmetric cyclic, unsymmetric cyclic, single reverse and large strain torsion. Materials tested were type 316 stainless steel and 1100-0 aluminum. Also data for 3 carbon steels was analyzed. A new constitutive model for metal deformation is introduced to analyze and predict these experiments. The model contains both isotropic and kinematic hardening components but overcomes some of the shortcomings of previous such models by introducing new material functions. The two important new features are: 1) The back stress moduli depend upon the position of the back stress within a surface defined by its previous maximum norm, and 2) During a reversing event the isotropic component initially softens. The effects of these features are discussed and implemented using simple functions in the constitutive model. The model captures key features of small strain uniaxial cyclic behavior very well including the additional hardening due to nonproportional cycling in tension-torsion. The predictions of the finite torsion results are not as close. The inclusion of plastic spin does not affect these results.